Eye-safe Er:YAG Lasers for Coherent Remote Sensing

by

Nick W. Chang

Thesis submitted for the degree of
Doctor of Philosophy

in

The University of Adelaide

School of Chemistry and Physics

August, 2012

Contents

Abstract

Multi-watt lasers with an output wavelength in the eye-safe band are required for many remote sensing applications, including Doppler or coherent laser radars (CLR's). Er:YAG lasers at 1617 nm or 1645 nm operating on the $^4I_{13/2}$ to $^4I_{15/2}$ transition can potentially satisfy this need. Although this transition has been known for many years, the development of diode pumping makes these lasers practical.

Doppler wind-field mapping requires single frequency, diffraction limited pulses at a high pulse repetition frequency (PRF) to provide a spatially dense array of samples, allow signal averaging with minimal loss of temporal resolution and to minimize the time required to scan an extended volume. Pulses with energies >few mJ and pulse durations of >100 ns are essential for these measurements. Such requirements can be satisfied by continuous-wave (CW) pumping of a Q-switched free-space laser.

In this thesis I describe the design and development of a single frequency, continuous wave, Er:YAG laser at 1645 nm that uses resonant pumping at 1470 nm. With an intra-cavity polarizer and uncoated etalon, it produces up to 30 mW in a narrow line-width, single frequency, plane polarized, diffraction limited, TEM_{00} output. The laser is suitable as a master oscillator of a CLR.

I also describe the development and characterization of an efficient high power Er:YAG laser that is resonantly pumped using CW laser diodes at 1470 nm. For CW lasing, it emits 6.1 W at 1645 nm with a slope efficiency of 40%, the highest efficiency reported for an Er:YAG laser that is pumped in this manner. In Q-switched operation, the laser produces diffraction-limited pulses with an average power of 2.5 W at 2 kHz PRF, and thus is suitable as the slave oscillator of a CLR. To our knowledge this is the first Q-switched Er:YAG laser resonantly pumped by CW laser diodes.

This thesis also presents an experimental investigation of the observed reduction in the average output power of Q-switched Er:YAG lasers at low PRF. The experimental results are compared with the predictions of a theoretical model developed using rate equations so the primary causes can be determined, and thus could be minimized in a future design.

Statement of Originality

This work contains no material which has been accepted for the award of any other degree or diploma in any university or other tertiary institution and, to the best of my knowledge and belief, contains no material previously published or written by another person, except where due reference has been made in the text.

I give consent to this copy of my thesis when deposited in the University Library, being made available for loan and photocopying, subject to the provisions of the Copyright Act 1968.

The author acknowledges that copyright of published works contained within this thesis resides with the copyright holder(s) of those works.

SIGNED: ....

DATE: ....

Supervisors: A/Prof. Peter J. Veitch and Prof. Jesper Munch.

Acknowledgments

First and foremost, I would like to extend my utmost gratitude to my supervisors, Peter Veitch and Jesper Munch. You provided me with an opportunity to work on this project and, moreover, you equipped me both academically and personally, while helping me discover the greatness of science. Your support ultimately motivated me to undertake research in Antarctica as a Lidar scientist - something I would have never dreamt of doing. I would especially like to convey my appreciation for proofreading this thesis while I have been located at this remote site down South.

I would also like to express thanks to David Ottaway whom helped supervise and guide me during the latter stages of this project, and to Murray Hamilton for his help and advice.

To David Hosken and to Won Kim, words cannot express my gratitude for your friendship and encouragement and for your offers of advice and direction during my PhD journey. I am grateful and thankful for having had seniors like you looking after me.

To Blair Middlemiss, Neville Wild and Trevor Waterhouse, thank you for providing excellent technical assistance and support when developing the hardware for the project. To the staff in the school: Carol, Jeanette, Mary, Ramona, Wayne and the rest of the front office staff - thank you for your administrative support and for caring for me during my studies.

To my colleagues in the optics group: Alex, Ka, Keiron, Lachlan, Matthew, Miftar, Muddassar, Nikita, Ori, Sean, Tom and the rest of the group. Thank you for the great times and memories from my time in Adelaide - I especially appreciate the coffees with many of you, as without them I couldn't have overcome the difficult times.

Finally, I would like to thank my Mum, Dad, Sisters, Kim, and my church friends. It's a blessing having you people in my life. Truly, I couldn't have done this without your love and support.

> *"Call to me and I will answer you and tell you great and unsearchable things you do not know."* – Jeremiah 33:3

Nick Chang, August 2012

List of Symbols

η_{abs}	Pump absorption fraction
η_{eff}	Pump delivery efficiency
η_{mode}	Mode overlap efficiency
η_{slope}	Slope efficiency
γ	Gain coefficient
λ	Wavelength
σ_{al}	Effective absorption cross section of the laser wavelength
σ_{ap}	Effective absorption cross section of the pump wavelength
σ_{el}	Effective emission cross section of the laser wavelength
σ_{ep}	Effective emission cross section of the pump wavelength
σ_l	Absorption cross section for the laser transition
σ_p	Absorption cross section for the pump transition
τ_s	Upper state storage lifetime
$\triangle_l$	Laser inversion density
$\triangle_l^z$	Laser inversion density per unit area (Rod-integrated)
$\triangle_p$	Pump inversion density
$\triangle_p^z$	Pump inversion density per unit area (Rod-integrated)
A_p	Pump cross section area
C_{up}	Upconversion rate
f_{lens}	Effective focal length of the thermal lens
F_c	Cavity finesse
f_l	Fractional Boltzmann population of the laser transition
f_p	Fractional Boltzmann population of the pump transition

G	Round trip gain of the laser
h_s	Gain medium height
I_l	Laser intensity
I_p	Pump intensity
L_{cav}	One-way cavity loss
l_s	Gain medium length
M^2	Beam propagation factor
N_2^z	Excited manifold density per unit area (Rod-integrated)
N_2^{Total}	Total excited upper-state (N2) population
N_t	Doping cencentration per unit volume
$P_{av(\text{CW})}$	Average power in CW operation
P_{cav}	Laser intra-cavity power
P_{out}	Output power
P_p	Pump power
P_{th}	Threshold power
r_0	Radius of the waist
R^t_{laser}	De-excitation rate via lasing
R_{oc}	Reflectivity of the output coupler
R^t_{pump}	Pump excitation rate
R_p	Reflectivity of the coating for double pass pumping
r_p	Radus of the pump
r_s	Radius of the gain medium
t_{scatter}	Backscatter time
v_l	Frequency of the laser wavelength
V_{pump}	Volume pumped by the pump light
v_p	Frequency of the pump wavelength
W_{ij}	Radiative decay rate from level i to level j

w_s	Gain medium width
AOM	Acousto-optic modulator
AR	Anti-reflection
BD	Beam diameter
CPFS	Coplanar folded slab
CW	Continuous wave
DA	Full divergence angle
DI	Deionized
EDFL	Erbium doped fibre laser
EO	Electro-optic
ESA	Excited state absorption
ETU	Energy-transfer-upconversion
FSR	Free spectral range
FWHM	Full width half maximum
GSD	Ground-state depletion
LIDAR	Light detection and ranging
MP	Multi-phonon
NA	Numerical aperture
OSA	Optical spectrum analyzer
PBSC	Polarization beam splitter cube
PRF	Pulse repetition rate
QWP	Quarter-wave plate
RTP	Rubidium Titanyle Phosphate
TEC	Thermo-electic cooler
TFP	Thin film polarizer
YAG	Yttrium aluminum garnet

List of Figures

List of Tables

1 Introduction

1.1 Atmospheric sensing using lidar

In a rapidly changing world with increasingly complex and competing socio-economic, defence and environmental pressures and constraints, the gathering of accurate and reliable data is a major issue that directly affects the validity of subsequent outcomes. This is particularly true for precision monitoring of the atmosphere and its boundary layer, where the sensitivity of currently available sensors greatly limits the utility of the data. There is a lack of sensors that can economically provide accurate and precise, high spatial and temporal resolution wind measurements covering large scale atmospheric volumes [1]. Precise wind-speed measurement is especially important for wind-power production as the power in the wind is proportional to the cube of the wind speed [2] and turbulence can affect reliability and lifetime of wind turbines and their components.

'Light detection and ranging' (LIDAR) is a remote sensing technique that uses a laser beam to probe the atmosphere by measuring/monitoring the backscattered light. The acronym 'LIDAR' for this kind of measurement technique was first introduced by Middleton and Spilhaus [3] in 1953. The name lidar is an analogy to radar ('radio detection and ranging'). The invention of the laser in 1960 [4] and of the giant pulse laser in 1962 [5] provided a powerful new tool for remote sensing.

Lidar systems measure the range of a target using short pulses of light. As a pulse propagates through the atmosphere, light is continuously scattered by air molecules

Figure 1.1: The schematic of a LIDAR system [6].

and by larger particles (water droplets, aerosols, etc.). A tiny fraction of the light is scattered back toward the receiver as shown in Figure 1.1. The detected signal is then analyzed to determine the properties of the target.

Assuming the pulse duration is negligible, the range, R, of the particles responsible for the backscatter can be determined from the time elapsed since the pulse emission, t_{scatter}, using:

$$R = \frac{ct_{\text{scatter}}}{2} \tag{1.1}$$

However, the pulse has a non-zero duration, τ_p. Since the detected light could have been scattered from any part of the pulse, there is an uncertainty in the range, or "range confusion", given by half the length of the pulse. Table 1.1 shows the minimum spatial resolution versus pulse duration.

Pulse duration, τ_p (ns)	Pulse length (m)	Minimum spatial resolution (m)
200	60	30
400	120	60
800	240	120

Table 1.1: Spatial resolution versus pulse duration.

Since the single to noise ratio (SNR) of the lidar is proportional to average power [7], the pulse repetition frequency (PRF) of low-pulse-energy systems should be as high as possible, but can not exceed the maximum value $\mathrm{PRF}_{\mathrm{max}}$:

$$\mathrm{PRF}_{\mathrm{max}} = \frac{c}{2R_{\mathrm{max}}}. \tag{1.2}$$

as the time between pulses (1/PRF) must be longer than the round trip time of flight of the pulse to the greatest range R_{max} to be measured. Table 1.2 shows the maximum lidar ranges that can be achieved for different PRFs.

PRF (kHz)	Max range (m)
10	15000
20	7500
50	3000

Table 1.2: $\mathrm{PRF}_{\mathrm{max}}$ versus lidar range.

1.2 Coherent lidar

There are two detection schemes for lidar: direct (or "incoherent") detection and coherent detection.

The direct detection scheme measures the intensity, time of flight, and polarization of the light backscattered by aerosols and dust. This allows the profiles of aerosol features [8,9] and boundary layer structure [10,11] of the atmosphere to be measured and monitored.

The coherent detection scheme is used for Doppler measurement or phase sensitive measurements. Coherent lidar, also known as coherent laser radar (CLR), determines the velocity of the target by measuring the frequency change of backscattered light due to the Doppler shift that is produced by the relative motion between its target and the lidar system. It can be used to measure the density, and wind speed of the scatterers as a function of range. Extensive studies [12–15] of the movement of aerosols, caused by atmospheric phenomena, have been investigated using CLR.

A system layout of a monostatic CLR is shown in Figure 1.2. The pulsed slave laser is injection seeded by light from a single-frequency master laser to make the pulsed laser produce a transform-limited pulse. A frequency shift is applied to the seeding beam to enable the direction of the radial wind velocity component to be determined unambiguously. The frequencies of the light in the transmitted pulse and that backscattered from the atmosphere are measured, relative to the frequency of the master laser, using the heterodyne photo-detectors (Detector 1 and 2).

Figure 1.2: A schematic of a coherent laser radar system [6].

The heterodyne beat signal is analyzed to retrieve the Doppler frequency shift, f_{doppler}, and thus calculate the line-of-sight or radial wind velocity, v, using:

$$v = \frac{f_{\text{doppler}}}{2}\lambda \tag{1.3}$$

where λ is the wavelength of the lidar transmitter. For example, for a target speed of

$\sim$ 20 km/hour, the Doppler frequency shift is about 10 MHz for a lidar wavelength of 1 µm.

In pulsed Doppler lidar at any particular wavelength, range and velocity resolution are competing performance specifications. As the transmitted pulse width τ_p is decreased to achieve improved range resolution, the spectral bandwidth of the pulse increases approximately as $1/(2\pi\tau_p)$ [16]. As the bandwidth increases, it becomes increasingly difficult to estimate the spectral peak in the presence of noise, and hence velocity precision suffers. Measurement in a single pulse is limited to a "range-velocity product" [17] of

$$\triangle V \triangle R \geq \frac{c\lambda}{8\pi} \tag{1.4}$$

where $\triangle V$ is the velocity resolution and $\triangle R$ is the range resolution. The trade-off range between these parameters can generally be improved by using a shorter wavelength.

1.3 Summary of published CLR systems

Until 1987, tunable CO_2 lasers at 9-11 µm were the only reported lidar systems [12, 18, 19]. These systems were capable, in general, of ranges >10 km [12, 18–25]. However, the majority of these systems had a range resolution on the order of 100's of meters [12, 18–21, 23, 24] and averaging over many pulses was required to obtain velocity resolutions <1 ms^{-1}. These systems also suffered from eye-safety concerns, compared to lidar operating in the eye-safe band, and the laser transmitters were large and bulky.

Tm/Ho systems operating at 2.1 µm [26] have advantages over CO_2 systems in terms of weight, size, operating lifetime and detectors. They also have less beam divergence for a given transmitter aperture and can have better range-resolved, single-shot velocity resolution. These systems have demonstrated ranges of >10 km

[16,27–33], but have a better range-velocity product [17] than CO_2 systems. They also offer better eye-safety.

Nd:YAG systems at 1 µm offer the best range-velocity product [15,34,35], and have reported atmospheric returns from a range of 26 km [15]. However the very low maximum permissible exposure for eye-safety makes systems at this wavelength unattractive.

1.4 Eye-safe CLR systems

Wavelengths between 1.4 µm and 1.8 µm are strongly absorbed by the cornea and vitreous humor of the eye [36], which is composed primarily of liquid water [37]. Light in this wavelength band is therefore attenuated significantly before reaching the retina, and this band of wavelengths is referred to as the 'eye-safe band'. As a result, more energy can be transmitted into the sky safely by systems operating in this wavelength band than systems operating at other wavelengths, which results in a greater range. A 1.6 µm system has a maximum permissible exposure that is 10x greater than that of a 2 µm system for a single pulse, and thus has a factor of 3 greater range.

There are several ways to obtain radiation in the eye-safe band including 1.5 µm Er-doped Fiber lasers (EDFL's) [38], 1.5 µm and 1.6 µm free-space erbium lasers [39–41] and the Nb-based lasers that employ nonlinear optical parametric oscillators (OPOs) [42].

EDFLs systems may have weight and volume advantages, however the very low pulse energies limits ranges to <2 km [38,43–47], even when averaging over tens of thousands of pulses. While the time required for such averaging might be reduced by increasing PRF, the max PRF for this range is 75 kHz.

Eye-safe laser beam generation using Nd/OPO systems has many advantages due to the maturity of Nd lasers and proven power-handing capability. Although average powers >30 W has been demonstrated with these systems [48], this multistage approach increases the number of components and thus adds difficulties when designing a rugged and reliable package. Moreover, the overall system (wall-plug) efficiency is limited by the optical conversion efficiencies of each stage.

Yb,Er:Glass lasers are an alternative to Nd-based eye-safe systems, as they emit eye-safe radiation directly, typically at ~1.54 µm, thus making such systems less complex. The use of free-space Yb,Er:Glass for coherent lidar at 1.535 µm was pioneered at The University of Adelaide [39], who demonstrated that an Yb,Er:glass slave laser could be injection-seeded to produce transform-limited pulses as required for coherent lidar, and that the pulses could be used for accurate measurement of the velocity of a diffusely reflecting hard target. However, the pulsed laser was lamp-pumped, and was thus very inefficient and could only be pulsed at very low repetition rates.

The free-space Yb,Er:glass CLR subsequently reported by Mitsubishi [49] produced 11 mJ pulses, but with an optical efficiency of only ~1%. It demonstrated ~6 km range after averaging 20 pulses, yielding a temporal resolution of ~1 s.

Heintze *et. al.* [6] reported development of a prototype diode-pumped Yb,Er:glass lidar. The Yb,Er:glass lidar transmitter consisted of a CW master laser and a Q-switched slave laser. A schematic of the Q-switched slave laser is shown in Figure 1.3. Light from the master laser injection-seeds the slave ring resonator via the polarizing beam splitter cube (PBSC). The slave laser resonator was designed to allow only TEM_{00} modes to oscillate.

The Pockels cell controls both the Q-switching and the out-coupling of the pulse. The gain medium was a co-planar folded zigzag slab [50,51] made from Kigre QX/Er alpha 17, Cr,Yb,Er:phosphate glass. It was side-pumped and conduction cooled through the top and bottom faces. The pump diodes were quasi-cw laser diodes at 976 nm, the output of which was fast-axis collimated using a Doric gradient-index cylindrical lens.

Figure 1.3: Schematic of the University of Adelaide Yb,Er:glass slave laser [40]. Abbreviations: FW denotes the forward wave; RW denotes reverse wave; BAW, Brewster's angle wedge; PZT, piezoelectric transducer, on which one of the resonator mirrors is mounted.

The slave laser was injection-seeded by a single-frequency (10 kHz line-width) EDFL master oscillator. A frequency shift (40 MHz) was applied to the injection-seeding beam using an acousto-optic modulator (AOM), to enable the direction of the radial wind velocity component to be determined unambiguously.

The beam quality of the output was M_h^2=1.4 and M_v^2=1.4 in the horizontal and vertical directions, respectively, which proved adequate for CLR applications [52], since they are comparable to the wavefront aberrations introduced by typical day-time refractive turbulence in the atmosphere. This Yb,Er:glass system was able to obtain range-resolved returns from the atmosphere with a range $>$ 2 km with a range and single-pulse velocity resolution of 75 m and 1.5 ms^{-1} respectively, from 1.1 mJ pulses.

However, the range and temporal resolution of the system were greatly limited by the performance of the Yb,Er:glass CLR. To improve the performance of the CLR, the pulsed laser should have a higher pulse energy and run at higher PRF. The poor thermal properties of the glass host limits the ability to scale this laser to high average powers [53].

Recently, a 1.62 µm Er:YAG CLR has been reported [32]. It produces a pulse energy of ∼3 mJ and has demonstrated signals from ranges approximately double that of the Mitsubishi system. This system uses a single-mode diode laser as the master oscillator. The broad bandwidth (∼1 MHz) of such diodes would limit single pulse velocity resolution to about 1 ms^{-1}.

1.5 Er:YAG lasers for CLR

Er:YAG gain media can potentially achieve higher average powers than the glass host, because the YAG crystalline host has a thermal conductivity about 15x higher than glass.

In addition, removal of the Yb sensitizer eliminates the possibility of back-conversion (BC) loss. Although sensitized erbium has the advantage of high pump absorption by using large Yb doping levels, if the relative Yb-Er concentration is not optimized, a back transfer process can occur, in which energy flows back to the Yb^{3+} sensitizer [54]. The energy back-conversion path in Yb,Er:glass is shown in Figure 1.4.

Figure 1.4: Energy back conversion (BC) path in Yb-sensitized Er^{3+} systems [55].

Er:YAG lasers can be resonantly pumped at either 1470 nm or 1532 nm as shown in Figure 1.5. The high quantum efficiency minimizes the waste heat from the pumping process and reduces thermally induced lensing and birefringence, thus yielding a laser that can operate efficiently at a variety of power levels. Unfortunately, it has a relatively small pump absorption cross-section, necessitating the use of either end pumping or higher doping levels.

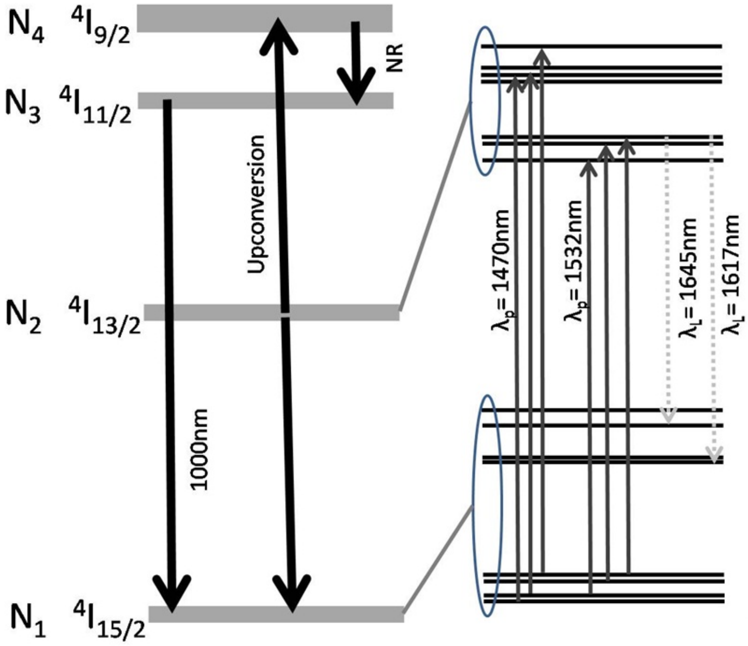

Figure 1.5: Energy-level diagram for Er:YAG. $N_1 - N_4$ correspond to the four lowest electronic states.

The earliest report of a resonantly pumped erbium laser was published by Killinger in 1989 [56]. The laser was cooled to 77 K and produced 25 mW CW output at 1645 nm using a 200 mW, 1470 nm F^+ center pump laser. Spariosu and Birnbaum [57, 58] successfully demonstrated room-temperature lasing at 1.6 µm with slope efficiencies up to 40%. They concluded that upconversion effects should not significantly hinder operation for 0.5% – 4% doping levels.

1.5.1 Fiber-laser-pumped Er:YAG lasers

More recently, EDFL's have been used to pump Er:YAG lasers because their narrow bandwidth and good pump beam quality improve pump absorption and spatial overlap of the pumped region with the laser mode. Er:YAG lasers pumped by EDFL's have been reported by many authors, as shown in Table 1.3.

EDFL pump power (W)	CW output power (W)	CW slope efficiency (%)	Q-switched performance	Reference
18	5	30	0.52 mJ/9 kHz	Setzler *et al* [59]
17	7	50	3.4 mJ/1.1 kHz	Young *et al* [60]
15	4.6	~35	6.5 mJ/1 kHz	Stoneman *et al* [41, 61, 62]
82	60.3	73	N/A	Shen *et al and* Jander *et al* [63–65]
72	31 (1617nm)	47	N/A	Kim *et al* [66]
72	20.9	~35	4.5 mJ / 2.5 kHz	Kim *et al* [67]
23	5.5 (1645 nm) 3 (1617 nm)	30 19	2 mJ/3 kHz	Spariosu *et al* [68]
16	8	57	4 mJ/1 kHz – 6 mJ/400 Hz	Chen *et al* [69, 70]
20	11	78	1.1 mJ/10 kHz	Moskalev *et al* [71]

Table 1.3: Summary of the early reported resonantly EDFL-pumped Er:YAG lasers.

The first EDFL-pumped erbium laser was published by Setzler *et al* in 2003 [59]. A 1.1 cm-long 1% Er:LuAG crystal was pumped by a 20 W unpolarized fiber laser at 1.53 µm and delivered 5 W CW output at 1.65 µm with a slope efficiency of 40%. The laser was Q-switched, and the maximum average output power was 4.8 W. The highest pulse-energy, 0.52 mJ, was generated at 9 kHz PRF with a pulse-width of 85 ns. This result demonstrated that resonantly pump erbium lasers could operate efficiently when repetitively Q-switched.

In 2004, further work on EDFL-pumped Er:YAG lasers was reported by the same group (Setzler *et al* [72] and Young *et al* [60]). They achieved a maximum CW output of 7 W at 1645 nm with a slope efficiency of 50% and 3.4 mJ repetitively Q-switched pulses at 1.1 kHz.

The highest reported power and slope efficiency (output power/incident pump) are 60 W and 80% respectively [66, 67].

However, pumping using EDFL's adds complexity, weight and volume to a laser system [73]. Additionally, the overall optical efficiency with EDFL pumping is typically only about 28% due to the efficiency of the EDFL [67]. For a compact, robust and efficient laser system, the fiber laser pumped architecture therefore seems to be less advantageous.

1.5.2 Diode-pumped Er:YAG lasers

Er:YAG lasers can also be resonantly pumped using InGaAsP/InP laser diodes [74] as indicated in Table 1.4.

Pump diode	CW output power	Q-switched performance	Reference
120 W/10Hz, 1.47 µm (Linewidth narrowed)	170 mJ/10Hz (QCW)	6.3 mJ/3 kHz	Setzler *et al* [55]
275 mW, 1.47µm 110 W /5ms, 1.47µm 300 W, VBG-1.5µm 300 W, VBG-1.5µm 650 W, VBG-1.47µm	6 mW 0.9 J/1 Hz (QCW) 51W 80W 50W	N/A	Garbuzov *et al* and Kudryashov *et al* [74–78]
50W, VBG-1.5µm	9W	N/A	Eichhorn [73, 79]

Table 1.4: Summary of the early resonantly diode-pumped Er:YAG lasers.

Garbuzov *et. al.* [74, 75] demonstrated the first low-power, high-brightness diode-pumped Er:YAG laser using an InP high-brightness fiber-coupled laser diode at 1470 nm. A CW output power of about 6 mW was achieved for 275 mW of input pump power.

In 2005 Setzler *et. al.* [55] reported a direct-diode-pumped Er:YAG laser operating in both quasi-CW and Q-switched modes using high-power, low-brightness diodes. The outputs of the low-brightness diodes were coupled into the gain-medium using a lens duct. Due to the highly divergent (∼40º half angle) pump beam, the Er:YAG rod had polished barrels with a thick SiO_2 coating to allow total internal reflection (TIR) to confine the pump beam for high-intensity pumping.

In 2007 Kudryashov *et. al.* [77, 78] demonstrated higher CW laser powers of 50 W and 80 W resonantly pumped at 1.5 µm and 1.47 µm, respectively, using volume-Bragg-grating (VBG) linewidth-narrowed diodes. The highest slope efficiency achieved was 29% using 1470 nm diodes. These results showed the potential of power-scaling resonantly diode-pumped Er:YAG lasers.

Eichhorn [73, 80] reported an alternative pumping approach using fiber coupled, high-spatial and high-spectral brightness laser diodes at 1.5 µm. The grating-narrowed linewidth and low divergence fiber-coupled pump allowed better absorption and mode overlap. Thus 9 W of CW output power was achieved with a slope efficiency of about 45%. This work showed that direct diode-pumped systems are simpler, lighter, and more compact than EDFL-pumped systems, while still be able to obtain a good slope efficiency.

While pumping using 1.5 µm diodes has yielded high output powers and slope efficiencies, pumping using 1.47 µm diodes may have advantages, as it utilizes a broader absorption feature in Er:YAG [72, 78]. As shown in Figure 1.6, the broad absorption band in Er:YAG near 1470 nm allows good spectral overlap with wide-band diodes, and thus should be less sensitive to wavelength shifting of the diodes due to temperature drift.

Additionally, as will be discussed in Chapter 2, pumping at 1470 nm offers 20% higher maximum pump inversion density than that of 1532 nm due to the wavelength dependance of the normalized Boltzmann factors in Er:YAG. This should reduce the effect of ground-state-depletion in lightly-doped Er:YAG lasers.

Figure 1.6: Absorbed fractions (blue and black plots) after typical wide-bandwidth diode pump emissions propagated through 15-mm long Er:YAG crystal. The wavelengths of the diodes were tuned to the centre of the absorption bands of Er:YAG near 1470nm and 1530nm Pump bleaching effects were neglected [78].

1.6 Thesis overview

This thesis reports the development of Er:YAG lasers suitable for use in a CLR that can have a single-pulse velocity resolution <1 ms^{-1}, a PRF of >100 Hz and pulse energies >few mJ. It includes a single-frequency master laser and a Q-switched slave laser. The high PRF was required to allow the measurement of a spatially dense array of samples, signal averaging with minimal loss of temporal resolution and to minimize the time required to scan an extended volume.

The single-pulse velocity resolution requirement also facilitates a good temporal resolution as it reduced the need for averaging of measurements over many pulses. It can only be achieved, however, if the fluctuation in the frequency of the master laser during the pulse flight time is less than the associated Doppler shift: <<1.2 MHz/ms at 1645 nm for time delays greater than about 100 µs.

It also requires that the pulse has a duration >100-200 ns and is transform limited, as the relatively narrow Fourier spectrum of such a pulse would facilitate the measurement of small Doppler shifts.

The structure of this thesis reflects steps involved in the design modeling, development, and testing of the lasers. In Chapter 2 the theory of quasi-three-level Er:YAG lasers is discussed, and two numerical models used to simulate the diode-pumped master laser are described.

Chapter 3 describes the development of a 1470 nm-diode-pumped laser head for the master laser. The characterization and performance of the single frequency Er:YAG master laser is described. The results are compared with models described in Chapter 2.

Chapter 4 describes the design and construction of a high power laser head for use in the pulsed laser. Characterization of the laser head while configured in a standing-wave resonator is presented.

Chapter 5 describes the development and characterization of the Q-switched slave laser. The initial Q-switched laser is firstly described, followed by a more robust Q-switched laser. This chapter concludes with a description of the characterization of the final Q-switched laser.

Chapter 6 presents an investigation of up-conversion, excited state absorption in the pulsed laser. An investigation of pump bleaching due to ground-state-depletion is also described. Optimum Q-switched Er:YAG designs are investigated using a rate equation model to minimize these losses for future Q-switched Er:YAG lasers.

Finally in Chapter 7, the performance of the eye-safe Er:YAG lasers is summarized, and potential future refinements that could be incorporated are discussed.

2 Er:YAG laser theory

2.1 Introduction

This chapter investigates the design of a diode-pumped Er:YAG laser using two quasi-three-level laser models. The laser parameters are checked and optimized using the models for the development of a master oscillator for a CLR transmitter.

The properties of the Er:YAG gain medium host are discussed in Section 2.2. The quasi-three-level nature of Er:YAG lasers are described in Section 2.3. Two numerical models were studied and employed to predict the performance of the proposed master laser design in Sections 2.4 and 2.5. This chapter concludes in Section 2.6 with a summary of the predicted results of an Er:YAG laser and the chosen parameters of the laser design.

2.2 Er:YAG gain medium

2.2.1 Physical properties

Er:YAG consists of the well known and widely used yttrium aluminum garnet (YAG, $Y_3Al_5O_{12}$) in which some of the trivalent aluminum ions are substituted by the laser active trivalent erbium ions (Er^{3+}). YAG is a popular host for laser gain media because it has a number of attractive properties compared to other laser hosts. For example, the thermal conductivity of YAG is about 20 times higher than glass and hence offers improved cooling and allows high average output power operation. Some of the important physical parameters are listed in Table 2.1.

Parameter	Value
Refractive index	1.838 at 632.8 nm
Density	4.56 g/cm^3
Mohs hardness	8.5
Thermal conductivity	0.13 Wcm^{-1}C^{-1}
Thermo-optic coefficient	9.8x10^{-6} C^{-1}
Melting point	1970 C

Table 2.1: Physical parameters of Er:YAG crystal [81].

2.2.2 Electronic energy structure

The trivalent erbium ion has a partially filled 4f shell. The number of 4f electrons and the corresponding quantum numbers for the lowest electronic states of the Er^{3+} ion are shown in Table 2.2. The electric field of the YAG crystal splits each electronic state into 2J+1 levels. The manifolds of crystal-field-split energy levels for the lowest energy electronic states of Er:YAG are shown in Figure 2.1. The energies of the crystal-field levels, in units of cm^{-1}, and the corresponding Boltzmann occupation factors are shown at the right of the figure.

Rare earth ion	Er^{3+}
Number of 4f electrons	11
Highest S	3/2
Highest L	6(I)
Lowest energy electronic states	15/2, 13/2, 11/2, 9/2

Table 2.2: Quantum numbers of the lowest energy electronic stats of the Er^{3+} [82].

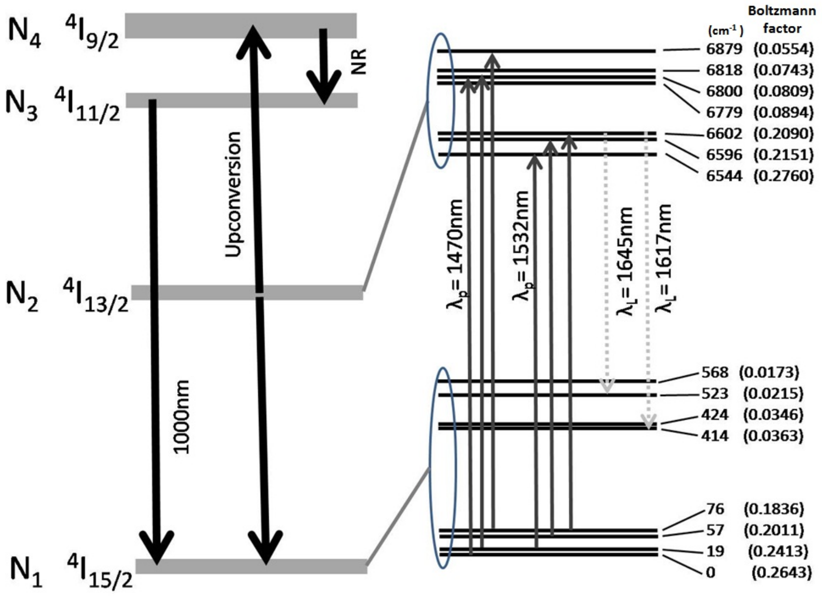

Figure 2.1: Crystal-field energy levels (cm^{-1}) for the two lowest electronic states in Er:YAG. N_1– N_4 correspond to the four lowest electronic states.

2.2.3 Er:YAG spectroscopy

Figure 2.2: Emission and absorption spectra of Er:YAG at room temperature [83].

Figure 2.2 shows the absorption and emission spectra for Er:YAG at 300 K. As can be seen in Figures 2.1 and 2.2, absorption by the $^4I_{15/2}$—$^4I_{13/2}$ transition has two strong bands around 1470 nm and 1532 nm. The same upper and lower manifolds ($^4I_{15/2}$—$^4I_{13/2}$) are also the source of the laser wavelengths at 1617 nm and 1645 nm. Thus Er:YAG can be resonantly pumped using a high power EDFL at 1532 nm [60, 66, 67] or InGaAsP/InP diode lasers at 1532 nm and 1470 nm [77, 78, 84, 85]. The latter has been demonstrated to improve the overall optical to optical efficiency of the system [78], compared to using an EDFL pump source. The high quantum efficiency (>90%) of resonant pumping coupled with the high thermal conductivity of the YAG host, makes the gain medium suitable for generating high-average power with diffraction-limited output. In this thesis, I use 1470 nm InGaAsP/InP diode lasers to resonantly pump Er:YAG because of the broadband absorption ($\backsim$10 nm) near 1470 nm.

2.2.4 Doping optimization

The erbium concentration needs to be high enough to provide sufficient pump absorption. However it must also be low enough to give an acceptable lasing threshold and to limit upconversion losses [86, 87]. Energy-transfer-upconversion (ETU) is a cross-relaxation process in which nearby excited Er^{3+} ions interact [88]. One ion in the $^4I_{13/2}$ excited state undergoes radiationless decay back to the ground state, transferring energy to another ion in the exctied state and exciting it to the $^4I_{9/2}$ state, resulting in the loss of the ions in the $^4I_{13/2}$ state.

Experimental and theoretical investigations of the effect of upconversion on Er:YAG laser performance reveal that upconversion can have a detrimental impact on laser performance [60, 86, 87, 89]. The main effect is to decrease the effective upper-state lifetime, leading to reduced energy storage, increased thermal loading, and a higher threshold pump power. Consequently it results in a lowered efficiency and reduced output power. The simplest way to manage upconversion is to use low erbium concentrations (<1%), thereby increasing the excited ion spacing [60, 66, 70, 86, 89].

Pump absorption

Dilute concentrations required to minimize upconversion result in long pump absorption lengths. This drives the laser architecture to an end-pumped geometry and also places significant constraints on the pump source as laser diodes generally have higher beam divergences than EDFL sources. Typically, the crystal length needs to be <2-3 cm so that the output of a diode, typically with a divergence of ∼10-30 mrad, can remain collimated to provide sufficient pump intensity.

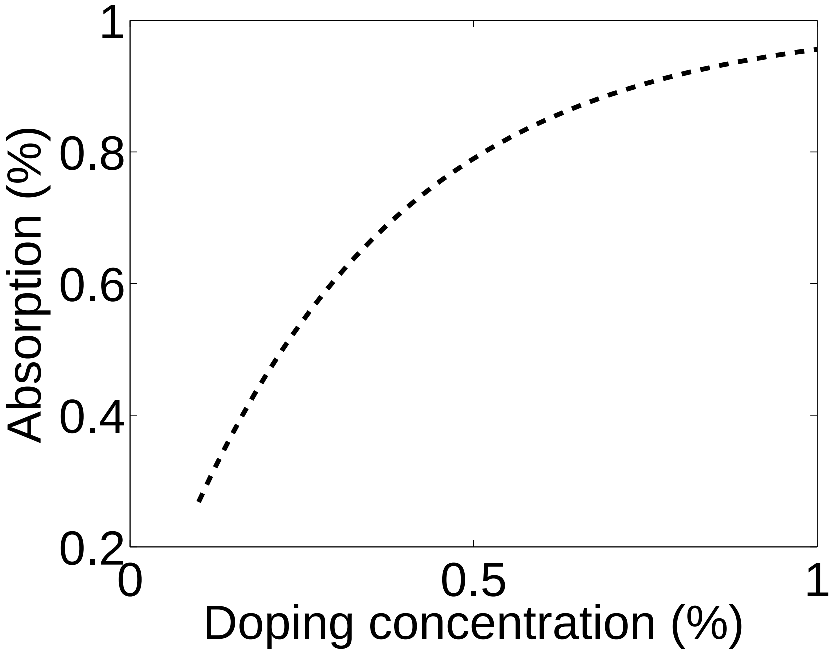

Figure 2.3: Pump absorption in 2 cm long Er:YAG versus different doping concentration.

The pump absorption versus doping concentrations for a 2 cm gain medium is plotted in Figure 2.3. The plot shows that absorption reduces significantly at concentrations below 0.5 % for which the absorption coefficient at 1470 nm is 0.78 cm^{-1} [72]. Thus, we have chosen an Er:YAG crystal with a doping concentration of 0.5% to provide low upconversion loss and sufficient pump absorption for a 2 cm pump length. Upconversion in Er:YAG will be further discussed in Chapter 6.

2.3 Quasi-three-level nature of Er:YAG lasers

The “quasi” nature of the quasi-three-level laser transition is illustrated in Figure 2.1. The lower laser level is one of the Stark-split levels of the ground state manifold, however it is not the lowest level. There is an appreciable fraction of the ground state population in the lower laser level in thermal equilibrium. Thus, unpumped Er:YAG has some re-absorption loss at the laser wavelength, and transparency is reached only for a sufficiently high pump intensity as discussed in Section 2.3.1. Higher pump intensities are required to provide net gain for laser operation. However high pump intensities result in ground state depletion, which reduces the pump absorption, as discussed in Section 2.3.2.

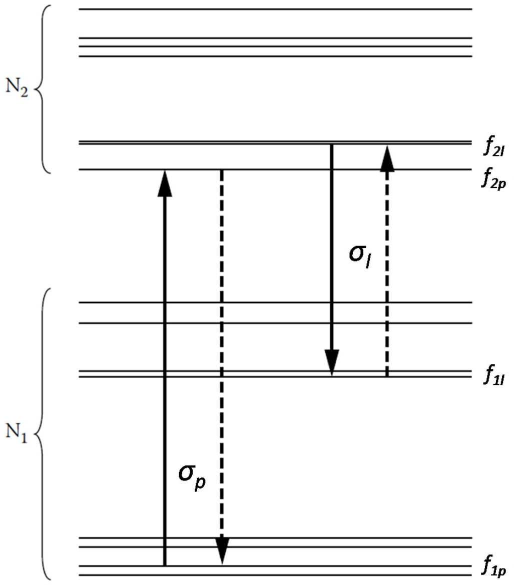

Figure 2.4: Symbols for the quasi-three-level laser model of Er:YAG.

The key features for resonantly pumped, quasi-three-level Er:YAG laser operation can be described using the simple model shown in Figure 2.4. N_1 represents the population density in the ground state manifold, and N_2 represents the population density in the first excited state manifold. f_{1p} (f_{2p}) is the fractional Boltzmann population in the lower (upper) state of the pump transition. f_{1l} and f_{2l} refer to the fractional Boltzmann populations for the laser transition. σ_p and σ_l are the absorption and emission cross sections for the pump and laser transitions, respectively.

The dashed arrows in Figure 2.4 represent the 'reverse' directions of the transitions, corresponding to re-absorption by the ground state at the laser wavelength and stimulated emission at the pump wavelength.

2.3.1 Re-absorption loss of Er:YAG lasers

In the quasi-three-level Er:YAG laser, the partial re-absorption of the laser radiation by the thermal population in the lower laser level introduces an additional loss. To reach population inversion for the laser transition, a minimum population density in the upper laser state is required. We can write the inversion density for the lasing transition, $\triangle_l$, as

$$\triangle_l = f_{2l}N_2 - f_{1l}N_1. \tag{2.1}$$

If there is no upconversion, then the total Er^{3+} concentration N_t is

$$N_t = N_1 + N_2. \tag{2.2}$$

Thus, the inversion density is

$$\frac{\triangle_l}{N_t} = \frac{f_{2l}N_2 - f_{1l}(N_t - N_2)}{N_t} = f_{2l}\left[\frac{N_2}{N_t} - \frac{f_{1l}}{f_{2l}}\left(1 - \frac{N_2}{N_t}\right)\right]. \tag{2.3}$$

Thus the minimum upper-state population for an inversion is given by

$$(N_2/N_t)_{min} = \frac{\frac{f_{1l}}{f_{2l}}}{1 + \frac{f_{1l}}{f_{2l}}} = \frac{f_{1l}}{f_{1l} + f_{2l}}. \tag{2.4}$$

Table 2.3 shows the wavelength dependence of $(N_2/N_t)_{\mathrm{min}}$ calculated using Equation 2.4 for Er:YAG at room temperature. The minimum upper-state population required for transparency is 5% higher for the 1617 nm laser transition than for the

1645 nm transition. Thus, an Er:YAG laser preferentially lases at 1645 nm as it has a lower threshold due to the smaller re-absorption loss. Dichroic coatings on the intra-cavity optics are therefore not required to suppress CW lasing at 1617 nm.

Laser wavelength	1645 nm	1617 nm
f_{1l}	0.022	0.037
f_{2l}	0.209	0.215
Temperature (K)	300	300
$(N_2/N_t)_{min}$for transparency	0.095	0.147

Table 2.3: $(N_2/N_t)_{\mathrm{min}}$ for Er:YAG at 1645 nm and 1617 nm.

2.3.2 Ground state depletion of Er:YAG lasers

Ground state depletion (GSD) occurs when the population in the ground state is reduced, hence reducing the pump absorption and resulting in lower laser efficiency. The analysis of GSD is performed using a similar approach as the re-absorption loss. Initially, we define the inversion density for the pump transition, $\triangle_p$:

$$\triangle_p = f_{2p}N_2 - f_{1p}N_{1p}. \tag{2.5}$$

Using Equation 2.2, the pump inversion density becomes

$$\frac{\triangle_p}{N_t} = \frac{f_{2p}N_2 - f_{1p}(N_t - N_2)}{N_t} = f_{2p}\left[\frac{N_2}{N_t} - \frac{f_{1p}}{f_{2p}}\left(1 - \frac{N_2}{N_t}\right)\right]. \tag{2.6}$$

Thus, the reverse pump transition places an upper limit on the upper-state population as the inversion density needs to be smaller than zero. The maximum pump inversion density can be calculated using the following equation

$$(N_2/N_t)_{\mathrm{max}} = \frac{\frac{f_{1p}}{f_{2p}}}{1 + \frac{f_{1p}}{f_{2p}}} = \frac{f_{1p}}{f_{1p} + f_{2p}}. \tag{2.7}$$

Table 2.4 shows dependence of $(N_2/N_t)_{\mathrm{max}}$ on the two pump wavelengths at room temperature. The maximum population density that can be stored in the upper state is 20% higher for the 1470 nm pump transition than for the 1533 nm pump transition, thus exploiting the advantage of pumping a Q-switched Er:YAG laser at 1470 nm.

Pump wavelength	1535 nm	1470 nm
f_{1p}	0.276	0.264
f_{2p}	0.241	0.089
Temperature (K)	300	300
Maximum inversion $(N_2/N_t)_{max}$	0.534	0.748

Table 2.4: $(N_2/N_t)_{\mathrm{max}}$ for Er:YAG at 1532 nm and 1470 nm pump wavelength.

2.4 Simplified model of an end-pumped CW Er:YAG laser

Many models of quasi-three level lasers have been published [90–92], however not all of them have dealt with the depletion of population in the lower manifold. An Yb:YAG laser model published by R. J. Beach [93] uses a simplified analysis to model the laser output power without using complex laser rate equations. It provides analytic equations for the laser output power, threshold power and the slope efficiency.

The model assumes a uniformly pumped gain medium using a plane wave analysis, ground state depletion due to intense pumping and re-absorption losses. It also allows the use of double-pass pumping through the gain medium.

The objective of this section is to employ the simplified model from Beach to investigate the design of an end-pumped CW Er:YAG laser. In Section 2.4.1, Beach's model is described, and it is then used to predict the performance of the Er:YAG master laser in Section 2.4.2.

2.4.1 Description of model

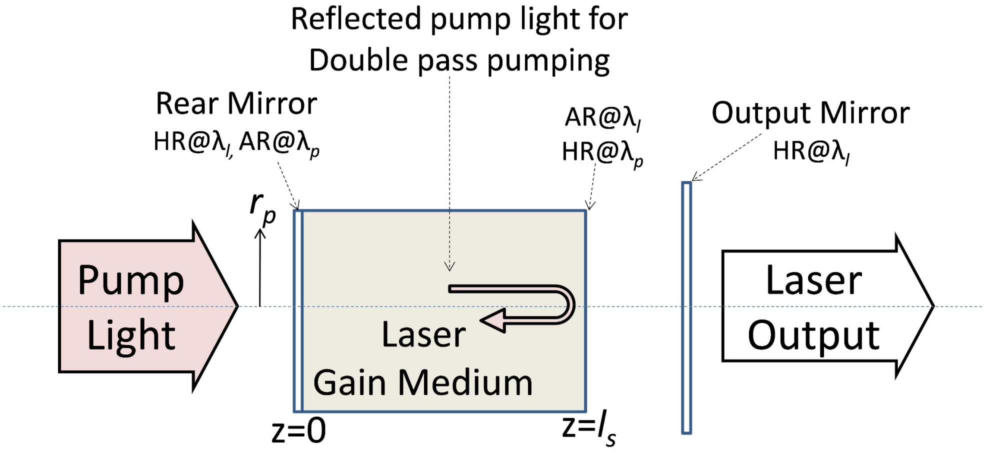

Figure 2.5: Schematic of a diode end-pumped CW laser resonator used in Beach's model.

A schematic of an end-pumped solid-state laser oscillator is shown in Figure 2.5. The left end of the gain medium is assumed to be dichroically coated, reflecting the laser light and transmitting the pump light. The other end of the gain medium is assumed to be coated to reflect the pump light for double-pass pumping, and to transmit the laser light. The laser output mirror at the right-hand end of the resonator is coated to partially reflect the laser light. Table 2.5 lists some of the important parameters that will be used in the model.

The model assumes that the output power, P_{out}, of the CW quasi-three level laser is linearly related to the input pump power:

$$P_{out} = \eta_{slope}(P_p - P_{th}). \tag{2.8}$$

These terms will be derived in the following sections using a steady-state analysis in which the rate of excitation of the lasant ions is set equal to the rate of their de-excitation. To simplify the analysis, the pump and laser beams are assumed to be plane waves and the inversion densities are written in terms of the rod-integrated upper state manifold density, N_2^z.

Parameter	Symbol
Pump power	P_p
Threshold power	P_{th}
Laser intra-cavity power	P_{cav}
Mode overlap efficiency between the laser and pump	η_{mode}
Slope efficiency	η_{slope}
Pump absorption fraction	η_{abs}
Erbium concentration per unit volume	N_t
Pump inversion density at 1470 nm per unit volume	$\triangle_p$
Laser inversion density at 1645 nm per unit volume	$\triangle_l$
Excited manifold density per unit area (Rod-integrated)	N_2^z
Pump inversion density per unit area (Rod-integrated)	$\triangle_p^z$
Laser inversion density per unit area (Rod-integrated)	$\triangle_l^z$
Normalized Boltzmann factor for lower laser Stark level	f_{1l}
Normalized Boltzmann factor for upper laser Stark level	f_{2l}
Normalized Boltzmann factor for lower pump Stark level	f_{1p}
Normalized Boltzmann factor for upper pump Stark level	f_{2p}
Absolute Er^{3+}cross section at 1645 nm	σ_l
Absolute Er^{3+}cross section at 1470 nm	σ_p
Er:YAG gain medium length	l_s
Pump mode radius	r_p
Pump cross section area	A_p
Reflectivity of the output coupler	R_{oc}
Reflectivity of the coating for double-pass pumping	R_p
Upper state storage lifetime	τ_s
Frequency of the laser wavelength	v_l
Frequency of the pump wavelength	v_p
One-way cavity loss	L_{cav}

Table 2.5: List of important parameters and symbols introduced in the model.

Pump excitation rate

The rate of excitation can be determined by calculating the rate at which pump photons are absorbed by the lasant ions in the laser rod. In the steady state, the fraction of incident pump power, η_{abs}, that is absorbed in a single-pass through the gain medium is

$$\eta_{abs} = 1 - \exp\left(-\sigma_p \int\limits_{z=0}^{z=l_s} [f_{1p}N_1(z) - f_{2p}N_2(z)]dz\right). \tag{2.9}$$

It is assumed that the entire population is in either the ground or upper state manifolds, which are coupled by pump and laser radiation:

$$N_1(z) + N_2(z) = N_t. \tag{2.10}$$

The pump inversion density, $\triangle_p$, is thus given by

$$\triangle_p = -\left[f_{1p}N_1(z) - f_{2p}N_2(z)\right] = (f_{1p} + f_{2p})N_2(z) - f_{1p}N_t. \tag{2.11}$$

Substituting Equation 2.11 into Equation 2.9, gives

$$\eta_{abs} = 1 - \exp\left(\sigma \int\limits_{z=0}^{z=l_s} -\left[f_{1p}N_1(z) - f_{2p}N_2(z)\right] dz\right) \tag{2.12}$$

$$= 1 - \exp\left(\sigma_p\left[(f_{1p} + f_{2p})N_2^z - f_{1p}N_tl_s\right]\right) \tag{2.13}$$

$$= 1 - \exp\left(\sigma_p\triangle_p^z\right), \tag{2.14}$$

where $N_2^z = \int_{z=0}^{z=l_s} N_2(z)dx$, which is solved in Equation 2.21, is the rod integrated excited state population, thus $\triangle_p^z$ is defined as the rod-integrated pump inversion density.

For double-pass pumping, the reflected pump intensity, $R_p\exp\left(\sigma_p\triangle_p^z\right)$, increases the effective pump power. Thus the pump rate, R_{pump}^t, at which photons are absorbed becomes:

$$R_{pump}^t = \frac{P_p\eta_{eff}}{hv_p}\left(1 - \mathrm{e}^{\left(\sigma_p\triangle_p^z\right)}\right)\left(1 + R_p\mathrm{e}^{\left(\sigma_p\triangle_p^z\right)}\right) \tag{2.15}$$

where R_p is the reflectivity of the pump at the end of the slab, and η_{eff} is the pump delivery efficiency.

Laser de-excitation rate

In the steady state, the excitation rate of the lasant ions in the gain medium is equal to the de-excitation rate via the laser output. The rate at which photons are de-excited by the intracavity beams and the spontaneous emission (last term) [93], R^t_{laser}, is given by

$$R^t_{laser} = \frac{P_{cav}\eta_{mode}}{hv_l}\left(\mathrm{e}^{\left(\sigma_l \triangle^z_l\right)} - 1\right) + \frac{P_{cav}\eta_{mode}}{hv_l}\mathrm{e}^{\left(\sigma_l \triangle^z_l\right)}(1-L_{cav})^2\left(\mathrm{e}^{\left(\sigma_l \triangle^z_l\right)} - 1\right) + \frac{N^z_2 A_p}{\tau_s} \tag{2.16}$$

where $\triangle^z_l = (f_{1l} + f_{2l})N^z_2 - f_{1l}N_t l_s$ is the rod-integrated laser inversion density, $P_{cav} = P_{out}/\left[R_{oc}/(1 - R_{oc})\right]$ is the laser cavity power reflected back by the output coupler, and η_{mode} is the overlap efficiency between the laser mode and pump.

Equation 2.16 can be rewritten

$$R^t_{laser} = \frac{P_{cav}\eta_{mode}}{hv_l}\left(\mathrm{e}^{\left(\sigma_l \triangle^z_l\right)} - 1\right)\left((1 - L_{cav})^2\mathrm{e}^{\left(\sigma_l \triangle^z_l\right)} + 1\right) + \frac{N_2 A_p}{\tau_s}. \tag{2.17}$$

Replacing P_{cav} by $P_{out}/\left[R_{oc}/(1 - R_{oc})\right]$ gives

$$R^t_{laser} = \frac{P_{out}\eta_{mode}}{hv_l}\frac{R_{oc}}{1 - R_{oc}}\left(\mathrm{e}^{\left(\sigma_l \triangle^z_l\right)} - 1\right)\left((1 - L_{cav})^2\mathrm{e}^{\left(\sigma_l \triangle^z_l\right)} + 1\right) + \frac{N_2 A_p}{\tau_s}. \tag{2.18}$$

Excited state manifold density in steady state

To complete the model, the steady-state rod-integrated excited manifold density, N^z_2, at the lasing threshold is determined. This occurs when the round trip gain equals the round trip losses, including the output coupler transmission and the one-way cavity loss, L_{cav}. That is, when

$$(1-L_{cav})^2 R_{oc}\mathrm{e}^{\left(2\sigma_l \triangle_l^z\right)} = 1 \tag{2.19}$$

or,

$$(1-L_{cav})^2 R_{oc}\mathrm{e}^{\left(2\sigma_l\left((f_{1l}+f_{2l})N_2^z - f_{1l}N_t l_s\right)\right)} = 1. \tag{2.20}$$

Solving Equation 2.20 for N_2^z gives

$$N_2^z = \frac{1}{f_{1l}+f_{2l}}\left(f_{1l}N_t l_s + \frac{1}{2\sigma_l}\ln\left(\frac{1}{(1-L_{cav})^2 R_{oc}}\right)\right). \tag{2.21}$$

Slope efficiency and threshold pump power

Finally, the slope efficiency, η_{slope}, and threshold pump power , P_{th}, are derived by equating the pump excitation rate (Equation 2.15) and laser de-excitation rate (Equation 2.18):

$$\begin{aligned}\frac{P_{out}\eta_{mode}}{h\upsilon_l}\frac{R_{oc}}{1-R_{oc}}\left(\mathrm{e}^{\left(\sigma_l\triangle_l^z\right)}-1\right)\left((1-L_{cav})^2\mathrm{e}^{\left(\sigma_l\triangle_l^z\right)}+1\right)+\frac{N_2^z A_p}{\tau_s} &= \\ \frac{P_p\eta_{eff}}{h\upsilon_p}\left(1-\mathrm{e}^{\left(\sigma_p\triangle_p^z\right)}\right)\left(1+R_p\mathrm{e}^{\left(\sigma_p\triangle_p^z\right)}\right)&.\end{aligned} \tag{2.22}$$

Equation 2.22 can be written in the form $P_{out} = \eta_{slope}(P_p - P_{th})$ where

$$\begin{aligned}P_{out} = \eta_{mode}\eta_{eff}\frac{\upsilon_p}{\upsilon_l}\frac{R_{oc}}{1-R_{oc}}\frac{\left(1-\mathrm{e}^{\left(\sigma_p\triangle_p^z\right)}\right)\left(1+R_p\mathrm{e}^{\left(\sigma_p\triangle_p^z\right)}\right)}{\left(\mathrm{e}^{\left(\sigma_l\triangle_l^z\right)}-1\right)\left((1-L_{cav})^2\mathrm{e}^{\left(\sigma_l\triangle_l^z\right)}+1\right)} \\ \times\left(P_p - \frac{h\upsilon_p}{\eta_{eff}}\frac{N_2^z A_p}{\tau_s}\frac{1}{\left(1-\mathrm{e}^{\left(\sigma_p\triangle_p^z\right)}\right)\left(1+R_p\mathrm{e}^{\left(\sigma_p\triangle_p^z\right)}\right)}\right)\end{aligned} \tag{2.23}$$

and

$$\eta_{slope} = \eta_{mode}\eta_{eff}\frac{v_p}{v_l}\frac{R_{oc}}{1-R_{oc}}\frac{\left(1-\mathrm{e}^{\left(\sigma_p\triangle_p^z\right)}\right)\left(1+R_p\mathrm{e}^{\left(\sigma_p\triangle_p^z\right)}\right)}{\left(\mathrm{e}^{\left(\sigma_l\triangle_l^z\right)}-1\right)\left((1-L_{cav})^2\mathrm{e}^{\left(\sigma_l\triangle_l^z\right)}+1\right)}, \tag{2.24}$$

$$P_{th} = \frac{hv_p}{\eta_{eff}}\frac{N_2^z A_p}{\tau_s}\frac{1}{\left(1-\mathrm{e}^{\left(\sigma_p\triangle_p^z\right)}\right)\left(1+R_p\mathrm{e}^{\left(\sigma_p\triangle_p^z\right)}\right)}. \tag{2.25}$$

2.4.2 Numerical prediction

The parameter values used in this section are listed in Table 2.6. It is important that these values are chosen realistically. For example, for 0.5% doping, the crystal length needs to be about 2 cm to ensure sufficient absorption. In addition, a pump flux of around 1 kW/cm^2 is required for the lasing threshold [74]. This can be achieved by combining two 300mW, telecommunication diode lasers (refer to Section 3.3) and focusing to a beam diameter of 0.02 cm, to provide a pump flux of 2 kW/cm^2.

Parameter	Symbol	Value
Erbium density for 0.5 % concentration	N_t	0.7×10^{20} cm^{-3}
Photon energy at 1645 nm	hv_l	1.21×10^{-19} J
Photon energy at 1470 nm	hv_p	1.35×10^{-19} J
Normalized Boltzmann factor for lower laser level	f_{1l}	0.022
Normalized Boltzmann factor for upper laser level	f_{2l}	0.209
Normalized Boltzmann factor for lower pump level	f_{1p}	0.264
Normalized Boltzmann factor for upper pump level	f_{2p}	0.089
Absolute Er^{3+}cross section at 1645 nm	σ_l	2.5×10^{-20} cm^2
Absolute Er^{3+}cross section at 1470 nm	σ_p	4.2×10^{-20} cm^2
Er:YAG crystal length	l_s	2 cm
Pump mode radius	r_p	0.012 cm
Upper state lifetime	τ_s	6.8 ms
Launched pump power	P_p	0.6 W
Pump delivery efficiency	η_{eff}	0.90
Mode overlap ratio	η_{mode}	0.90
One-way cavity loss	L_{cav}	0.02, 0.03, 0.04
Reflectivity of the coating for double-pass pumping	R_p	0.98

Table 2.6: Er:YAG parameters [72, 87] used in modeling .

Threshold power vs. output coupler reflectivity

The threshold power was calculated using Equation 2.25, for various output coupling reflectivities, R_{oc} = 0.9 to 0.99. Three values of intracavity loss, L_{cav}, were used in the threshold calculation. The threshold power as a function of R_{oc} for for both single and double-pass pumping is plotted in Figure 2.6. A significantly lower threshold (≈30%) is obtained for double-pass pumping as the extra pass allows more pump absorption. The double-pass pumping architecture requires a high reflection coating at the pump wavelength on the exit face of the crystal.

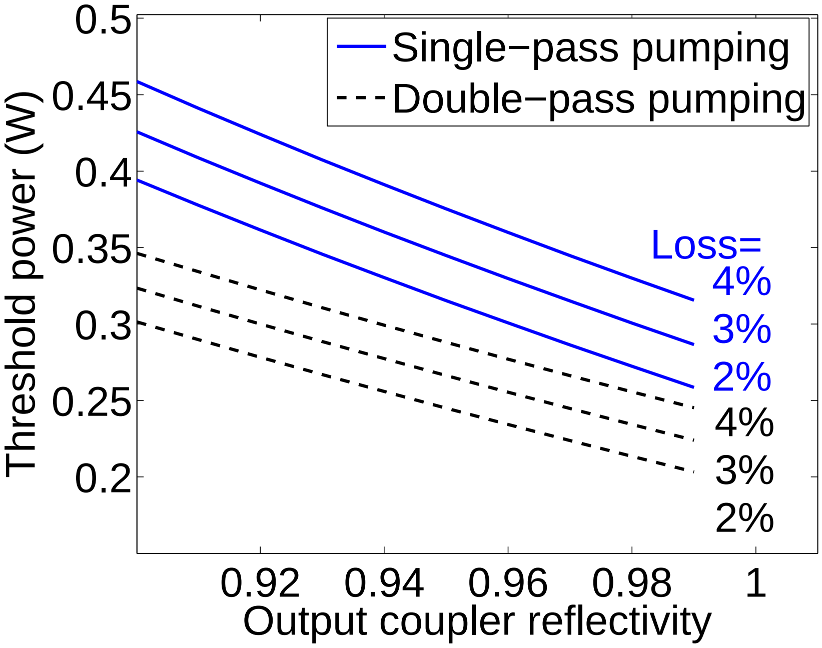

Figure 2.6: Plot of laser threshold power against output coupler reflectivity for several intracavity losses.

As expected, the lasing threshold increases as the reflectivity decreases for both pumping methods. Due to limited pump power, it is practical to have a threshold <300 mW, thus double-pass pumping and R_{oc} >0.95 should be used.

The cavity loss also has a significant influence on the threshold. For example, the threshold is 20% (50 mW) higher for a 4% loss compared to 2%. The possible sources of such loss are scattering from the optics, coating defects and gain medium impurities. We assume a high loss scenario (i.e. 4% loss) to ensure that there is sufficient pump power to overcome the threshold for high loss conditions.

Slope efficiency vs. output coupler reflectivity

The slope efficiency was calculated using Equation 2.24. Figure 2.7 plots the slope efficiency as a function of R_{oc}. The slope efficiency increases as the reflectivity decreases, but then decreases when the reflectivity becomes too small. It is clear that double-pass pumping offers much better efficiency for R_{oc} <85%. Although a maximum slope efficiency of about 45% and 30% (for double-pass and single-pass pumping, respectively) can be achieved for a R_{oc} of 70%, it may not deliver the highest output power as the lasing threshold is also increased. Thus a higher R_{oc} is possibly required to lower the threshold and hence provide the highest output power.

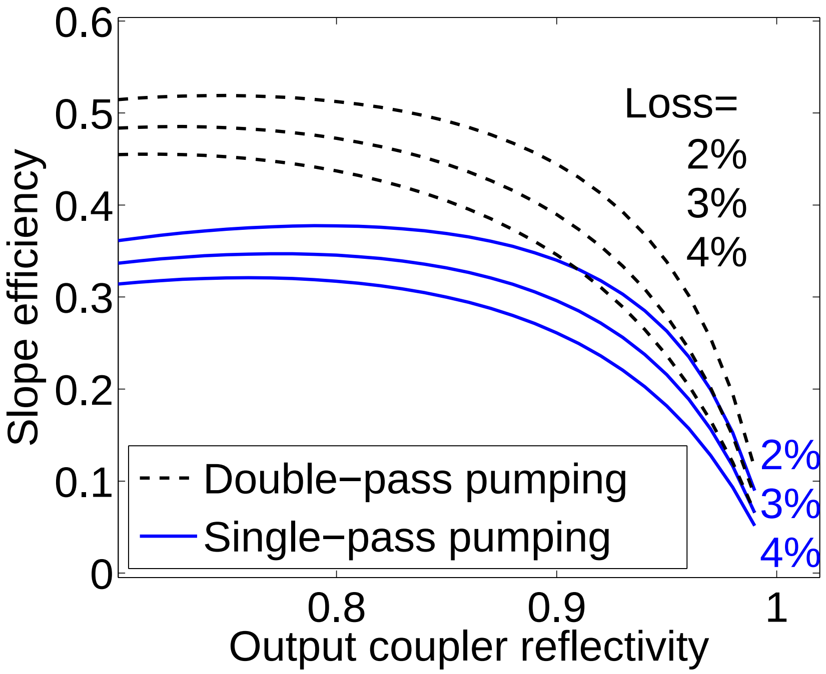

Figure 2.7: Plot of the predicted slope efficiency versus output coupler reflectivity for several intracavity losses.

Laser output power vs. output coupler reflectivity

Finally, a Rigrod analysis [94] is performed using Equation 2.23, where the output power is calculated as a function of R_{oc} for a 600 mW pump power. The results are shown in Figure 2.8. The model predicts an optimum reflectivity for the output coupler of 92% for double-pass pumping and 95% for single-pass pumping.

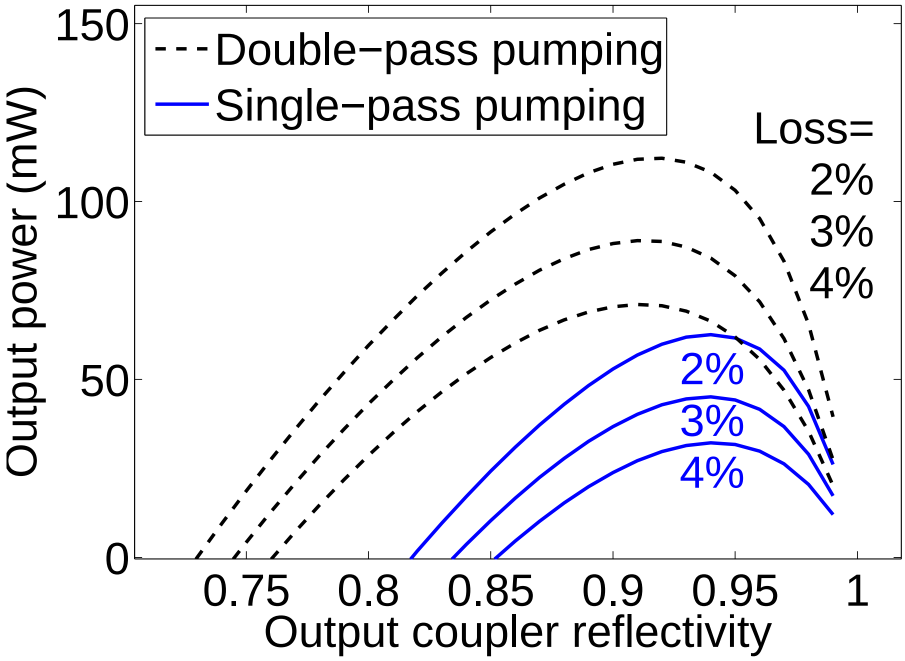

Figure 2.8: Plot of the predicted laser output power versus output coupler reflectivity for a 600 mW pump power.

The optimum reflectivity is not sensitive to the change of cavity loss. However, increasing the one-way cavity loss from 2% to 4% results in a large change in the laser output power. To maximize the output power and allow for uncertainty in the actual reflectivity of the output coupler, we chose to try both 95% and 98% (nominal) output couplers.

The predicted output power versus incident pump power for these two output couplers is shown in Figure 2.9. Once again, a significantly better performance is obtained from the double-pass pumping than by the single-pass pumping architecture.

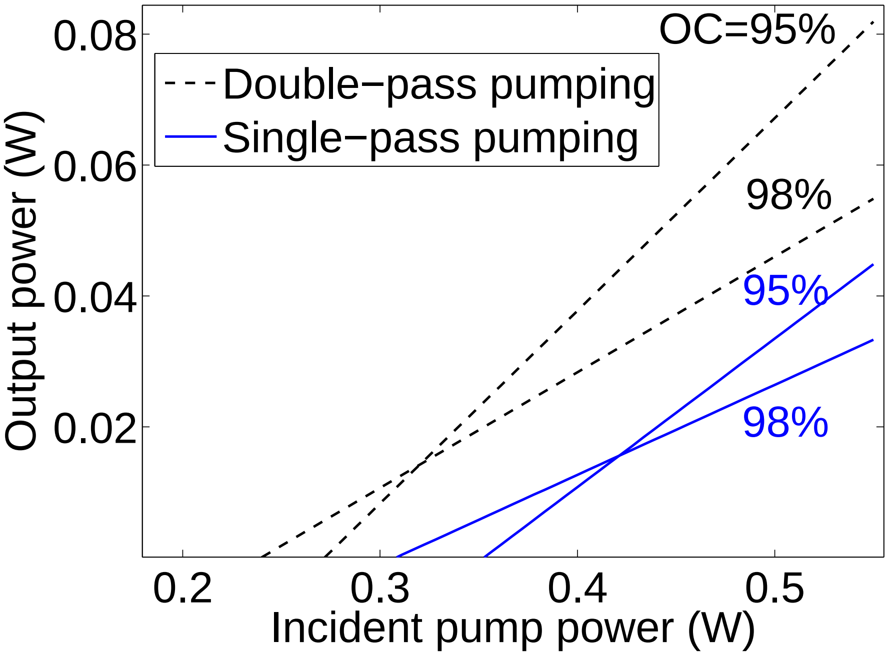

Figure 2.9: Plot of the predicted output power versus incident pump power with 95% and 98% output couplers for single and double-pass pumping. The one-way cavity loss, L_{cav}, is 3%.

2.5 Numerical model by F. Auge

The above model does not predict either the gradual dependence of the laser intensity in z-axis, or the gain variation for the pump powers above the threshold. Thus, the plot of output power in Figure 2.9 indicates a slope efficiency that is independent of pump power. In reality, Quasi-three-level lasers have a lower slope efficiency close to threshold due to the nature of laser re-absorption, and then the slope efficiency becomes constant like four level lasers at higher pump powers [91,95]. However this quasi-three-level behavior induced by the non-negligible re-absorption losses is not predicted in Beach's model due to the approximation of the constant slope efficiency.

Moreover, the transverse spatial profiles of the pump and laser beams, which also have strong influence in quasi-three level solid state lasers, are not included in the simple plane-wave model discussed previously. Thus, a separate analysis based on a numerical model of Yb:YAG lasers by F. Auge [96] is discussed in this section.

The Auge model, originally developed for CW Yb^{3+} doped lasers, takes into account the re-absorption of the laser, transverse mode evolution in z-axis of the pump and laser, overlap of the beams, and transverse mode profile of the laser and the pump. In addition to Auge's original model, a few other features are included for Er:YAG lasers: ground state depletion in the gain medium, and double-pass propagation of the pump beam. Since we expect the laser to have negligible thermal effects [61] due to the 90% quantum efficiency, the model will not consider any thermal dependence.

2.5.1 Description of model

A schematic of the Auge model is shown in Figure 2.10. Note that the model considers the spatial (z & r axis) dependence of the pump and laser beams.

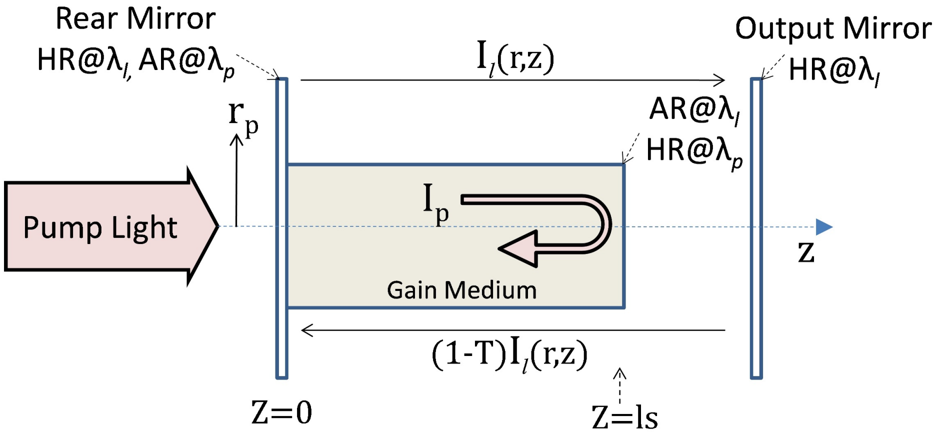

Figure 2.10: Schematic of a diode end-pumped CW laser resonator used in Auge's model.

It assumes that the pump and laser beams have Gaussian profiles and can be described in cylindrical coordinates (r, z) [97]. Table 2.7 lists some of the important parameters that are used in the model.

Parameter	Symbol
Pump intensity	I_p
Laser intensity	I_l
Radius of the pump waist	r_{p0}
Radius of the laser waist	r_{l0}
Radius of the gain medium	r_s
Effective emission cross section at 1645 nm	σ_{el}
Effective absorption cross section at 1645 nm	σ_{al}
Effective emission cross section at 1470 nm	σ_{ep}
Effective absorption cross section at 1470 nm	σ_{ap}
Absorption coefficient	α
Gain coefficient of the laser	γ
Round trip gain of the laser	G
Beam propagation factor of the pump	M_p^2

Table 2.7: Parameters used in the model

Spatial profile

The expressions for the pump and cavity radii are given by the following:

$$r_p(z) = r_{\mathrm{p0}} \left\{ 1 + \left[M_p^2 \frac{\lambda}{\pi n r_{\mathrm{p0}}} \left(z - z_{\mathrm{p0}} \right) \right]^2 \right\}^{1/2} \tag{2.26}$$

$$r_l(z) = \omega_{\mathrm{l0}} \left\{ 1 + \left[\frac{\lambda}{\pi n r_{\mathrm{l0}}} \left(z - z_{\mathrm{l0}} \right) \right]^2 \right\}^{1/2} \tag{2.27}$$

where n is the index of refraction of the crystal, r_{p0} and r_{l0} are the waists of the pump and cavity beams inside the crystal and $z_{p0}(z_{l0})$ is the position of the waist in the crystal. The locations of the waist are $z_{\mathrm{p0}} = l_s/2$ and $z_{\mathrm{l0}} = 0$, corresponding to the experiment shown in Figure 2.10.

Figure 2.11 shows the evolution along the z axis of the pump and cavity radii inside the crystal for a pump waist value of 0.128 mm with a beam profile close to TEM_{00}. The laser beam has a waist size which is 90% of the pump waist located at the front of the slab ($z = 0$), assuming a flat-concave resonator. The overlap between the modes can have a strong influence as it determines the volume of the laser gain extractable within the pumped volume.

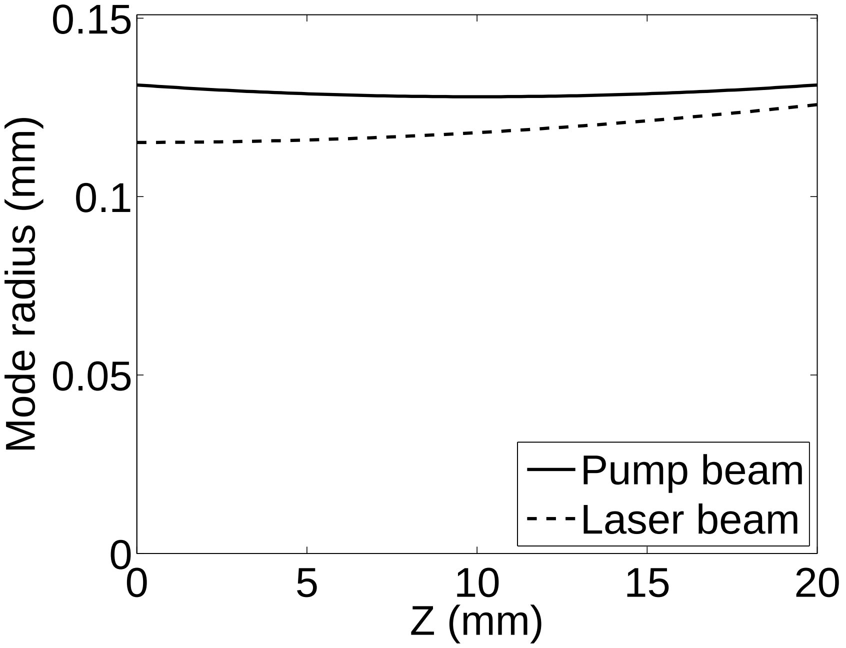

Figure 2.11: Plot of predicted pump and cavity radii along the z axis of the crystal.

Laser and pump intensity

Neglecting spatial hole-burning, the laser intensity, I_l, is given at each point of the gain medium by

$$I_l(r_s,z) = (1+R_{\mathrm{oc}})\frac{2P_{cav}}{hv_l\pi r_l^2(z)}\exp\left[-\frac{2r^2}{r_l^2(z)}\right]. \tag{2.28}$$

The pump intensity, I_p, is given by

$$I_p(r_s,z) = \frac{2P_p(z)}{hv_p\pi r_p^2(z)}\exp\left[-\frac{2r^2}{r_p^2(z)}\right] \tag{2.29}$$

where $P_p(z)$ is the pump power in the gain medium and, $r_p(z)$ and $r_l(z)$ are the radii of the pump and laser beams in the gain medium.

The gain coefficient (cm^{-1}) of the laser is:

$$\gamma = \sigma_{el} N_2 - \sigma_{al} N_1. \tag{2.30}$$

In the steady-state regime, the solutions of N_1 and N_2 can be found and give the expression for γ as [96]

$$\gamma = N_t \frac{\sigma_{el}\sigma_{ap}\frac{I_p}{hv_p} - \frac{\sigma_{al}}{\tau_s}}{\sigma_{ap}\frac{I_p}{hv_p} + (\sigma_{el} + \sigma_{al}\frac{I_l}{hv_l} + \frac{1}{\tau_s})}, \tag{2.31}$$

where σ_{al}/τ_s corresponds to re-absorption losses. The final expression of the laser round-trip gain, G, per double-pass is [96]

$$G = \left[1 + \int_0^{l_s} dz \int_0^{r_s} \frac{4\gamma(r,z)}{r_l^2(z)} \exp\left(-\frac{2r^2}{r_l^2(z)}\right) rdr\right]^2, \tag{2.32}$$

where r_s is the radius of the gain medium.

At lasing threshold, the round trip gain equals to the total loss, G_{th}:

$$G_{th} = \frac{1}{(R_{\mathrm{oc}} - L_{\mathrm{cav}})}. \tag{2.33}$$

Equation 2.32 can be solved numerically to find the round trip gain versus the intracavity power at a given pump power. Thus, for a given pump power, the output power is determined by knowing the corresponding intra-cavity power where the gain equals to the losses. An example calculation will be shown in Figure 2.13.

Reduced absorption due to ground-state-depletion

In the Auge model, the absorption coefficient is estimated using experimental results from the Yb:YAG gain medium. In this model, the absorption coefficient is predicted as the gain medium architecture has not been decided. Thus, the effective pump absorption cross-section is predicted theoretically using

$$\sigma_{ap}(P_p) = \left[\sigma_p(f_{1p}N_1(P_p) - f_{2p}N_2(P_p))\right]/N_t \tag{2.34}$$

where N_1 and N_2 are calculated at the steady state using the rate-equation model described in Chapter 6.

The dependence of the pump absorption coefficient (cm^{-1}), α, on pump power is

$$\alpha(P_p) = \sigma_{ap}(P_p)N_t, \tag{2.35}$$

and is plotted in Figure 2.12.

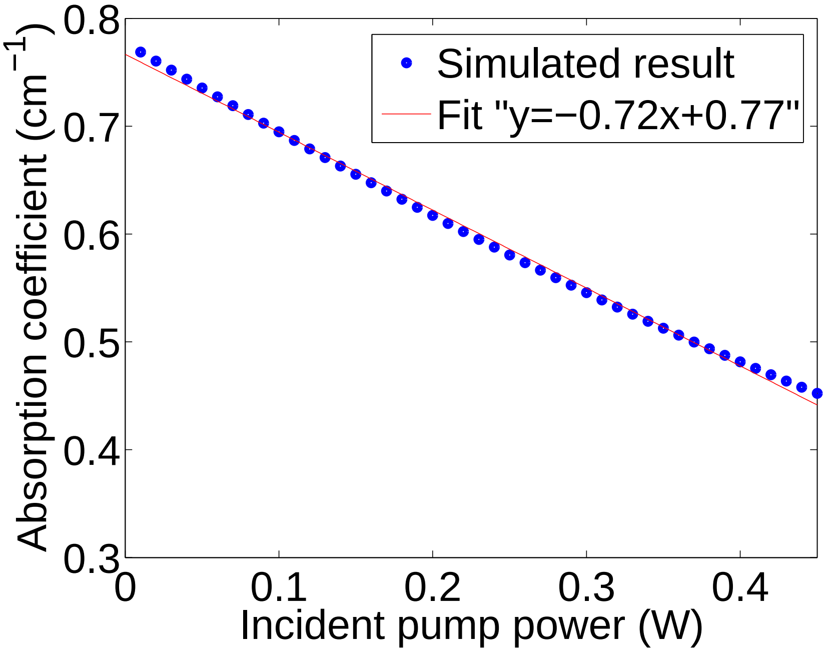

Figure 2.12: Absorption saturation versus launched pump power.

The result shows that as the population in the lasing state increases, the ground state depletes and reduces the pump absorption. Thus, to include this effect, we approximate the bleaching of the pump absorption by

$$\alpha(P_p) = 0.77 - 0.72P_p. \tag{2.36}$$

This allows the lasing threshold to be predicted more accurately.

The model is calculated numerically using Matlab, which determines the corresponding absorption coefficient for the given pump power if the lasing threshold is not reached. Once lasing is achieved, the model will assume the absorption coefficient is fixed for any higher pump powers, as the ground state population is expected to recover due to lasing de-excitation.

Numerical simulation

The numerical simulation begins with a pump power << threshold pump power: $P_p << P_{th}$. As P_p is increased, $\alpha(P_p)$ decreases as discussed above. The threshold pump power is determined when the round-trip gain (G) equals to the total loss (G_{th}), and then $\alpha(P_p)$ is clamped at $\alpha(P_{th})$.

Further increasing P_p results in lasing. The round trip gain, G, at each pump power is calculated as a function of P_{cav}. The resulting output powers are determined from the corresponding P_{cav} of the intersections between G and G_{th} using Equation 2.37

$$P_{out} = \frac{P_{cav}(1 - R_{oc})}{R_{oc}}. \tag{2.37}$$

Figure 2.13 shows the effect of varying P_{cav} on $G(P_{cav})$, and the intracavity powers are determined by the intersections between G and G_{th} at different pump powers. For example, at 350 mW of pump power, the corresponding intracavity power is 0.7 W, thus the output power $P_{\mathrm{out}} = 0.7\mathrm{W} \times (1 - 0.95)/0.95 = 0.036\,\mathrm{W}$. The resulting output powers are plotted as a function of P_p in Figure 2.15.

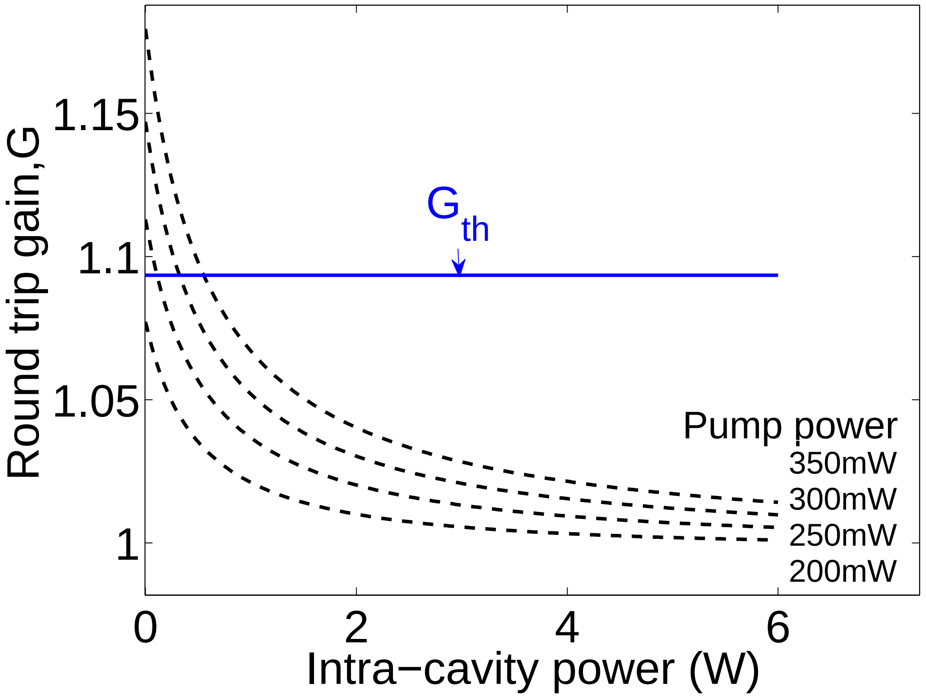

Figure 2.13: Plot of the predicted round-trip gain, G, for a given pump power and intracavity power at the lasing wavelength. The threshold gain, G_{th}, assumes $R_{oc} = 0.95$, $L_{cav} = 0.025$. Lasing requires the net gain to be equal to the threshold, and thus we can determine the intracavity power of the laser for given pump power.

2.5.2 Numerical prediction

Parameter	Symbol	Value
Er:YAG crystal length	l_s	2 cm
Pump mode radius	r_p	0.011 cm
Launched pump power	P_p	0.55 W
Mode overlap efficiency	η_{mode}	0.95
One-way cavity loss	L_{cav}	0.025
Output coupler reflectivity	R_{oc}	0.98, 0.95

Table 2.8: Er:YAG parameters used in modeling.

Table 2.8 shows the laser parameters used in the model. Assuming no lasing ($P_{cav} = 0$ W), the predicted round-trip gain $G(P_{cav} = 0$ W), versus pump powers are calculated in Figure 2.14 for single and double-pass pumping. While the gain threshold is about 1.1, double-pass pumping clearly offers a higher gain. The threshold of the laser for single-pass pumping is about 400 mW, while a lower threshold of 300 mW is achieved for double-pass pumping. The predicted thresholds are similar to the result discussed in Section 2.4.2.

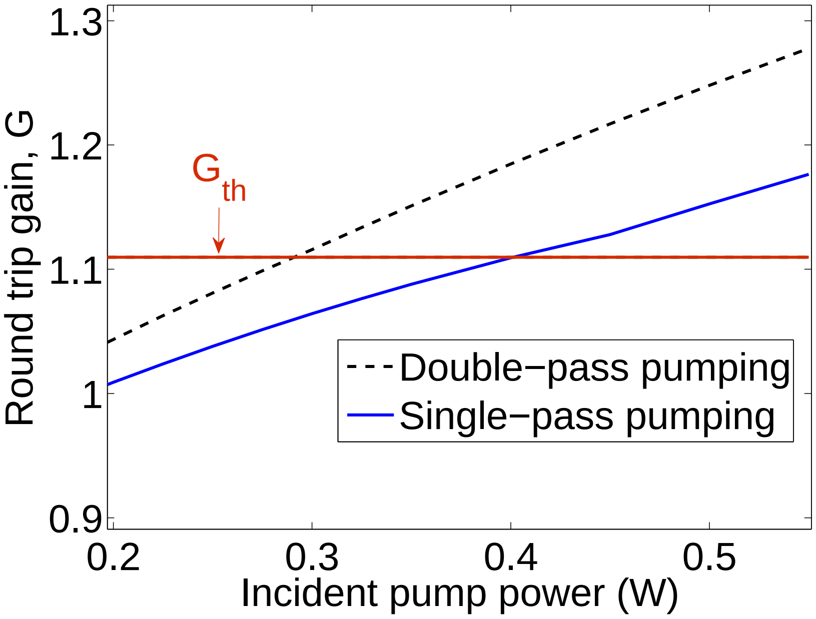

Figure 2.14: Plot of the predicted round trip gain versus incident pump power for a single-pass and double-pass of the pump in the Er:YAG crystal.

The laser output power is calculated using Equation 2.37 as illustrated in Figure 2.13. The intracavity laser powers, P_{cav}, are determined at the $G = G_{th}$ intersections so that P_{out} could be calculated.

Figure 2.15 plots the output power as a function of the pump power. The simulation assumed output couplers with $R_{oc} = 95\%$ and 98% for single-pass and double-pass pumping techniques. As expected, much better laser performance is predicted using double-pass pumping, and an output power of about 50 mW is predicted using a R=95% output coupler at 0.6 W of pump power.

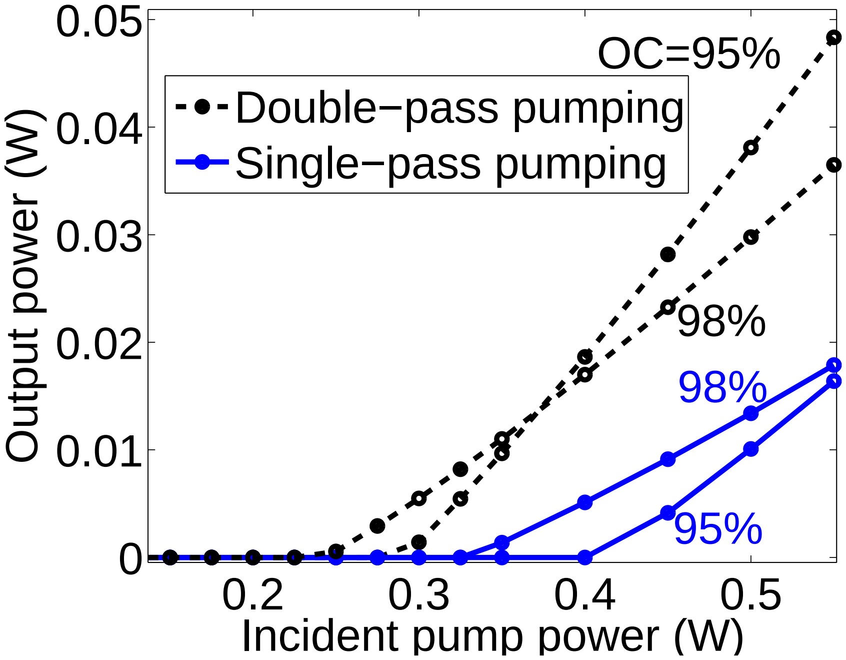

Figure 2.15: Predicted output power versus incident pump power for a single-pass and a double-pass of the pump in the crystal.

2.5.3 Discussion

The model developed here, based on Auge's model, predicts a similar laser performance to R.J. Beach's model. Both models predict a laser threshold of around 300 mW and an output power of 50-70 mW. One advantage of the Auge model is the ability to include the spatial evolution of the pump and laser beam inside the crystal. This allows the single transverse mode (TEM_{00}) profile of the fiber coupled pump diode to be included, thus providing a better prediction of the mode overlap between the laser and the pump.

As mentioned in Section 2.2.4, upconversion in Er:YAG can potentially increase the lasing threshold, however this influence is not included in both models. An investigation, using a rate equation model, was thus carried out in Appendix B, which predicts the upconversion influence on the lasing threshold. The result shows that upconversion should only increase the lasing threshold by <100 mW, which ensures that a 600 mW pump source should be sufficient for the laser design.

2.6 Conclusion

The design of a Er:YAG laser has been proposed, and the performance of the laser was predicted using two different laser models. The results predicted by both models basically agree with one another, thus making sure the design of the laser is practical.

Using a 0.6 W pump source, the models predicted a laser output power of about 50 mW and a threshold of about 300 mW. The development and characterizations of the Er:YAG laser will be described in the next chapter.

3 Single frequency Er:YAG master laser development

3.1 Introduction

As discussed in Chapter 1, a coherent laser radar (CLR) requires a low power, single frequency CW master oscillator. The design of a low power Er:YAG laser was discussed in Chapter 2 and two numerical models were presented. In this chapter, the development and testing of the low power laser are described, and the performance of the laser is compared to the numerical models.

The slab and slab holder development of the laser head is described in Section 3.2. The pump design of the laser is described in Section 3.3, followed by the design of the standing-wave resonator in Section 3.4. Section 3.5 describes the performance of the low power laser, which produces up to 30 mW in a narrow line-width, single frequency, plane polarized, diffraction limited TEM_{00} output. Section 3.6 describes the measurement of the frequency stability of 12 kHz over 1.66 µs, followed by the beam quality measurement described in Section 3.7.

Some of the results reported in this chapter have been published in the IEEE Journal of Quantum Electronics [84]. A copy of this paper is included in Appendix A.1.1.

3.2 Slab and slab holder

3.2.1 End-pumped slab geometry

The Er:YAG laser gain medium, with a doping concentration of 0.5 at.%, was purchased from Northrop Grumman Synoptics (USA). Slab cutting, polishing and finishing was performed by BAE Systems Australia Ltd. (Holden Hill, South Australia, Australia).

A schematic of the slab is shown in Figure 3.1. The finished slab has a length (l_s) of 20.0±0.1 mm, width (w_s) of 3.0±0.1 mm, and height (h_s) of 3.0±0.1 mm. The slab-end closest to the pump diodes is also the end mirror of the resonator, and is thus coated for high reflection (R $>$ 99.5%) at 1645 nm and high transmission (T $>$ 99.5%) at the 1470 nm pump wavelength. The other end of the slab is coated for antireflection (R $<$ 0.5%) at 1645 nm and high reflection (R $>$ 99.5%) at 1470 nm. The four large surfaces of the slab are fine ground.

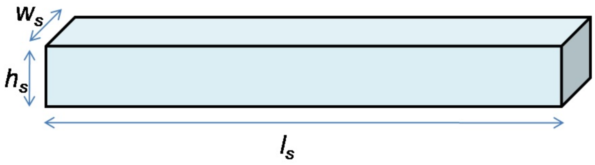

Figure 3.1: 3-D schematic of the laser slab.

3.2.2 Design of the slab holder

A schematic of the laser head and a front view of the slab holder are shown in Figure 3.2. The end-pumped, top/bottom cooled laser head geometry simplifies heat removal from the rectangular gain medium, as the pumped and cooled surfaces are separated. Since a collimated pump source is used, the pump light is confined in the slab without additional coatings on the surfaces, thus preventing complicated engineering constraints on the laser head design.

As discussed in Chapter 2, the quantum efficiency of the resonantly pumped

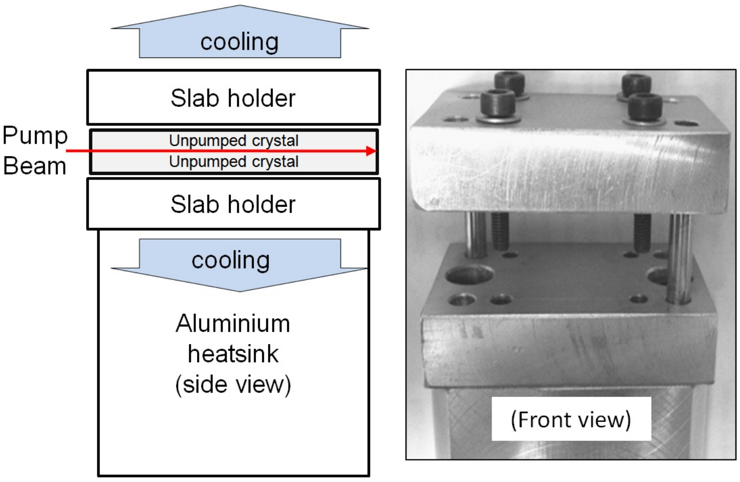

Figure 3.2: A schematic of the slab holder.

Er:YAG gain medium is 90%, and thus the expected heat deposited in the crystal will be less than 0.1 W for a pump power of 0.6 W. Because of the low heating, the use of two convection-cooled aluminium slab holders would provide sufficient cooling of the top and bottom faces of the slab.

Laser slab mounting

To ensure good thermal contact between the heat sinks and the slab, a layer of indium foil (125 µm thick) was cut to the same dimensions as the laser slab and placed on the areas of the slab that come in contact with the heat sink. Two positioning pins were used to guide the top heatsink during the assembly to provide uniform clamping. To achieve uniform crush on the indium, each bolt (with fine thread) is tightened gradually in sequence. An uneven thermal contact will result in the creation of asymmetric horizontal or vertical thermal gradients inside the gain medium, thus creating a thermal wedge that would refract the laser mode out of gain region, and hence reduce the laser efficiency.

3.3 Pump configuration

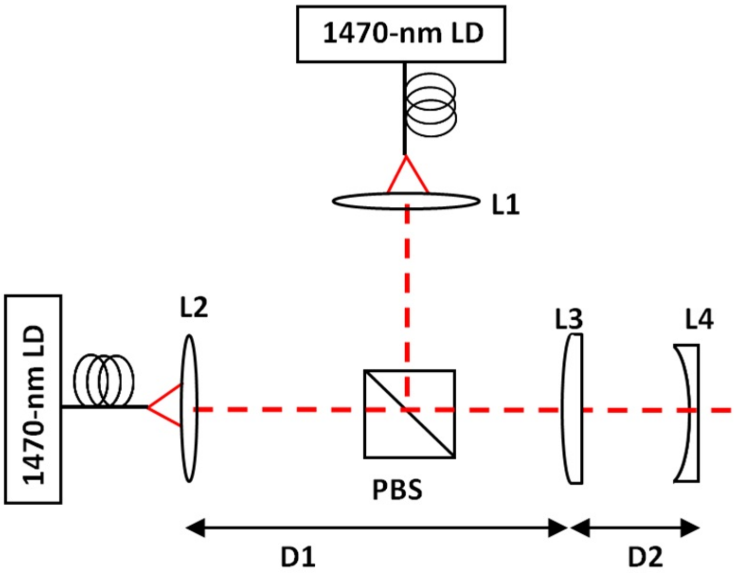

Figure 3.3: A schematic of the pump configuration.

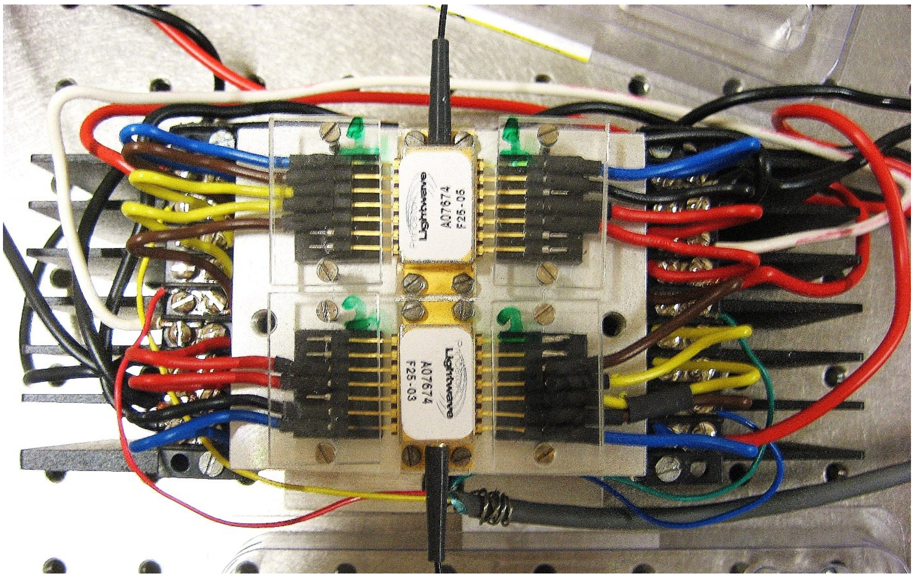

Figure 3.4: The setup of the pump laser diode packages, mounted on top of an Al heatsink.

A schematic of the pump configuration is shown in Figure 3.3. It consists of two high-brightness CW single-mode InP diode lasers “HP-S-1480-PM” purchased from Princeton Lightwave Inc. (New Jersey, USA). The specifications of the diode lasers are found in Appendix C. This 1470-nm ridge-waveguide laser is packaged in a standard telecom, 12-pin-butterfly module and has a polarization-maintaining fiber output. The output polarization is aligned to the key of the fiber connector. The diode is actively cooled by an internal thermo-electric cooler (TEC) to provide wavelength stability, and the heat of the module is removed via a heatsink as shown in Figure 3.4. The diode specifications are given in Table 3.1.

Parameter	Single mode InP laser diode
Center wavelength	1470-1485 nm
Output power	300 mW
Polarization	Linear polarized output (PM fiber)
Spectral width	10 nm
Forward current	1600 mA
Reverse voltage	2 V
TEC current	6 A
TEC voltage	4.2 V
Numerical aperture (NA)	0.14 (SMF-28)

Table 3.1: Specifications of the 1470nm laser diode.

3.3.1 Pump collimation

The output of the fiber is collimated using a 2 mm focal length, fiber collimator (HPUCO-33A-1470-p-2AS) from OZ Optics Ltd. (Carp, ON, Canada). This collimator can be directly coupled to the FC/APC fiber connector, which simplifies beam collimation.

The collimated beam diameter (BD) and full divergence angle (DA) of the pump beams can be calculated using Equation 3.1 and 3.2 [98],

$$BD = 2 \times f \times NA \tag{3.1}$$

$$DA = \frac{Core\,Diameter}{f}. \tag{3.2}$$

Therefore, the fiber collimator is expected to deliver a ~0.25 mm radius output with a divergence of ∼0.26 degrees (full angle). The radius (half 1/e^2 diameter) of the beam was measured using a knife edge experiment at several distances from the collimator. The results are plotted in Figure 3.5.

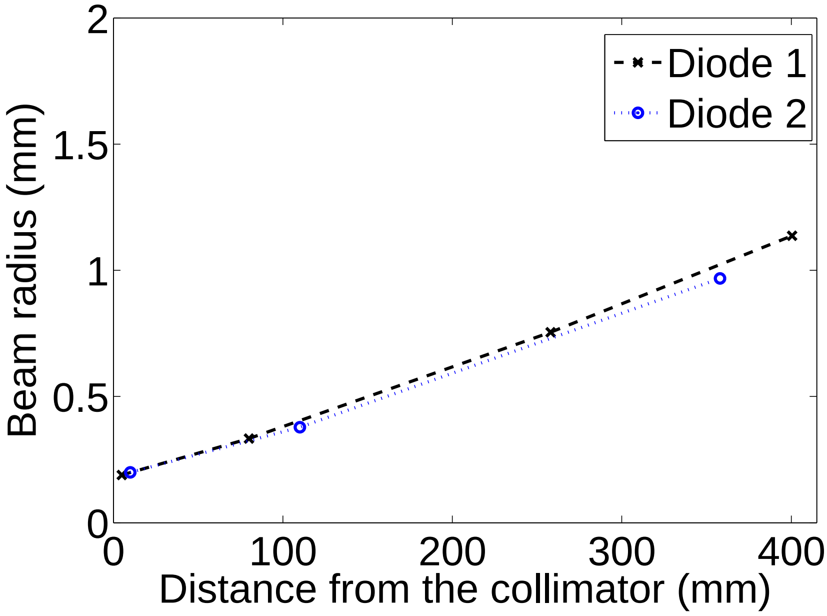

Figure 3.5: Beam divergence of the collimated outputs of the two diodes.

These measurements show that the radius of the beams expand from ∼0.2 mm to ∼1.2 mm over a propagation of 400 mm. This corresponds to a divergence of about 0.27 degrees, thus agreeing with the expected value. The matching of the beam divergences should allow good spatial overlap when merging two beams using an optical combiner.

3.3.2 Optimization of the pump wavelength

For efficient laser operation, the pump wavelength needs to be matched to the absorption band of the gain medium by tuning the temperature of the pump diodes. This was achieved using the layout shown in Figure 3.6. The retro-reflected pump beam was separated using a polarization-beam-splitter cube(PBSC) and a quarter-wave plate(QWP). The reflected beam was then measured using a grating spectrometer (OSA), and the pump diodes were temperature tuned to provide maximum absorption at the desired operating current.

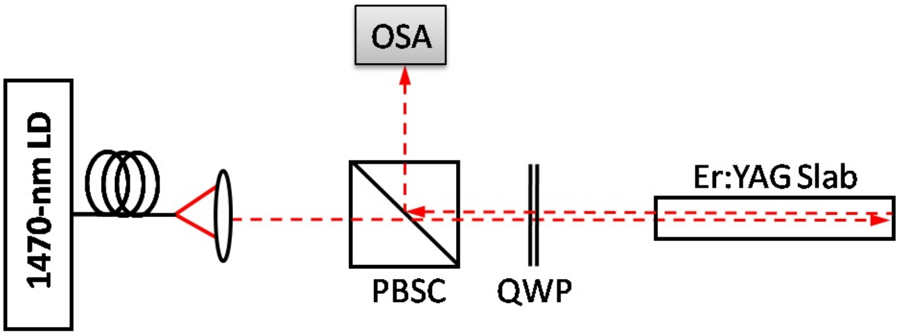

Figure 3.6: Setup for pump absorption optimization

The spectra of the retro-reflected pump light with and without the Er:YAG slab are compared in Figure 3.7. The left-hand spectrum is the pump reflected using a mirror, showing no absorption at a wavelength of 1470 nm. The spectrum on the right is the retro-reflected pump via the Er:YAG slab, and it confirms that the peak absorption occurs around 1470 nm wavelength, which agrees with the published absorption spectrum [72]. The nominal spectral width of the pump diode, ~10 nm, broadly covers the absorption features around 1470 nm as shown in the right figure (dips correspond to the absorption peaks).

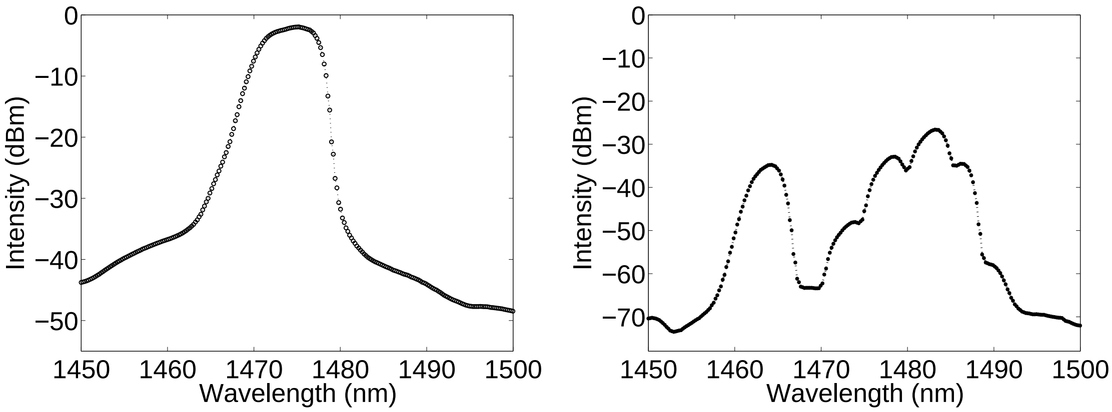

Figure 3.7: Spectra of the pump without absorption (Left) and with absorption after the gain medium (Right)

3.3.3 Pump combining

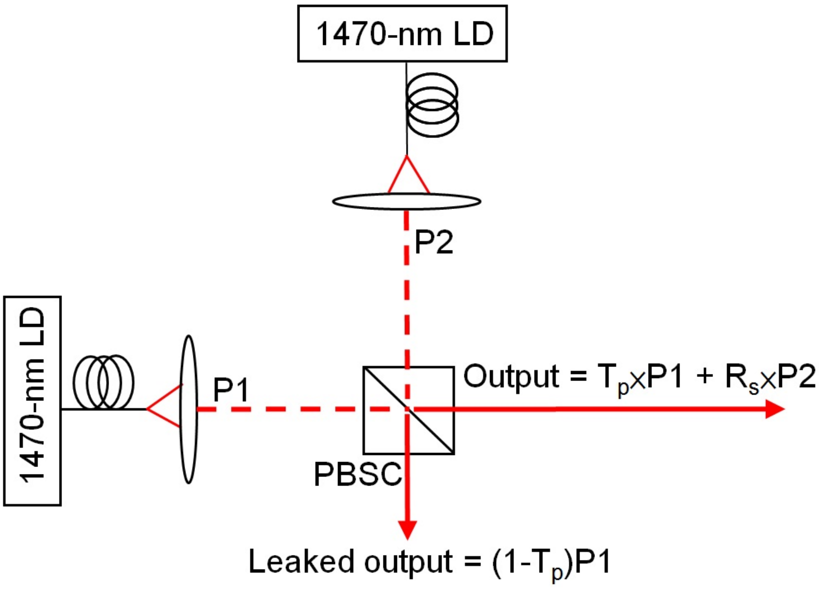

Figure 3.8: Schematic of the combined pump beams.

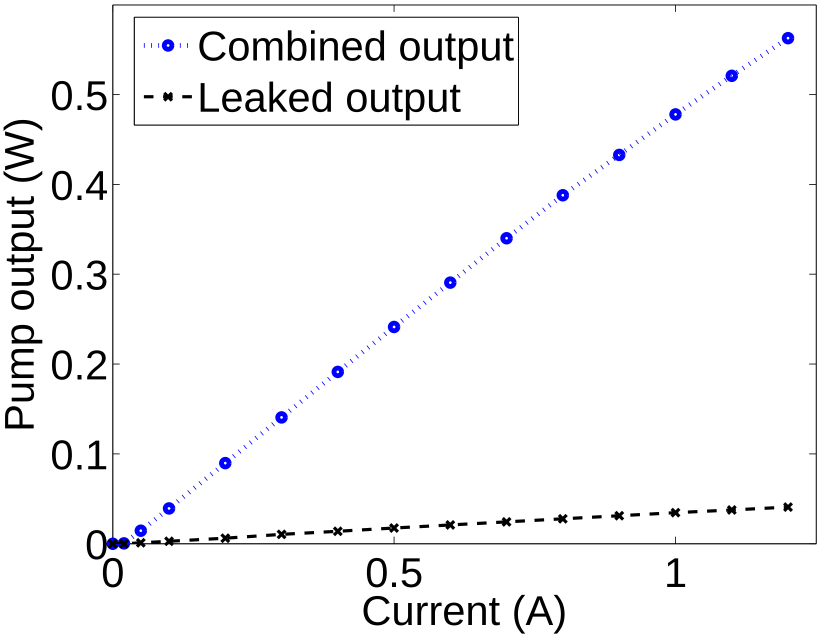

Figure 3.9: Output powers from the PBSC (combined and leaked) versus diode operating current.

The pump beams are combined using a polarization beam splitter (IR-PCBC 3275, China Optics) as shown in Figure 3.8. The leakage output from the bottom face of the cube is because the transmittance for T_p is only 90%, while the reflectance R_s is $> 99.5\%$. The efficiency of the combiner was checked using two calibrated power meters. A plot of the output powers versus diode current is shown in Figure 3.9. The maximum combined pump power is about 550 mW at an operating current of 1.2 A, with about 40 mW of total leakage power from the other output. The leaked output is used as a reference to monitor the total launched pump power.

3.3.4 Pump focusing

To reach the desired threshold pump density ($\sim$ 1000 W/cm^2 as predicted in Chapter 2), the diameter of the pump beam in the gain medium needs to be ~0.2 mm. The required focusing optics were determined using the Paraxia 2.0 ABCD program [99]. The labels used in the model are defined in Figure 3.10 and their characteristics are listed in Table 3.2. The modeling predicted that the imaging system required a -25 mm plano-concave lens and a 25.4 mm plano-convex lens to provide a beam diameter of about 0.20 mm inside the gain medium.

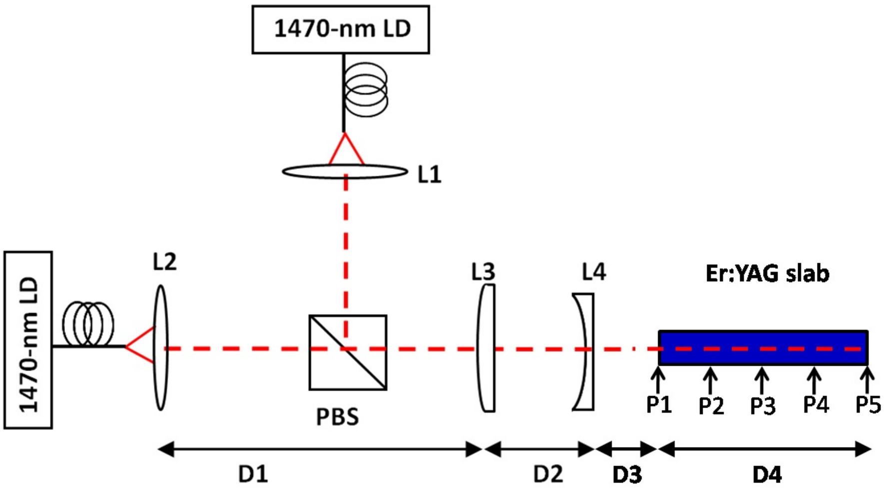

Figure 3.10: Definition of path lengths for the pump configuration

Parameters	Value
Lens L1	f = 2 mm
Lens L2	f = 2 mm
Lens L3	EFL = 25.4 mm
Lens L4	EFL = -25 mm
D1	60 mm
D2	17.5 mm
D3	10 mm
D4	40 mm

Table 3.2: Pump design parameters. The lengths correspond to those in Figure 3.10

Figure 3.11 shows the predicted evolution of the beam radius between the output of the pump and the end of the gain medium, and the plot shows that the low divergence in the Er:YAG gain medium keeps the beam radius < 0.12 mm over 40 mm length within the slab.

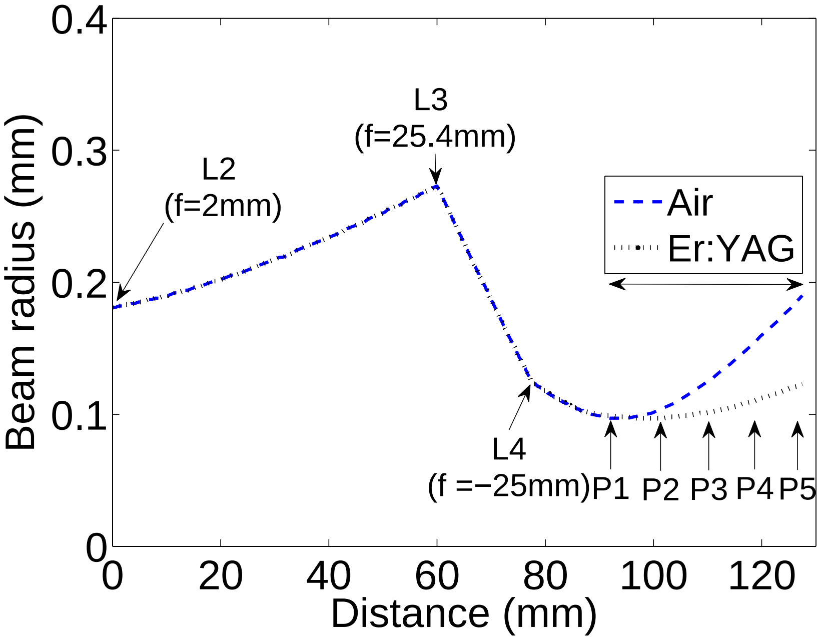

Figure 3.11: Pump beam radius evolution between the output of the collimating lenses and the end of the gain medium.

Validation of model

The model was also used to calculate the beam size for the case where the gain medium was removed. The measured beam size was then compared to the prediction, as shown in Table 3.3.

Location	Measured mode radius in Air (mm)	Predicted mode radius in Air (mm)	Predicted mode radius in YAG (mm)
L2	0.181	input to model	–
L3	0.273	input to model	–
L4	(N/A)	0.126	–
P1	0.098	0.103	0.103
P2	0.107	0.099	0.098
P3	0.125	0.117	0.100
P4	0.152	0.149	0.109
P5	(N/A)	0.188	0.123

Table 3.3: Comparison of the predicted and measured pump beam radii.

The measured beam size in air agrees well ($\pm 5\,\mu$m) with the predicted values, therefore the pump beam should have a 0.2 mm diameter and low divergence within the crystal as shown in Figure 3.11. This will allow the pump light that is not absorbed after the first pass through the gain medium to be retro-reflected with low divergence and increase the total absorption. The double-pass pumping technique will improve pump absorption in the low Er doped gain medium and provide more uniform inversion, both of which will improve efficiency.

A photograph of the pump configuration is shown in Figure 3.12. The picture shows that space between the optics and mounts have been minimized so that the laser can be kept compact.

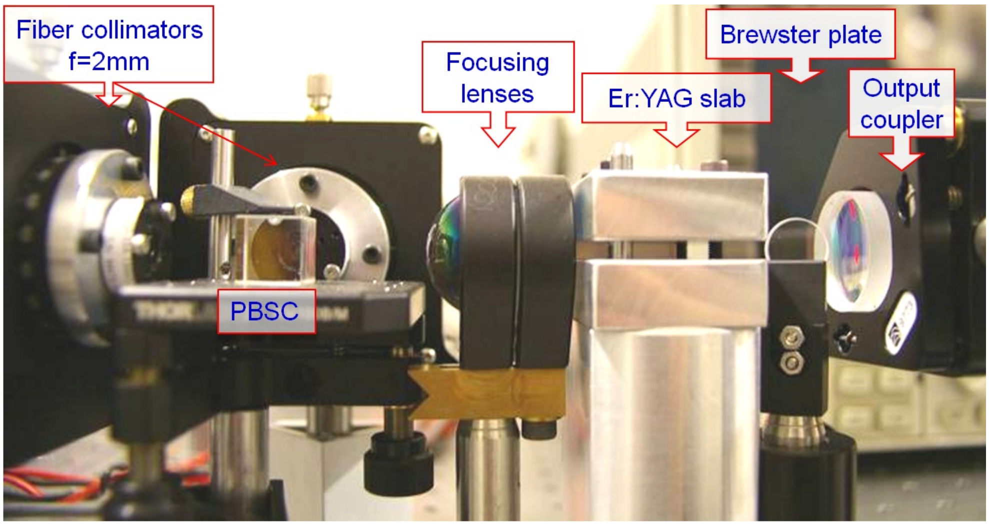

Figure 3.12: A photo of the pump setup and the laser resonator.

3.3.5 Fluorescence of pumped gain medium

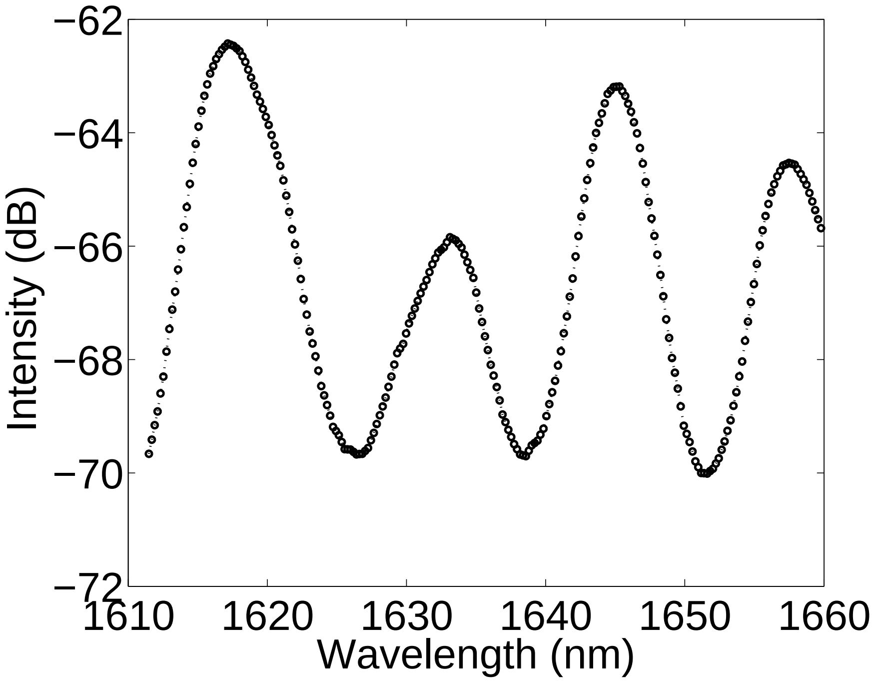

Figure 3.13: Measured fluorescence spectrum of Er:YAG.

The spectrum of the $^4I_{13/2}$ to $^4I_{15/2}$ fluorescence in the Er:YAG gain medium, measured using a grating OSA, is shown in Figure 3.13. The measurement resolves 4 emission peaks at 1617 nm, 1634 nm, 1645 nm and 1657nm emissions, and is in good agreement with the published result [72]. As was described in Section 2.2.3, although the emission line at 1617 nm has a higher emission cross section, CW Er:YAG lasers lase at 1645 nm because of the lower threshold due to the lower re-absorption loss at 1645 nm.

3.4 Resonator design

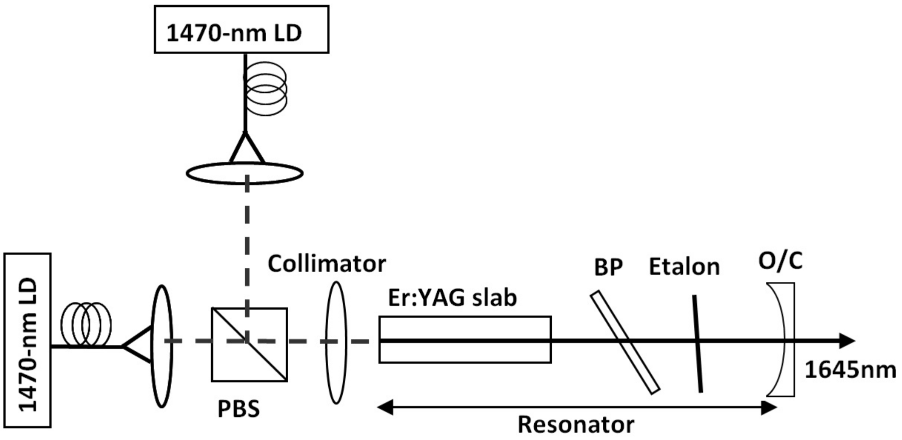

Figure 3.14: Schematic of the laser. Abbreviations: LD, laser diode; BP, Brewster-angled plate; O/C, Output coupler.

This section describes the design of the standing-wave resonator used to achieve TEM_{00} output. I begin by discussing the requirements of the laser together with the background theory, and then describe the resonator development.

A schematic of the laser resonator is shown in Figure 3.14. The laser resonator has a Brewster-angled plate and an 8 mm thick, uncoated etalon, to provide a linearly-polarized and single-frequency output as required for a master laser in a CLR. The slab-end closest to the pump diodes is the end mirror of the resonator, and the output coupler is coated for high reflectivity at 1645 nm.

The resonator length is minimized so as to maximize the free-spectral-range (FSR) and thus facilitate single frequency operation. However it should also provide sufficient space for the intra-cavity optics. A Paraxia ABCD model was used to design a resonator that satisfies these requirements and would provide adequate stability.

3.4.1 TEM$_{00}$ mode selection

Diffraction-limited TEM$_{00}$ output from a quasi three-level gain medium can be obtained by matching the TEM$_{00}$ mode diameter with the diameter of the pumped volume. Then, re-absorption losses from the unpumped volume attenuate higher order modes [100].

In general, the mode size is determined by the combination of the curvatures of the resonator mirrors, lenses within the resonator, thermal lensing and resonator apertures [101]. The thermal lensing is expected to be weak, as will be discussed in Section 3.4.2. Thus additional optics will be required to provide mode confinement sufficient for a stable resonator. Instead of using lenses in the resonator, the stability will be obtained using a concave output coupler.

3.4.2 Thermal lensing estimate

The thermal lensing in the gain medium is estimated based on the quantum defect of the laser. I assume that the thermally induced lens can be described by considering the refractive index change due to temperature. It is also assumed the slab is in good thermal contact with a heat sink of fixed temperature. An analytical solution for the focal length of the thermal lens can thus be derived [102]. The effective focal length (EFL) for the entire slab can be expressed by:

$$f_{\text{lens}} = \frac{\pi K r_p^2}{P_h (dn/dT)} \left[\frac{1}{1 - \exp(-\alpha l)} \right] \tag{3.3}$$

where K is the thermal conductivity of the laser material, P_h the fraction of the pump power that results in heating, dn/dT is the change of refractive index with temperature, α is the absorption coefficient and r_p is the radius of the pump beam.

The calculation is based on an end-pumped Er:YAG slab with a length of 20 mm, pumped with a 0.1 mm radius beam from a fiber coupled single-mode laser diode. In Equation 3.3, the heat load considered is 10% of the pump power (90% quantum efficiency). The material parameters for Er:YAG are $dn/dT = 7.3 \times 10^{-6}$ K^{-1}, $\alpha_0 = 7.8$ cm^{-1}, $K = 0.13$ W·m$^{-1} \cdot$ K^{-1}. The dependence of thermal lensing on pump power is plotted in Figure 3.15. The predicted focal length is <2 m for pump powers >400 mW.

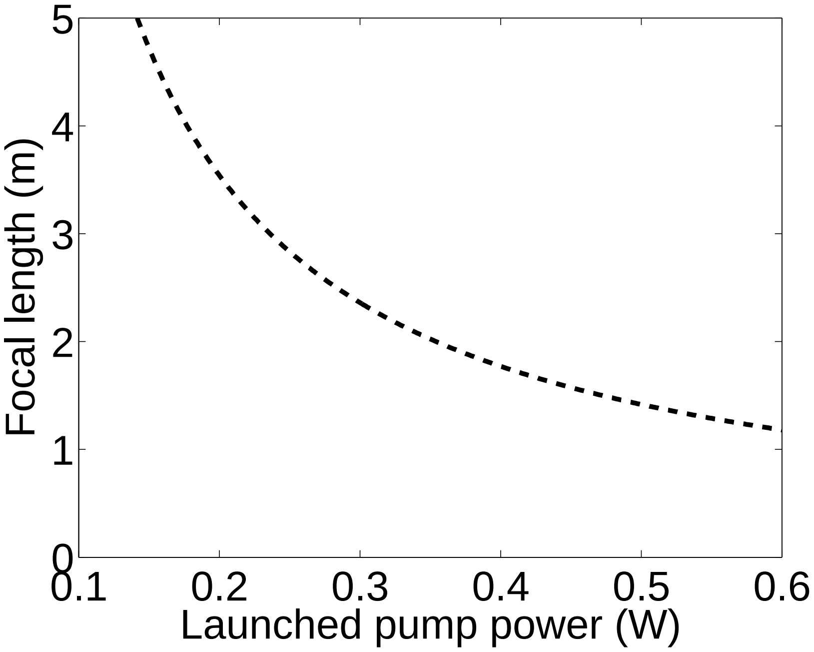

Figure 3.15: Plot of the predicted thermal lens for the Er:YAG gain medium.

3.4.3 ABCD matrices and resonator stability

ABCD transfer matrices can be used to design laser resonators [94]. The transformation analysis of a Gaussian laser beam using ABCD matrices allows the beam size and radius of curvature to be evaluated at any point in an optical system [94, 103].

To describe combinations of optical components, ABCD transfer matrices may be multiplied together to produce an overall system ray matrix. An optical resonator can thus be modeled by the ABCD round-trip matrix, corresponding to one complete round trip within the resonator from a specific reference plane in the resonator [94]. This allows the resonator eigen-equation to be determined, as it reproduces itself after one complete trip around the resonator. The resonator design based on this ray transfer matrix analysis is described in Section 3.4.4.

The resonator stability can also be determined using the round-trip ABCD matrix. The matrix half trace, m, can be calculated using [94]

$$m = \frac{A+D}{2}, \tag{3.4}$$

which does not vary with choice of reference plane within the resonator. For a geometrically stable resonator with purely real ABCD elements, m must be in the range

$$-1 \leq m \leq 1 \tag{3.5}$$

While resonators with $m = 0$ have the greatest stability, in practice resonators with -0.5 $< m <$ 0.5 have adequate stability.

3.4.4 Resonator model

The standing-wave resonator was modeled using the Paraxia 2.0 ABCD program. Various constraints were considered in the modelling [101], including

- Allowable mirror to slab distances.
- Stability over a range of thermal lensing values.
- Mode matching between the laser and the pump modes to prevent higher-order modes.

The resonator model is shown in Figure 3.16, and the parameters used are shown in Table 3.4. The length of the resonator is kept short to maximize the FSR, so as to simplify the use of etalons to achieve single frequency operation.

The size of the pump beam was determined in Section 3.3; it provides a 0.2 mm soft aperture in the slab (locations A1 and A2 in Figure 3.16). Thus, the mode sizes at locations A1 and A2 were investigated for various thermal lens values and D3 distances.

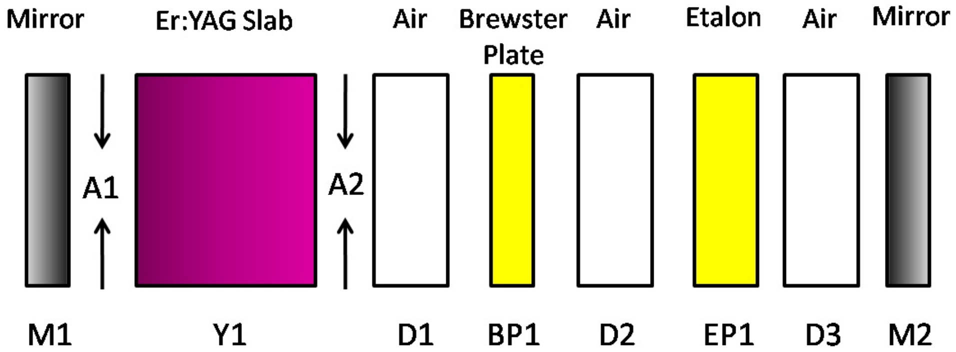

Figure 3.16: The standing-wave resonator Paraxia model.

Mirror M1	Mirror M2 (Radius of curvature)	Thermal lens EFL	D3	Mode radius A1	Mode radius A2	ABCD half trace stability (m)
Flat	5 cm	100 cm	10 mm	0.105 mm	0.118 mm	-0.576
Flat	5 cm	130 cm	10 mm	0.105 mm	0.118 mm	-0.568
Flat	5 cm	200 cm	10 mm	0.105 mm	0.118 mm	-0.559
Flat	5 cm	130 cm	15 mm	0.094 mm	0.112 mm	-0.759
Flat	5 cm	130 cm	5 mm	0.111 mm	0.122 mm	-0.374

Table 3.4: Paraxia resonator modeling results.

Selected results are shown in Table 3.4. The thermal lensing has minimal effect on the mode size for focal lengths between 1 m to 2 m as the focusing in the resonator is dominated by the mirror curvature. In contrast, the resonator stability and mode size are sensitive to the length D3. Thus, the output coupler needs to be positioned to within ±5 mm (D3) to achieve the desired mode size and have adequate resonator stability (m = -0.5).

A standing-wave resonator length of 50±5 mm was determined to be a suitable length, while D1, D2 and D3 values were set to 5 mm, 5 mm and 10±5 mm. The use of a concave output coupler with 5 cm radius of curvature was chosen to provide a good mode overlap (>95%) between the laser and pump and a stable standing-wave resonator. The mode radius at A1 and A2 is about 0.11 mm, which is very close to the pump radius.

3.5 Master laser performance

3.5.1 Multi-mode operation

Figure 3.17 shows the Er:YAG laser without the intra-cavity etalon and Brewster-angled plate. A calibrated thermal power meter was used to measure the output power of the laser with a typical uncertainty of around 1-2 mW.

The measured multi-mode output power is plotted as a function of the pump power in Figure 3.18. A maximum output power of 50 mW with a slope efficiency of 19% was obtained using a R=95% (nominal) output coupler. A slightly lower slope efficiency with an output power of 37 mW was obtained using a R=98% output coupler. The lowest threshold power, about 250 mW, was achieved using the 98% output coupler.

Figure 3.19 shows the spectrum of the multi-longitudinal mode output, recorded using a calibrated grating OSA.

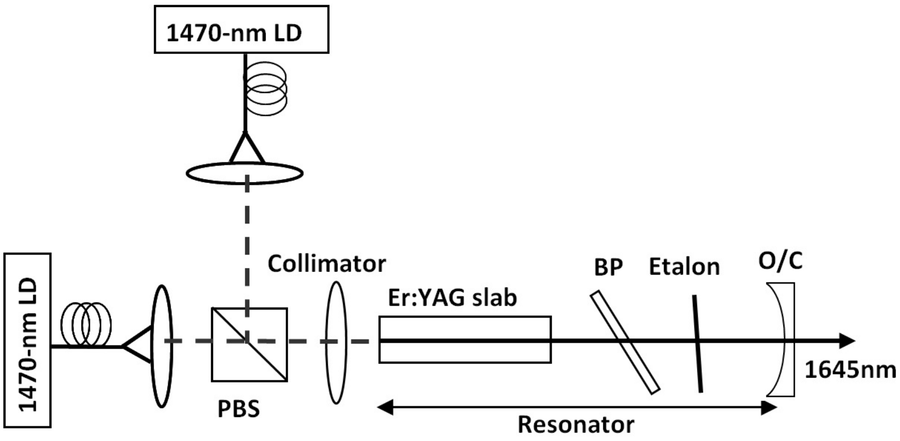

Figure 3.17: A schematic of the standing wave laser without the Brewster plate and etalon.

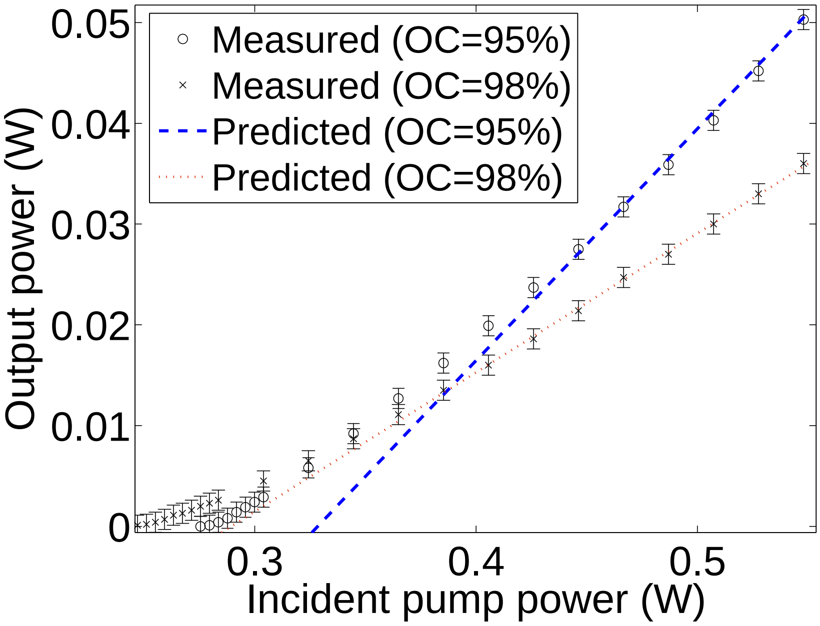

Figure 3.18: Plot of output power in multiple longitudinal mode versus incident pump power. The lines are the predictions of the Beach model, as discussed in the text.

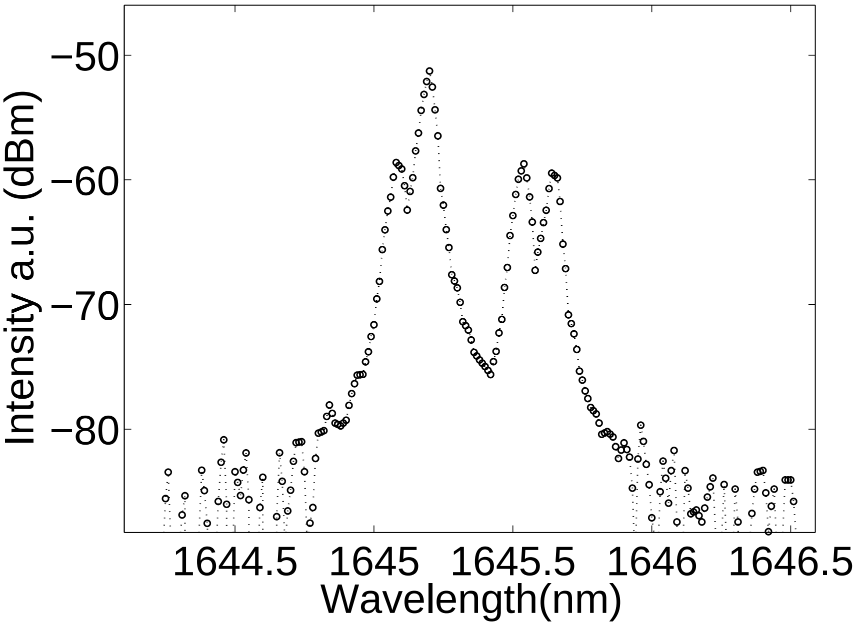

Figure 3.19: Spectrum of the multi-longitudinal mode output, measured using a grating OSA.

Comparison with numerical models

The predictions of the Beach and Auge models discussed in Chapter 2 were compared with the measured output power. The values of the parameters used for the models are listed in Table 3.5. In each case, the radii of the pump and laser modes and the cavity loss were adjusted to match the output for the 95% output coupler.

Parameter	Beach's model	Auge's model
Upper state Boltzmann occupation factor	0.209	0.209
Lower state Boltzmann occupation factor	0.022	0.022
Stimulated emission cross section	5.5×10^{-21} cm^2	5.5×10^{-21} cm^2
Pump absorption cross section	1.1×10^{-21} cm^2	1.1×10^{-21} cm^2
Pump radius	0.120 mm	0.114 mm
Laser mode radius	0.102 mm	0.108 mm
Upper state lifetime	6.8 ms	6.8 ms
Cavity loss	3.4%	2.5%
Output coupler reflectivity	95%, 98%	95%, 98%
Double pass pumping	Yes	Yes

Table 3.5: Parameters used for the multi-mode laser model.

The predictions of the Beach model (Section 2.4) are plotted on Figure 3.18. As indicated above, the pump radius and cavity loss were set to be 0.12 mm and 3.4%, respectively, to fit with the measured power for the 95% output coupler. The predicted power for the 98% output coupler uses these values and agrees well with the measurement at high pump power. Recall that the Beach model is a steady-state assumption, and is thus unable to predict the gradual increase in slope efficiency of a quasi-three level laser near threshold.

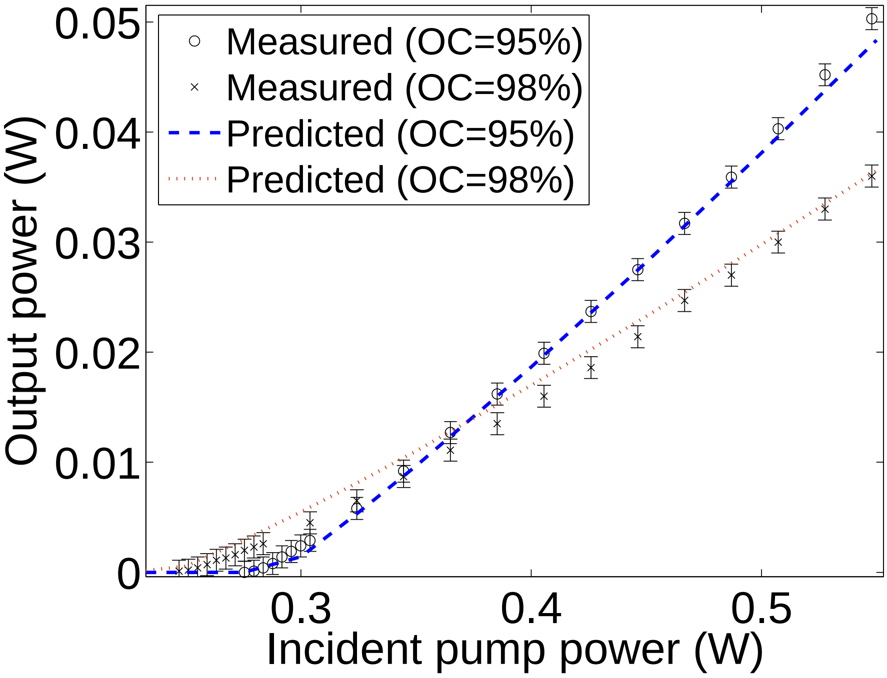

Figure 3.20: Plot of the measured output power and the predictions of the Auge model.

The predictions of the Auge model [96] are plotted in Figure 3.20. This model calculates the laser gain at each pump power, thus allowing it to predict the gradual increase in the slope efficiency near the threshold. The values used for the Auge model are basically identical to those for the Beach model; only two minor adjustments were made for the pump radius (6 microns smaller) and the cavity loss (0.9% less).

In summary, we have validated both models using the experimental results. The good agreement obtained indicates that these models are useful for predicting the performance of CW Er:YAG lasers.

3.5.2 Single frequency operation

Single frequency operation was achieved using the resonator discussed in Section 3.4.4. Without an etalon, the master laser was expected to produce longitudinal modes which are separated by the FSR of the cavity, about 2.5 GHz, within the laser gain bandwidth. An 8 mm thick, uncoated etalon has a 12 GHz FSR with a finesse of about 1.1, thus allowing sufficient suppression on the adjacent modes to allow single frequency operation [104, 105].

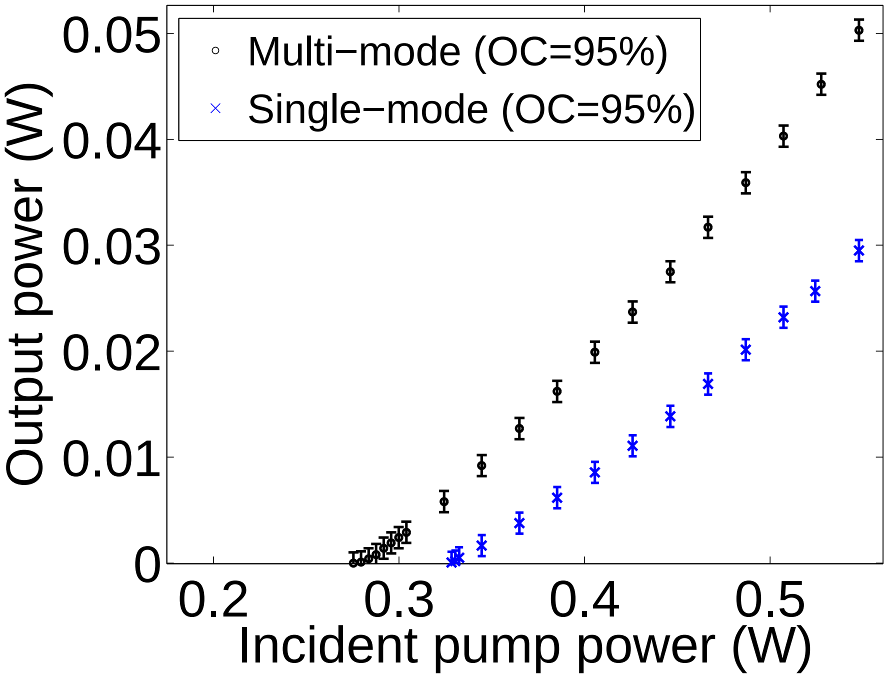

Figure 3.21: Plot of output power versus incident pump power. (o) multiple longitudinal mode; (x) single frequency.

The output power of the single frequency laser with a 95% output coupler is shown in Figure 3.21, where it is compared to the multi-mode output power. The etalon and Brewster plate in the resonator appear to increase the threshold and reduce the slope efficiency, but an output power of 30 mW is still obtained.

The spectrum of the laser output was measured using a calibrated grating optical spectrum analyzer and a self-built scanning Fabry–Perot cavity [106]. The spectral resolution of the grating OSA is 0.05 nm and therefore it was unable to resolve the individual longitudinal modes of the laser.

As no appropriate Fabry-Perot cavity was available, a confocal Fabry-Perot cavity was constructed (shown in Figure 3.22) using two $R = 99\%$ output couplers, both with a radius of curvature of 10 mm. The cavity finesse was calculated using:

$$F_c = \pi \frac{R^{1/2}}{(1-R)}, \tag{3.6}$$

giving $F_c = 156$.

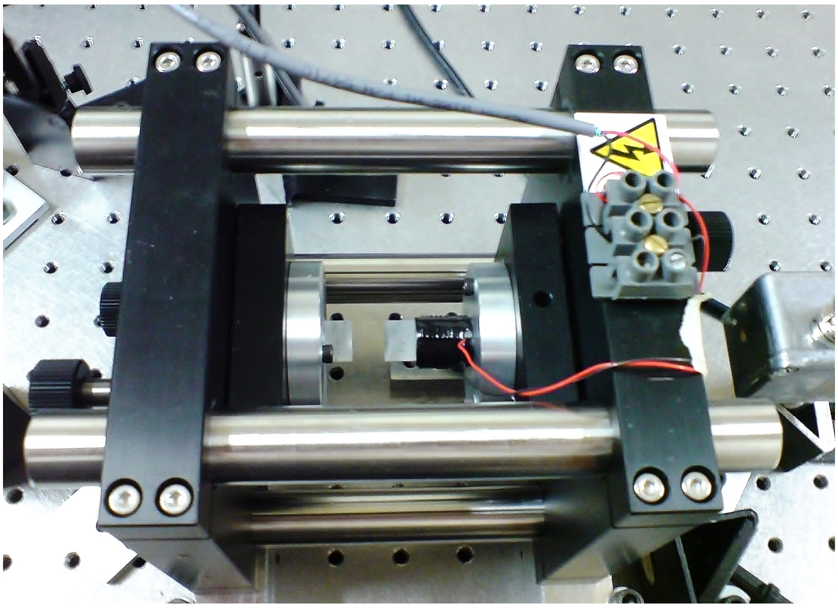

Figure 3.22: The scanning Fabry-Perot cavity.

The two mirrors were separated by a distance of 1 cm using rigid Invar rods, and the exit output coupler was mounted on a piezoelectric actuator (Piezomechanik, HPSt500/15-8/15). This resulted in a FSR = 15 GHz, yielding a factor of 3 better resolution (0.05 nm) than the grating OSA.

One advantage of a confocal Fabry-Perot interferometer is its insensitivity to the input beam alignment, as the cavity is mode degenerate [107]. However, the master laser still needed to be mode-matched to form a waist of diameter 0.07 mm at the center of the confocal cavity. This was achieved using two lenses.

The transmission of the Fabry-Perot for the multi-mode laser is shown in Figure 3.23. In contrast, a typical spectrum of the single-frequency laser is shown in Figure 3.24. The absence of peaks between the main resonances of the Fabry-Perot confirms single-frequency lasing.

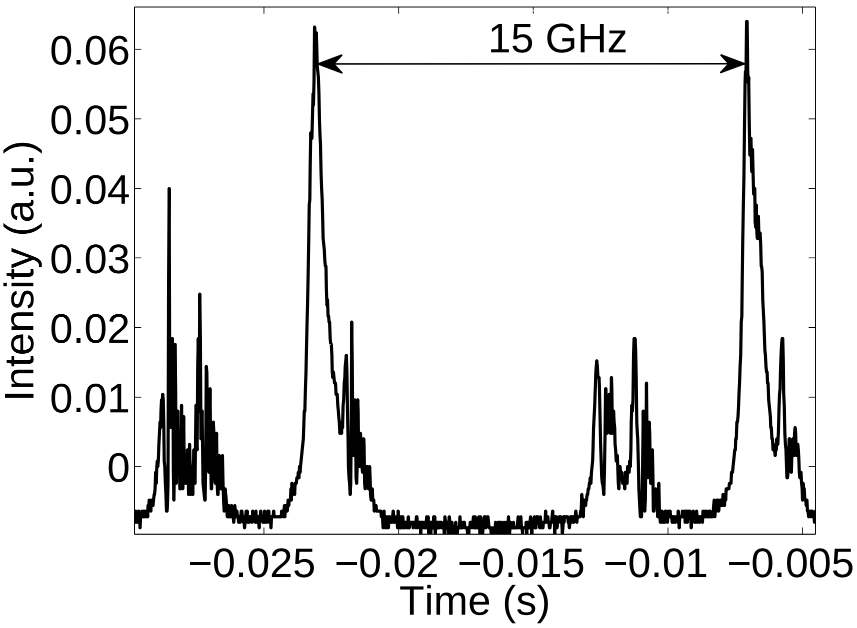

Figure 3.23: Fabry–Perot scan of the multi-mode Er:YAG master laser output, showing multi-frequency operation.

The spectrum from the grating OSA in Figure 3.25 confirms that the laser is lasing only at 1645 nm.

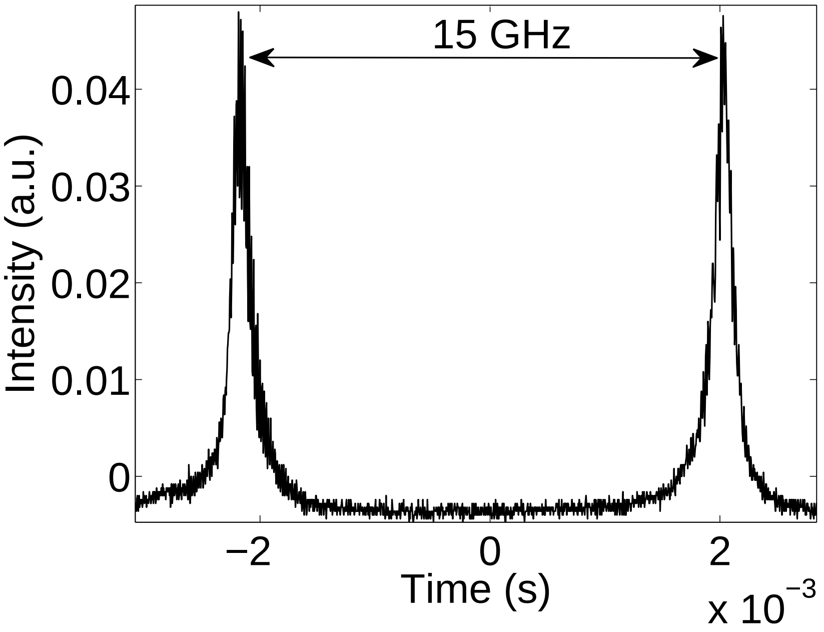

Figure 3.24: Fabry–Perot scan of a Er:YAG master laser, showing single-frequency operation at an output power of 27 mW.

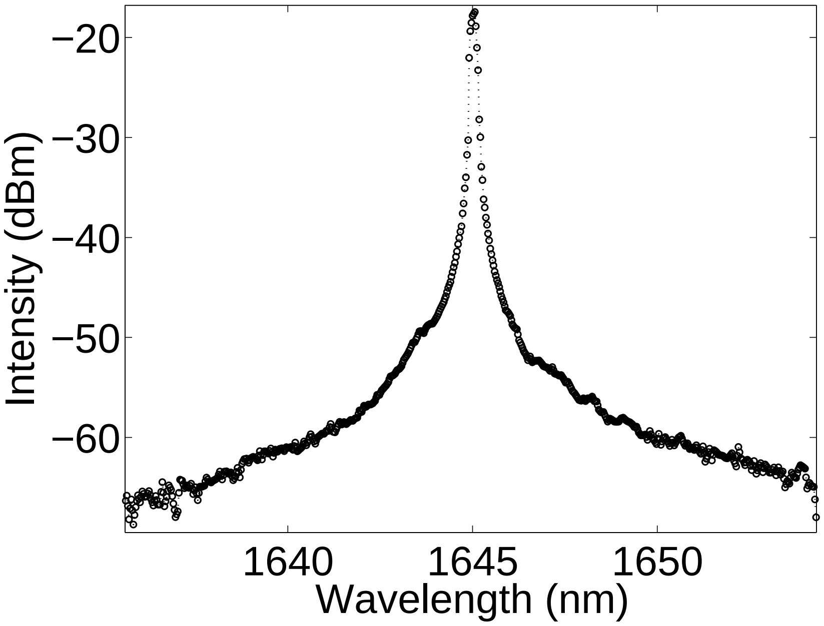

Figure 3.25: Single frequency operation checked by the grating OSA over a 20 nm spectral range.

3.6 Self heterodyne linewidth measurement

The fluctuation of the laser frequency over time intervals relevant to the CLR application was measured using the self-beating heterodyne detection method [108, 109]. A schematic of the measurement system is shown in Figure 3.26 [108, 109].

Figure 3.26: Self-heterodyne linewidth measurement setup [109]. The acousto-optic modulator (AOM) shifts the heterodyne beat frequency to the modulation frequency ω_m. (ω_m= 80 MHz).

In this measurement, the laser beam is split into two beams. One is frequency shifted by 80 MHz using an acousto-optic modulator, and the other delayed by transmission through an acoustically shielded, 20 km long, single-mode optical fiber. This delay corresponds to a CLR range of about 15 km. The two laser beams were recombined using a 50/50 fiber coupler and the beat-frequency spectrum measured using a reverse-biased InGaAs PIN photodiode and an RF spectrum analyzer. For a long delay, the superimposed beams are essentially uncorrelated, and the output spectrum becomes a simple self-convolution of the laser output spectrum, from which the laser linewidth can be retrieved.

Figure 3.27 shows the measurement of relative frequency fluctuation averaged over 100, 500 and 1000 sweeps with the 20-km delay. The width (FWHM) of the relative frequency fluctuation is observed to be 11 kHz from a single 20 ms sweep measurement. The width of the spectral fluctuation averaged over 1000 sweeps is 12 kHz which is not a significant broadening compared to the single sweep measurement. Since the product of the delay time (100 μs) and the line-width is larger than 1, we can conclude that the intrinsic line-width of the laser is also about 12 kHz [109]. A frequency shift of 12 kHz corresponds to an aerosol velocity of 0.01 ms^{-1}, which is much less than the required 0.1 ms^{-1} single-pulse velocity sensitivity.

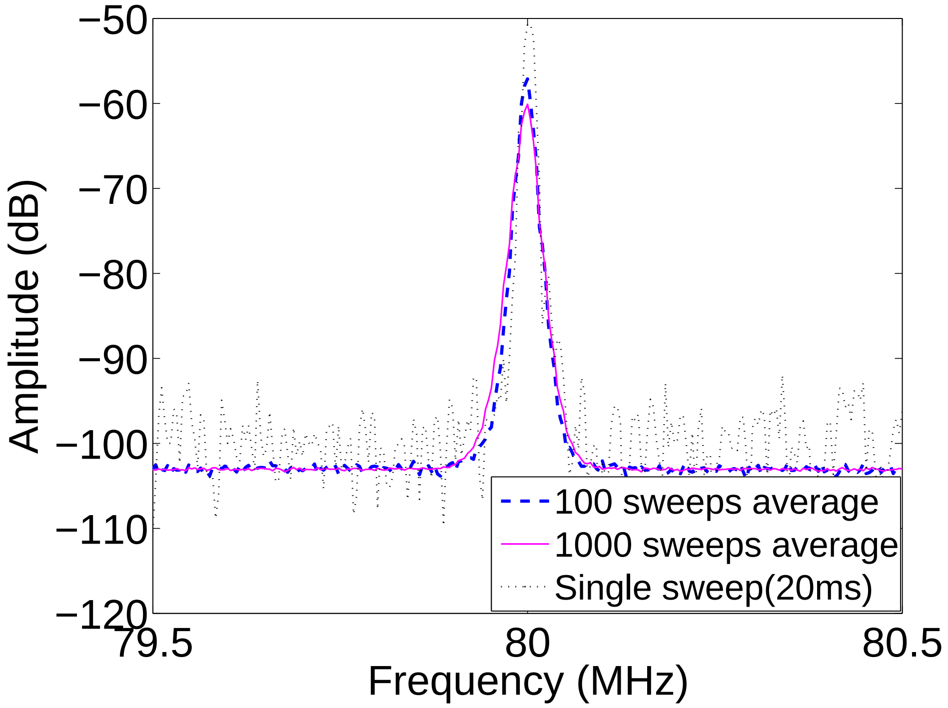

Figure 3.27: Frequency fluctuation spectrum of the single frequency Er:YAG laser, measured using a self-beat heterodyne system.

3.7 Beam quality measurement

The intensity profile of the laser mode, measured using an IR camera, is shown in Figure 3.28.

Laser beam quality can be measured using Hartmann or Shack-Hartmann wavefront sensors [110], by measuring the transmission through a mode-matched passive optical cavity [111], or by the approach recommended by the ISO Standard 11146 [112] where the spot size of the beam is recorded at a focus and at points be-

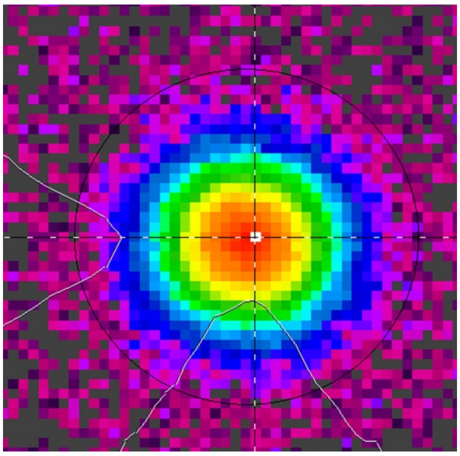

Figure 3.28: Intensity profile of the Er:YAG laser output.

yond the Rayleigh range. Laser beams that are produced by a stable resonator which are not perfectly Gaussian have $M^2 > 1$, while diffraction-limited Gaussian beams have $M^2=1$ [81,113]. The last approach was employed to measure the beam quality as this technique offers accurate measurement with a simple experiment setup.

The output of the master laser was focused to a waist and the spot-size of the beam was measured at multiple points near the waist and outside the Rayleigh range. The beam propagation factor, M^2, was calculated using

$$M^2 = \frac{r_0 \theta \pi}{\lambda} \tag{3.7}$$

where r_0 is the waist radius, $r(z)$ is the values of spot-size at a distance, z, and θ is far field divergence angle obtained by fitting a curve of the form

$$r(z)^2 = r_0^2 + \theta^2 z^2. \tag{3.8}$$

The spot-size was measured by translating a knife-edge across the beam and recording the distance travelled to block 10% then 90% of the beam power and multiplying this value by a factor of 0.781 to obtain the $1/e^2$ diameter [114]. This approach assumes a near-Gaussian profile with $r(z)$ being the radius that encloses $1/e^2$ or 86.5% of the beam energy. The $1/e^2$ definition was adopted in this case, as the laser beam has a Gaussian intensity shape (Figure 3.28). If beams are far from diffraction limited, then the Gaussian definition of spot-size becomes less meaningful and alternative definitions should be used [115]. The beam quality analysis code, written in Matlab, is included in Appendix D.

Plots of the spot-size data for both axes, together with a least squares fit to the data using Equation 3.8, are shown in Figure 3.29. The beam propagation factors were measured independently for the x and y-axes, and the corresponding curves of best fits, give $M_x^2 = 1.02$ and $M_y^2 = 1.08$.

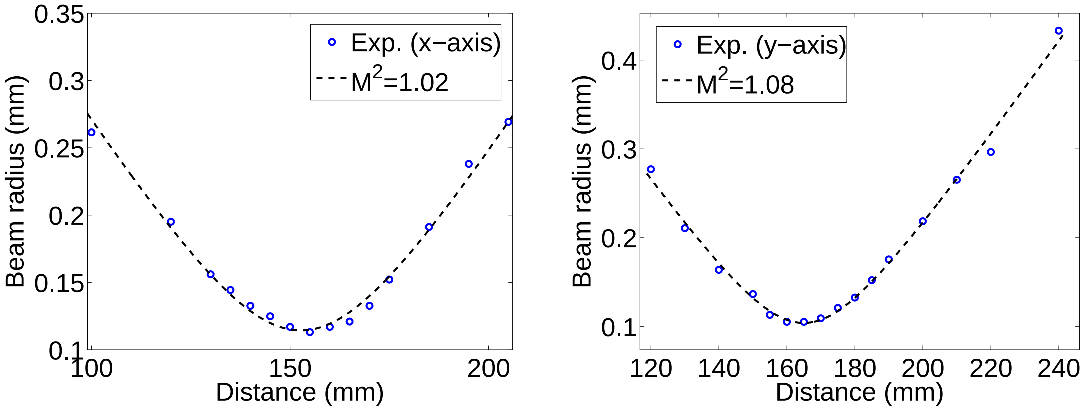

Figure 3.29: Measurements of beam quality for the 27 mW single frequency master laser showing near-diffraction limited output in both x- and y-directions. The measurement has an uncertainty of ± 3% due to the accuracy of the translation stage used to measure the beam waist.

3.8 Conclusion

In this Chapter, I've presented the design and testing of a single frequency, continuous wave, Er:YAG laser that produces a 30 mW, diffraction-limited beam with a frequency stability better than 12 kHz for delay times of 100 µs. The laser is well suited to use as the master oscillator in a coherent laser radar system: the power will allow robust injection seeding of the pulsed slave laser in high vibration environments and the frequency stability will allow high precision single-pulse wind velocity measurements.

Direct pumping of Er:YAG using laser diodes at 1470 nm, rather than pumping using an EDFL, provides a simpler and cheaper system [77]. It also delivers improved wall-plug efficiency, despite the larger line-width and poorer brightness of the diodes, as it removes the inefficiency associated with the EDFL.

4 Design and construction of the Er:YAG slave laser head

4.1 Introduction

As described in Chapter 1, Doppler wind-field mapping requires mJ-energy pulses with durations >100-200 ns and PRFs >100 Hz to provide a spatially dense array of samples, to allow signal averaging with minimal loss of temporal resolution and to minimize the time required to scan an extended volume. The high PRF requirement suggests that the Q-switched, Er:YAG free-space laser should be CW pumped. The objective of this chapter is to describe the development and characterization of a high power Er:YAG laser head that is pumped by a broad bandwidth CW laser diode at 1470 nm. The development of the laser head for a multi-watt LIDAR transmitter needs to consider the following important requirements:

- It should produce an output power of 3-5 W in a short multi-mode CW standing-wave laser, to allow for a possible decrease in average power due to losses in components needed to Q-switch the laser.
- The damage threshold of the laser components need to be higher than the peak power of the Q-switch pulses (i.e., 5 mJ pulses with 100 ns duration).
- The laser head requires good thermal management to minimize thermal lensing

and thus, allow good spatial overlap between the modes and efficient laser operation.

- For remote sensing applications, the laser head needs to be robust and able to operate for long periods without maintenance. This requirement places constrains on the portability, simplicity and cooling method for the laser system.

Extensive testing was performed using a standing-wave laser configuration, thus allowing the essential information about the effectiveness of thermal control and important properties of the laser head to be characterized.

This chapter begins with Section 4.2 describing the specifications of the Er:YAG laser slab. The design of the slave laser is discussed in Section 4.3. The development the slab holder of the laser head is discussed in Section 4.4, followed by the discussion of the pump module in Section 4.5. The standing-wave laser built using the laser head is characterised in Section 4.16.

4.2 Slave laser gain medium design

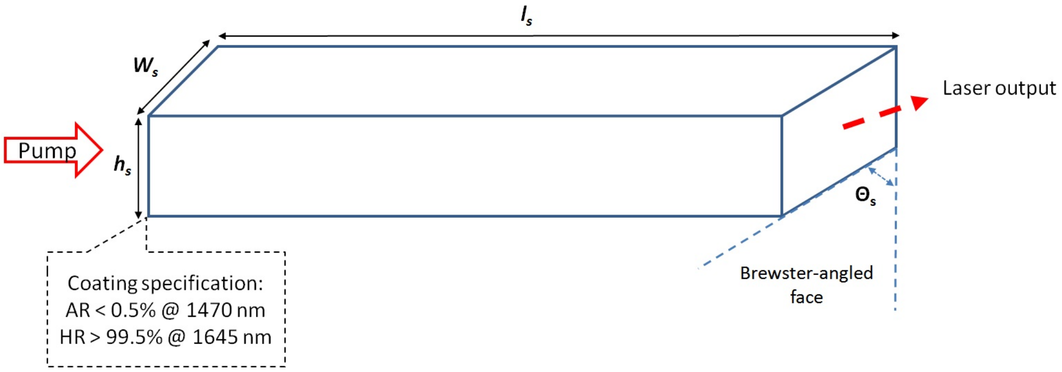

Figure 4.1: Schematic of the laser slab.

The schematic of the gain medium is shown in Figure 4.1. The gain medium is an end-pumped, straight-through (non-zigzag) slab with a Brewster-angled intra-resonator face. A pump intensity of 3 kW/cm^2 is used as it's well above the required lasing-threshold described in Chapter 2. The slab-end closest to the pump diodes is also the end mirror of the resonator, and is coated for high reflection (R >99.5%) at 1645 nm and high transmission (T >99.5%) at the 1470 nm pump wavelength. The output window of the slab is cut at the Brewster angle, θ_s, of 28.8±0.5 degrees, thereby eliminating the intra-cavity coating, which is more susceptible to damage by high intra-cavity fluxes, and providing the polarization discrimination required for electro-optic Q switching.

For the initial development, we chose to modify one of the gain media used for the master laser. The Er:YAG laser gain medium, with a doping concentration of 0.5 at.%, has a Brewster window polished and finished by Jung Precision Optics Pty Ltd. (Salisbury, South Australia, Australia). The finished slab has a length (l_s) of 20±0.1 mm (long side), width (w_s) of 3.0±0.1 mm, and height (h_s) of 3.0±0.1 mm. The slab sides are fine ground for improved thermal contact to the slab holder.

4.3 Numerical simulation of the CW laser

The design of the slave laser head when operating in a CW laser is simulated using the Beach model described in Chapter 2. The parameter values are listed in Table 4.1. As for the numerical simulation of the low power master laser in Chapter 2, a Rigrod analysis [94] was performed for the output power as a function of R_{oc}.

The results are shown in Figure 4.2, and predict an optimum output-coupler reflectivity of 95% for the assumed 35 W of pump power. The optimum reflectivity is only weakly sensitive to cavity loss. However, a slightly higher cavity loss of 3% will result an output power of <4 W, thus losses due to the Q-switch components should be carefully evaluated.

Parameter	Symbol	Value
Erbium density for 0.5% concentration	N_t	0.7×10^{20} cm^{-3}
Photon energy at 1645 nm	$h\nu_l$	1.21×10^{-19} J
Photon energy at 1470 nm	$h\nu_p$	1.35×10^{-19} J
Normalized Boltzmann factor for lower laser level	f_{1l}	0.022
Normalized Boltzmann factor for upper laser level	f_{2l}	0.209
Normalized Boltzmann factor for lower pump level	f_{1p}	0.264
Normalized Boltzmann factor for upper pump level	f_{2p}	0.089
Absolute Er^{3+}cross section at 1645 nm	σ_l	2.5×10^{-20} cm^2
Absolute Er^{3+}cross section at 1470 nm	σ_p	4.2×10^{-20} cm^2
Er:YAG crystal length	l_s	2 cm
Pump mode radius	r_p	0.07 cm
Upper state lifetime	τ_s	6.8 ms
Launched pump power	P_p	35 W
Pump delivery efficiency	η_{eff}	0.80
Mode overlap ratio	η_{mode}	0.85
One-way cavity loss	L_{cav}	0.01, 0.02, 0.03
Reflectivity of the coating for double pass pumping	R_p	0 (single pass)

Table 4.1: Parameters used to model the high power CW Er:YAG laser.

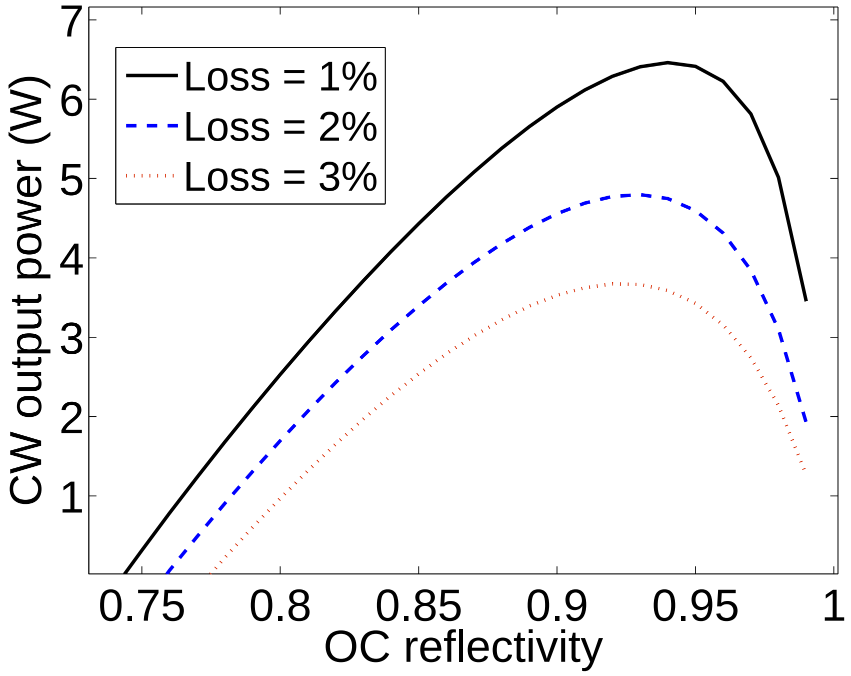

Figure 4.2: The predicted CW output power is plotted as a function of the reflectively of the output coupler (OC) for several loss values.

4.4 Slab holder

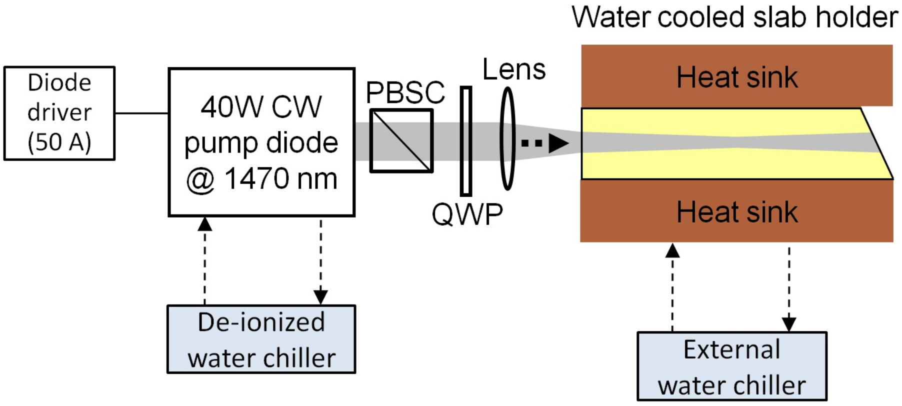

Figure 4.3: Schematic of the high power slave laser head.

As show in Figure 4.3 the laser head consists of a slab holder and a pump diode. The slab holder for the slave laser head clamps the Er:YAG gain medium from both sides. It was designed by a 3D mechanical CAD (computer-aided design) program “Solidworks” [116], and manufactured by EAS Toolcraft Pty. Ltd. The 3D schematic of the water-cooled slab holder design is shown in Figure 4.4 and the mechanical drawings of the components are shown in Appendix E.

The slab holder consists of three main parts: the base and the two copper blocks. Each of the copper blocks has cooling channels, which are connected to an external water chiller. Three ceramic spacers are used to support the copper blocks and limit the compression of the crystal. The laser head temperature was stabilized using water at about 20 ºC.

To reduce the thermal impedance of the Er:YAG-copper interface a 0.125 mm thick layer of indium foil was inserted between the slab and copper. Thus, remove the surface irregularities of the machined copper surface and the fine ground slab can be filled by malleable Indium to improve the thermal contact between the surfaces.

To achieve an intimate, even and reproducible thermal contact without applying excessive clamping stress to the crystal, the following techniques were used to

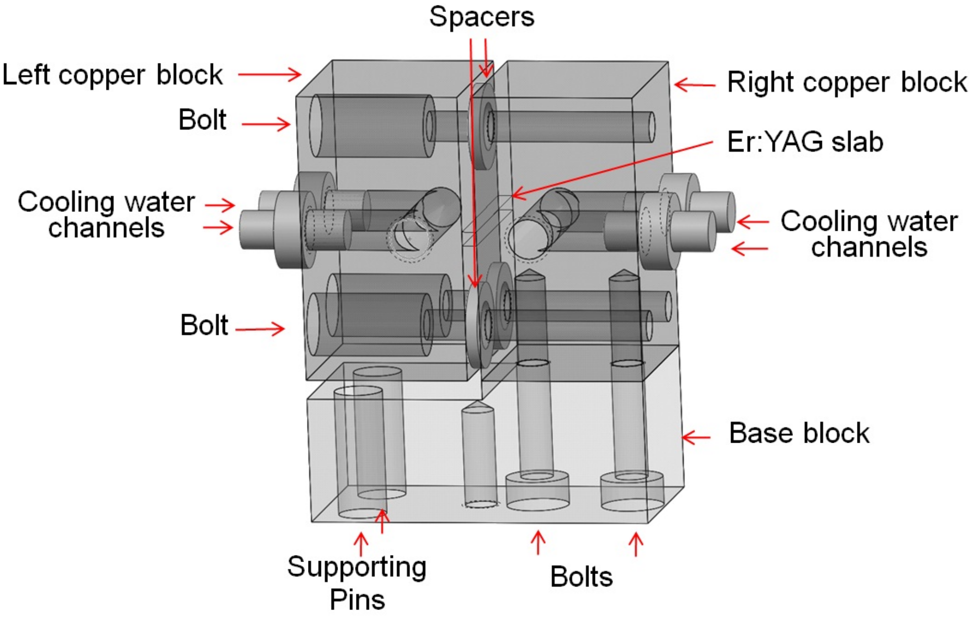

Figure 4.4: Schematic of the slab holder design

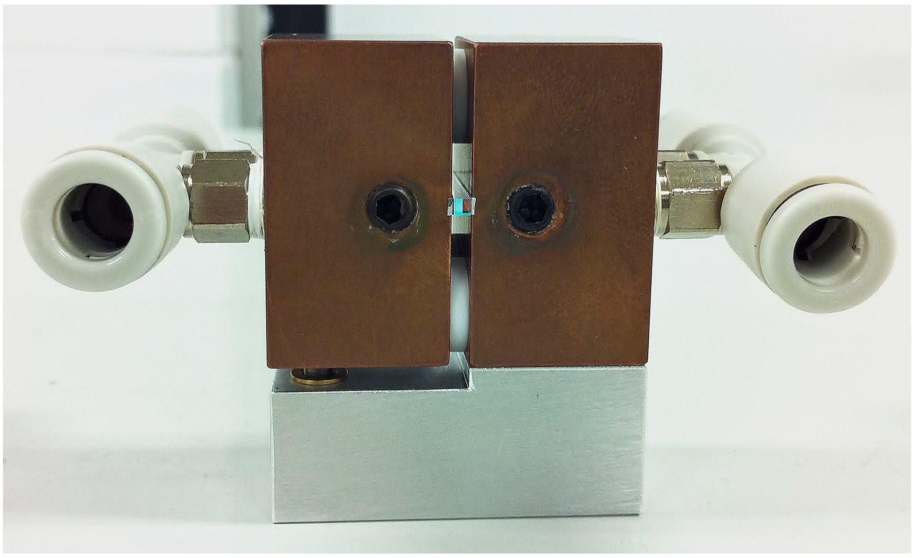

Figure 4.5: Picture of the Er:YAG laser slab holder.

assemble the heatsink-indium-Er:YAG-indium-heatsink sandwich. Firstly, position the pieces of indium foil on the copper blocks (facing up) using a plastic reference jig, then lightly roll the foil onto the copper blocks to reduce the copper indium thermal resistance. Using the right copper block (shown in Figure 4.4) as the base, carefully place the Er:YAG slab on the Indium foil and position the slab using a plastic spacer.

The left copper block (resisted by the bolts) was assembled using three custom made bolts, which were designed to resist the top block during assembly. The Macor (a machineable glass-ceramic) spacers, which have a height tolerance of ±5 µm, allow a crush that is 10% of the thickness of the Indium foil, thus assisting with reproducibility and preventing over tightening. The finished slab holder assembly is shown in Figure 4.5.

4.5 Pump diode

The laser diode selection focused on two criteria: the output divergence and its spectral properties. High brightness pumping using multi-mode laser diodes is generally more challenging to achieve good collimation, because these diodes use stacked linear-arrays of emitters to produce high brightness and each emitter typically has a divergence of 10-40 degrees [117]. The pump diode is required to provide a pump power >30 W to overcome the lasing-threshold.

Diode emitters operating in the telecommunication c-band usually emit at a wavelength of 1460 nm at room temperature. Thus, the wavelength of the emitters needs to be selected to operate near 1470 nm at room temperature. In addition the centre wavelengths of the emitters need to be within 10 nm to ensure that the emission bandwidth matches the absorption linewidth of Er:YAG.

4.5.1 Pump diode specifications

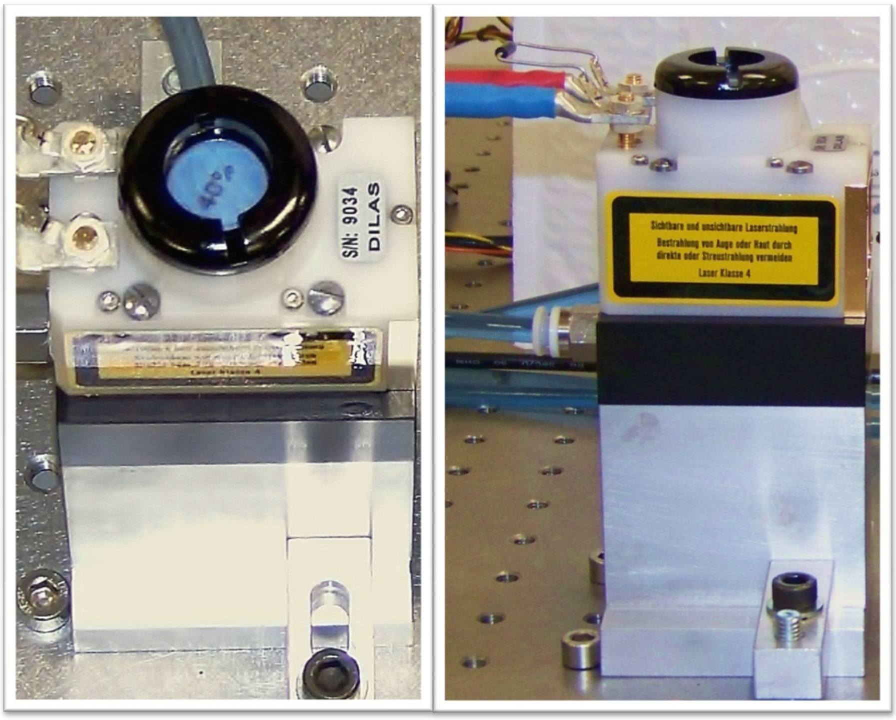

Figure 4.6: The 40 W laser diode is attached to a black-Delrin water cooled manifold on an aluminium base.

A custom 40 W, actively cooled laser diode (E7B-1470-40C-VS1.12) from DILAS Inc. was used to resonantly pump the gain medium of the slave laser. Pictures of the diode module are shown in Figure 4.6. The specifications for the diode are found in Appendix F, and are summarized in Table 4.2. The module consists of 3 bar arrays stacked vertically, and is packaged in a sealed housing. The fast and slow-axis collimation lenses form a rectangular output aperture with a divergence <20 mrad, thus allowing high brightness focusing inside the Er:YAG gain medium. The output of the diode module is linearly polarized, making the laser power scalable by combining another pump diode using a polarization beam combiner. The diode is water cooled by micro channels.

The emission spectrum provided by the manufacturer is shown in Figure 4.7. The spectral linewidth of the pump light is <13 nm, and the flat-top spectral profile is

Parameter	DILAS, E7B-1470-40W diode module
Center wavelength	1465-1475 nm
Output power	40 W
Polarization	Linear polarized output
Spectral width	<13 nm
Threshold current	4.2 A
Operating current	36 A
Operating voltage	3.15 V
Operating Temperature	20-30 ºC

Table 4.2: Specifications of the 40 W pump laser diode for the laser head.

typical for diode modules with multiple emitters. As discussed in Chapter 2 (Figure 2.2), Er:YAG has a broader absorption band at 1470 nm compared to 1532 nm. Thus, pumping at 1470 nm with broadband diode modules is appropriate.

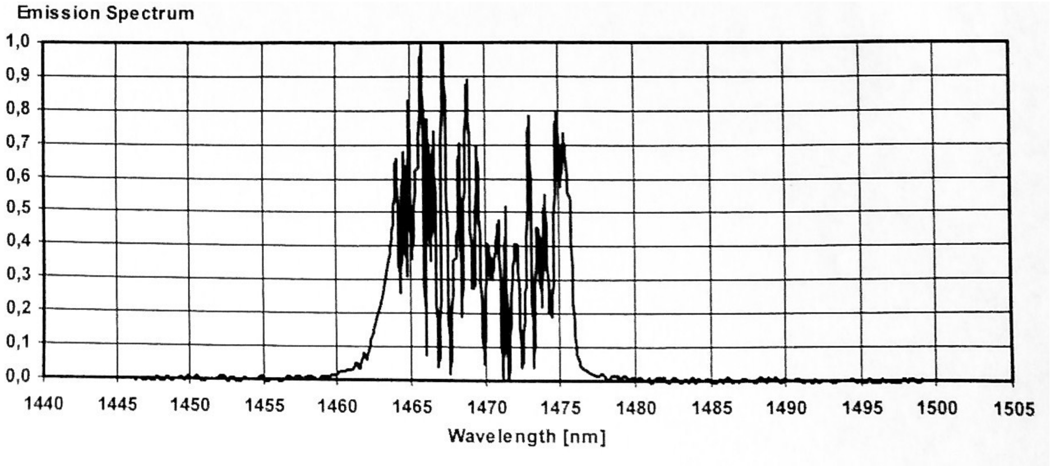

Figure 4.7: The emission spectrum (for a current of 38 A) of the pump diode, as provided by the manufacturer.

4.5.2 Laser diode cooling

The DILAS laser diode module was mounted on a Delrin water manifold, a non-conductive plastic material (as shown in Figure 4.6). O-ring gaskets were used to seal the water connections between the diode and the manifold. The conductivity of the de-ionized water (DI-water) coolant is stabilized by the chiller to meet the criteria listed in Table 4.3 to avoid corrosion within the diode module.

Cooling water flow	1 L/min
Temperature of cooling water	25-35 ºC
Conductivity	<2 µS/cm
pH-value	5.5 - 8
Water filter	<5 µm

Table 4.3: Requirements for the DI-water used to cool the DILAS laser diode.

Figure 4.8 shows the DI-water chiller (Termotech Model P208-16676) used in the cooling system, and the control panel containing a bypass valve and other components. The DI-water chiller can provide temperature stability of 0.1 K and, importantly, has an internal conductivity stabilizer as required by the pump diode module, as listed in Table 4.3. The water bypass panel, shown on the right in Figure 4.8, regulates the flow rate (1 L/min) of the chiller module (listed in Table 4.3). A flow switch (Gems FS-3) is incorporated in the bypass circuit and interlocks the driver of the pump diode to prevent any cooling failure.

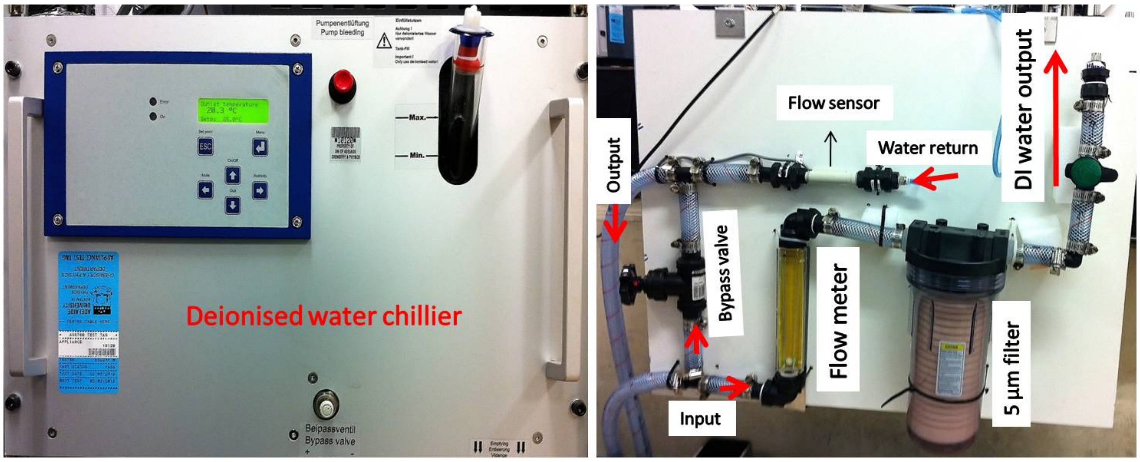

Figure 4.8: The deionized water cooling system for the pump laser diode.

4.5.3 Laser diode operation and characterization

The output of the laser diode was measured using a calibrated power meter (Ophir Nova II). Figure 4.9 shows the plot of the output power of the laser diode when increasing the drive current. The threshold of the diode is about 4.5 A, and an output power of 44 W is obtained at a current of 35 A. The slope of the output power is about 1.45 W/A.

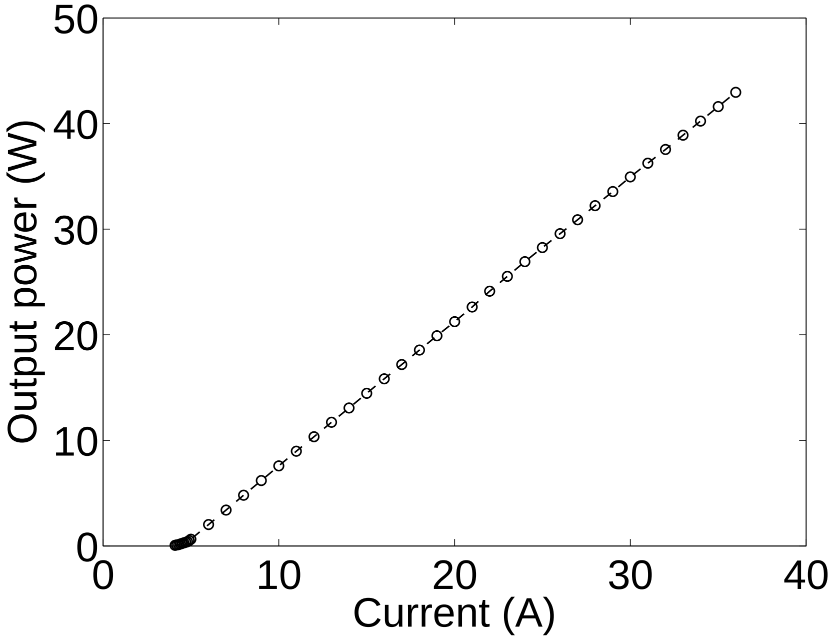

Figure 4.9: Measured output power of the laser diode (DILAS E7B-1470-40C-VS1.12) versus current.

Pump laser wavelength versus current

The wavelength of the pump light was measured using a calibrated fibre-coupled grating OSA (ANDO). The emission spectra for several current settings are shown in Figure 4.10. At a low current setting (10 A), the centre wavelength of the output is about 1465 nm. It shifts to longer wavelengths for currents of 25 A and 33 A. The bandwidth of the spectrum broadens at higher currents to about 10 nm at 33 A. The water temperature was 25 ºC during this measurement; with higher water temperatures resulting in the centre wavelength shifting to longer wavelengths. The measured spectrum at 33 A agrees well with the spectrum shown in Figure 4.7.

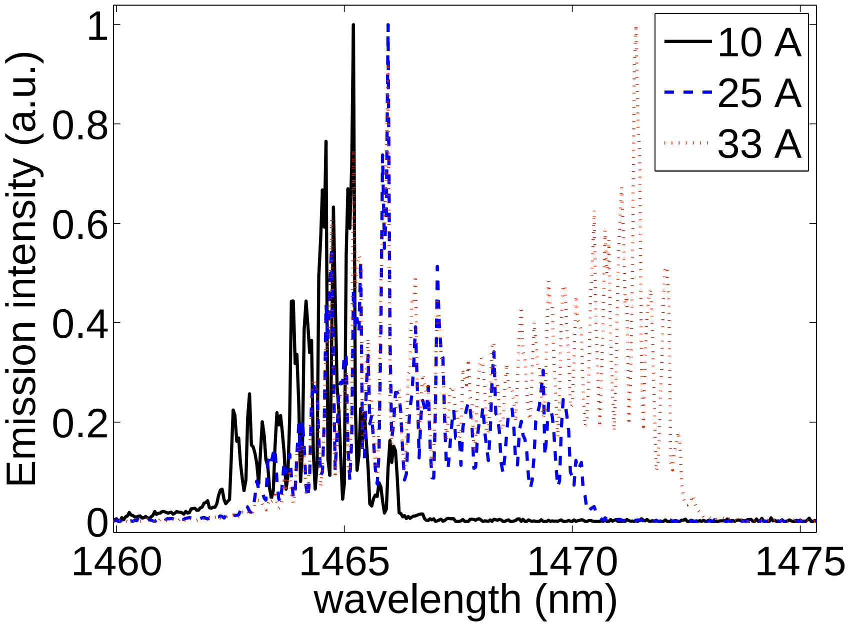

Figure 4.10: Spectra of the laser diode output at several current settings. The temperature of the cooling water was 25 ºC.

4.5.4 Pump focussing

The specified width and divergence of the pump output are listed in Table 4.4. The beam propagation factor, M^2, of the diode is ∼100 as specified by the manufacturer. As discussed in Section 4.3, the output of the diode needs to be imaged to a pump radius of 0.7 mm. Figure 4.11 shows the evolution of the pump size when focused by a f=100 mm lens, where L1 is the focusing lens and P1 - P3 are the locations of the YAG gain medium.

	Fast axis	Slow axis
$1/e^2$ width	13 mm	13 mm
FWHM divergence	<15 mrad	<20 mrad

Table 4.4: Dimensions and divergence of the pump beam as specified by the manufacturer.

The predicted pump radii are summarized in Table 4.5. The calculation predicted that to achieve a pump radius equal to or smaller than 0.7 mm in the crystal would require use of a lens with a focal length <100 mm.

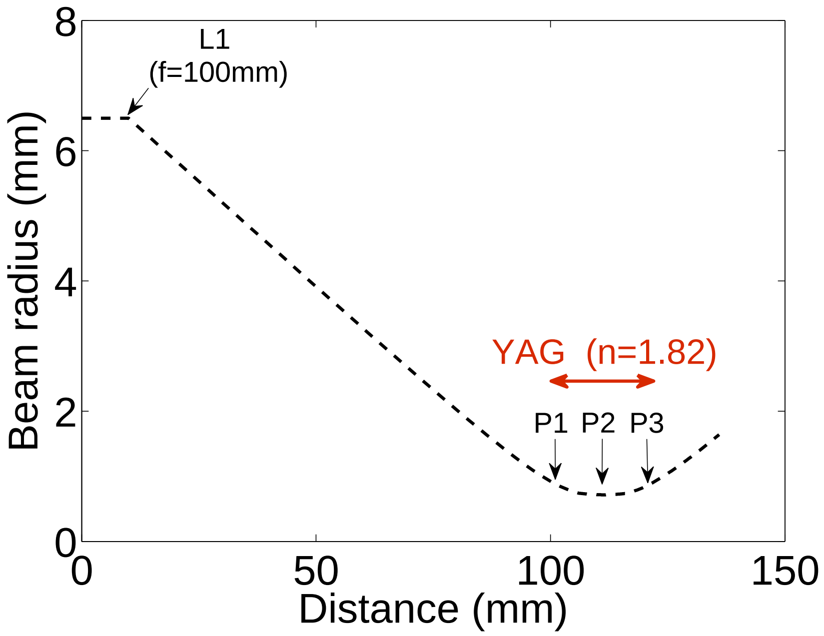

Figure 4.11: Pump beam radius evolution between the output of the laser diode and the end of the gain medium.

Location	Predicted radii (mm)
L1	6.5
P1	0.79
P2	0.71
P3	0.79

Table 4.5: The predicted pump beam radii at several locations.

4.5.5 Thermal lensing due to pump

Thermal lensing and thermal stress-induced birefringence can arise when there are temperature gradients in the gain medium caused by (but not limited to) non-uniform heating and surface cooling. These limit the maximum power extractable from the gain medium. To avoid these deleterious effects, thermal gradients in the gain medium need to be minimized by implementing suitable pumping and cooling geometries. As mentioned in Chapter 3, a resonantly pumped Er:YAG laser has a small quantum defect (90%), and one would hence expect much less thermal lensing.

Thermal lensing prediction

The thermal lensing in the slave laser crystal was estimated using the approach mentioned in Chapter 3. The calculation was based on an end-pumped Er:YAG slab with a length of 20 mm and a pump radius of 0.7 mm. For 30 W of pump power and the heat due to the quantum defect of 10%, this corresponds to 3 W of heat load.

The dependence of thermal lensing on pump power was calculated using Equation 3.3 and is plotted in Figure 4.12. Thus, we expect a focal length of about 2 meters for a pump power of 30 W.

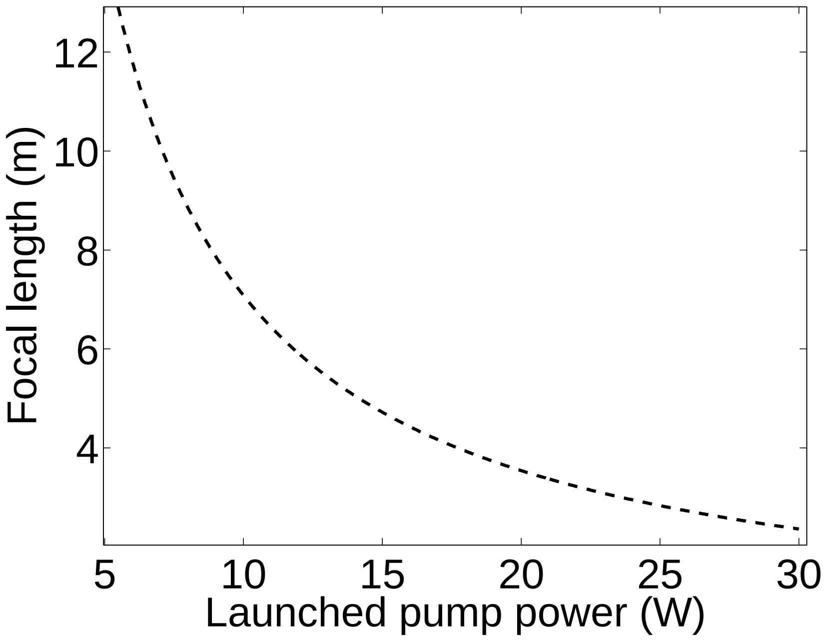

Figure 4.12: Predicted thermal lensing versus launched pump power for the slave laser head.

It was hoped the thermal lensing could provide enough mode confinement for a stable resonator using flat mirrors without extra optics in the resonator. Thus, ABCD half-trace stabilities were evaluated using the parameters shown in Table 4.6. The thermal lens effective focal lengths (EFL) were 1, 2 and 3 meters as predicted Figure 4.12. Several resonator lengths have been calculated to determine the optimum length for the Q-switched resonator.

Resonator length	Thermal lens EFL	Mode radius in YAG (Vertical plane)	Mode radius in YAG (Horizontal plane)	Half-trace stability (Vertical plane)	Half-trace stability (Horizontal plane)
50 mm	2 m	0.37 mm	0.5 mm	0.89	0.68
150 mm	2 m	0.49 mm	0.73 mm	0.70	0.07
250 mm	2 m	0.56 mm	1.01 mm	0.52	-0.50
50 mm	1 m	0.32 mm	0.44 mm	0.78	0.36
150 mm	1 m	0.43 mm	0.97 mm	0.42	-0.83
250 mm	1 m	0.52 mm	unstable	0.05	unstable
50 mm	3 m	0.41 mm	0.55 mm	0.92	0.78
150 mm	3 m	0.53 mm	0.76 mm	0.80	0.30
250 mm	3 m	0.61 mm	0.94 mm	0.68	-0.01

Table 4.6: Modelled mode size and stability results.

For TEM_{00} operation the mode size of the laser needs to match the soft aperture of the pump (radius of 0.6 mm). For a 200 cm thermal lens the design resonator length should be <250 mm for efficient TEM_{00} operation. The predicted ABCD half trace stabilities are, in general, adequate to provide a stable resonator using flat-mirrors ($-1< m <1$).

4.6 Laser head characterization

The wavelength of the pump was optimized to maximize the pump absorption. A standing-wave laser was built using the laser head with flat output mirrors, so that the performance of the laser head could be characterized using a multi-mode laser [81, 118].

4.6.1 Pump absorption

To optimize the pump absorption, the temperature of the cooling water was tuned to the operating current (33 A) of the diode. The transmitted pump of the Er:YAG slab was measured by a power meter, and the highest absorption occurred for a water temperature of 35 ºC, at which ~55-60% of the pump power was absorbed.

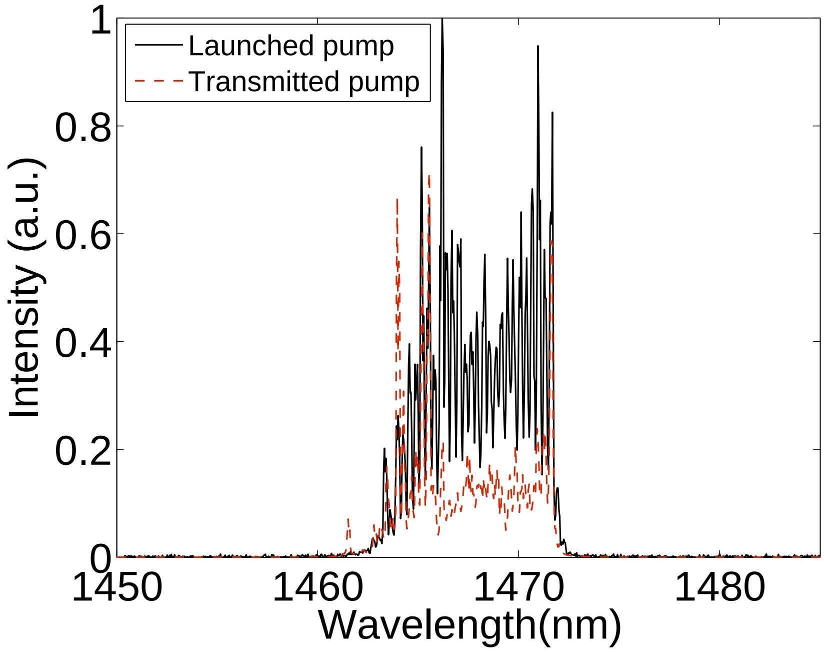

Figure 4.13: Spectra of the launch pump and the transmitted pump after the gain medium at 33 A of pump current and a water temperature of 35 ºC.

Figure 4.13 shows the spectra, measured by a grating OSA, of the launched and the transmitted pump light at 33 A. Both spectra were normalized, and the area of the transmitted pump was multiplied by a factor of 0.45 (55% absorbed). The uniformity of the transmitted spectrum agree with the broad absorptions of Er:YAG around 1470 nm [72].

The absorption spectrum shown in Figure 4.14 was generated by finding the difference between the spectra shown in Figure 4.13. Two distinct peaks are shown on the graph: one at 1467 nm and another one at 1472 nm, which are consistent with the published absorption spectrum [72].

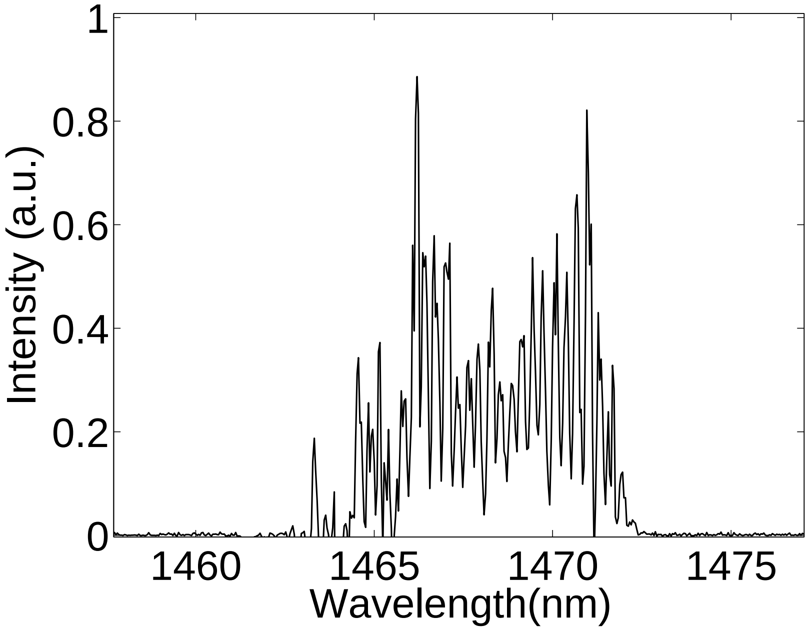

Figure 4.14: Spectrum of the absorbed pump by the gain medium at a pump current of 33 A.

4.6.2 Short-resonator in CW operation

The laser head was characterized using the standing-wave resonator shown in Figure 4.15.

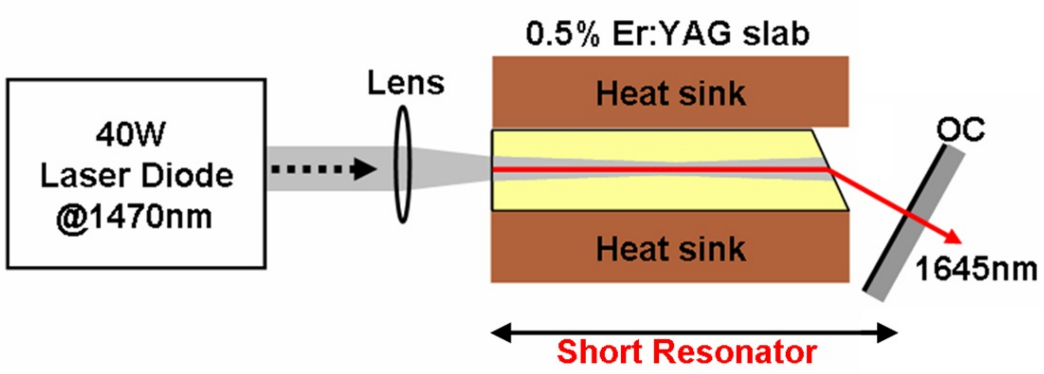

Figure 4.15: Schematic of the standing wave resonator (top view).

The achieved multi-mode output powers of the standing wave laser for R = 85%, 90% and 95% output couplers are shown in Figure 4.16. The highest CW output power (6.1 W) was obtained using the R = 95% output coupler. The result was similar to the performance predicted in Section 4.3 for a threshold power of about 13 W and peak output power of about 6 W for a loss of 1%.

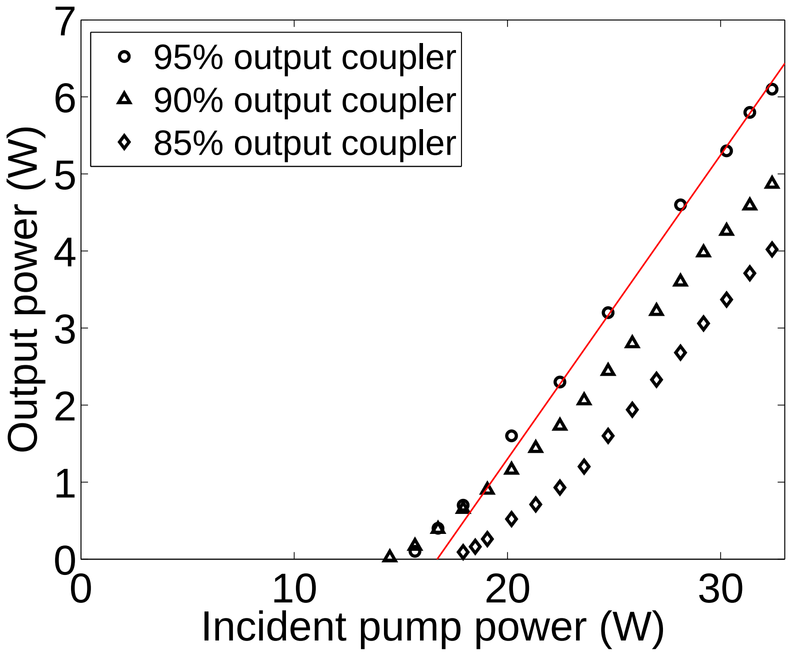

Figure 4.16: Multi-mode output power for CW lasing using the slave laser head, with R = 85%, 90% and 95% output couplers.

The multi-mode slope efficiency was 40% for the 95% output coupler - this is the highest efficiency reported for a direct, broadband, diode-pumped Er:YAG laser. Previous results [78] have achieved good slope efficiency (~30%) using Bragg-grating-linewidth-narrowed (<4 nm) laser diodes at 1470 nm and 1532 nm. The results shown here indicates that good slope efficiency can also be achieved using the broadband pump sources at 1470 nm. These results have been published in Optics Express [85]. A copy of that paper is included in Appendix A.1.2.

The spectral content of this laser output was measured using a calibrated grating OSA (Anritsu Inc.). The spectrum is shown in Figure 4.17. No other emission lines were observed within the laser gain bandwidth (1600-1650 nm) indicating that the laser was only oscillating at 1645 nm.

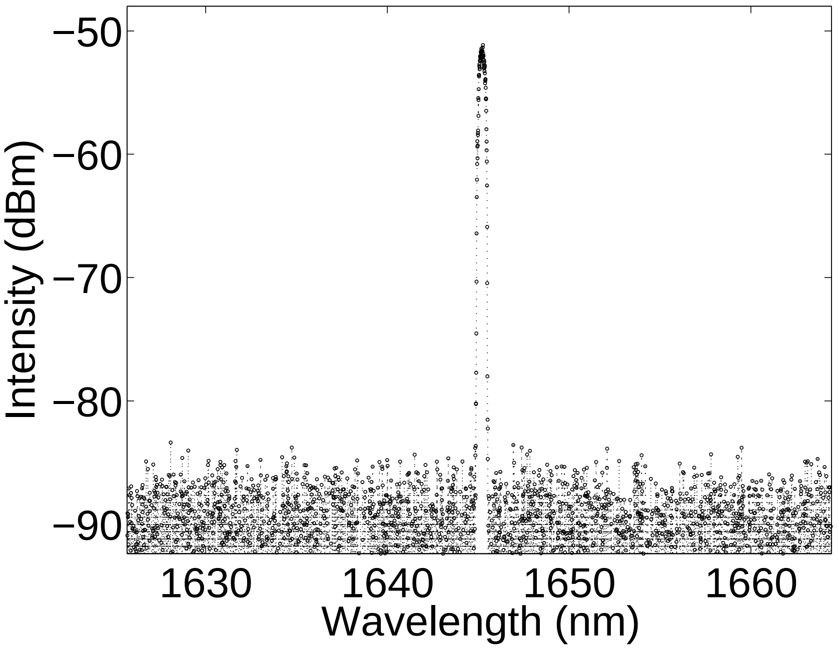

Figure 4.17: Spectrum of the standing wave Er:YAG laser in CW operation

4.7 Conclusion

This chapter has described the design and optimization of a water-cooled, multi-watt slave laser head, which will be used to develop a robust Er:YAG Q-switched laser (described in Chapter 5). The customized fast-axis and slow-axis collimated pump diode module used to end pump the gain medium allows good collimation of the pump inside the slab. The diode was cooled, tuned and temperature stabilized using a DI-water chiller.

The laser head was tested using a multi-mode, flat-flat standing wave resonator. A maximum output power of 6.1 W with 40% slope efficiency confirmed that good performance is achievable using broadband pump sources at 1470 nm. Thus, the design of the laser head satisfied the requirements of performance, simplicity and reduced cost compared to an EDFL-pumped Er:YAG laser.

The next chapter shall describe the Q-switch resonator design and performance, using the slave laser head presented in this chapter.

5 Q-switched resonantly pumped Er:YAG laser

5.1 Introduction

This chapter reports the development and characterization of the Q-switched Er:YAG laser built using the high power laser head described in Chapter 4. In Section 5.2 the initial Q-switched laser is described. A more robust Q-switched laser was subsequently developed, as described in Section 5.3. The characterizations of the final Q-switched laser using both 5% and 15% transmission output couplers are reported in Sections 5.4 and 5.5, respectively. The chapter is summarized in Section 5.6.

5.2 Initial Q-switched laser

Figure 5.1 shows a schematic of the initial design of the Q-switched laser, which was assembled using a spare master laser slab. The PBSC and the quarter-wave plate (QWP) form an isolator to prevent back-reflections of the pump. The focusing lens of the pump has a focal length of 100 mm. The pumped end of the laser slab is HR coated at 1645 nm. The HR coating has a damage threshold of 350 MW/cm^2, according to the manufacturer who tested it using 10 ns pulses at 1064 nm. The damage-threshold of the AR coating on the intra-cavity end of the slab was not specified by the manufacturer. The QWP, Pockels Cell and thin film polarizer

(TFP) combine to form the Q-switch of the laser. The R = 98% flat output coupler is used as the end mirror of the resonator.

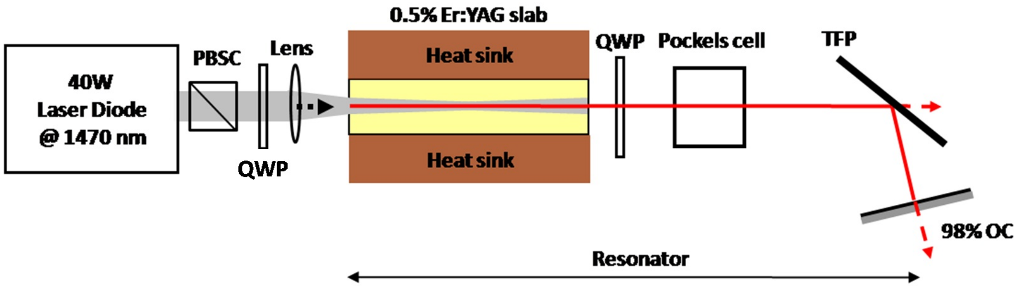

Figure 5.1: The initial Q-switched laser, which used a spare master laser slab. Abbreviations: QWP, quarter wave plate; TFP, thin film polarizer.

5.2.1 Q-switching

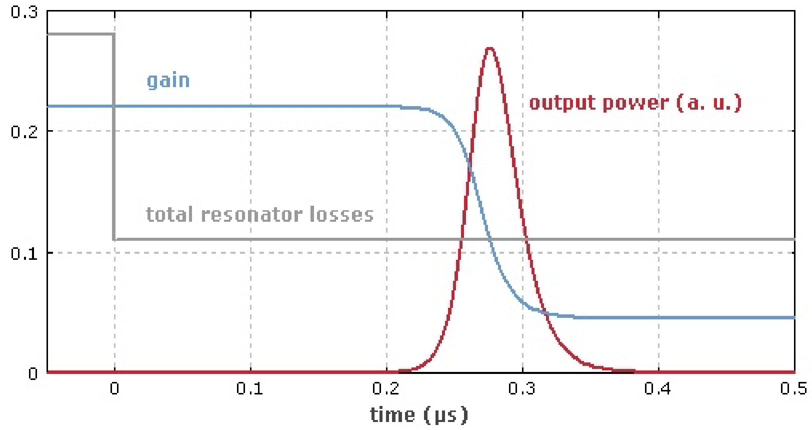

Figure 5.2: A giant pulse is formed after the opening of the Q-switch. Total resonator loss is about 100% at low Q factor, and the loss is decreased to about 0 when the resonator is switched to high Q.

The "Q-switching" technique is used to produce intense, short bursts of oscillation from lasers [119, 120]. Q-switching is achieved by modulating the losses in a resonator. Typically the losses are controlled by either an acousto-optic or electro-optic (EO) modulator. In the Q-switched Er:YAG laser, the quality factor, Q, of the resonator is lowered using an EO modulator during the pumping so that the gain (that is, population inversion) can build up to a very high value without laser oscillation, as illustrated in Figure 5.2.

After the stored energy reaches the desired level, the resonator is suddenly switched to a high Q using the EO modulator. The loss is then less than the round-trip gain, and thus lasing occurs. The intensity in the resonator builds up quickly, producing a short and intense pulse of light. The components in the resonator of the Q-switched laser therefore require robust optical coatings to sustain the high peak power of the pulse.

The EO modulator

A Rubidium Titanyle Phosphate (RTP) Pockels cell, purchased from Raicol Crystals Ltd., was employed as the electro-optic modulator. The Pockels cell consisted of two RTP elements in a temperature compensating design as illustrated in Figure 5.3 [121].

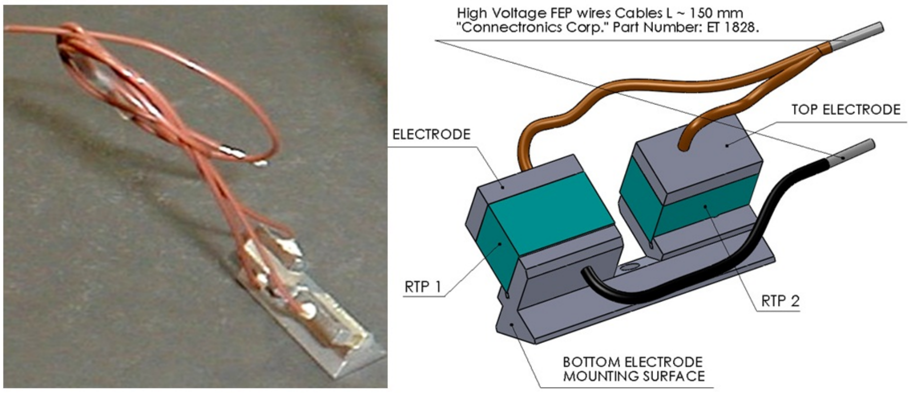

Figure 5.3: A picture (left) and schematic (right) of the RTP Pockels cell used in the Er:YAG Q-switched laser.

The unique properties of RTP, including high electrical resistivity and a high damage threshold, make it suitable for robust Q-switch operations. RTP Pockels cells also have advantages of low insertion loss, high extinction ratio, wide spectral range and exhibits no piezoelectric ringing [122]. The specifications of the RTP

Pockels cell are listed in Table 5.1.

Specifications	Value
Transmission at 1645 nm	T > 98.5%
Half-wave voltage at 1645 nm	1200 V
Contrast ratio	>200:1 at 633 nm
Dimensions	4 × 4 × 20 mm
AR coating	R <0.1%
Damage threshold	> 600 MW/cm^2 at 1064 nm (10ns)

Table 5.1: Specifications of the RTP Pockels cell at 1645 nm

The Pockels Cell was mounted on a kinematic stage (New Focus 9071) that allowed precise four-axis tilt adjustment. It was driven by a high voltage Q-switch driver, which was designed and built with the help of Mr Neville Wild and Mr Bob Nation at The University of Adelaide.

Thin Film Polarizer

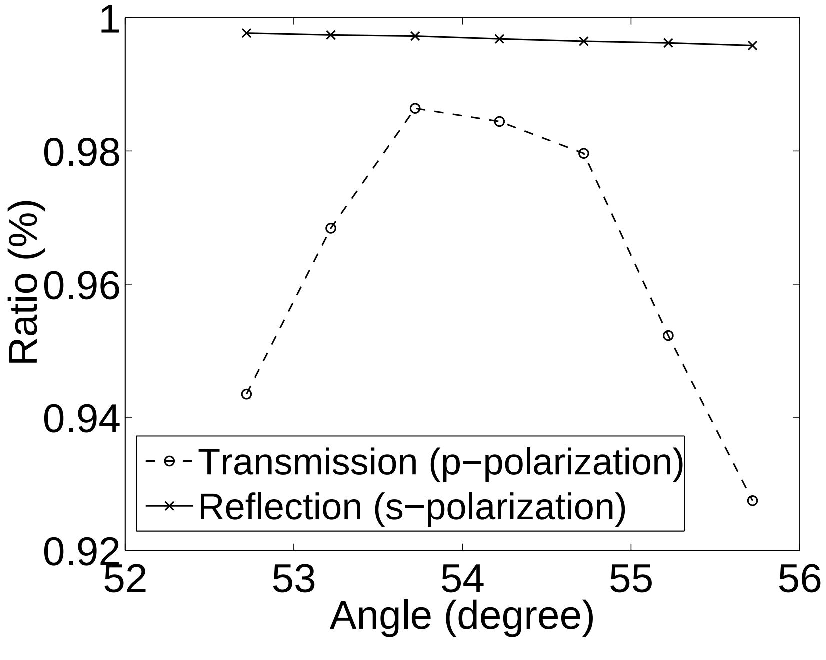

Figure 5.4: The measured transmission and reflection of the TFP as a function of incident angle. The optimum angle is about 53.7º.

The TFP was purchased from Altechna Co. Ltd. The measured performance of the TFP as a function of incident angle is plotted in Figure 5.4. The transmission of p-polarization is very sensitive to the incident angle. It had a maximum transmission of 98.6% at 53.7º so the TFP was aligned with this incident angle. The reflectivity for s-polarization is generally $> 99.5\%$. The damage threshold of the 1645 nm AR coating was 10 J/cm^2 (10 ns pulse), as tested at 1064 nm by the manufacturer.

During pumping, the Pockels cell voltage (V_{pc}) is 0 volts so s-polarized light reflected by the TFP and incident on the PC and gain medium is rotated to p-polarization as it double passes the QWP and is thus transmitted through the TFP. The Q factor in the resonator during pumping is thus low.

At the end of the pumping, V_{pc} becomes 600 volts (quarter-wave voltage) and thus the incident s-polarization is rotated to the fast-axis of the QWP. The s-polarization is thus maintained and the Q factor becomes high, and lasing occurs.

5.2.2 Results for the initial Q-switched laser

The Q-switched laser was aligned using the optical axis defined by a short-resonator laser assembled using the laser head. Irises were positioned along the optical axis so a HeNe laser could be aligned to the optical axis. The HeNe was then used to align the laser components.

The output power of the initial Q-switched laser in CW operation is plotted in Figure 5.5. The lasing threshold is about 22.5 A , and an output power of 1.8 W was obtained at 33 A.

In Q-switched operation, the pump current was initially set below threshold to avoid damage due to high peak power, and then the current was slowly increased. Q-switched pulses were observed at about 22.5 A, which is similar to the CW threshold. An average power of about 1 mW was measured at 22.7 A. The output power then clamped at 2 mW due to damage of the AR coating at higher pump powers. Figure

5.6 shows the 500 ns pulse measured at an output power of 2 mW and at a 50 Hz PRF.

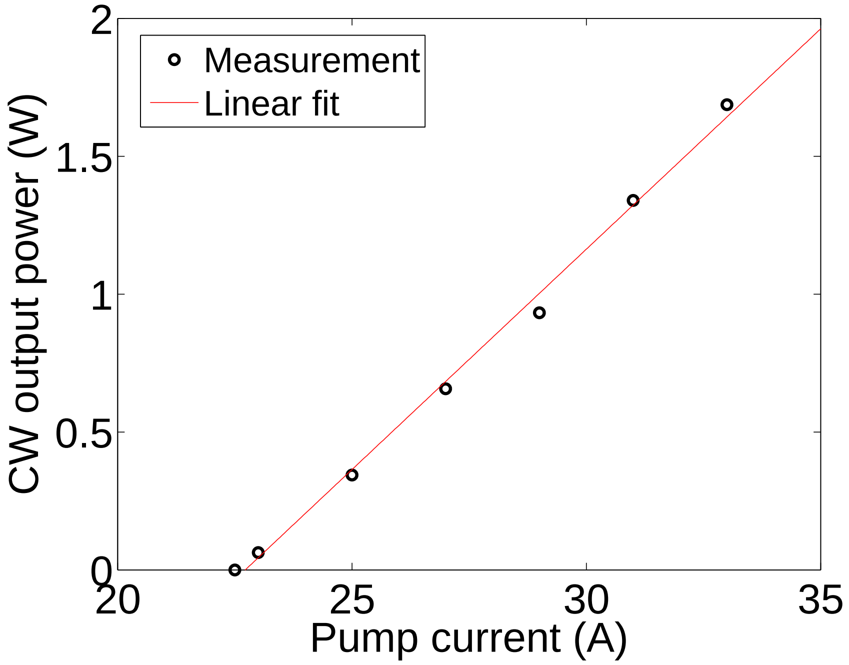

Figure 5.5: Performance of the preliminary laser in CW operation.

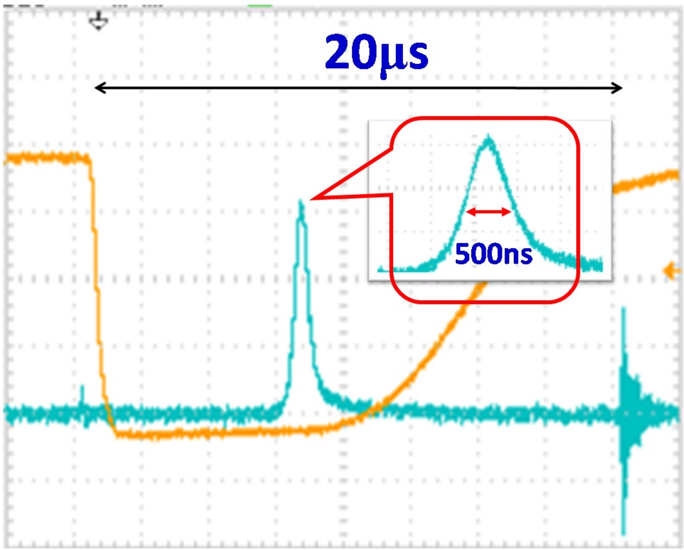

Figure 5.6: The 500 ns Q-switched pulse at an average power of 2 mW.

Q-switched operation was successfully demonstrated using the master laser slab, however the maximum pulse energy achieved without coating damage was <1 mJ.

The damage is shown in Figure 5.7. The first attempt resulted in an eruption with a diameter of ∼0.3 mm in the centre of the slab. Similar outcomes occurred at different positions of the coating. A more robust coating was required to improve the performance of the Q-switched laser, however it would increase the cost of the gain medium.

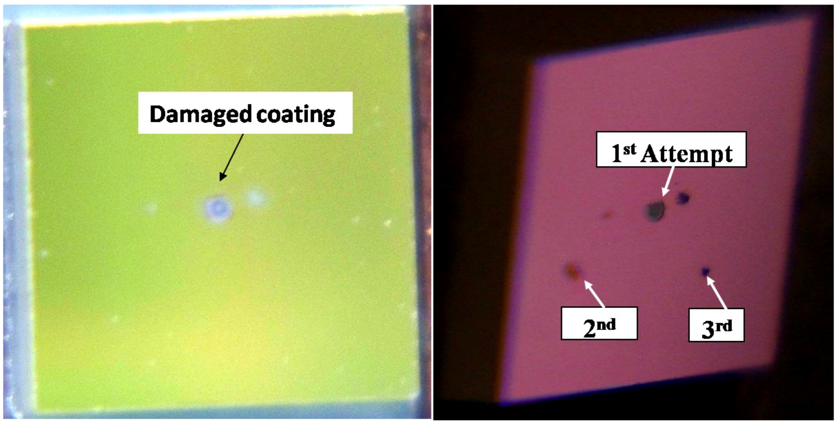

Figure 5.7: Optical coating damages due to high intra-cavity peak power of the Q-switch pulses. The left picture clearly shows the eruption due to the Q-switch pulse. The right picture shows similar damage occurred at different locations on the coating.

The intra-cavity end of the slab was therefore polished at Brewsters angle to avoid the need for an optical coating. In addition, the Brewster-angled face provided the polarization discrimination required for the Q-switched laser.

5.3 Final Q-switched laser

A schematic of the final Q-switched laser is shown in Figure 5.8. The slab face closest to the diode is the end mirror of the resonator, and is coated for high reflectivity (R > 99.7%) at 1645 nm and high transmission (T > 99.8%) at 1470 nm. The intra-resonator end of the gain medium is Brewster-angled, which provides the polarization discrimination required for electro-optic Q switching, thus replacing the TFP. The output coupler is a flat mirror with 5% transmission. As discussed

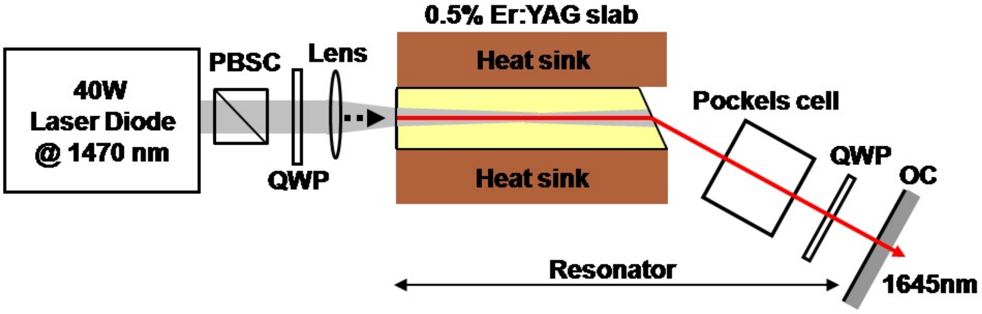

Figure 5.8: Schematic of the final Q-switched Er:YAG laser. Abbreviations: QWP, quarter wave plate; OC, output coupler.

in Chapter 4, the resonator length needed to be $>$ 15 cm so that the mode would fill the pump volume for TEM_{00} operation, and thus a physical resonator length of about 17 cm was selected. The PBSC and the quarter-wave plate are used to isolate the diodes against back-reflections.

Pictures of the Q-switched resonator are shown in Figure 5.9. The overall length and width of the laser are about 35 cm and 20 cm, respectively. The compactness of the resonator provides potential portability for remote sensing applications.

A metal aperture, attached to an aluminium heat sink, was used to block unabsorbed pump power exiting the slab, thus preventing the unabsorbed pump (>15 W) from damaging the Pockels Cell and reflecting off other components. If required, the metal aperture could also be used as a hard aperture to attenuate higher-order transverse modes of the laser.

5.4 Q-switching using R = 95% output coupler

The Q-switched laser was initially characterized using a 5% transmission output coupler - the optimum output coupling fraction for CW operation measured in Chapter 4.

The output powers of the laser in CW and high PRF ($>$ 2kHz) Q-switched opera-

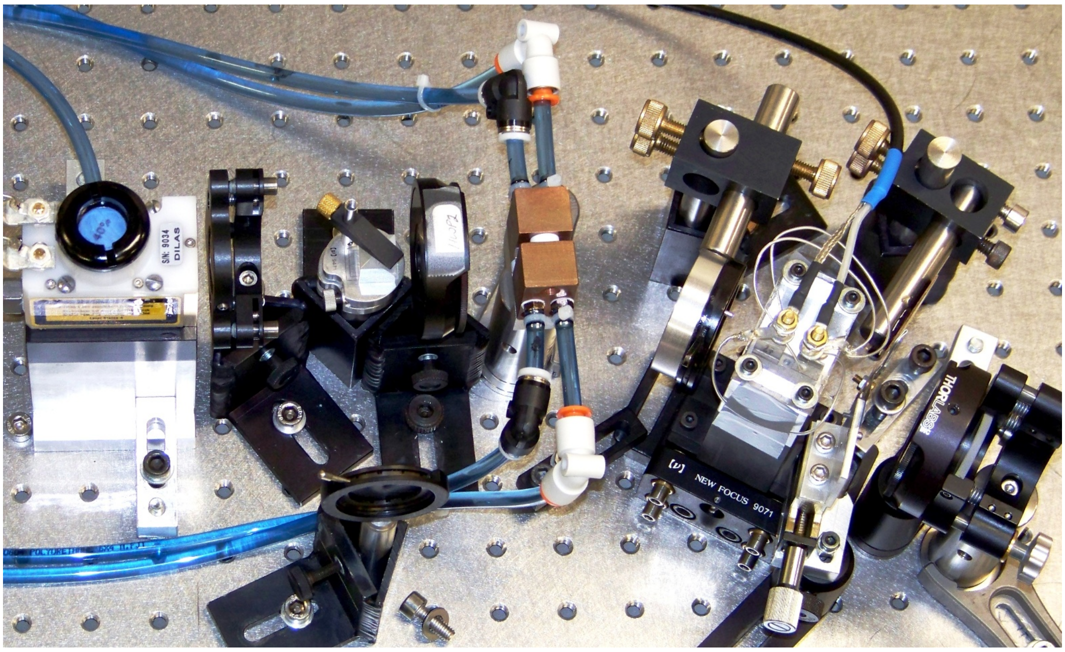

(Top view)

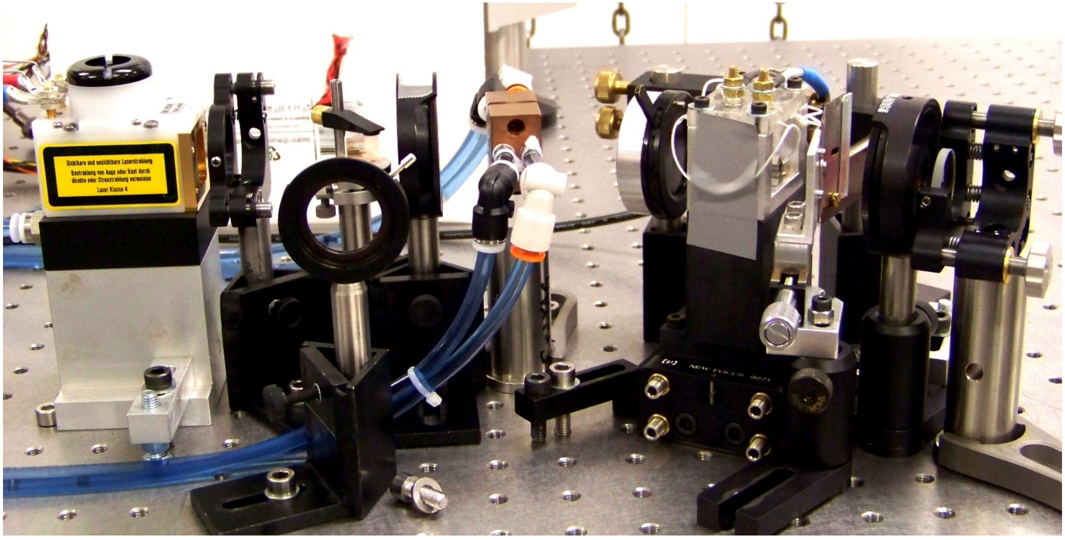

(Side view)

Figure 5.9: Photographs of the final Q-switched laser.

tion are plotted in Figure 5.10. As expected, the additional intra-cavity components result in an increased threshold compared to CW lasing of the reduced-length laser described in Section 4.6.2. The similarity between the average output power in CW and Q-switched lasing indicates that there was no noticeable increase in losses when Q-switching at a 2 kHz PRF.

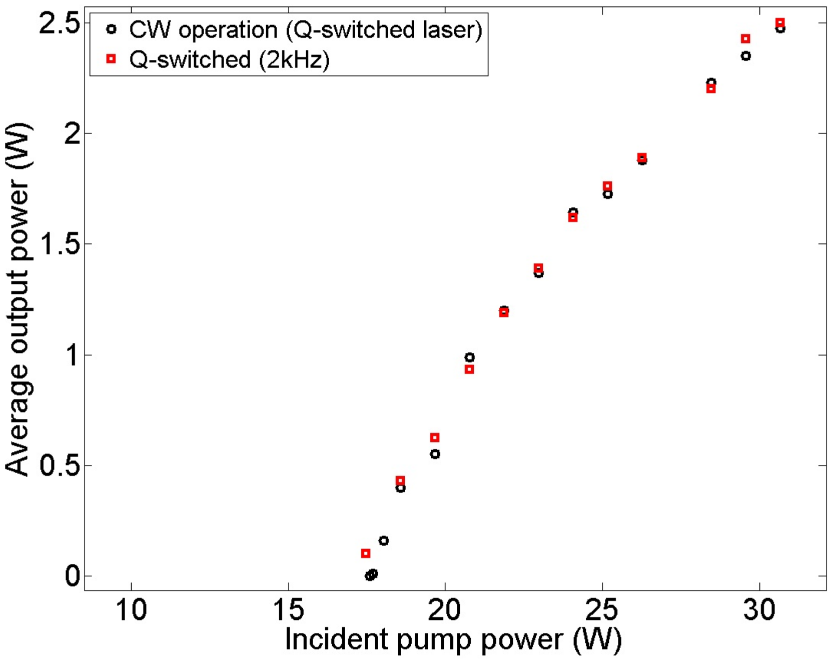

Figure 5.10: Plot of the average output power versus incident pump power for CW and Q-switched (2kHz) operation of the laser.

5.4.1 Q-switched laser performance

The Q-switched pulse train is shown in Figure 5.11. The measurement shows that no pre-lasing occurred during pumping, thus allowing the inversion to be built up.

The average output power as a function of PRF is plotted in Figure 5.12. The results were recorded using four different pump powers: 20 W, 23.5 W, 28.4 W and 30.6 W. The highest average output power achieved was 2.5 W for a PRF of 2 kHz. In general, the average output powers show no significant variation for PRF > 1 kHz. At lower PRFs, the average output power is reduced.

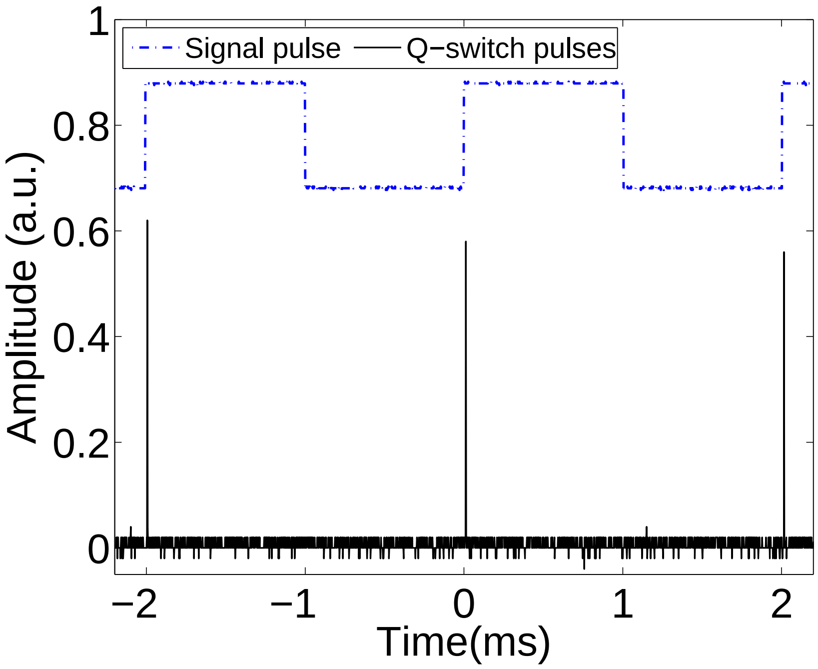

Figure 5.11: A plot of the pulse train, showing no existence of pre-lasing before a Q-switch pulse.

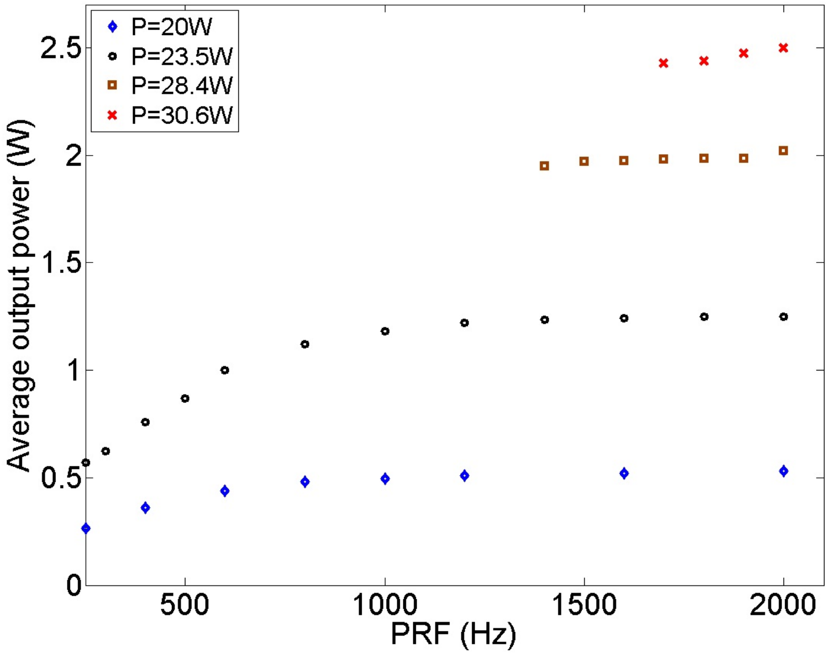

Figure 5.12: Plot of the dependence of average output power on PRF for various incident pump powers.

The expected dependence of the average power on PRF for a CW-pumped Q-switched laser is given by

$$P_{av(\mathrm{PRF})} = P_{av(\mathrm{CW})}\left[(\tau_s/t_q)[1 - \exp(-t_q/\tau_s)]\right] \tag{5.1}$$

where $P_{av(\mathrm{CW})}$ is the average power in CW operation, τ_s is the effective lifetime of the upper state and $t_q = 1$ / PRF [123]. Since Figure 5.10 shows that the average power for both CW and PRF = 2 kHz lasing are identical at these pump powers, we plot in Figure 5.13 the measured $P_{av(\mathrm{PRF})}/P_{av(\mathrm{2kHz})}$ ratio and the ratio expected assuming that (a) $\tau_s = 6.9$ ms, (the fluorescent lifetime of the upper lasing state [83]), and (b) $\tau_s = 2.3$ ms (a lifetime estimated from the data recorded at low PRF).

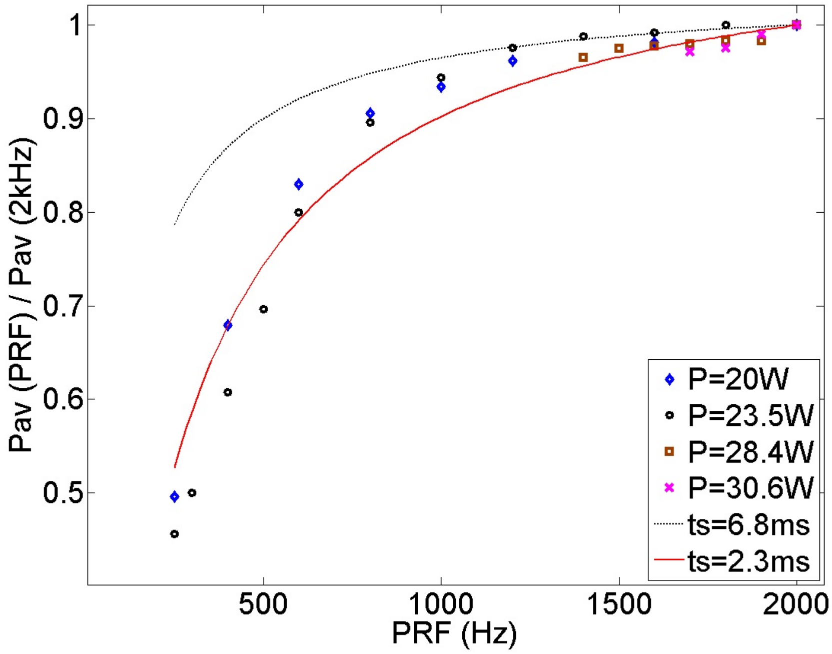

Figure 5.13: Measured (symbols) and expected (lines) ratio of average power at different PRF.

It is clear that the decrease in average power at low PRF is not consistent with the assumption that the effective lifetime is 6.8 ms at low PRF. Another loss mechanism must therefore be decreasing the lifetime of the upper lasing state. An investigation of the causes will be discussed in Chapter 6.

Pulse energy versus PRF

The dependence of pulse energy on PRF at 23.5 W pump power is plotted in Figure 5.14. This pump power was chosen so that the pulse energy could be evaluated at low average power to reduce the risk of coating damage. The measured pulse duration at 250 Hz PRF is about 100 ns, as required for the LIDAR applications.

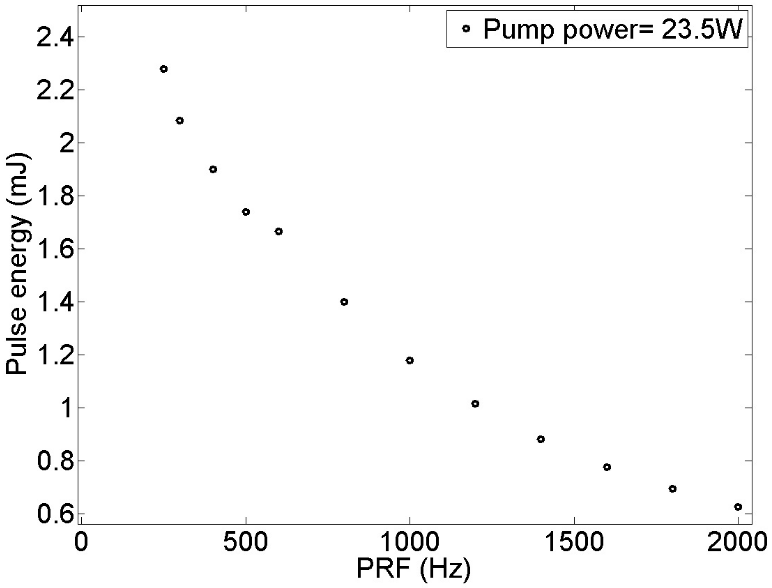

Figure 5.14: Plot of the dependence of pulse energy on PRF for an incident pump power = 23.5 W.

The laser could not be operated at PRFs <250 Hz due to damage of the HR coating of the slab by the increased intra-cavity peak power of the pulses. The estimated intra-cavity peak power that caused the damage was 2.4 J/cm^2 (45 MW/cm^2), which is significantly smaller than the damage threshold specified by the manufacturer. A picture of the damaged coating is shown in Figure 5.15.

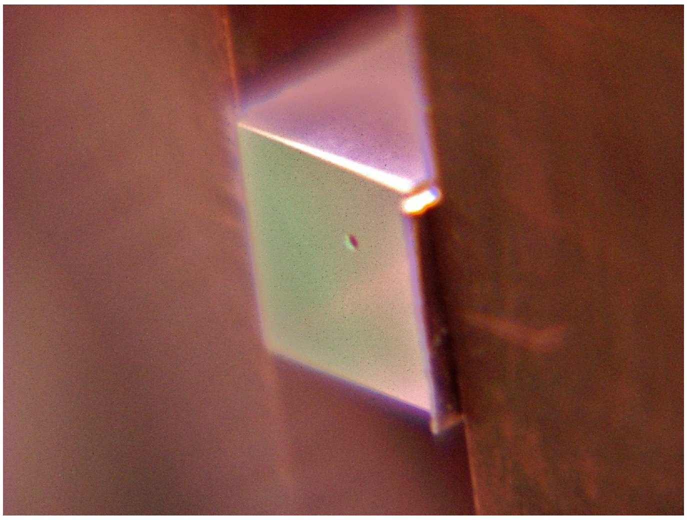

Figure 5.15: Damage to the high reflectivity coating on the Er:YAG slab for a pulse energy of 2.3 mJ at 100 ns duration.

Pulse width measurement

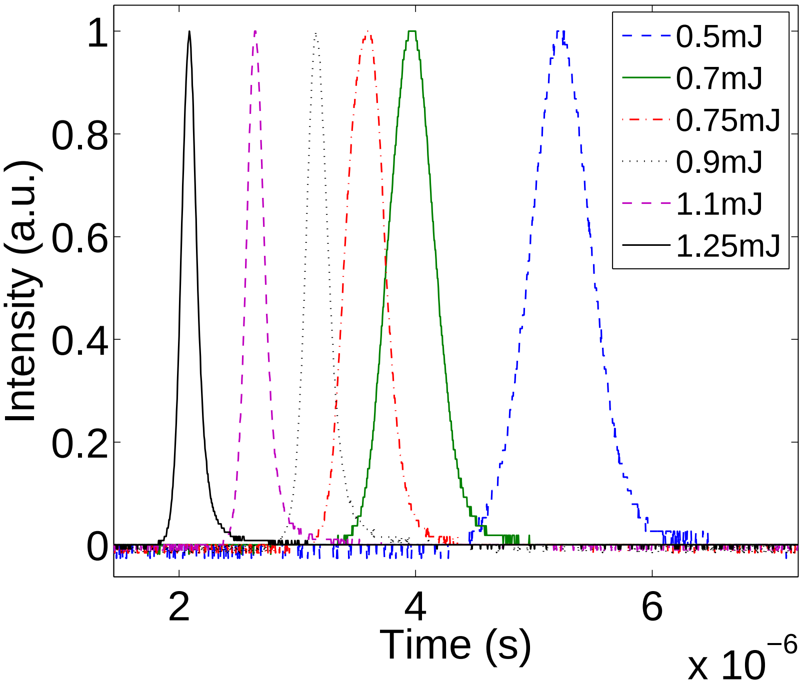

Figure 5.16: Plot of normalized pulse waveforms versus time for several pulse energies.

The duration of the pulses at 600 Hz PRF were measured for several pump powers. To prevent damage to the photo-diode by the high peak intensity, neutral density filters were used during the measurement. The normalized temporal pulse waveforms are shown in Figure 5.16. As the pulse energy is increased, the build-up time and pulse width decrease, as expected.

The pulse width is plotted as a function of pulse energy in Figure 5.17. For wind-sensing applications the optimum transmitter pulse width is several hundred ns, resulting in a good compromise between velocity resolution and range resolution. The Q-switched Er:YAG laser readily produces pulse widths in this range in the Q-switched mode.

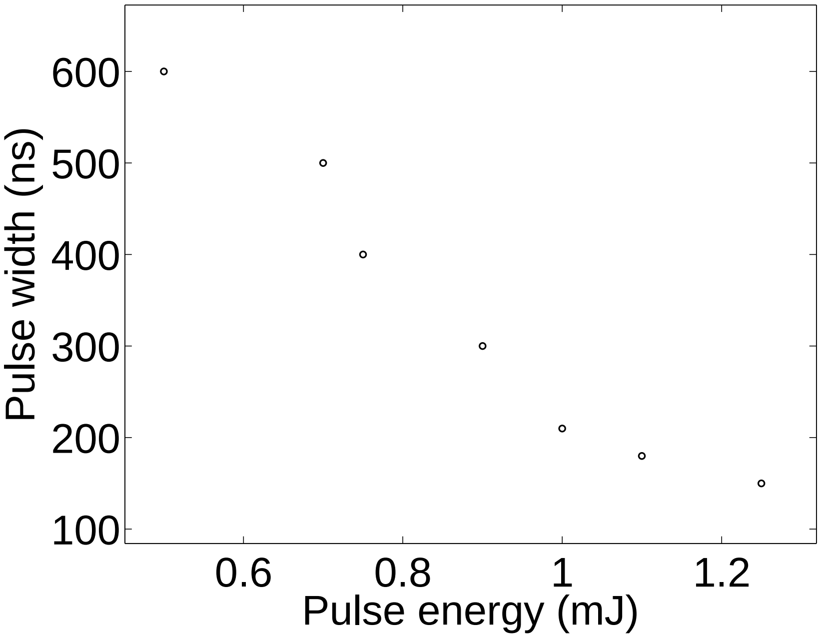

Figure 5.17: Pulse width as a function of pulse energy for several pump powers at 600 Hz PRF.

Beam quality measurement

The far-field intensity profile of the output of the Q-switched laser is shown in Figure 5.18 (right). To study the propagation characteristics of the output, the beam quality was also measured. At the highest average output power of 2.5 W at 2 kHz, the measured beam diameter as it passes through a waist is shown in

Figure 5.18 (left). Using the fitting function described in Chaptesolidr 3, the beam quality was calculated to be $M^2 = 1.04$. This indicates that the laser output is near diffraction-limited.

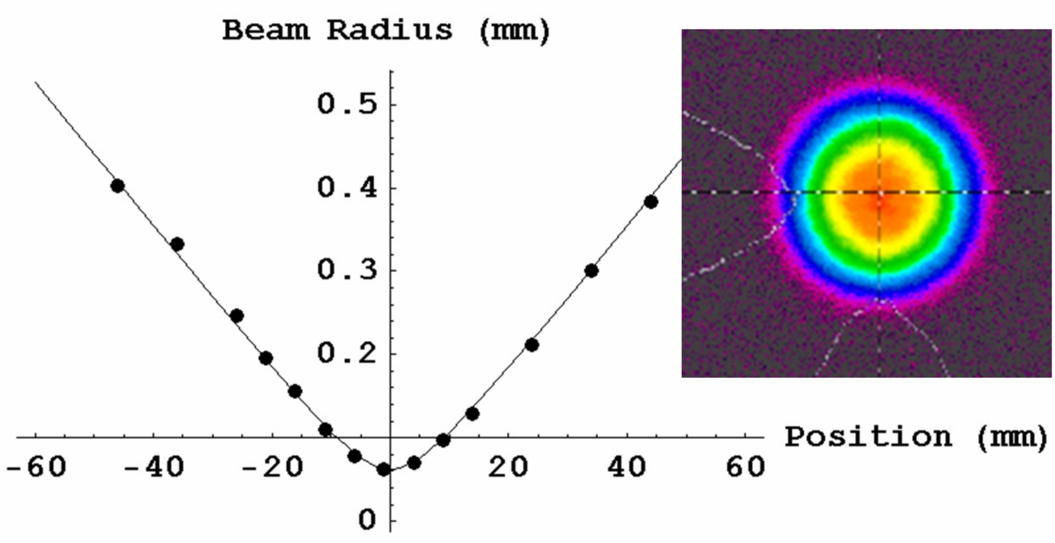

Figure 5.18: (Left) Plot of the measured beam size of the output of the Q-switched laser at an average output power of 2.5 W (dots), and the M2 = 1.04 curve of best fit. (Right) Intensity profile of the laser output.

5.4.2 Summary

An efficient, resonantly-pumped Q-switched Er:YAG laser has been demonstrated using a 95% output coupler. In reduced-length resonator configuration, CW output powers up to 6.1 W at 1645 nm have been obtained with a multi-mode slope efficiency of about 40%. In pulsed operation, the Q-switched laser produced diffraction-limited pulses with an average power of 2.5 W at a 2 kHz PRF. The highest single pulse energy obtained was 2.3 mJ with a pulse duration of 100 ns at a 250 Hz PRF. The results described in this section have been published in Optics Express [85].

5.5 Improved Q-switched pulse energy using R=85% output coupler

To produce higher pulse energies, a more-robust HR coating of the Er:YAG slab would be required. An alternative approach is to use a more transmissive output coupler so the intra-cavity intensity is reduced. Thus, the output coupler of the laser shown in Figure 5.8 and 5.9 was changed from 95% to 85% reflectivity.

5.5.1 Q-switched laser performance

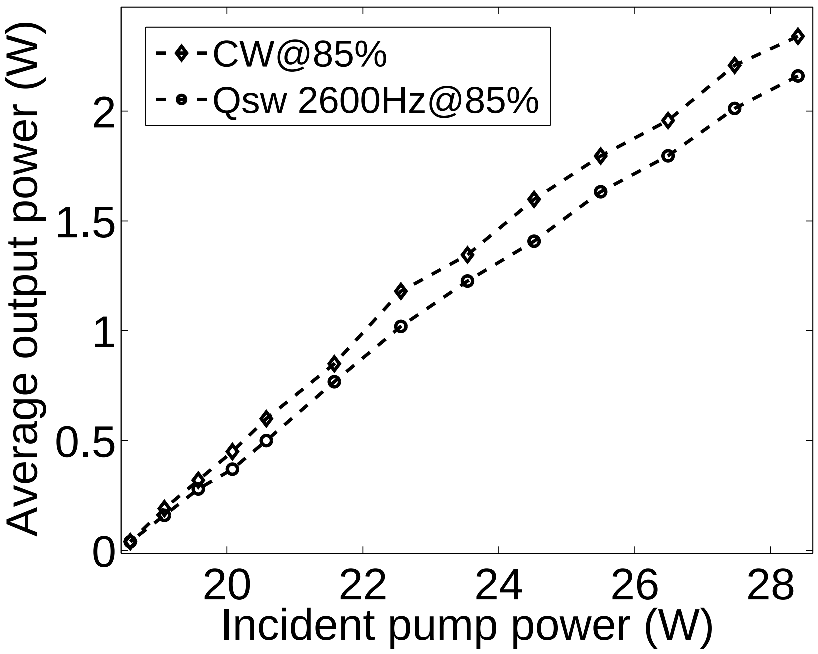

Figure 5.19: Plot of the average output power versus pump power for CW and Q-switched (2.6 kHz) operation of the laser.

The output power of the Q-switched laser was measured in both CW and Q-switched operation at a 2.6 kHz PRF. The average output powers are plotted as a function of the pump power in Figure 5.19. As expected the threshold for lasing has increased significantly. The highest CW output power achieved was 2.3 W. In Q-switched operation (2.6 kHz), the slope efficiency reduced about 7%, and a lower output power of 2.16 W is measured. The reduced efficiency could be due to a stronger upconversion loss caused by the higher inversion threshold required for the 85% output coupler [72, 86, 89].

The average output powers as a function of the PRF for four different pump powers, 26.3 W, 28.5 W, 30.7 W and 33 W, are plotted in Figure 5.20. Constant output powers were observed for PRFs > 1000 Hz for all pump powers. Significant power reduction occurred for PRFs <500 Hz. Similar characteristics were seen in Figure 5.12.

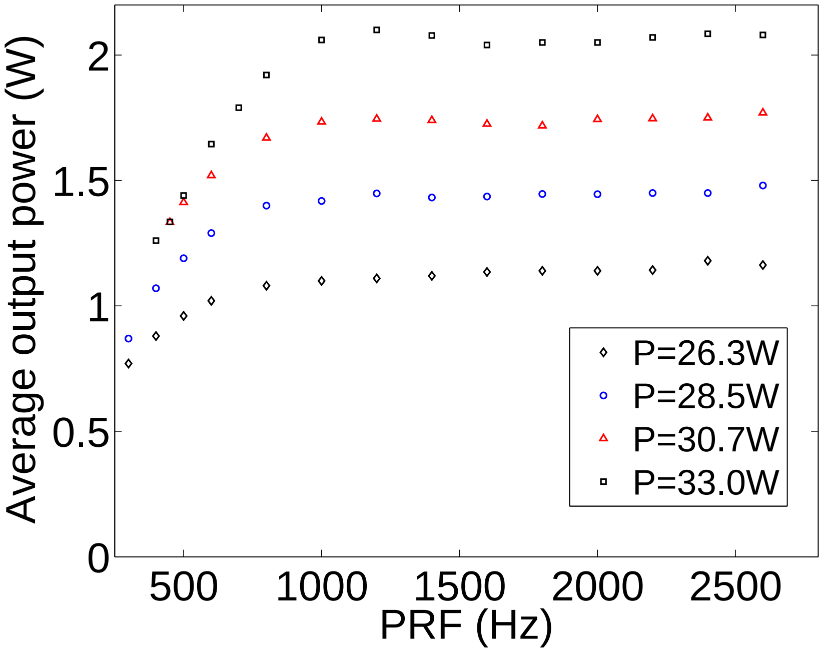

Figure 5.20: Plot of the dependence of average output power on PRF for various incident pump powers.

A comparison between the measured and expected Q-switching efficiency is shown in Figure 5.21. As was discussed in Section 5.4.1, the Q-switching efficiency predicted using a 6.8 ms upper state lifetime of erbium, is about 20% higher than the measured results for PRFs <250Hz.

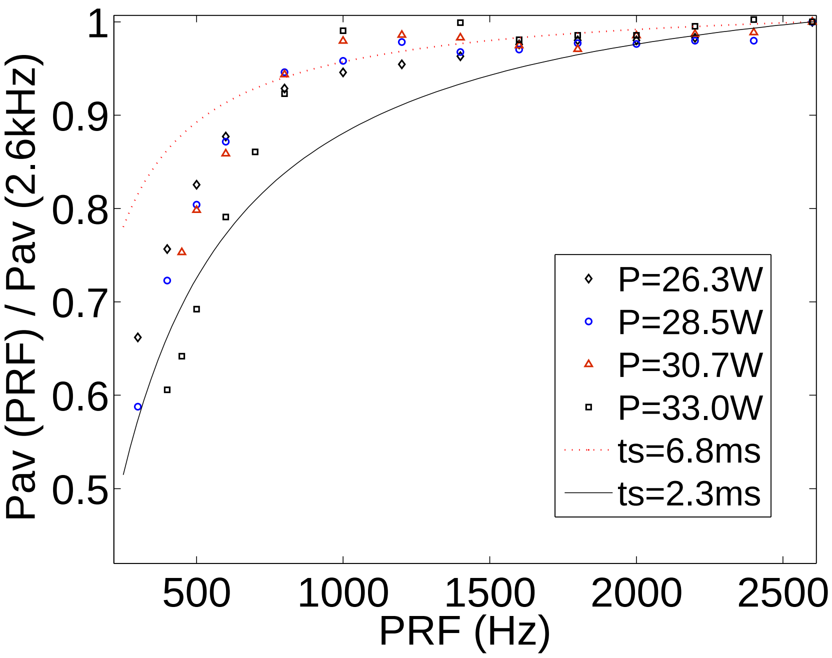

Figure 5.21: Measured (symbols) and expected (lines) ratio of average power at different PRF.

Pulse energy versus PRF

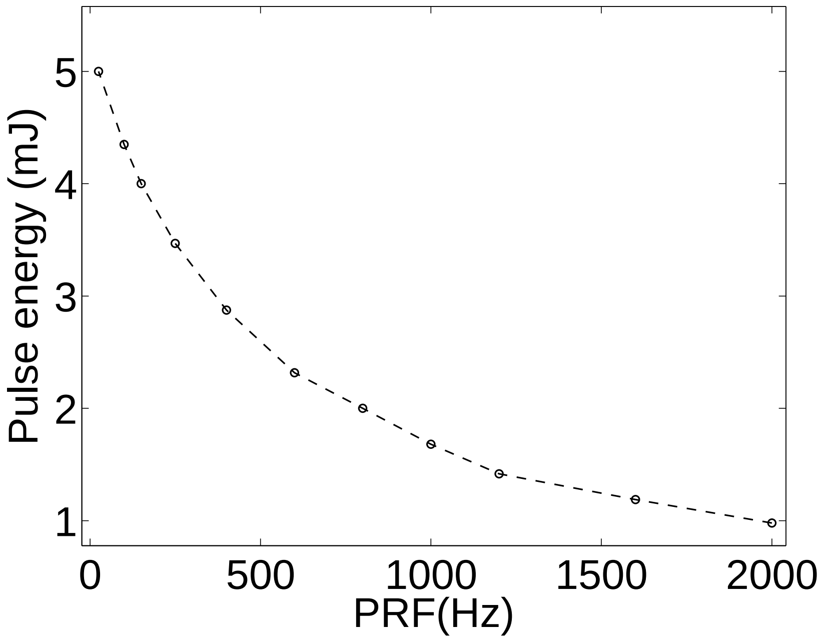

Figure 5.22: Plot of the dependence of pulse energy on PRF for a pump power of 33 W.

The dependence of the pulse energy on PRF, for a pump power of 33 W, is plotted in Figure 5.22. The highest pulse energy of 5 mJ was measured at a 30 Hz PRF. The pulse duration was 100 ns, corresponding to a peak power of 50 kW.

Pulse width measurement

The durations of the pulses measured at different PRFs with a pump power of 33 W are shown in Figure 5.23. The pulse build-up time reduces as the pulse energy is increased. The shortest pulse width, just below 100 ns, was measured at 5 mJ with the R=85% OC.

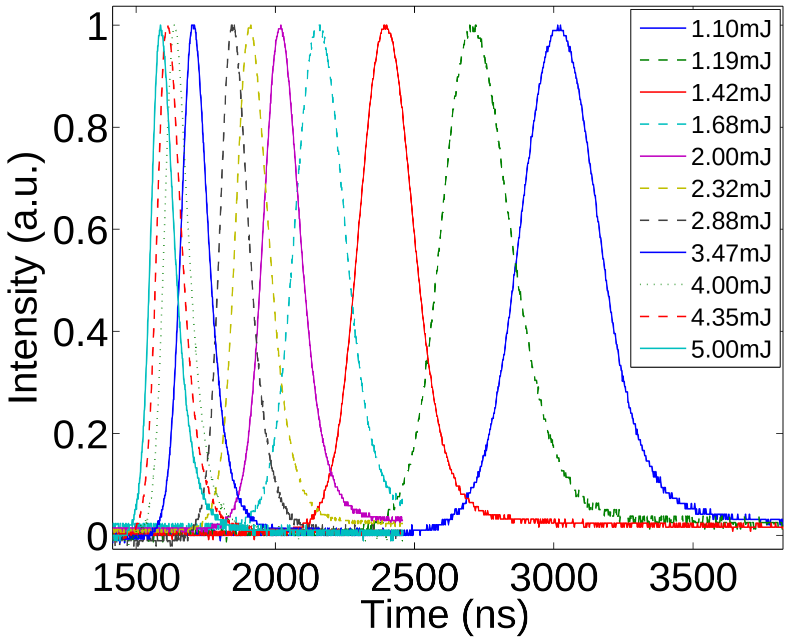

Figure 5.23: Plot of the normalized pulse waveforms versus time for several pulse energies.

5.5.2 Summary

Robust Q-switched operation was demonstrated without coating damage using the 15% transmission output coupler. A much improved pulse energy of 5 mJ at 30 Hz PRF was achieved. In high PRF operation, an average output power of 2.2 W was obtained at 2.6 kHz.

5.6 Conclusion

This chapter has described the development and characterizations of the Q-switched resonantly-pumped Er:YAG laser built using the laser head described in Chapter 4. The final slab design employs a Brewster-angled surface to prevent coating damage.

In Q-switched operation, the laser produced diffraction-limited pulses with an average power of 2.5 W at 2 kHz PRF using the R=95% output coupler. The highest pulse energy of 5 mJ was achieved using the R=85% output coupler. To our knowledge this is the first Q-switched Er:YAG laser resonantly pumped by CW laser diodes.

The decrease in average power at low Q-switch PRF is not consistent with the assumption that the effective lifetime is 6.8 ms at low PRF. Other loss mechanisms must therefore be decreasing the lifetime of the upper lasing state. The causes of the lifetime reduction in Q-switched Er:YAG lasers are discussed in Chapter 6.

6 Investigation of losses in Er:YAG lasers

6.1 Introduction

It was revealed in Chapter 5 that the average power of the Q-switched Er(0.5%):YAG laser reduced unexpectedly at low PRFs. The corresponding effective lifetime of the laser was about 2 ms, which is lower than the expected lifetime of 6 ms in Er:YAG. Similar outcomes have been reported by other groups [70, 72, 124], who proposed an estimated effective lifetime of ∼2.3 ms for both erbium-doped fibre laser (EDFL) pumped (1532 nm) and diode pumped (1532 nm and 1470 nm) Er:YAG lasers.

Several causes have been proposed for the reduced effective lifetime: cooperative energy transfer upconversion (ETU) [60,64,72,86,89], excited state absorption (ESA) [70], ground-state depletion (GSD) [72], and amplified spontaneous emission [70]. Figure 6.1 illustrates ETU and ESA, which can be followed by a combination of multi-phonon (MP) relaxation and radiative decay.

Among these candidates, energy-transfer upconversion (ETU) has been known that it can have a very detrimental impact on laser performance particularly in pulsed operation or laser configurations requiring a high upper-laser-level excitation density [60, 64, 72, 89]. The ETU process is commonly utilised for generating 2.9 µm emission in highly (∼50%) doped Er:YAG [126]. To minimize ETU in Er:YAG lasers operating at 1.6 µm, the doping concentration of erbium is normally kept low,

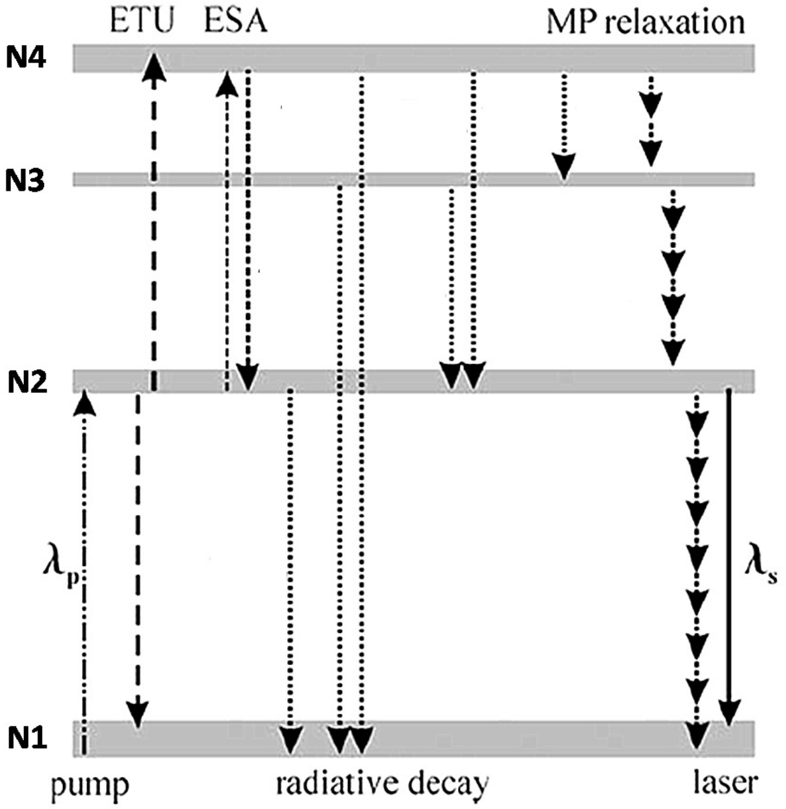

Figure 6.1: General scheme for resonant pumping of a quasi-three-level Er:YAG medium, showing ETU and ESA, followed by MP relaxation. λ_p is the pump wavelength (1470 nm) and λ_s is the lasing wavelength (1645 nm) [125].

typically <1% [60]. However ETU loss can still become significant in 0.5% Er:YAG if the pump intensity is high. Thus, it has been proposed that pulsed Er:YAG lasers should use even lower doping concentrations, <0.5%, to further reduce the upconversion loss [60, 69, 127]. But lower dopant also reduces pump absorption, hence reducing the efficiency of the laser.

Laser efficiency can also be impacted by reduced pump absorption due to GSD, or "pump bleaching", which is not widely discussed for Er:YAG lasers. This is probably because GSD is not apparent in CW operation where the population inversion is clamped at the lasing threshold, or in high PRF (>1 kHz) operation where the ground-state population recovers due to frequent lasing. However, significant pump bleaching can occur in pulsed operation at low PRFs [128], thus reducing the efficiency.

The objective of this chapter is to report an experimental investigation of the dominant losses in the Q-switched Er:YAG laser described in Chapter 5, and compare the measurements with a numerical model. The aim is to improve the efficiency of future Q-switched Er:YAG lasers.

In Section 6.2, the measurement of pump bleaching due to GSD is reported. In Section 6.3, I describe the measurement of ETU and ESA using fluorescence measurements. A simple rate equation model is used to analyse the results in Section 6.4. In Section 6.5, an evaluation of an optimum design of Q-switched Er:YAG lasers is carried out using the rate equation model. The chapter is summarized in Section 6.6.

6.2 Pump absorption efficiency

In pulsed operation, ground-state depletion (GSD) may degrade pump absorption compared to CW operation [129], thus reducing the laser efficiency at low PRFs. I therefore investigated GSD, initially with CW pumping, and then with pulsed pumping.

6.2.1 CW pumping

A schematic of the pump absorption experiment is shown in Figure 6.2. To prevent the pump wavelength shifting due to a change of diode current, the incident pump power was adjusted by a half-wave plate that changed the pump transmission through the PBSC. Power meters P1 and P2 measured the pump after the Er:YAG gain medium and the pump reflected by the PBSC, respectively. Power meter P2 was calibrated so that it could be used to determine the pump power incident on the Er:YAG slab. The absorption was then calculated using the incident and the

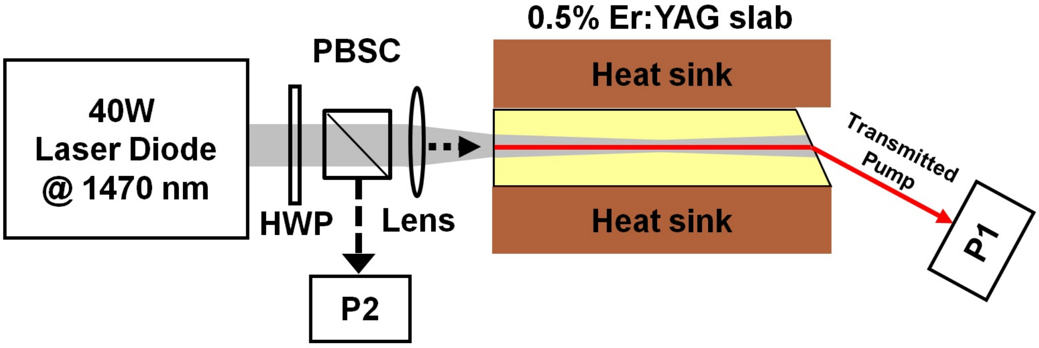

Figure 6.2: Pump absorption experiment without lasing. P1 and P2 are power meters.

transmitted pump powers.

The measured pump absorption is plotted in Figure 6.3 as a function of the incident power pump. Two predicted pump absorptions: with absorption coefficients (α) of 0.78 cm^{-1} and 0.62 cm^{-1}, are also shown in the figure. The calculation assumed no GSD or ETU.

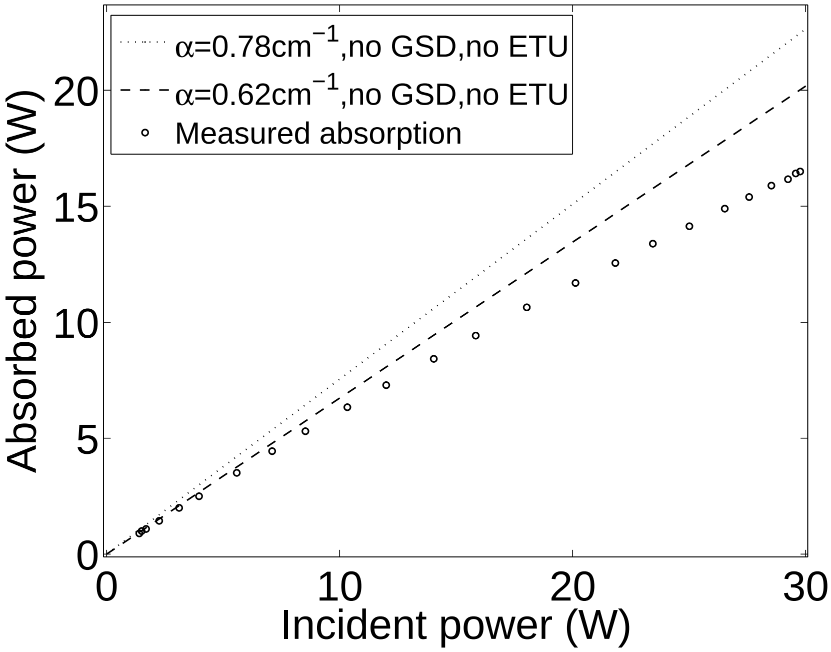

Figure 6.3: Pump absorption versus incident pump power. The straight lines are the prediction absorption of a 1.8 cm Er:YAG gain medium with different absorption coefficients.

Although the reported peak absorption coefficient in Er(0.5%):YAG is 0.78 cm^{-1}at 1470 nm [72, 87], the predicted absorption did not agree with the measurement. A closer agreement was found using α = 0.62 cm^{-1}, yielding an absorption of about 65% at pump powers <10W. This observation is consistent with Setlzer's measurement [72], which yielded an absorption coefficient of 0.55 cm^{-1} for a quasi-CW low-brightness-diode-pumped Er:YAG rod. The reduced absorption is possibly due to the broad bandwidth of laser diodes, which reduces the spectral overlap between the diode and the absorption bandwidth of Er:YAG.

The measured absorption decreases as the incident pump power is increased. Other factors, such as GSD and ETU, may have caused the the absorption to saturate, as will be discussed further in Sections 6.3 and 6.4.

6.2.2 Absorption for pulsed pumping

A mechanical chopper was used to pulse the CW pump source at 40 Hz, and the transmitted pump was measured using a photo-diode. The chopper was located close to the waist of the pump to minimize the time required to chop the beam, as shown in Figure 6.4.

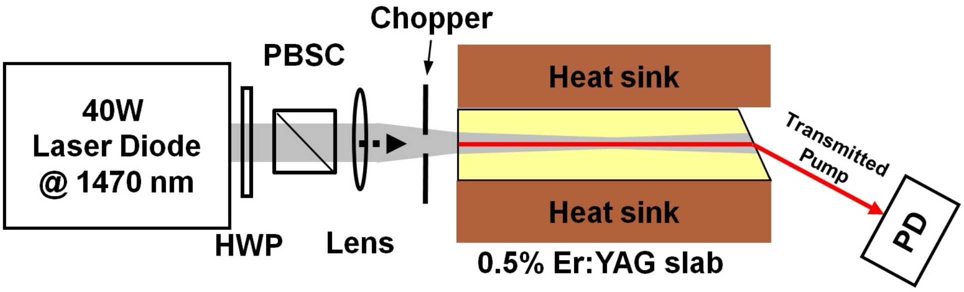

Figure 6.4: Pump absorption measurement for pulsed pumping.

The transmitted pump power is plotted in Figure 6.5 as a function of time. The rate at which the pump power is absorbed decreases significantly after about 2 ms of pumping. After about 10 ms, no additional pump power is absorbed.

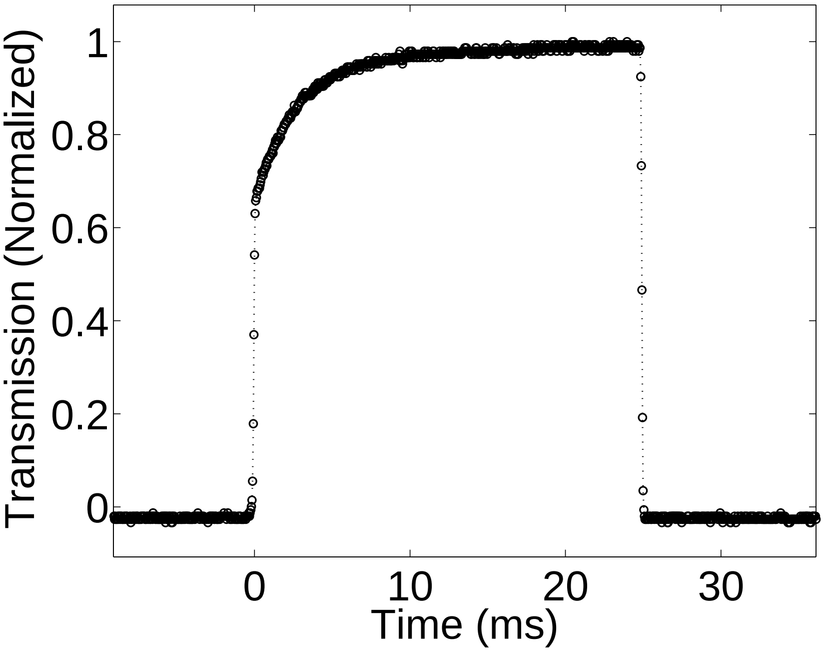

Figure 6.5: Transmission of the pump versus time measured for pulsed pumping with 35 W incident on the chopper.

This saturation of the pump absorption will result in a decrease in the average laser power for PRFs <500 Hz. A similar decrease would occur if the lifetime of the upper state decreased at low PRFs, and hence the decrease in efficiency at low PRF can be 'explained' by a reduced effective lifetime.

6.3 Measurements of upconversion and excited-state-absorption

In the ETU process illustrated in Figure 6.1 [125], two nearby erbium atoms in the $^4\mathrm{I}_{13/2}$ (N_2) manifold interact to promote one erbium atom to the $^4\mathrm{I}_{9/2}$ (N_4) manifold and de-excite the other erbium atom to the $^4\mathrm{I}_{15/2}$ (N_1) ground-state manifold [88]. Subsequent rapid non-radiative relaxation transfers the ions into the $^4\mathrm{I}_{11/2}$ (N_3) state, which fluoresces near 1 µm (90%) and 2.9 µm (10%) [130]. If upconversion is too strong, the population in the N_2 state will be depleted, thus reducing the upper state inversion, for pulse-repetition operation. Simultaneously, an increase in the heat dissipation will further degrade the performance of the laser.

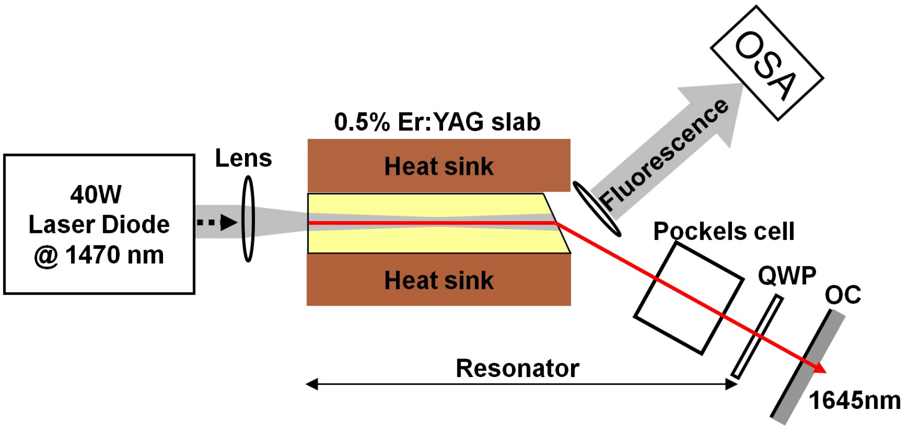

Figure 6.6: Experimental setup for the fluorescence measurement.

Experiments were conducted to measure the fluorescence following ETU in storage-mode pumping conditions. The schematic of the apparatus used for these experiments is shown in Figure 6.6. The fluorescence from the Er:YAG slab was coupled into a grating OSA using a 1 inch-diameter lens with 10 cm focal length. The lens was positioned close to the Brewster-angled face of the slab to maximise the collection of the fluorescence.

6.3.1 Upconversion fluorescence versus pump power

The fluorescence at near infra-red wavelengths was measured at different pump powers without lasing (not Q-switched). The spectra for several pump currents are shown in Figure 6.7. The upconversion fluorescence near 1 µm is much weaker than the fluorescence at the laser wavelength (1.6 µm).

The power of the 1 µm emission is plotted as a function of the pump power in Figure 6.8. The emission was expected to increase non-linearly at high pump power because the process involves the interaction between two excited ions. However, a linear increase of the 1 µm emission was noticed, possibly due to the relatively low

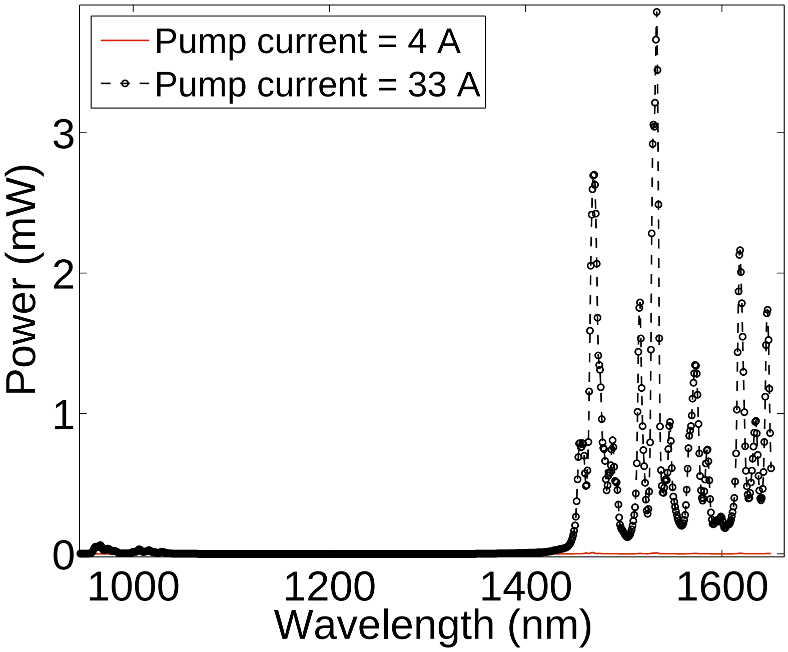

Figure 6.7: Fluorescence spectra for Er(0.5%):YAG at different pump currents.

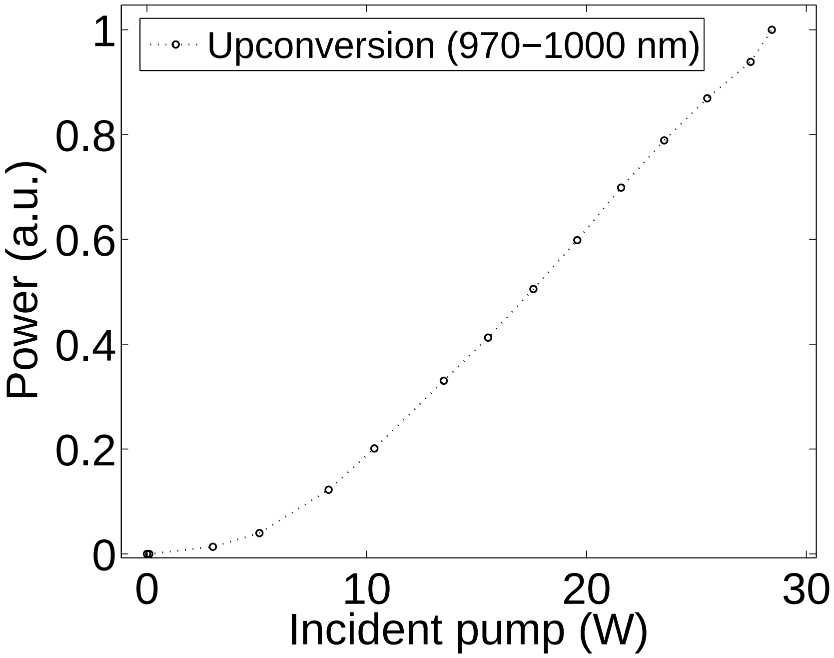

Figure 6.8: Plot of 1 µm emission following ETU, for 0.5% Er:YAG, versus pump power.

pump power level. The result is consistent with Chen's measurement [70], and his analysis showed that the magnitude of the two-ion upconversion process was small in Er(0.5%):YAG and cannot account for the decrease in laser efficiency as proposed in the literature.

6.3.2 Excited-state-absorption

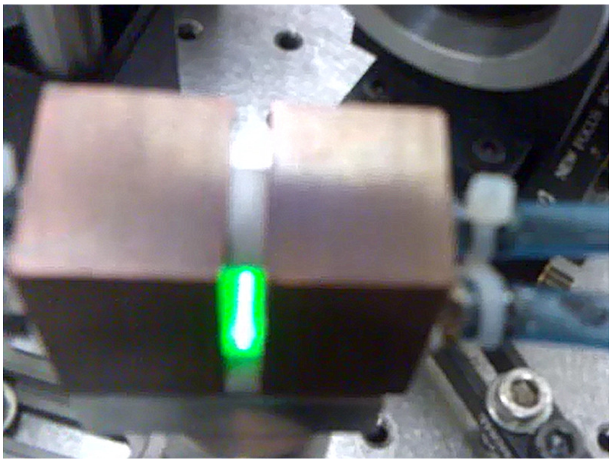

Figure 6.9: Green flashes observed from the Er(0.5%):YAG slab during Q-switched operation.

During Q-switched operation, relatively intense green flashes were observed as shown in Figure 6.9. The green emission has been identified to be due to a combination of the three-ion transition in the $^4I_{11/2}$ level [70,131,132] and the two-photon absorption of the intra-cavity light at 1645 nm in the $^4I_{13/2}$ level [133–135]. The fluorescences were measured for several Q-switch PRFs using the apparatus shown in Figure 6.6. The spectra are shown in Figure 6.10.

Figure 6.10 shows that the 550 nm emission was ~35 dB smaller than the 1 µm emission at 2000 Hz PRF, and at low PRFs (<400 Hz) the green emission increased ~5dB, while the 1 µm emission was constant. The fluorescence was further investigated by plotting the normalized power at these wavelengths versus PRF in Figure 6.11, and the 550 nm emission was noticed increasing significantly when the Q-

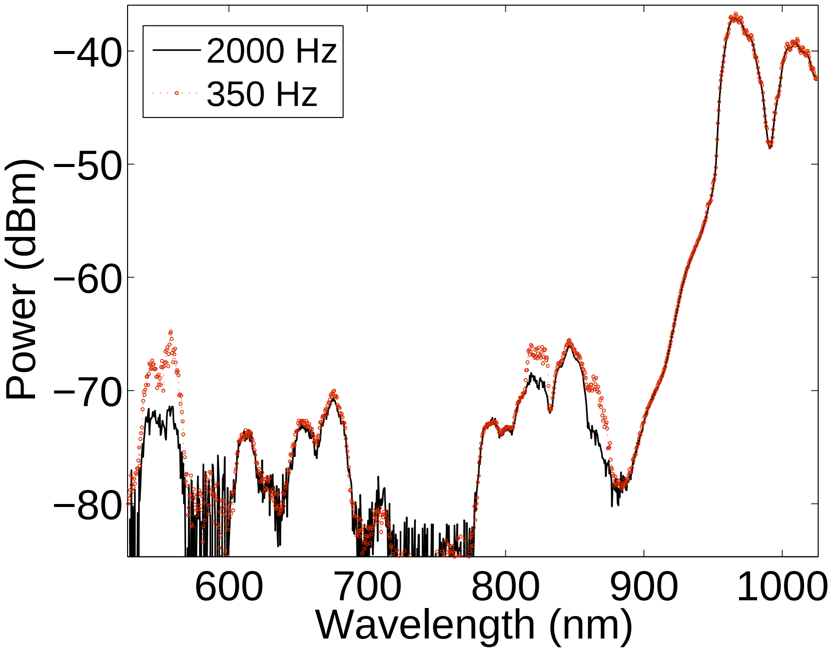

Figure 6.10: Spectra of the fluorescence of Q-switched Er(0.5%):YAG at several PRFs.

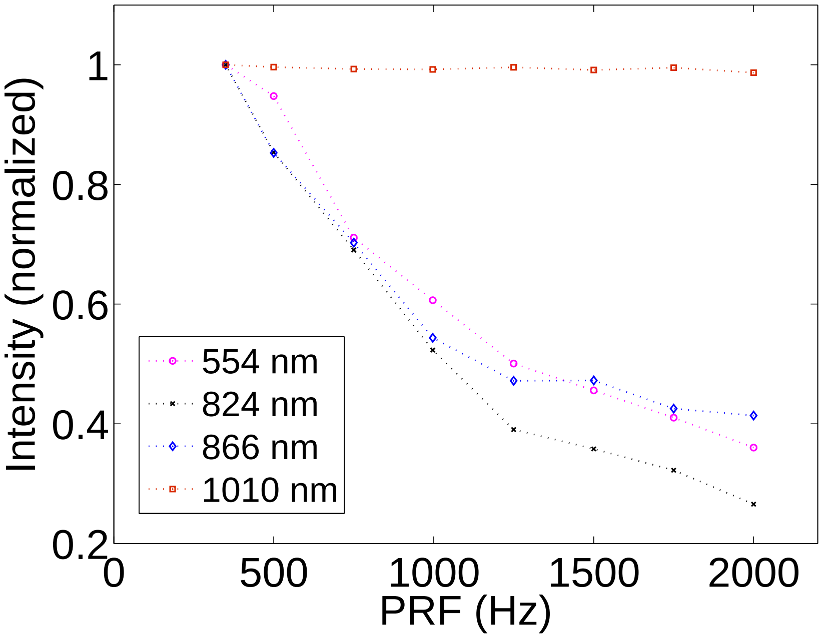

Figure 6.11: The power of the fluorescence, normalized to its 400 Hz PRF value for each wavelength, versus PRF.

switching frequency was reduced from 2000 Hz to 500 Hz, while the emission near ∼1 µm was unchanged.

The same result was obtained in Chen's experiment [70] in which the CW green emission was identified to be due to a second order upconversion process as it involves three ions in the $^4I_{11/2}$ level to generate population in the $^2H_{11/2}$ level, which relaxes non-radiatively to the $^4S_{3/2}$ level, which in turn radiates green light in transition to the ground state. In Chen's measurement the CW green fluorescence was 1000-2000-fold smaller than the 1 µm emission following by ETU, thus he concluded that the three-ion upconversion has negligible impact on the laser performance.

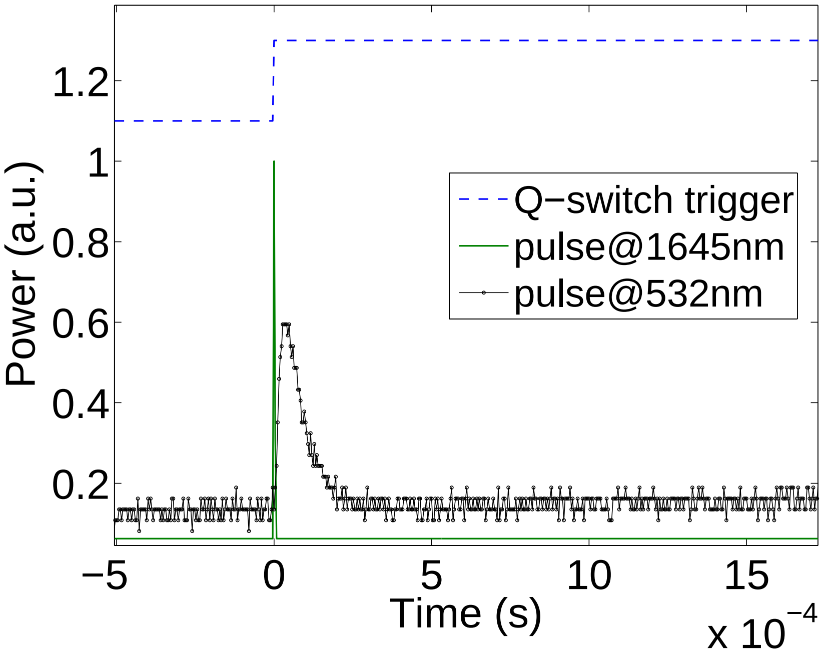

Figure 6.12: Comparison of the green fluorescence and the laser pulse observed during Q-switching of the Er:YAG laser.

Another mechanism that could cause the green emission is a two-photon absorption of the intra-cavity laser light at 1645 nm, which involves a transition from the $^4I_{13/2}$ (N_2) state of the Er^{3+} ion to the near-resonant $^2H_{11/2}$ level, followed by rapid non-radioactive decay to the $^4S_{3/2}$ level [133]. This was identified by measuring the temporal shape of the green pulses using an oscilloscope that was triggered by the

Q-switched pulse. Figure 6.12 shows a plot of the power of the green pulse and the Q-switched laser pulse versus time. The synchronization between the green pulse and Q-switch pulse confirms that the physical process responsible for the intense green emission during Q-switched operation is the two-photon absorption in the $^4I_{13/2}$ level. The absence of any intermediate levels and the quadratic behaviour with the green emission support this conclusion.

However the green flashes at 550 nm is very weak (30 dB less than the 1 µm emission) equating to a negligible loss in the Q-switching output at 1645 nm. Therefore Chen concluded that the two-ion absorption of the intra-cavity light could not be the main cause of the reduced efficiency at low PRFs.

6.4 Numerical simulation of pumping in presence of GSD and ETU

6.4.1 Rate equation model

The results described in Section 6.2.2 are analysed using a rate equation model, in which the influences of both GSD and ETU are included. The rate equations (Equation 6.1-6.4) shown below correspond to the four lowest Er^{3+} manifolds:

$$\frac{\mathrm{d}N_1}{\mathrm{d}t} = +\frac{P_p}{hv_pV_{pump}}\left[1-\exp\left(-\sigma_p(f_{2p}N_2-f_{1p}N_1)l_s\right)\right]+N_2W_{21}+N_3W_{31}+N_4W_{41}+C_{up}N_2^2 \tag{6.1}$$

$$\frac{\mathrm{d}N_2}{\mathrm{d}t} = -\frac{P_p}{hv_pV_{pump}}\left[1-\exp\left(-\sigma_p(f_{2p}N_2-f_{1p}N_1)l_s\right)\right]-N_2W_{21}+N_3W_{32}+N_4W_{42}-2C_{up}N_2^2 \tag{6.2}$$

$$\frac{\mathrm{d}N_3}{\mathrm{d}t} = N_3(W_{31}+W_{32})+N_4W_{43} \tag{6.3}$$

$$\frac{\mathrm{d}N_4}{\mathrm{d}t} = -N_4(W_{43}+W_{42}+W_{41})+C_{up}N_2^2 \tag{6.4}$$

where N_1 is the $^4\mathrm{I}_{15/2}$ level, N_2 is the $^4\mathrm{I}_{13/2}$ level, N_3 is the $^4\mathrm{I}_{11/2}$ level, N_4 is the $^4\mathrm{I}_{9/2}$ level, P_p is the incident pump power (W), V_{pump} is the pumped volume, C_{up} is the upconversion parameter, and W_{ij} is the radiative decay rate from level i to level j. The decay rates are given in Table 6.1 [130, 136].

Parameter	Value
W_{21}	121 s^{-1}
W_{31}	118 s^{-1}
W_{32}	14.9 s^{-1}
W_{41}	51 s^{-1}
W_{42}	57 s^{-1}
W_{43}	1.7×10^5 s^{-1}

Table 6.1: Radiative decay rate for Er:YAG at room temperature.

The N_1 and N_2 level describe Er^{3+} absorption and emission in the 1.4-1.6 µm region. The N_3 and N_4 level describe the pair upconversion population from the N_2 level; the higher order processes are neglected in this model. The rate equations consider the change of the pump absorption over time, and thus can realistically investigate the effects of GSD and ETU on the storage efficiency of the laser.

The total population density $N_{\mathrm{total}} = N_1 + N_2 + N_3 + N_4$ and $\mathrm{d}N_{\mathrm{total}}/\mathrm{d}t{=}0$. The equations were solved numerically using Matlab, and allowed the lower-state and upper-state populations to be calculated at a given time ($N_1(t)$ and $N_2(t)$). Once the ground-state population is known, the absorption coefficient, $\alpha(t)$, and total pump absorption (t) can be determined using the following equations:

$$\text{Absorption coefficient}\,\alpha(t) = \sigma_p(f_{1p}N_1(t) - f_{2p}N_2(t)) \tag{6.5}$$

$$\text{Total pump absorption }(t) = 1 - \exp\left[-\alpha(t)l_s\right]. \tag{6.6}$$

The total excited N_2 population, $\mathrm{N}_2^{Total}(t)$, of a pumped volume V_{pump} is calculated using

$$N_2^{\mathrm{Total}}(t) = N_2(t) \times V_{\mathrm{pump}}. \tag{6.7}$$

6.4.2 Effect of GSD on pump absorption

The parameters used in the simulation are listed in Table 6.2.

Parameter	Symbol	Value
Erbium density for 0.5% concentration	N_t	0.7×10^{20} cm^{-3}
Photon energy at 1645 nm	$h\nu_l$	1.21×10^{-19} J
Photon energy at 1470 nm	$h\nu_p$	1.35×10^{-19} J
Normalized Boltzmann factor for lower laser level	f_{1l}	0.022
Normalized Boltzmann factor for upper laser level	f_{2l}	0.209
Normalized Boltzmann factor for lower pump level	f_{1p}	0.264
Normalized Boltzmann factor for upper pump level	f_{2p}	0.089
Absolute Er^{3+}cross section at 1645 nm	σ_l	2.5×10^{-20} cm^2
Absolute Er^{3+}cross section at 1470 nm	σ_p	3.2×10^{-20} cm^2
Estimated absorption coefficient	α	0.62 cm^{-1}
Er:YAG crystal length	l_s	1.8 cm
Pump radius	r_p	0.085 cm
Upper state lifetime	τ_s	6.8 ms
Launched pump power	P_p	35 W
Upconversion parameter for 0.5% Er:YAG	C_{up}	2×10^{18} cm^3/s [87, 88]

Table 6.2: Parameters used in the model

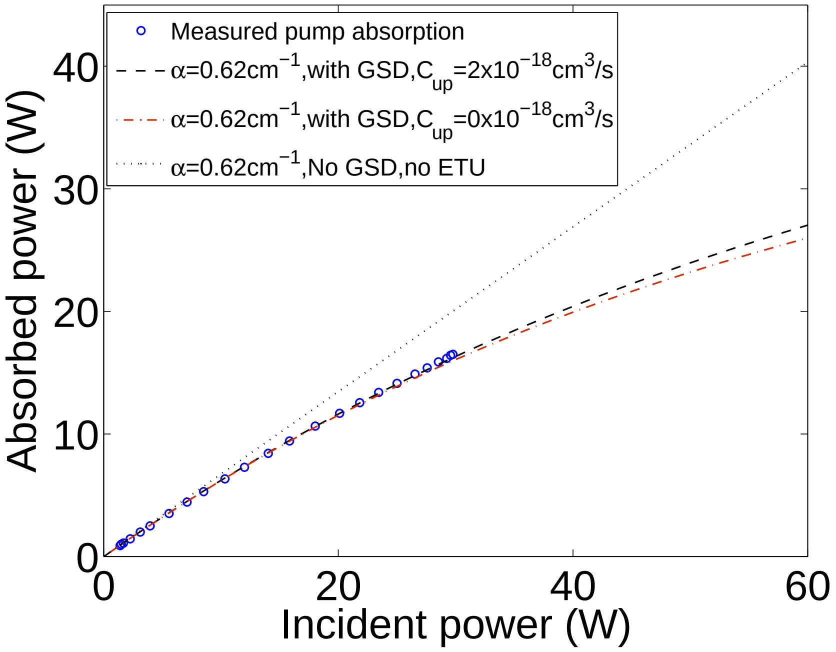

Figure 6.13: Predicted and measured pump absorption versus incident CW pump power.

The pump absorption predicted by the rate equation simulation for CW pumping (t≈∞) is compared with the measurement in Figure 6.13. For pump power >5 W GSD decreases the pump absorption. A systematic underestimate between the GSD-only prediction and the measurement at high pump powers is apparent. Adding ETU with C_{up}=2x10^{-18}cm^3/s, which de-excites the N_2 population more quickly than spontaneous emission, increases the pump absorption slightly and improves the agreement.

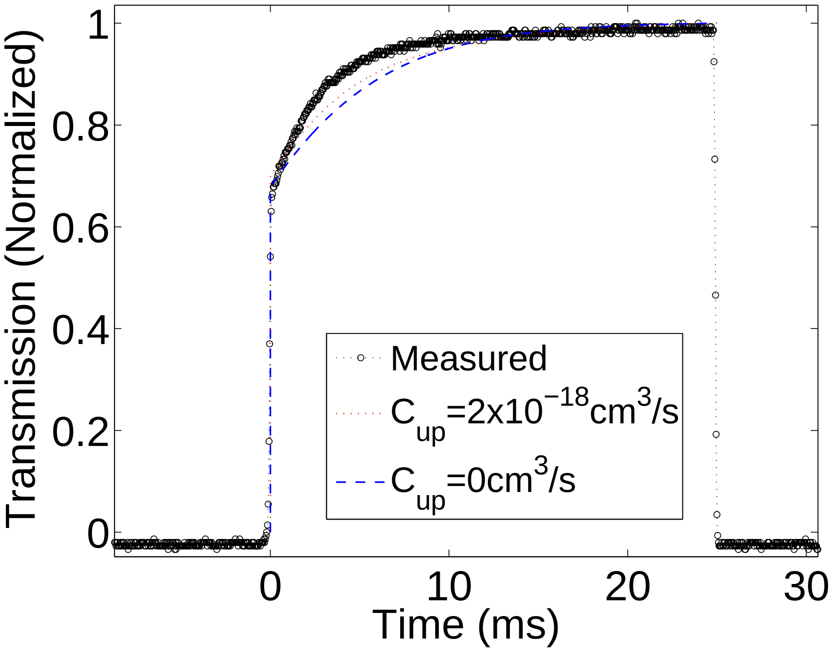

Figure 6.14: Comparison of the measured pump transmission and the simulated pump transmission for pulsed 35 W pumping.

The simulation shows that the absorption is only weakly sensitive to the upconversion at this pump level (35 W), and that the reduced absorption is mainly caused by GSD.

Equation 6.6 can also be used to calculate the pump transmission over time. The normalized predicted and measured pump transmission for pulsed 35 W pumping are plotted in Figure 6.14. In general the simulation and the measurement are in good agreement. A slightly higher pump transmission was measured on the rising edge

(<0.5 ms), which could be due to a more focused pump at the core of the volume causing a higher transmission at the beginning of the pumping. The inclusion of upconversion (C_{up}=2×10^{-18} cm^3/s) improves the agreement between the prediction and the measurement.

The predicted absorption coefficients are plotted in Figure 6.15 as a function of time for several pump powers. The dashed lines assume $C_{up} = 0$ cm^3/s and the dotted lines assume $C_{up} = 2 \times 10^{-18}$ cm^3/s.

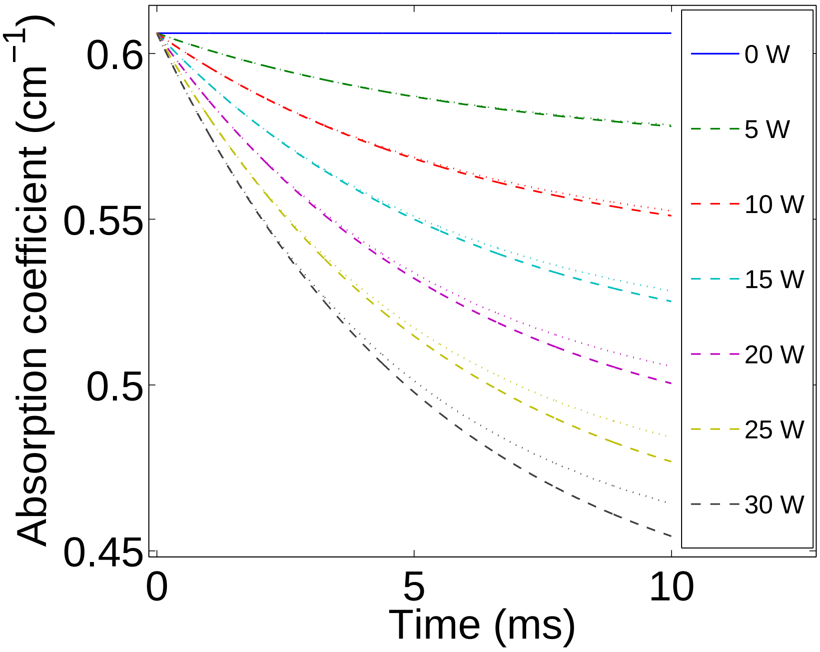

Figure 6.15: Predicted absorption coefficient versus pumping time for several pump levels. Dashed lines assumes only GSD effect (no ETU) and the dotted lines assumes both GSD and ETU (C_{up}=2x10^{-18} cm^3/s)

As for the CW pumped Er(0.5%):YAG, the simulation shows that reduction in the absorption coefficient due to GSD (with C_{up}=0 cm^3/s) dominates the absorption characteristics, especially for pumping durations >2 ms. At 30 W pump the absorption coefficient reduces from 0.62 cm^{-1} to 0.5 cm^{-1} in 4 ms - a 20% decrease. The predicted absorption coefficient increases slightly when ETU (C_{up}=2x10^{-18} cm^3/s) is included.

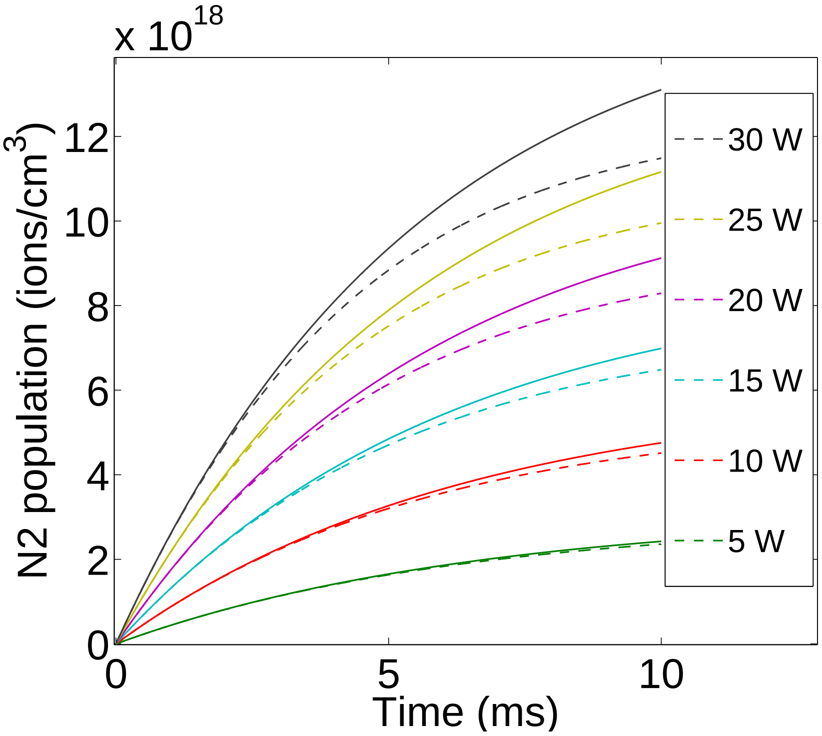

Figure 6.16: Predicted N_2 population versus pumping time for several pump powers. Solid lines assume only GSD effect (no ETU) and the dashed lines assume both GSD and ETU (C_{up}=2x10^{-18} cm^3/s)

Figure 6.16 plots the predicted N_2 population as a function of time for several pump powers. Similar to the result in Figure 6.15, the N_2 population is weakly sensitive to ETU for pumping durations < 5 ms. For longer pumping durations (i.e., 10 ms) N_2 population is suppressed more noticeably due to both GSD and ETU.

The result reveals that increasing the pump absorption can potentially improve the performance of Er(0.5%):YAG lasers operating at low PRFs.

6.5 Techniques for improving pump absorption

The pump absorption could be improved by either increasing the length of the gain medium or by increasing the doping concentration. An analysis of these alternatives is described below.

6.5.1 Increasing absorption length for Er(0.5%):YAG

The total N_2^{Total} population was calculated using Equations 6.2 and 6.7 as a function of slab length for several pump durations. The results are shown in Figure 6.17. For a pump duration >2.5 ms, doubling the slab length from 1.8 cm to 3.6 cm would result in a large increase in stored energy.

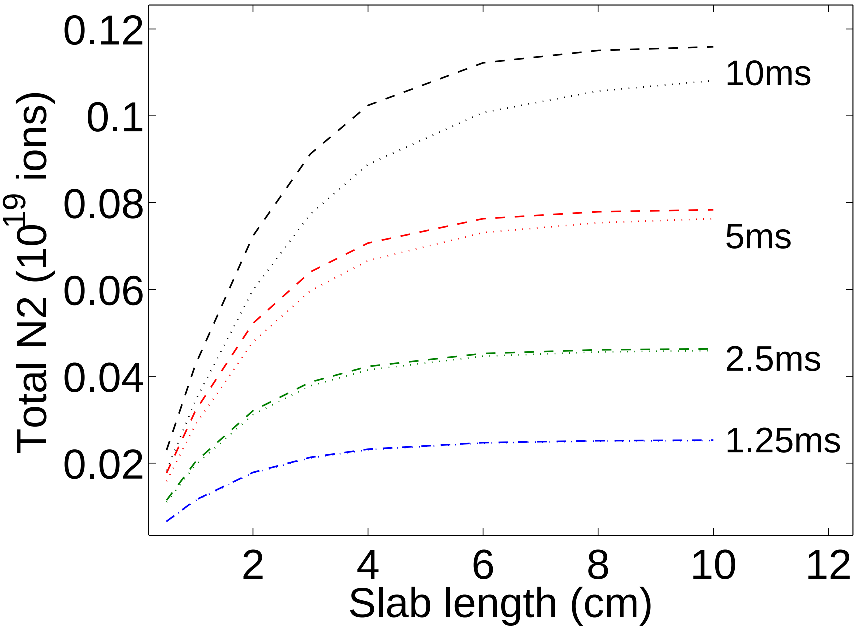

Figure 6.17: N_2^{Total} versus slab length for different pumping durations at 35 W. The dashed lines assume no upconversion and dotted lines assume C_{up}= 2x10^{-18} cm^3/s for Er(0.5%):YAG.

The average output power of a pulsed laser will, in general, increase as the number of ions excited per second, $N_2^{Total} \times PRF$, increases. Thus, in Figure 6.18, we plot the dependence of this quantity on slab length. As for the previous plot, the model predicts a significant improvement in efficiency might be obtained by increasing the slab length. Note, however, that since the 1.6 µm Er transition is a quasi-three-level system, the threshold and the N_2 population remaining at the end of each pulse would also increase with slab length, and decrease the efficiency for excessively long gain media. Additionally, obtaining uniform pump collimation over >6 cm when using low-brightness diodes could be problematic.

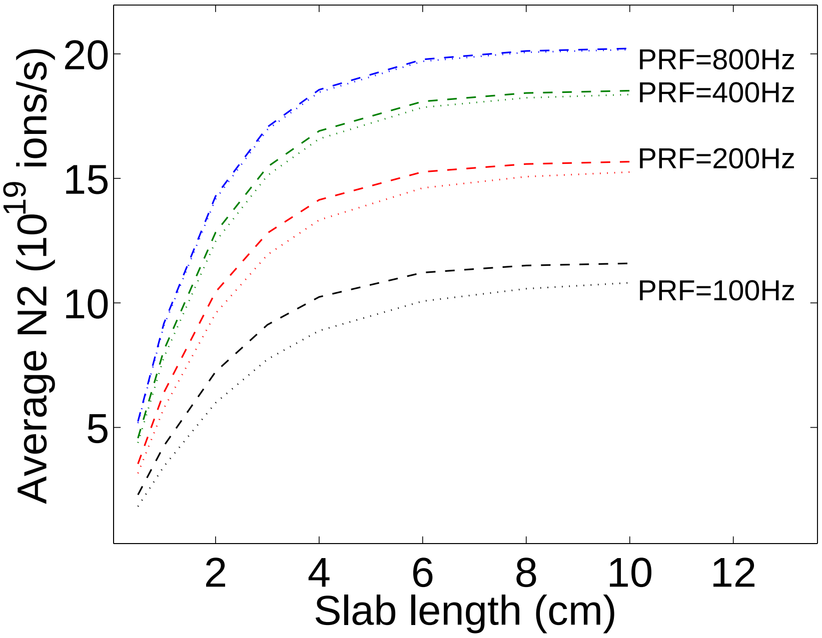

Figure 6.18: Average N_2^{Total} population (ions/s) at different PRFs. The dashed lines assume no upconversion and dotted lines assume C_{up}= 2x10^{-18} cm^3/s for Er(0.5%):YAG.

6.5.2 Improving absorption using more heavily doped Er:YAG

Pump absorption can also be improved by using higher dopings, but ETU would increase [89, 126, 137].

The results of a brief analysis are shown in Figure 6.19, where N_2^{Total} for a 1.8 cm Er:YAG gain medium is plotted as a function of pump duration for 0.5% and 1.0% dopings. Although a higher ETU loss is found for 1% doping, as expected, overall a 20% improved population is predicted using a 1% Er:YAG gain medium for 4 ms pumping duration than that of a 0.5% Er:YAG. The result shows that a Er(1%):YAG slab may potentially increase N_2^{Total}, thus improving the laser efficiency.

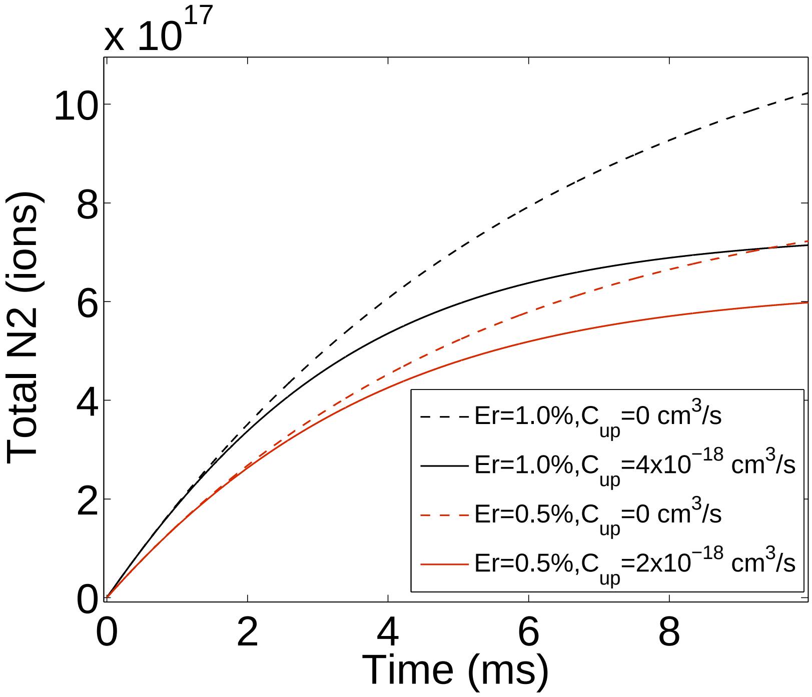

Figure 6.19: N_2^{Total} population for 1% and 0.5% doping Er:YAG.

6.6 Conclusion

This chapter described an investigation of the reduced efficiency of low PRF Q-switched Er:YAG lasers. Fluorescence measurements showed the existence of both ETU and ESA, but the power in that fluorescence was negligible compared to that due to spontaneous emission at 1.6 µm.

Pump absorption measurements found that the absorption was lower than that expected for low-brightness-diode pumped Er(0.5%):YAG lasers. Increasing the pump absorption thus may be the key to improving the Q-switched efficiency at low PRFs.

A model was developed to determine the effects of reduced pump absorption due to ground-state depletion (GSD) and ETU. The ETU parameter used in the model was estimated by comparison with the measured absorption of a CW pump. This model showed that reduced pump absorption is largely due to GSD, and thus decreases the efficiency of low PRF Q-switched Er(0.5%):YAG lasers.

The model also predicts that the efficiency of Er(0.5%):YAG lasers operating at low PRFs could be improved by using longer Er(0.5%):YAG gain mediums to increase pump absorption.

7 Conclusion

This thesis has described the development of continuous wave master and pulsed slave Er(0.5%):YAG lasers for use in CLR systems. In contrast to other resonantly-pumped Er:YAG lasers, these lasers are directly pumped with 1470 nm laser diodes, which removes the expense and complexity associated with EDFL pumping.

The master laser produced a 30 mW linearly-polarized diffraction-limited beam with a linewidth < 12 kHz, which is well suited to use as a master laser. Comparison of the observed output power with the predictions of a numerical model showed good agreement. These results have been published in ref. [84] (Appendix A.1.1).

The slave laser head achieved a multi-mode CW output power of 6.1 W with a 40% slope efficiency, showing that good efficiency can be achieved when using low-brightness-diode-pumping. In Q-switched operation, the laser produced diffraction-limited pulses with an average power of 2.5 W at 2 kHz PRF using a R=95% output coupler; the highest pulse energy of 5 mJ was achieved using a R=85% output coupler. This is, to our knowledge, the first Q-switched Er:YAG laser resonantly-pumped by CW laser diodes. This result was published in ref. [85] (Appendix A.1.2).

An investigation of the reduction in efficiency of the pulsed laser at low PRF showed that it is largely due to ground state depletion, rather than ETU and/or ESA as is commonly suggested.

7.1 Future directions

Increasing the length of the Er:YAG slab would improve the efficiency at low PRF, significantly increasing the pulse energy and thus the single-pulse range. Such an increase could, however, decrease the efficiency at high PRF as the gain medium furtherest from the pump may not be pumped past transparency, resulting in re-absorption losses, and the scatter losses would also increase. An investigation of the optimization for PRFs required for the CLR applications is therefore suggested.

CLR systems require that the pulsed laser is injection seeded. Thus, the Q-switched standing-wave resonator described in Chapter 5 should be injection seeded using the layout shown in Figure 7.1.

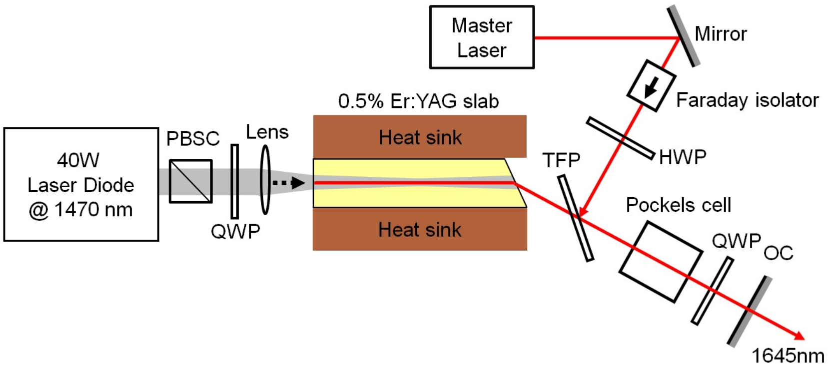

Figure 7.1: Schematic of injection seeding system.

Alternatively, either a double end-pumped zigzag Er:YAG gain medium, shown in Figure 7.2 [138,139], or an end-pumped coplanar-folded zigzag (CPFS) gain medium, shown in Figure 7.3 [50,140,141] could be developed. This gain medium could then be incorporated in the ring resonator used for the Er:Yb:glass CLR, as shown in Figure 7.4.

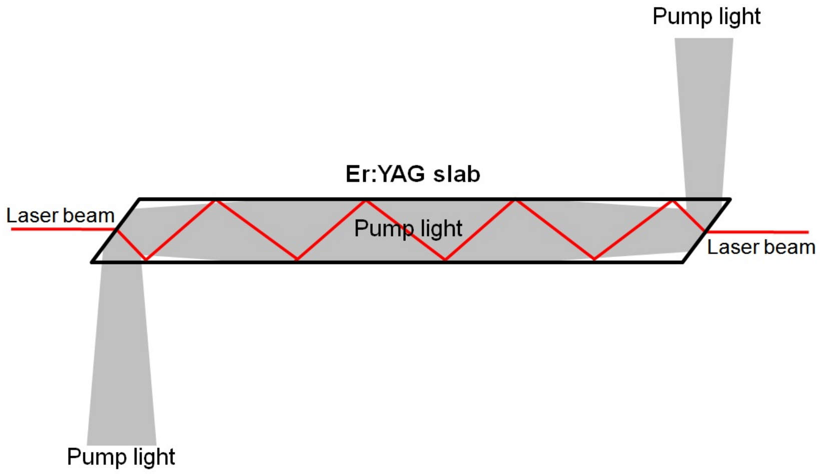

Figure 7.2: Schematic of double end-pumped gain medium. The pump lights are reflected off the end faces of the slab. The laser mode takes a zigzag path with the TIR at the cooled sidefaces maintained by a thin layer of silicon dioxide.

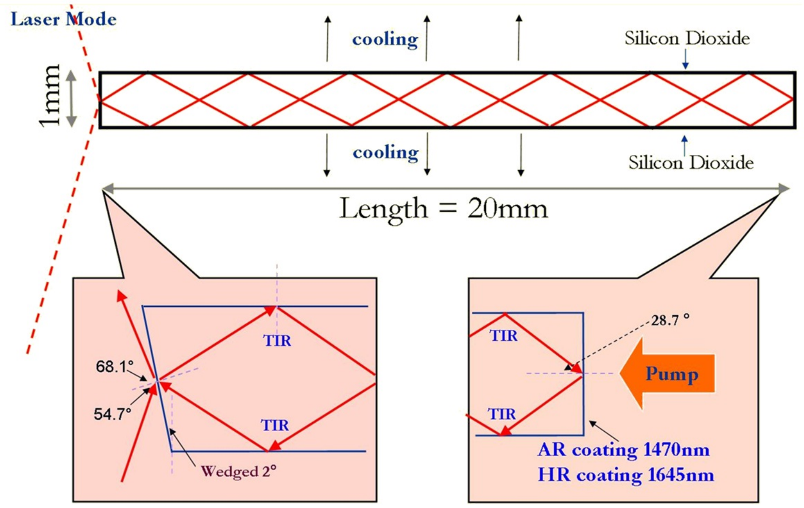

Figure 7.3: Schematic of an end-pumped CPFS gain medium. The pump light is focused into the end face of the slab. The laser mode takes a zigzag path with the TIR at the cooled faces maintained by a thin layer of silicon dioxide. The design of the CPFS slab is described in Appendix G.

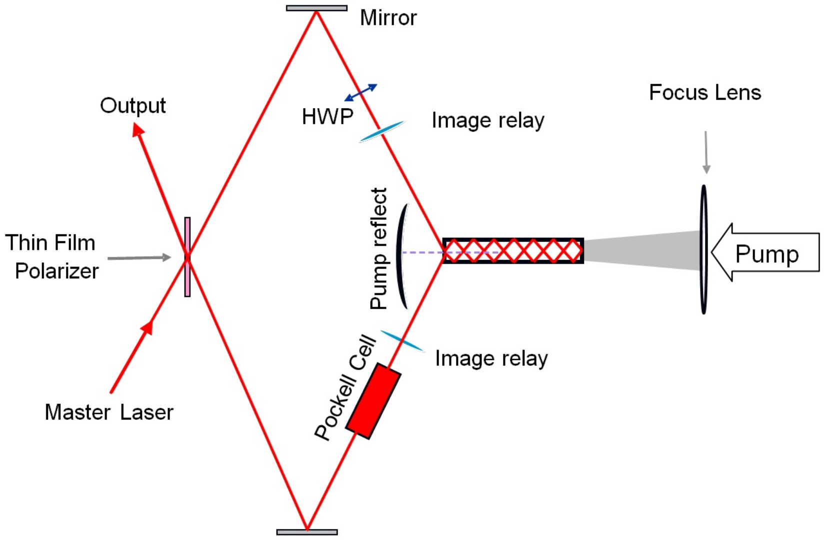

Figure 7.4: Ring resonator design incorporating the CPFS slab.

While the proposed concepts may contribute to solving the issues encountered in this thesis, their investigation is well outside the scope of this thesis, and should be the subjects of future studies.

A Publications

This appendix contains publications both associated with and arising as a result of this work.

A.1 Publications associated with this work

A.1.1 Stable, single frequency Er:YAG lasers at 1.6 µm

Nick W. Chang, David J. Hosken, Jesper Munch, David Ottaway, and Peter J. Veitch, IEEE J. Quantum Electron, **46**, 1039 (2010)

Chang, N.W., Hosken, D.J., Munch, J., Ottaway, D. & Veitch, P.J. (2010) Stable, single frequency Er: YAG Lasers at 1.6m.
IEEE Journal of Quantum Electronics, v. 46(7), pp. 1039-1041

A.1.2 Resonantly diode-pumped continuous-wave and Q-switched Er:YAG laser at 1645 nm.

N. W. Chang, N. Simakov, D.J. Hosken, J. Munch, D.J. Ottaway and P.J. Veitch, Optics Express, 18, 13673 (2010)

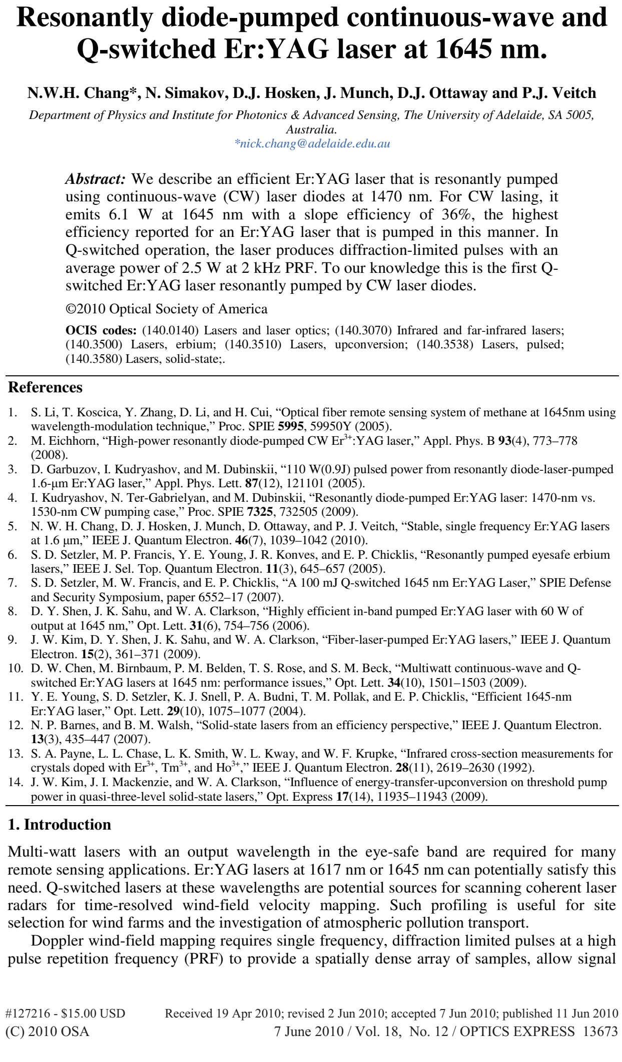

Resonantly diode-pumped continuous-wave and Q-switched Er:YAG laser at 1645 nm.

N.W.H. Chang*, N. Simakov, D.J. Hosken, J. Munch, D.J. Ottaway and P.J. Veitch

Department of Physics and Institute for Photonics & Advanced Sensing, The University of Adelaide, SA 5005, Australia.
**nick.chang@adelaide.edu.au*

Abstract: We describe an efficient Er:YAG laser that is resonantly pumped using continuous-wave (CW) laser diodes at 1470 nm. For CW lasing, it emits 6.1 W at 1645 nm with a slope efficiency of 36%, the highest efficiency reported for an Er:YAG laser that is pumped in this manner. In Q-switched operation, the laser produces diffraction-limited pulses with an average power of 2.5 W at 2 kHz PRF. To our knowledge this is the first Q-switched Er:YAG laser resonantly pumped by CW laser diodes.

OCIS codes: (140.0140) Lasers and laser optics; (140.3070) Infrared and far-infrared lasers; (140.3500) Lasers, erbium; (140.3510) Lasers, upconversion; (140.3538) Lasers, pulsed; (140.3580) Lasers, solid-state;.

References

1. S. Li, T. Koscica, Y. Zhang, D. Li, and H. Cui, “Optical fiber remote sensing system of methane at 1645nm using wavelength-modulation technique,” Proc. SPIE **5995**, 59950Y (2005).
2. M. Eichhorn, “High-power resonantly diode-pumped CW Er^{3+}:YAG laser,” Appl. Phys. B **93**(4), 773–778 (2008).
3. D. Garbuzov, I. Kudryashov, and M. Dubinskii, “110 W(0.9J) pulsed power from resonantly diode-laser-pumped 1.6-μm Er:YAG laser,” Appl. Phys. Lett. **87**(12), 121101 (2005).
4. I. Kudryashov, N. Ter-Gabrielyan, and M. Dubinskii, “Resonantly diode-pumped Er:YAG laser: 1470-nm vs. 1530-nm CW pumping case,” Proc. SPIE **7325**, 732505 (2009).
5. N. W. H. Chang, D. J. Hosken, J. Munch, D. Ottaway, and P. J. Veitch, “Stable, single frequency Er:YAG lasers at 1.6 μm,” IEEE J. Quantum Electron. **46**(7), 1039–1042 (2010).
6. S. D. Setzler, M. P. Francis, Y. E. Young, J. R. Konves, and E. P. Chicklis, “Resonantly pumped eyesafe erbium lasers,” IEEE J. Sel. Top. Quantum Electron. **11**(3), 645–657 (2005).
7. S. D. Setzler, M. W. Francis, and E. P. Chicklis, “A 100 mJ Q-switched 1645 nm Er:YAG Laser,” SPIE Defense and Security Symposium, paper 6552–17 (2007).
8. D. Y. Shen, J. K. Sahu, and W. A. Clarkson, “Highly efficient in-band pumped Er:YAG laser with 60 W of output at 1645 nm,” Opt. Lett. **31**(6), 754–756 (2006).
9. J. W. Kim, D. Y. Shen, J. K. Sahu, and W. A. Clarkson, “Fiber-laser-pumped Er:YAG lasers,” IEEE J. Quantum Electron. **15**(2), 361–371 (2009).
10. D. W. Chen, M. Birnbaum, P. M. Belden, T. S. Rose, and S. M. Beck, “Multiwatt continuous-wave and Q-switched Er:YAG lasers at 1645 nm: performance issues,” Opt. Lett. **34**(10), 1501–1503 (2009).
11. Y. E. Young, S. D. Setzler, K. J. Snell, P. A. Budni, T. M. Pollak, and E. P. Chicklis, “Efficient 1645-nm Er:YAG laser,” Opt. Lett. **29**(10), 1075–1077 (2004).
12. N. P. Barnes, and B. M. Walsh, “Solid-state lasers from an efficiency perspective,” IEEE J. Quantum Electron. **13**(3), 435–447 (2007).
13. S. A. Payne, L. L. Chase, L. K. Smith, W. L. Kway, and W. F. Krupke, “Infrared cross-section measurements for crystals doped with Er^{3+}, Tm^{3+}, and Ho^{3+},” IEEE J. Quantum Electron. **28**(11), 2619–2630 (1992).
14. J. W. Kim, J. I. Mackenzie, and W. A. Clarkson, “Influence of energy-transfer-upconversion on threshold pump power in quasi-three-level solid-state lasers,” Opt. Express **17**(14), 11935–11943 (2009).

---

1. Introduction

Multi-watt lasers with an output wavelength in the eye-safe band are required for many remote sensing applications. Er:YAG lasers at 1617 nm or 1645 nm can potentially satisfy this need. Q-switched lasers at these wavelengths are potential sources for scanning coherent laser radars for time-resolved wind-field velocity mapping. Such profiling is useful for site selection for wind farms and the investigation of atmospheric pollution transport.

Doppler wind-field mapping requires single frequency, diffraction limited pulses at a high pulse repetition frequency (PRF) to provide a spatially dense array of samples, allow signal

#127216 - $15.00 USD Received 19 Apr 2010; revised 2 Jun 2010; accepted 7 Jun 2010; published 11 Jun 2010

averaging with minimal loss of temporal resolution and to minimize the time required to scan an extended volume. Pulses with energies > few mJ and pulse durations of > 100 ns are essential for these measurements. Such requirements can be satisfied by CW pumping of a Q-switched free-space laser.

Lasers operating near 1645 nm are also useful for atmospheric trace gas measurements of methane, a critical greenhouse gas [1]. Additionally, high power CW lasers operating in this band are potentially useful for third generation interferometric gravitational wave detectors and range-Doppler imaging of hard targets using pseudo random phase modulation.

The development of reliable, high power Er:YAG lasers is facilitated by the use of resonant pumping. This minimizes the waste heat from the pumping process, reducing thermally induced lensing and birefringence to yield a laser that can operate efficiently at a variety of power levels. Er:YAG lasers can be resonantly pumped at either 1470 nm or 1532 nm, using either laser diodes [2–5] or erbium-doped fiber lasers (EDFL) [6–11].

EDFL pumping allows efficient pump absorption due to its narrow bandwidth and good spatial overlap of the pumped region with the laser mode because of the excellent pump beam quality. High power and good optical efficiency have been achieved using this approach; the highest reported power and slope efficiency are 60 W and 80% respectively [8]. However, this pumping approach adds complexity, weight and volume to the laser system. Additionally, the overall optical efficiency with EDFL pumping is typically only about 28% due to the efficiency of the EDFL [9].

Direct pumping using high power laser diodes is complicated, however, by their low brightness and broad bandwidth. Nevertheless, Eichorn [2] demonstrated that pumping of Er:YAG lasers using fibre-coupled, CW 1535 nm laser diodes that were bandwidth narrowed to 1 nm yielded a multi-mode output power of 7 W at a slope efficiency 54%, neglecting the loss in pump power due to the fibre coupling. Kudryashov *et al* have recently investigated pumping using CW, 1470 nm and 1532 nm laser diodes that were bandwidth narrowed using external volume Bragg gratings [4]. The initial measurement with the broad bandwidth (10-12 nm) diodes obtained a multi-mode slope efficiency of ~20%. Reducing the bandwidth to about 0.6 nm, which is similar to the linewidth of the strongly absorbing transitions within the absorption bands, yielded a slope efficiency for the 1470 nm system of 28% for output powers up to 60 W. Pumping using low power, fibre-coupled broadband 1470 nm diodes to produce a diffraction-limited TEM_{00} output has also been investigated: an output power of 50 mW with a slope of efficiency of 20% was reported [5].

In this paper we report a CW laser that is pumped by a broad bandwidth laser diode at 1470 nm that produces 6.1 W with a slope efficiency of 36%. We also describe Q-switched operation of this laser. To our knowledge, there have been no reports of Q-switched Er:YAG lasers resonantly pumped by a broad bandwidth, CW diode.

2. Description of Laser

A schematic of the laser is shown in Fig. 1. The pump source is a CW, 40 W, fast axis collimated, three bar, laser diode array operating at 1470 nm, with a full-width at half maximum (FWHM) bandwidth of 12 nm. The output of the diode is imaged using a 100 mm focal length lens to produce a 1.3 mm diameter waist with a divergence of 65 mrad inside the slab. The gain medium is a 20 × 3 × 3 mm^3, Er^{3+}(0.5%):YAG slab. The slab face closest to the diode is also the end mirror of the resonator, and is coated for high reflectivity (R > 99.7%) at 1645 nm and high transmission (T > 99.8%) at 1470 nm. The other end is cut at Brewster's angle, thereby providing the polarization discrimination required for electro-optic Q-switching. A Rubidium Titanyle Phosphate (RTP) Pockels cell and an anti-reflection coated (R < 0.5%) quarter-wave plate (QWP) are used as the Q-switch. The output coupler is a flat mirror with 5% transmission and the physical resonator length is ~17 cm.

#127216 - $15.00 USD Received 19 Apr 2010; revised 2 Jun 2010; accepted 7 Jun 2010; published 11 Jun 2010

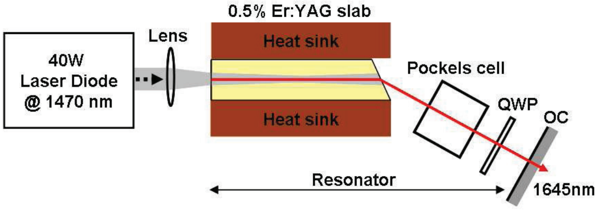

Fig. 1. Schematic of the Q-switched Er:YAG laser. Abbreviations: QWP, quarter wave plate; OC, output coupler.

3. Results

For initial testing, the Pockels cell and QWP were removed and the resonator length reduced to 7 cm. The multi-mode output power of this CW laser as a function of the incident pump power is plotted in Fig. 2. This laser had a slope efficiency of 36% which, to the best of our knowledge, is the highest efficiency reported for an Er:YAG laser that is pumped by broadband diodes at 1470 nm. Since only 55% of the pump power is absorbed, the slope efficiency with respect to the absorbed power is ~60%.

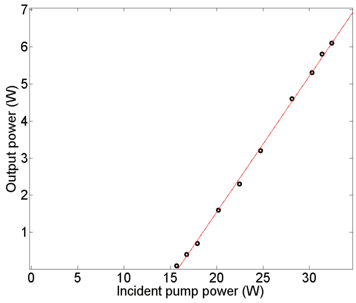

Fig. 2. Plot of multi-mode CW output power versus incident pump power for the reduced-length laser.

The spectral content of the laser output was measured using an optical spectrum analyser, which showed that the laser oscillated at 1645 nm only. Lasing at another emission peak around 1617 nm is also possible. However, it generally has a higher lasing threshold because it requires more excited Er ions (~14.6%) in the upper laser level manifold to reach transparency. Therefore, to lase at 1617 nm, additional wavelength discrimination in the resonator would be required to suppress the 1645 nm emission.

Figure 3 shows the average output power of the Q-switched laser for both CW and pulsed operation. As expected, the additional intra-cavity components result in an increased threshold compared to CW lasing of the reduced-length laser, shown in Fig. 2. The similarity between the average output power in CW and Q-switched lasing indicates that there was no increase in losses due to up-conversion or amplified stimulated emission (ASE) when Q-switching at 2 kHz PRF with incident pump powers up to 30.6 W.

#127216 - $15.00 USD Received 19 Apr 2010; revised 2 Jun 2010; accepted 7 Jun 2010; published 11 Jun 2010

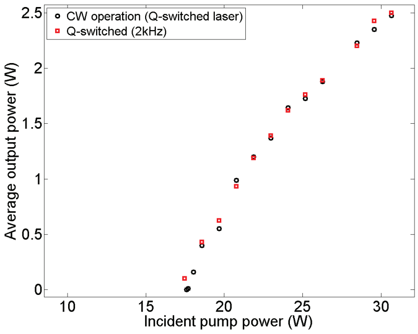

Fig. 3. Plot of the average output power versus incident pump power for CW and Q-switched (2kHz) operation of the laser shown in Fig. 1.

The intensity profile of the output of the Q-switched laser at an average output power of 2.5 W, and a plot of the measured beam size as it passes through a waist are shown in Fig. 4. The curve of best fit, for which $M^2 = 1.04$, is also plotted. This indicates that the laser output is near diffraction-limited.

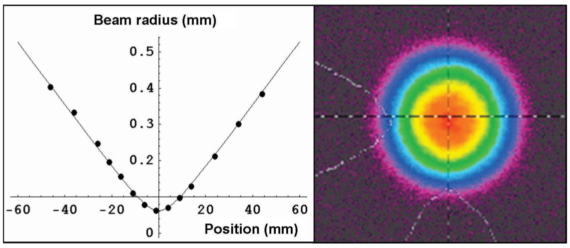

Fig. 4. (Left) Plot of the measured beam size of the output of the Q-switched laser at an average output power of 2.5 W (dots), and the $M^2 = 1.04$ curve of best fit. (Right) Intensity profile of the laser output.

The dependence of the average output power on PRF is shown in Fig. 5. The laser could not be operated at low PRFs and high pump power due to damage of the (low quality) optical coatings caused by the increased intra-cavity peak power (~45 MW/cm^2) of the pulses. The highest measured pulse energy was 2.3 mJ with a pulse duration of ~100 ns at 250 Hz PRF for an incident pump power of 23.5 W. The dependence of pulse energy on PRF at this pump power is plotted in Fig. 6.

#127216 - $15.00 USD Received 19 Apr 2010; revised 2 Jun 2010; accepted 7 Jun 2010; published 11 Jun 2010

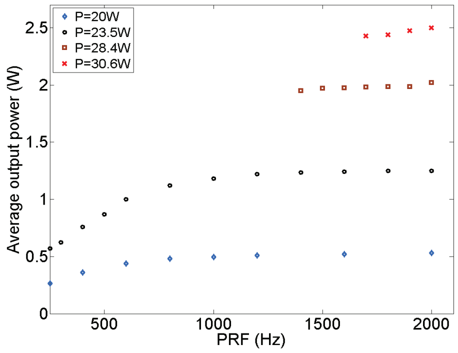

Fig. 5. Plot of the dependence of average output power on PRF for various incident pump power values.

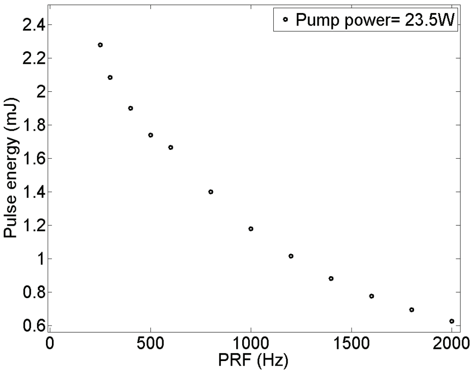

Fig. 6. Plot of the dependence of pulse energy on PRF for an incident pump power = 23.5 W.

The expected dependence of the average power on PRF for a CW pumped Q-switched laser is given by

$$P_{av}(\mathrm{PRF}) = P_{av}(\mathrm{CW})\,[1 - \exp(-t_q/t_s)]$$

where P_{av}(CW) is the average power in CW operation, t_s is the effective lifetime of the upper state and t_q = 1 / PRF [12]. Since Fig. 3 shows that the average power for both CW and PRF = 2 kHz lasing are identical at these pump powers, we plot in Fig. 7 the measured P_{av}(PRF) / P_{av}(PRF = 2 kHz) ratio and the ratio expected assuming that (a) t_s = 6.9 ms, (the fluorescent lifetime of the upper lasing state [13]), and (b) t_s = 2.3 ms (a lifetime estimated from the data recorded at low PRF).

#127216 - $15.00 USD Received 19 Apr 2010; revised 2 Jun 2010; accepted 7 Jun 2010; published 11 Jun 2010

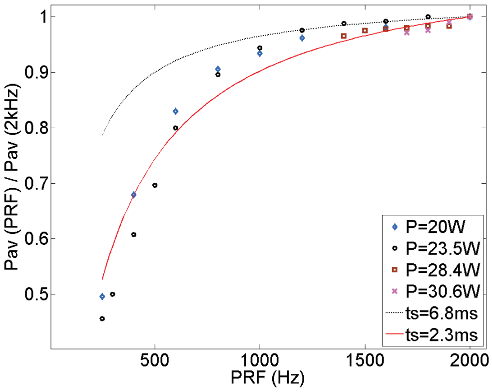

Fig. 7. Measured (symbols) and expected (solid lines) ratio of average power at different PRF.

It is clear that the decrease in average power at low PRF is not consistent with the assumption that the effective lifetime is 6.8 ms at low PRF. Another loss mechanism must therefore be decreasing the lifetime of the upper lasing state. Reduced upper state lifetimes for Q-switched Er:YAG lasers pumped by EDFLs have been reported by a number of authors [10,11,14]. Several mechanisms have been proposed to explain this reduction, including up-conversion [11,14] and ASE [10]. Such mechanisms would result in an upper state lifetime reduction that is dependent on the population of the upper state, which is consistent with the result shown in Fig. 7.

We are currently investigating the cause of the lifetime reduction in 1470 nm diode-pumped Er:YAG lasers using spectroscopic techniques. Initial measurements show both up-conversion and excited state absorption but negligible ASE. We expect to report a more detailed analysis in a later paper.

4. Summary

We have demonstrated an efficient Er:YAG laser that is resonantly pumped using CW diodes at 1470 nm. Using a reduced-length resonator, CW output powers up to 6.1 W at 1645 nm have been obtained with a multi-mode slope efficiency of 36%. In pulsed operation, the laser is Q-switched at 2 kHz PRF to yield diffraction-limited pulses with an average power of 2.5 W. The highest single pulse energy obtained was 2.3 mJ with a pulse duration of 100 ns at 250 Hz PRF. Higher pulse energy should be achieved by employing a more-robust high reflection coating on the Er:YAG slab.

Acknowledgment

This research was funded by the Australian Research Council and the WA Department of Environment. The authors also thank Blair Middlemiss, Trevor Waterhouse, and Neville Wild for their technical support.

B Upconversion investigation

B.1 Introduction

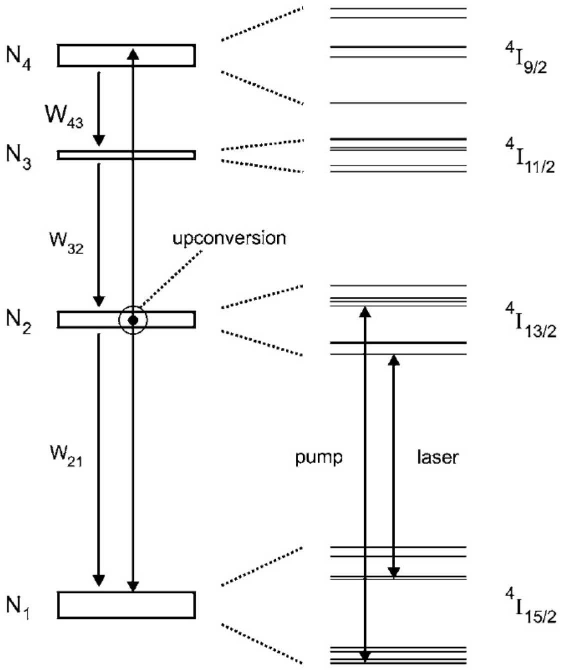

Figure B.1: Four lower manifolds involved in 1.6 µm emission and upconversion.

The effect of upconversion on the lasing threshold of the laser discussed in Chapter 2 was investigated using the rate equations shown below. These equations correspond to the four lower Er^{3+} manifolds as shown in Figure B.1 [87]. The model includes the influences due to GSD and ETU.

$$\frac{dN_1}{dt} = +\frac{P_p}{hv_pV_{pump}}\left[1 - \exp\left(-\sigma_p(f_{2p}N_2 - f_{1p}N_1)l_s\right)\right] + N_2W_{21} + N_3W_{31} + N_4W_{41} + C_{up}N_2^2 \tag{B.1}$$

$$\frac{dN_2}{dt} = -\frac{P_p}{hv_pV_{pump}}\left[1 - \exp\left(-\sigma_p(f_{2p}N_2 - f_{1p}N_1)l_s\right)\right] - N_2W_{21} + N_3W_{32} + N_4W_{42} - 2C_{up}N_2^2 \tag{B.2}$$

$$\frac{dN_3}{dt} = N_3(W_{31} + W_{32}) + N_4W_{43} \tag{B.3}$$

$$\frac{dN_4}{dt} = -N_4(W_{43} + W_{42} + W_{41}) + C_{up}N_2^2 \tag{B.4}$$

where N_1 is the $^4\mathrm{I}_{15/2}$ level, N_2 is the $^4\mathrm{I}_{13/2}$ level, N_3 is the $^4\mathrm{I}_{11/2}$ level, N_4 is the $^4\mathrm{I}_{9/2}$ level, P_p is the incident pump power (W), C_{up} is the upconversion parameter, and W_{ij} is the radiative decay rate from level i to level j as shown in Figure B.1. The decay rates are given in Table B.1.

Parameter	Value
W_{21}	121 s^{-1}
W_{31}	118 s^{-1}
W_{32}	14.9 s^{-1}
W_{41}	51 s^{-1}
W_{42}	57 s^{-1}
W_{43}	1.7×10^5 s^{-1}

Table B.1: Radiative decay rate for Er:YAG at room temperature.

The N_1 and N_2 level describe Er^{3+} absorption and emission in the 1.4-1.6 µm region. The N_3 and N_4 level describe the pair upconversion population from the N_2 level; the higher order processes are neglected in this model. The total population density $N_{\text{total}} = N_1 + N_2 + N_3 + N_4$ and $\mathrm{d}N_{\text{total}}/\mathrm{d}t$=0. The equations were solved numerically using Matlab, and allowed the lower-state and upper-state populations to be calculated at a given time ($N_1(t)$ and $N_2(t)$).

B.2 Numerical prediction

The population in each level is numerically solved using MATLAB until the steady state is reached. Figure B.2 shows a result of the population transportation over 60 ms duration for a pump power of 550 mW. The result shows a non-negligible upconversion population, where about 20% of the populated ions are populated in N3 and N4 levels through upconversion.

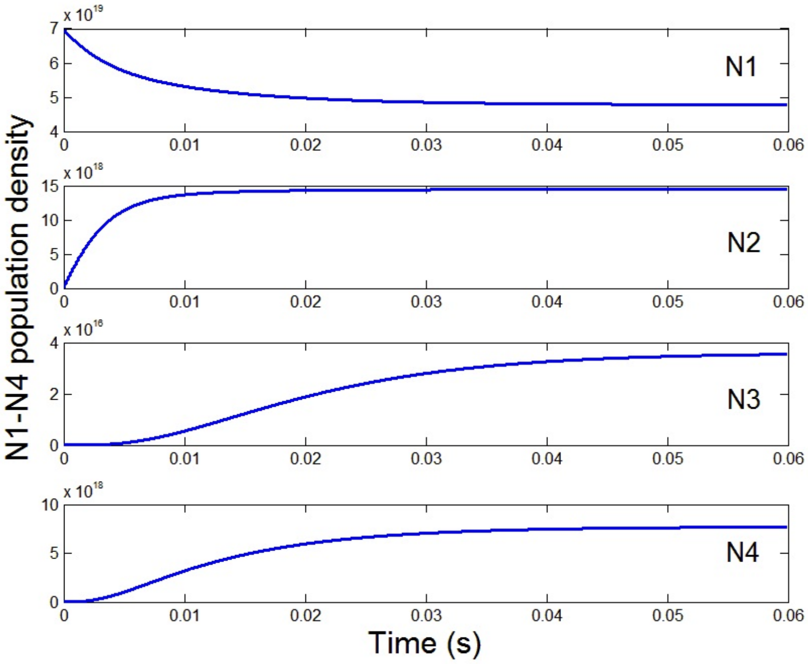

Figure B.2: Population transport over time for 550 mW of pump power.

Knowing the population distribution in each level, the laser inversion density ($f_{2l}N_2 - f_{1l}N_1$) can be calculated, thus allowing us to find the gain coefficient (cm^{-1}), γ, using Equation 2.30. Knowing the gain coefficient and the length of the gain medium, the Matlab program then calculates the round trip gain (G) of the laser, and the lasing threshold is determined when the total gain overcomes the resonator loss (G_{th}).

Figure B.3 shows a plot of the round trip gain versus pump power with different upconversion rates. The parameters used in the simulation are based on Table 2.6

in Section 2.4. Equation B.2 shows that the N_2 population is excited to N_4 at a rate proportional to its own square, thus increasing the threshold power. The loss due to ETU is investigated for serveral upconversion values from $1 \times 10^{-18}\,\mathrm{cm}^{-3}/\mathrm{s}$ to $4 \times 10^{-18}\,\mathrm{cm}^{-3}/\mathrm{s}$. As published by various groups [87, 89, 137], the C_{up} value for a 1% at. Er:YAG crystal is between $4 \times 10^{-18} - 5 \times 10^{-18}\,\mathrm{cm}^{-3}/\mathrm{s}$. For 0.5% doping concentration, we expect the upconversion coefficient to be around $2.5 \times 10^{-18}\,\mathrm{cm}^{-3}/\mathrm{s}$.

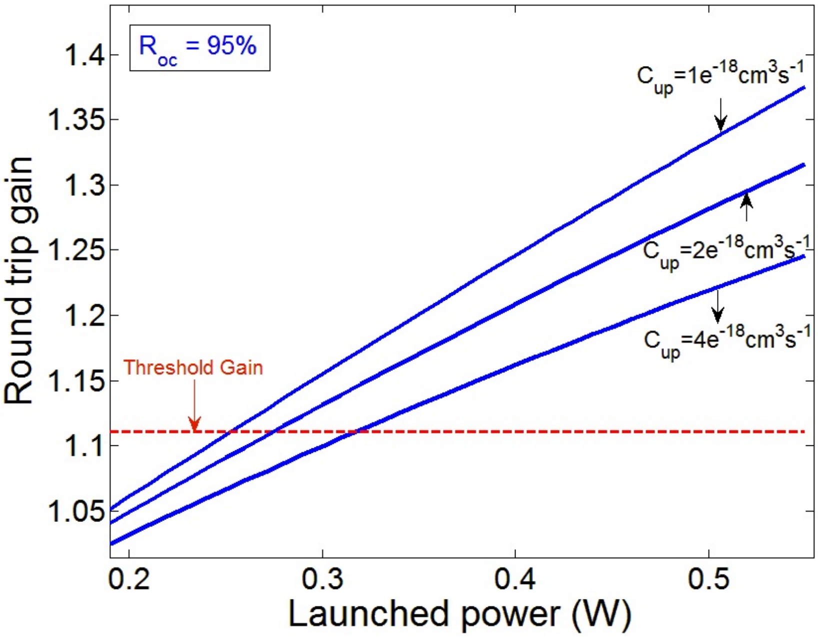

Figure B.3: Round trip gain versus launched power at different upconversion values.

Figure B.3 plots the round trip gain as a function of the pump power for C_{up} values from $1 \times 10^{-18}\,\mathrm{cm}^{-3}/\mathrm{s}$ to $4 \times 10^{-18}\,\mathrm{cm}^{-3}/\mathrm{s}$. As the C_{up} is increased, the round trip gain reduces therefore more pump power is required to reach the threshold.

The threshold power is plotted in Figure B.4 as a function of the upconversion value for different R_{oc} couplers. For a $R_{oc} = 90\%$ output coupler, the threshold is 200 mW higher if $C_{up} = 4 \times 10^{-18}\,\mathrm{cm}^{-3}/\mathrm{s}$. For output couplers with R_{oc} >95%, ETU increases the threshold no more than 90 mW. Thus, the master laser should use R_{oc} >95% couplers to ensure sufficient pump power is available for the threshold.

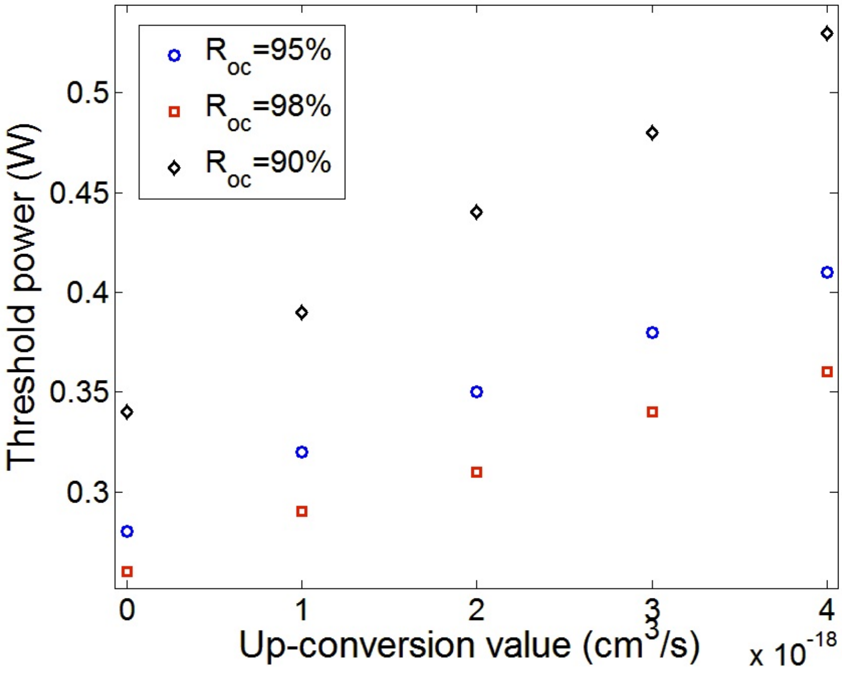

Figure B.4: Predicted threshold pump power as a function of a upconversion parameter.

Note that the slope efficiency is also indirectly influenced by ETU because pump bleaching due to GSD can occur because of the higher threshold.

B.3 Summary

The effect of upconversion loss on the Er:YAG laser, discussed in Chapter 2, is investigated for different output couplers. The results show that upconversion may increase the threshold >100 mW when using for R <90% output couplers. For a total pump power of 0.6 W, the master should use R_{oc} >95% to ensure the threshold is <<0.6 W.

C Single-mode laser diode characteristics

The single-mode laser diodes used in Chapter 3 were purchased from Princeton Lightwave Inc. (New Jersey, USA). The specifications of the fiber-coupled laser diodes are shown in Figures C.1 to C.9.

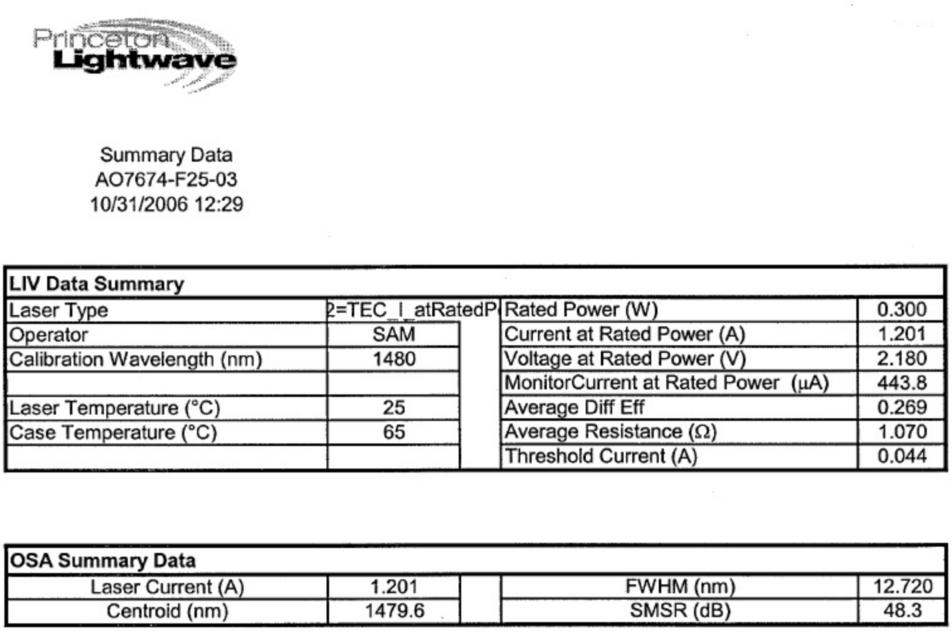

Princeton Lightwave

Summary Data
AO7674-F25-03
10/31/2006 12:29

LIV Data Summary				
Laser Type	2=TEC_I_atRatedP		Rated Power (W)	0.300
Operator	SAM		Current at Rated Power (A)	1.201
Calibration Wavelength (nm)	1480		Voltage at Rated Power (V)	2.180
			MonitorCurrent at Rated Power (μA)	443.8
Laser Temperature (°C)	25		Average Diff Eff	0.269
Case Temperature (°C)	65		Average Resistance (Ω)	1.070
			Threshold Current (A)	0.044

OSA Summary Data				
Laser Current (A)	1.201		FWHM (nm)	12.720
Centroid (nm)	1479.6		SMSR (dB)	48.3

Figure C.1: Specifications of the first laser diode (1 of 4).

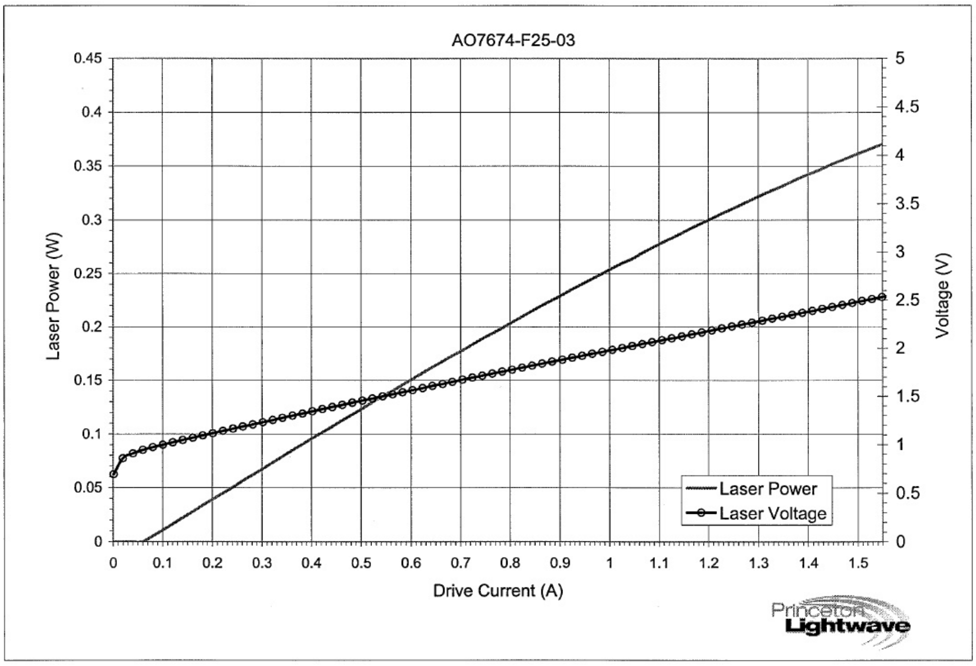

Figure C.2: Performance of the first laser diode (2 of 4).

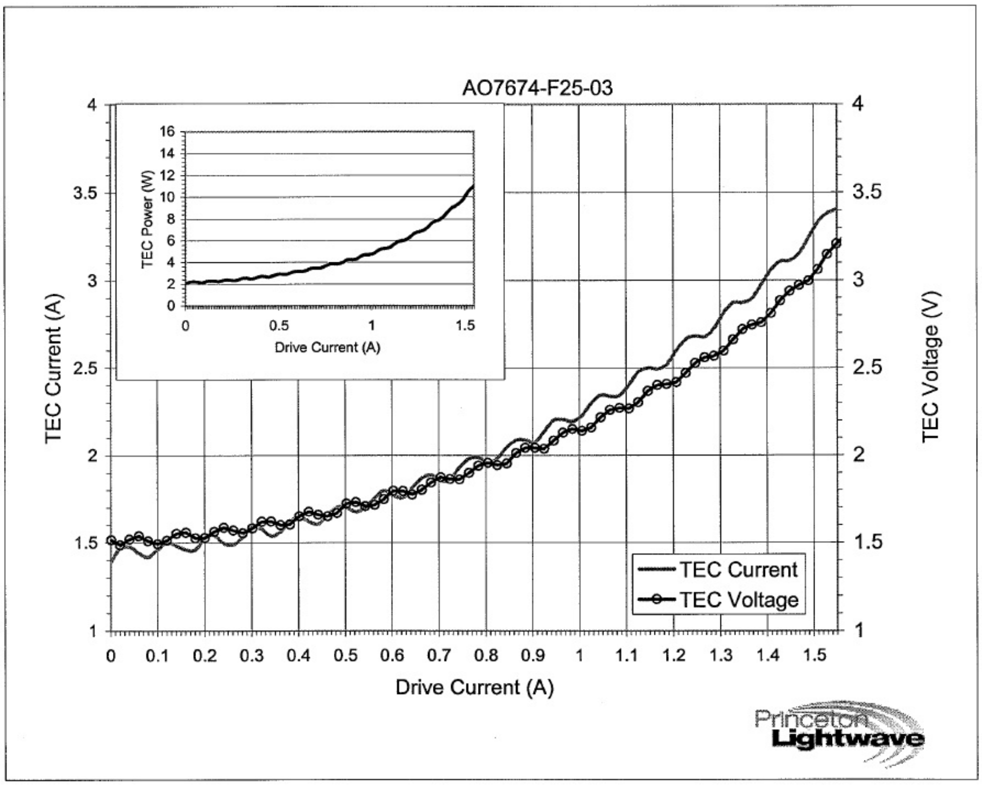

Figure C.3: Cooling characteristics of the first laser diode (3 of 4).

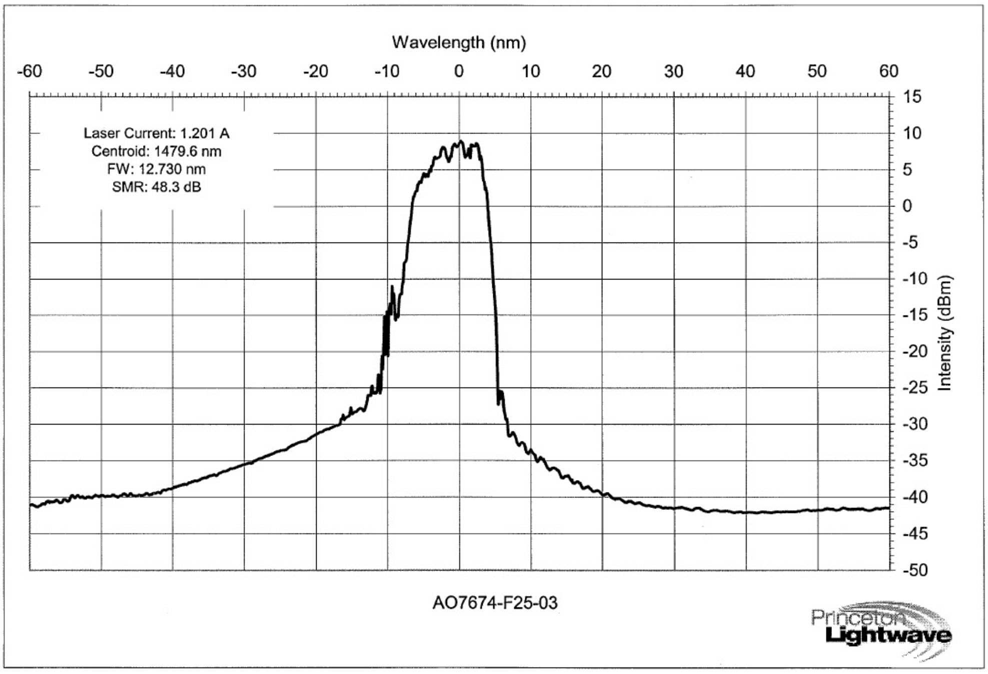

Figure C.4: Spectral properties of the first diode (4 of 4).

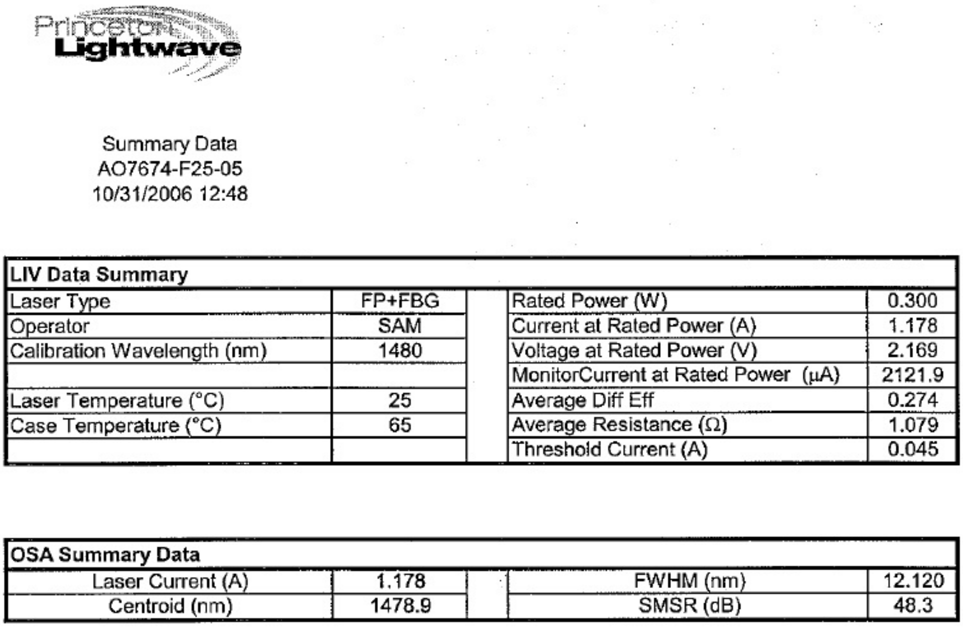

Summary Data
AO7674-F25-05
10/31/2006 12:48

LIV Data Summary

Laser Type	FP+FBG	Rated Power (W)	0.300
Operator	SAM	Current at Rated Power (A)	1.178
Calibration Wavelength (nm)	1480	Voltage at Rated Power (V)	2.169
		MonitorCurrent at Rated Power (µA)	2121.9
Laser Temperature (°C)	25	Average Diff Eff	0.274
Case Temperature (°C)	65	Average Resistance (Ω)	1.079
		Threshold Current (A)	0.045

OSA Summary Data

Laser Current (A)	1.178	FWHM (nm)	12.120
Centroid (nm)	1478.9	SMSR (dB)	48.3

Figure C.5: Specifications of the second laser diode (1 of 4).

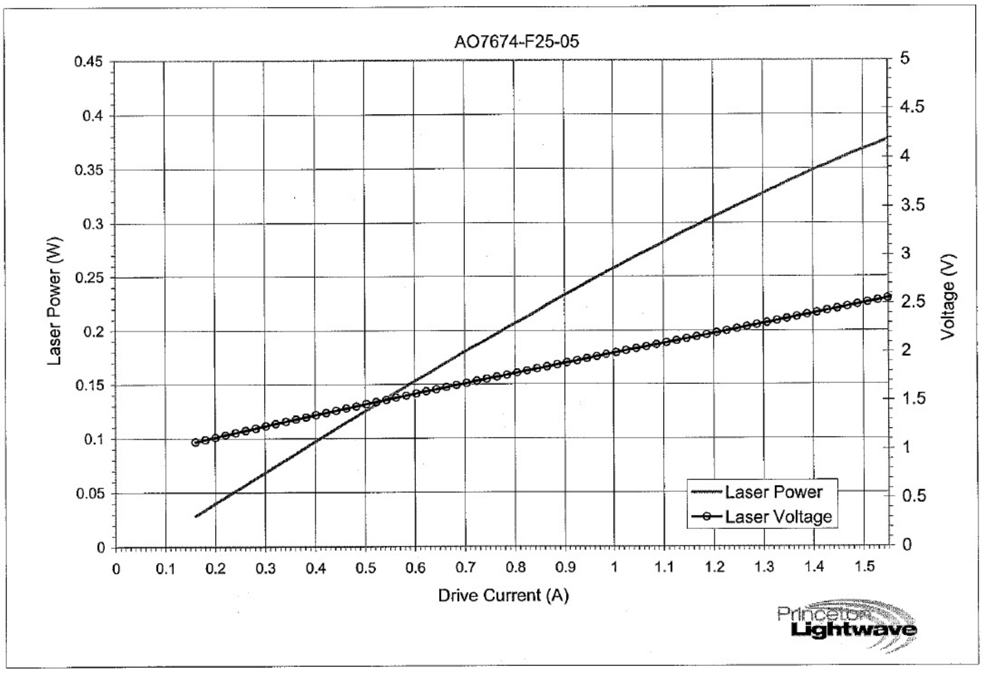

Figure C.6: Performance of the second diode (2 of 4).

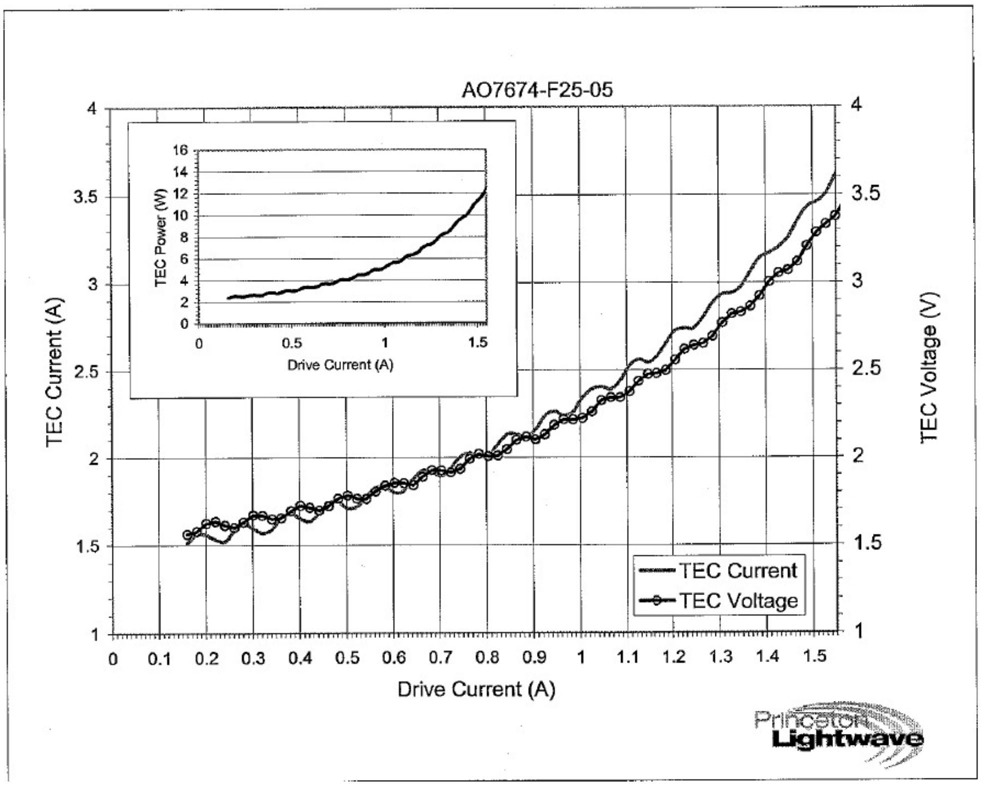

Figure C.7: Cooling characteristics of the second diode (3 of 4).

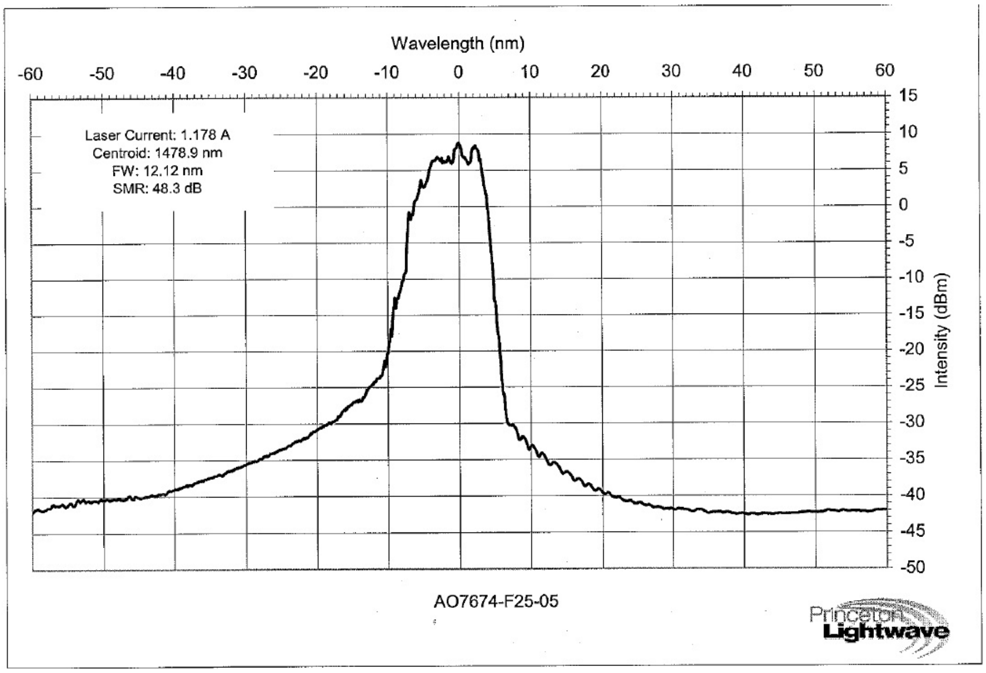

Figure C.8: Spectral properties of the second diode (4 of 4).

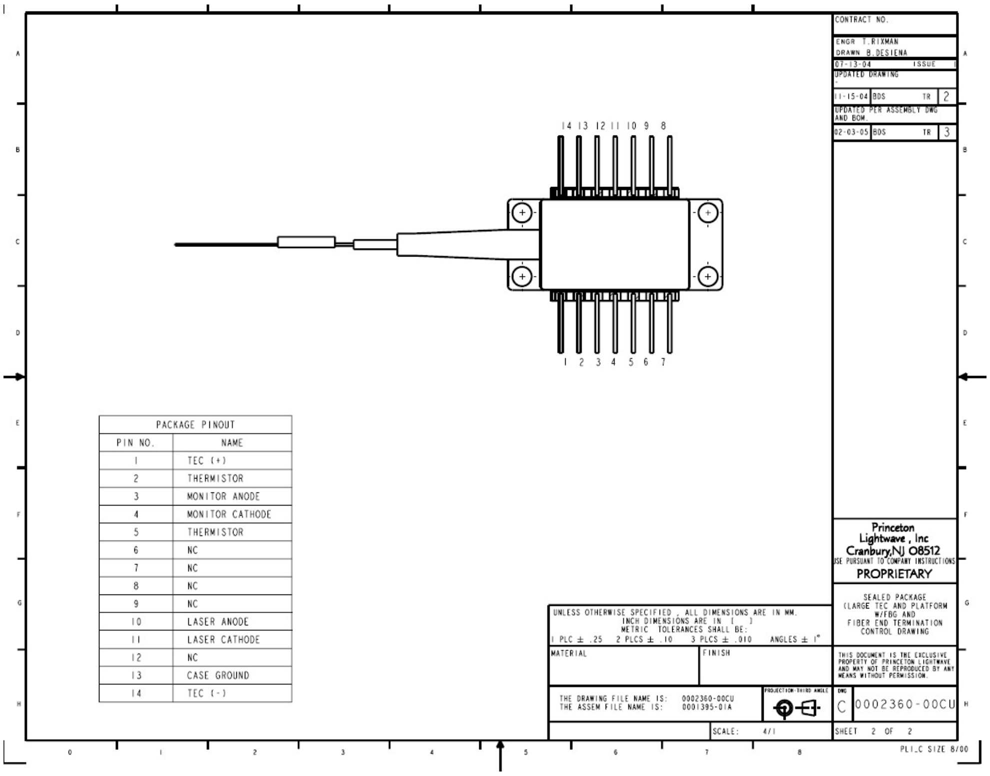

PACKAGE PINOUT	
PIN NO.	NAME
1	TEC (+)
2	THERMISTOR
3	MONITOR ANODE
4	MONITOR CATHODE
5	THERMISTOR
6	NC
7	NC
8	NC
9	NC
10	LASER ANODE
11	LASER CATHODE
12	NC
13	CASE GROUND
14	TEC (-)

Figure C.9: Specifications of the diodes.

D Beam quality analysis in Matlab

This appendix contains the Matlab code used to calculate the beam quality of the lasers described in this thesis.

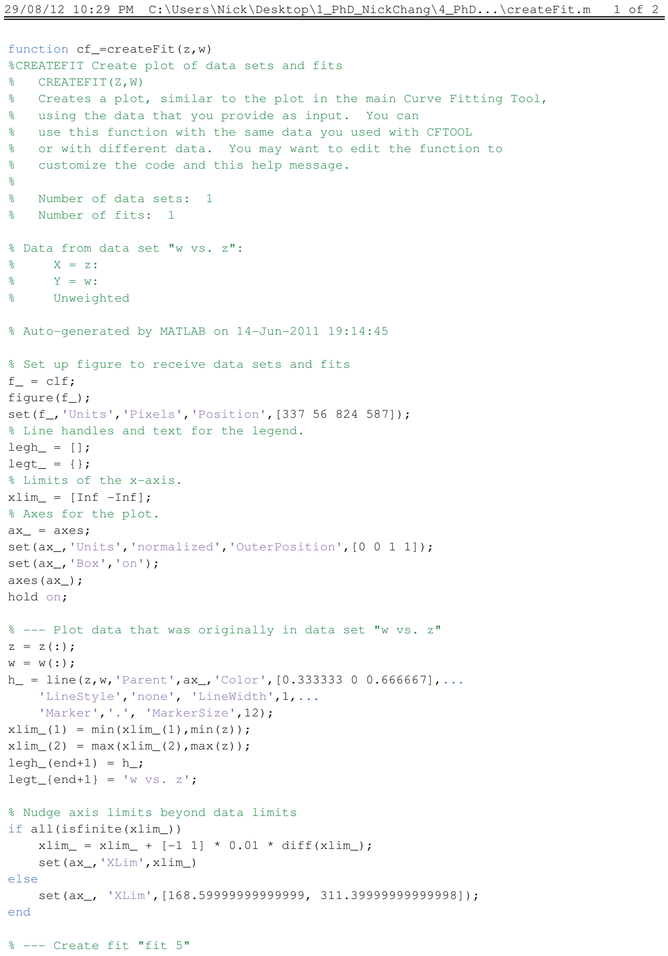

29/08/12 10:29 PM C:\Users\Nick\Desktop\1_PhD_NickChang\4_PhD...\createFit.m   1 of 2

```
function cf_=createFit(z,w)
%CREATEFIT Create plot of data sets and fits
%   CREATEFIT(Z,W)
%   Creates a plot, similar to the plot in the main Curve Fitting Tool,
%   using the data that you provide as input.  You can
%   use this function with the same data you used with CFTOOL
%   or with different data.  You may want to edit the function to
%   customize the code and this help message.
%
%   Number of data sets:  1
%   Number of fits:  1

% Data from data set "w vs. z":
%     X = z:
%     Y = w:
%     Unweighted

% Auto-generated by MATLAB on 14-Jun-2011 19:14:45

% Set up figure to receive data sets and fits
f_ = clf;
figure(f_);
set(f_,'Units','Pixels','Position',[337 56 824 587]);
% Line handles and text for the legend.
legh_ = [];
legt_ = {};
% Limits of the x-axis.
xlim_ = [Inf -Inf];
% Axes for the plot.
ax_ = axes;
set(ax_,'Units','normalized','OuterPosition',[0 0 1 1]);
set(ax_,'Box','on');
axes(ax_);
hold on;

% --- Plot data that was originally in data set "w vs. z"
z = z(:);
w = w(:);
h_ = line(z,w,'Parent',ax_,'Color',[0.333333 0 0.666667],...
    'LineStyle','none', 'LineWidth',1,...
    'Marker','.', 'MarkerSize',12);
xlim_(1) = min(xlim_(1),min(z));
xlim_(2) = max(xlim_(2),max(z));
legh_(end+1) = h_;
legt_{end+1} = 'w vs. z';

% Nudge axis limits beyond data limits
if all(isfinite(xlim_))
    xlim_ = xlim_ + [-1 1] * 0.01 * diff(xlim_);
    set(ax_,'XLim',xlim_)
else
    set(ax_, 'XLim',[168.59999999999999, 311.39999999999998]);
end

% --- Create fit "fit 5"
```

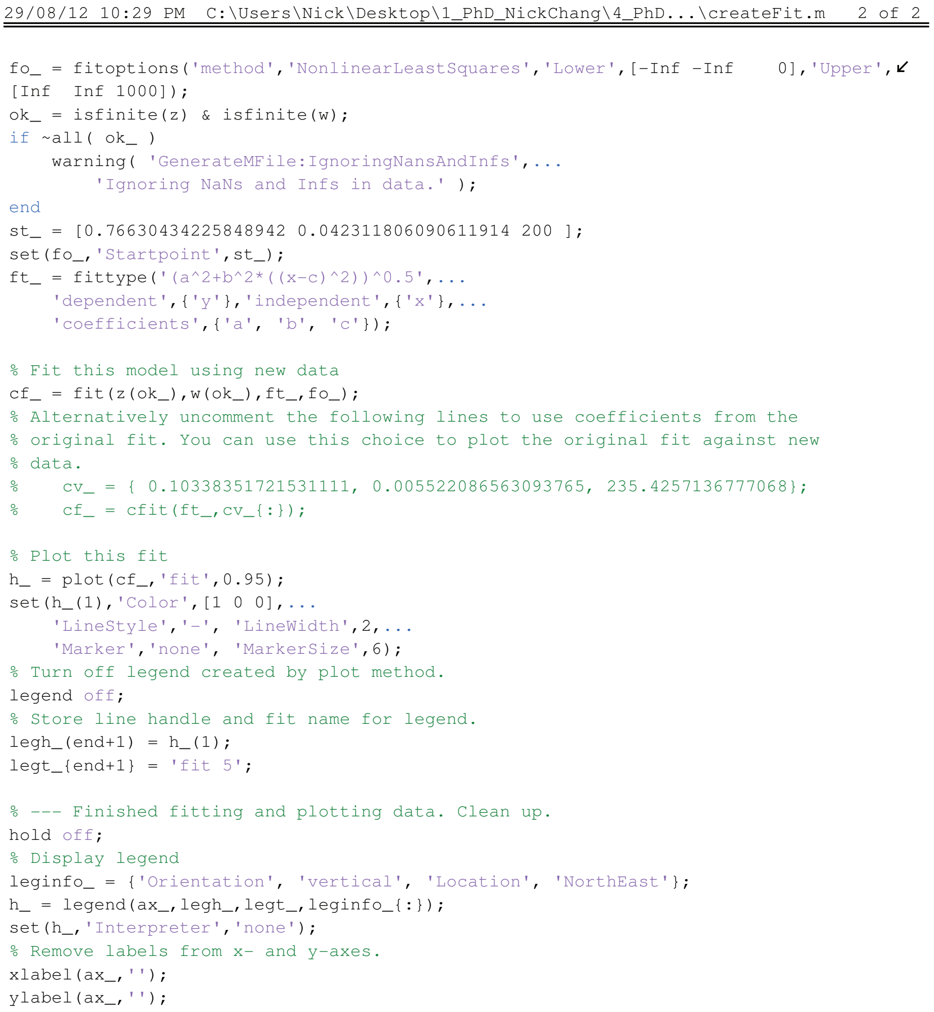

29/08/12 10:29 PM C:\Users\Nick\Desktop\1_PhD_NickChang\4_PhD...\createFit.m   2 of 2

```
fo_ = fitoptions('method','NonlinearLeastSquares','Lower',[-Inf -Inf    0],'Upper',↙
[Inf  Inf 1000]);
ok_ = isfinite(z) & isfinite(w);
if ~all( ok_ )
    warning( 'GenerateMFile:IgnoringNansAndInfs',...
        'Ignoring NaNs and Infs in data.' );
end
st_ = [0.76630434225848942 0.042311806090611914 200 ];
set(fo_,'Startpoint',st_);
ft_ = fittype('(a^2+b^2*((x-c)^2))^0.5',...
    'dependent',{'y'},'independent',{'x'},...
    'coefficients',{'a', 'b', 'c'});

% Fit this model using new data
cf_ = fit(z(ok_),w(ok_),ft_,fo_);
% Alternatively uncomment the following lines to use coefficients from the
% original fit. You can use this choice to plot the original fit against new
% data.
%    cv_ = { 0.10338351721531111, 0.005522086563093765, 235.4257136777068};
%    cf_ = cfit(ft_,cv_{:});

% Plot this fit
h_ = plot(cf_,'fit',0.95);
set(h_(1),'Color',[1 0 0],...
    'LineStyle','-', 'LineWidth',2,...
    'Marker','none', 'MarkerSize',6);
% Turn off legend created by plot method.
legend off;
% Store line handle and fit name for legend.
legh_(end+1) = h_(1);
legt_{end+1} = 'fit 5';

% --- Finished fitting and plotting data. Clean up.
hold off;
% Display legend
leginfo_ = {'Orientation', 'vertical', 'Location', 'NorthEast'};
h_ = legend(ax_,legh_,legt_,leginfo_{:});
set(h_,'Interpreter','none');
% Remove labels from x- and y-axes.
xlabel(ax_,'');
ylabel(ax_,'');
```

```
clear all;
close all;
%Result obtain on 03July/2011 using a 23cm resonator at 31W output power
zy=[100 110 120 130 140 150 155 160 165 170 175 180 185 190 200 210 220 240]; %↙
distance in mm
zx=[100 120 130 135 140 145 150 155 160 165 170 175 185 195 205]
x=[0.335 0.25 0.2 0.185 0.17 0.16 0.15 0.145 0.15 0.155 0.17 0.195 0.245 0.305 0.345]

y=[0.49 0.42 0.355 0.27 0.21 0.175 0.145 0.135 0.135 0.14 0.155 0.17 0.195 0.225 0.28↙
0.34 0.38 0.555]; %measured diameter

wx=x; %measured diameter
wy=y;

dis =0; %distance correction (rough estimate)
%z=z+dis;
wx=wx.*1.561./2; %beam diameter conversion. ==> and halfed to get radius
wy=wy.*1.561./2;
wavelength = 1645e-6;%wavelength in mm.

ix=1;
iy=3;
ax=0;
ay=0;

figure(1)
z=zx;
plot(z,wx,'o','MarkerSize',6)
res = createFit(z(ix:(length(z)-ax)),wx(ix:(length(wx))-ax)) %gives structure data↙
after the fitting
a1=res.a;
b1=res.b;
msq=(a1*b1*pi)/(wavelength)
p=legend('Exp. data',['M^2=',num2str(msq),],'Location','NorthEast');set(p,'FontSize',↙
20,'FontName','Arial');
p1=title('X-axis M^2');set(p1,'FontSize',20,'FontName','Arial');
p2=xlabel('Distance (mm)');set(p2,'FontSize',20,'FontName','Arial');
p3=ylabel('Beam Waist radius (mm)');set(p3,'FontSize',20,'FontName','Arial');
h=gca; % returns handle to current axis in the current figure.
get(h,'FontSize') % displays the default Font size
set(h,'FontSize',18) % sets the font size of axis values to 12

figure(2)
z=zy;
plot(z,wy,'o','MarkerSize',6)

res = createFit(z(iy:(length(z)-ay)),wy(iy:(length(wy)-ay))) %gives structure data↙
after the fitting
a1=res.a;
b1=res.b;
msq=(a1*b1*pi)/(wavelength)
p=legend('Exp. data',['M^2=',num2str(msq),],'Location','NorthEast');set(p,'FontSize',↙
20,'FontName','Arial');
p1=title('Y-axis M^2');set(p1,'FontSize',20,'FontName','Arial');
p2=xlabel('Distance (mm)');set(p2,'FontSize',20,'FontName','Arial');
```

E High power laser head schematics

This appendix contains the schematics, designed using 'Solidworks', sent to EAS Toolcraft Pty. LTD. for the manufacture of the laser head described in this thesis.

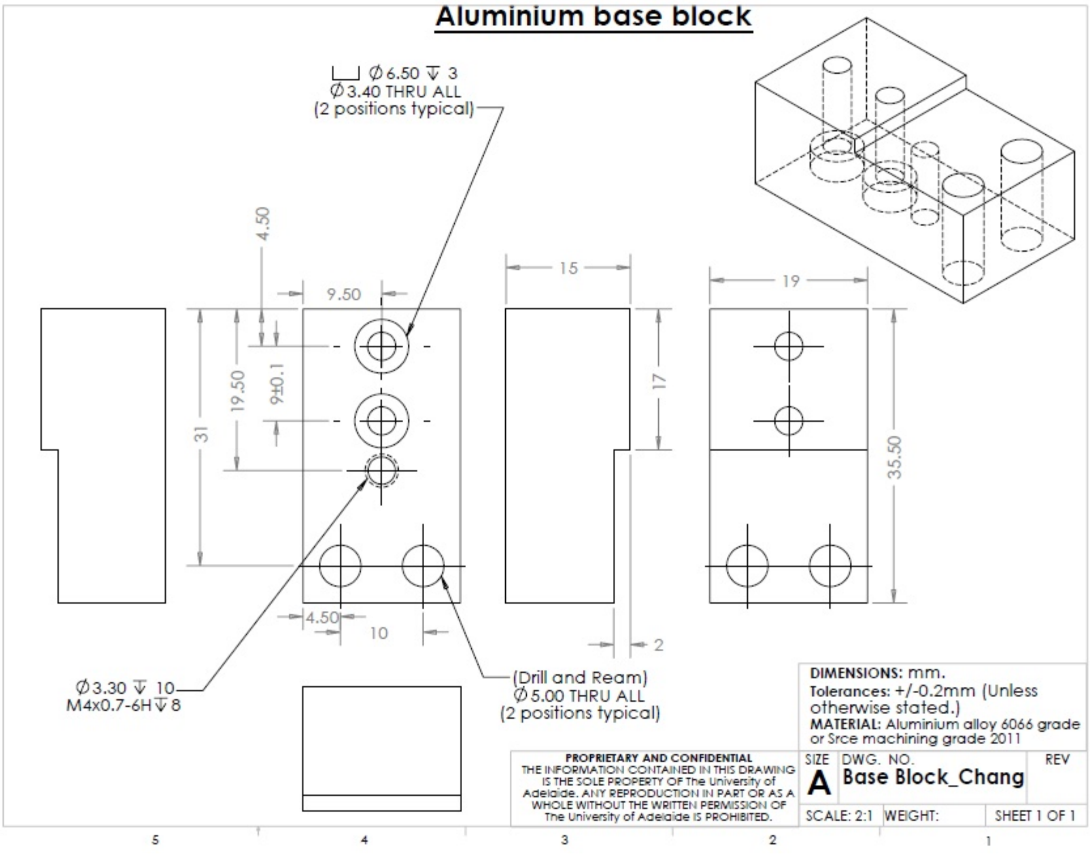

Figure E.1: The schematic of the base block of the laser head.

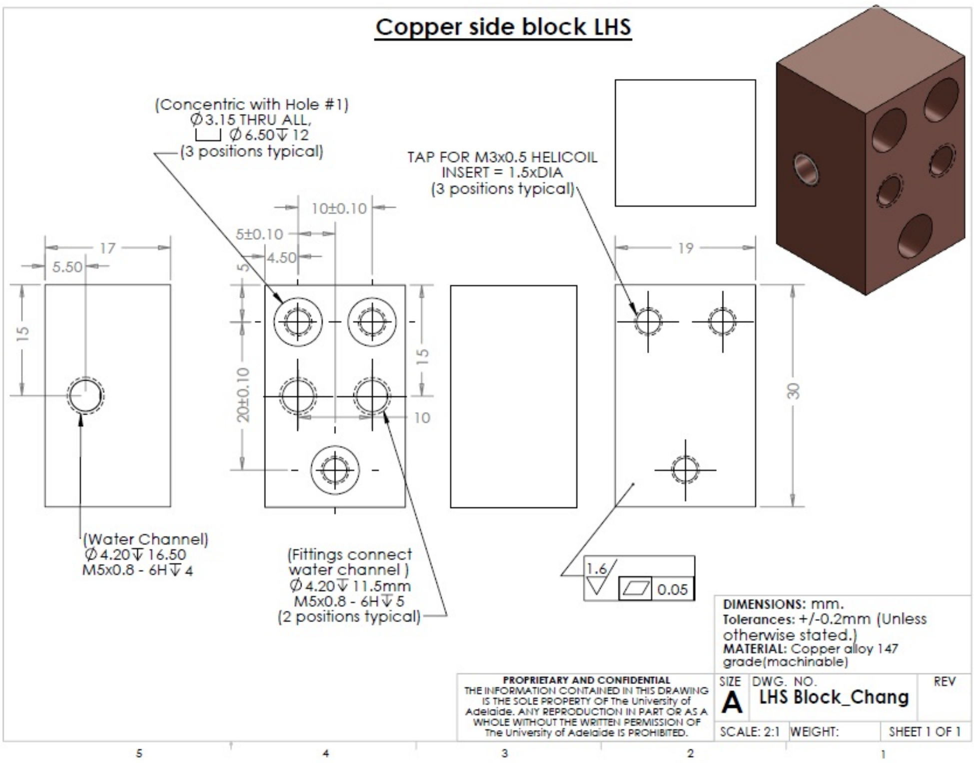

Figure E.2: The schematic of the left block of the laser head.

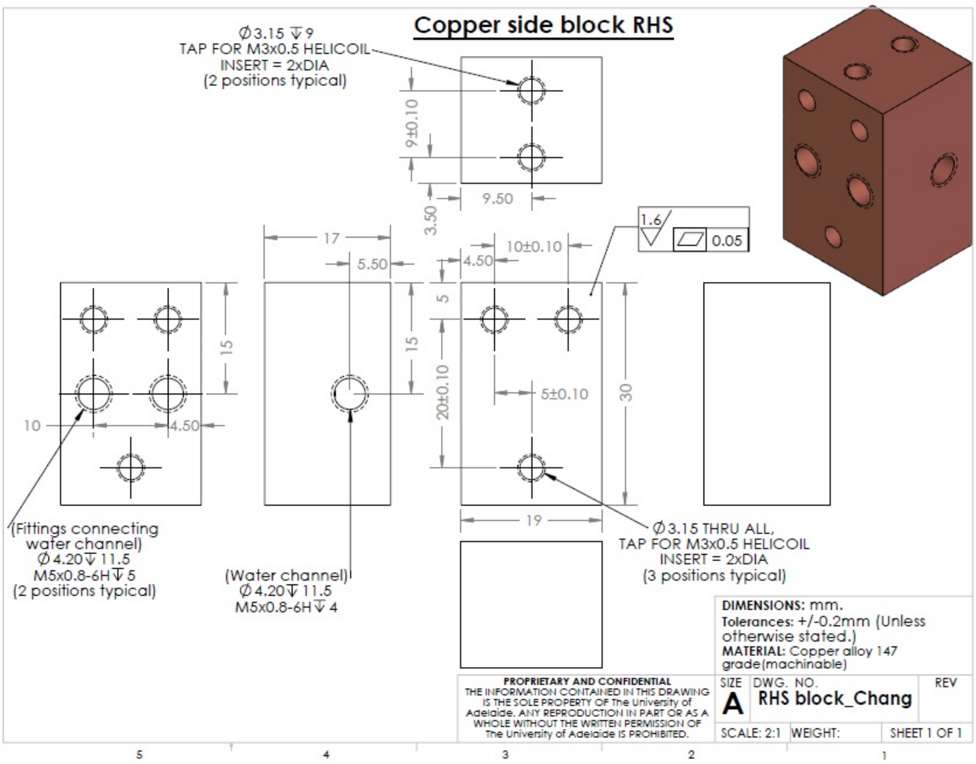

Figure E.3: The schematic of the right block of the laser head.

F Broadband pump diode specifications

The custom 40 W, actively cooled laser diode (E7B-1470-40C-VS1.12) was purchased from DILAS Inc. (Germany). The specifications of the laser diodes are shown in Figure F.1.

Figure F.1: Specifications of the DILAS laser diode.

G CPFS Er:YAG slab design

This appendix contains the design and schematic sent to BAE Systems Australia Ltd. (Holden Hill, South Australia, Australia) for the manufacture of the CPFS slab.

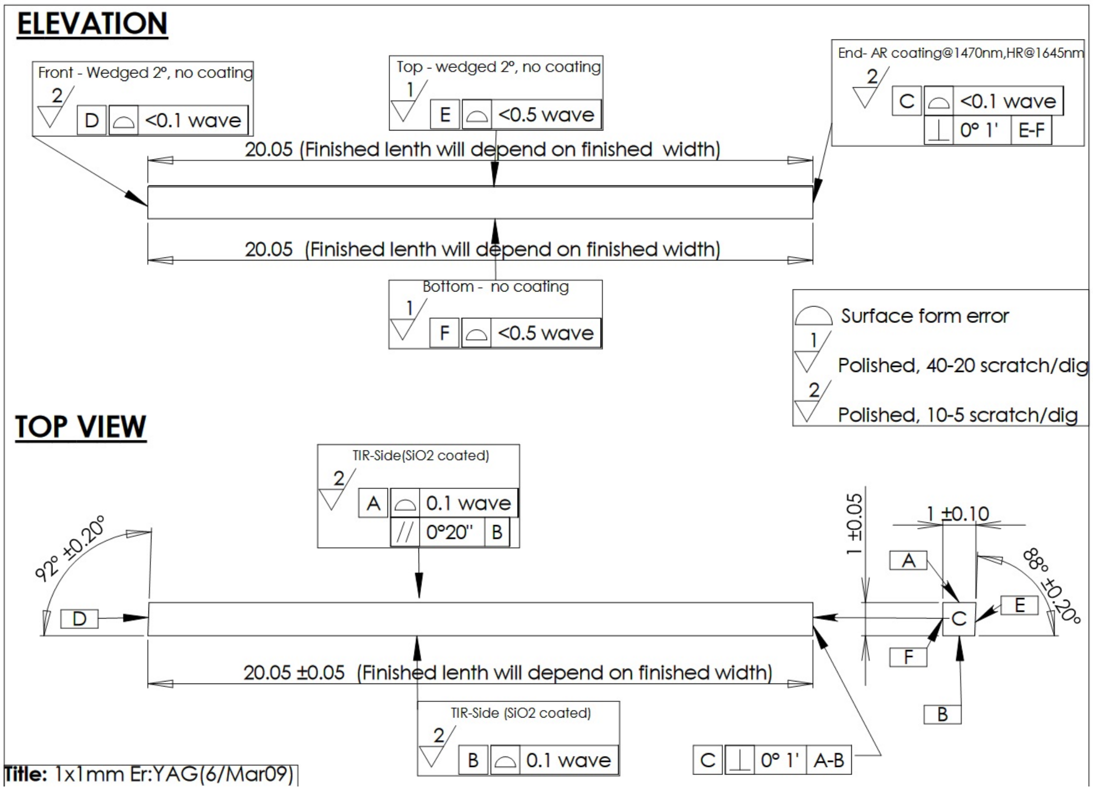

Figure G.1: The schematic of the CPFS Er:YAG slab.

Er:YAG slab design

The University of Adelaide, Department of Physics,
Optics group, Nick Chang

Material:

- 0.25% doped Er:YAG – Supplied by client as a block

Quantiy:

- Three of "1mm x 1mm x 20.05mm" slab. (11 bounces each side)
- Three of "1.5mm x 1.5mm x 19.12mm" slab. (7 bounces each side)
- 6 slabs in total

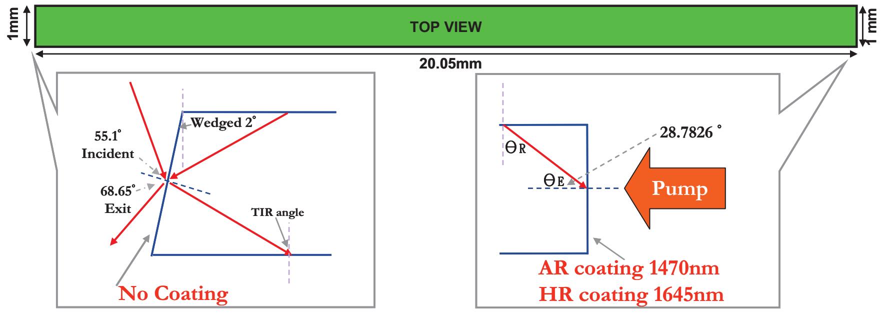

Manufacture requirements:

- Slab length will be specified after measurement of finished width.
- All corners sharp no chips.

Coatings:

- Sides A and B, IBS silicon dioxide, thickness 3.5 μm
- End-face C,
    - Rx > 99.5% @ 1645nm, π Polarization, at 28.8° incident angle (HR@1645nm)
    - Min Rx @ 1470nm (AR@1470nm)

Laser operating configuration:

- Zigzag optical path between total internal reflection faces, sides A and B
- TEM00 pulses (5mJ, 100ns /pulse) operation from 40W pump power.
- Pumping through end-face C.
- Face D:
    - Laser incident angle = 55.1 degrees.
    - Laser exit angle = 68.65 degrees.

NOTE:

- If any specification is problematic or any queries, please contact:
    - Nick Chang, Ph: 08-83033041, Mob: 0433767625 or Email: nick.chang@adelaide.edu.au
    - A/Prof. Peter Veitch, Ph: 08-83035040, or Email: peter.veitch@adelaide.edu.au

Er:YAG slab design Summary

Requirments:

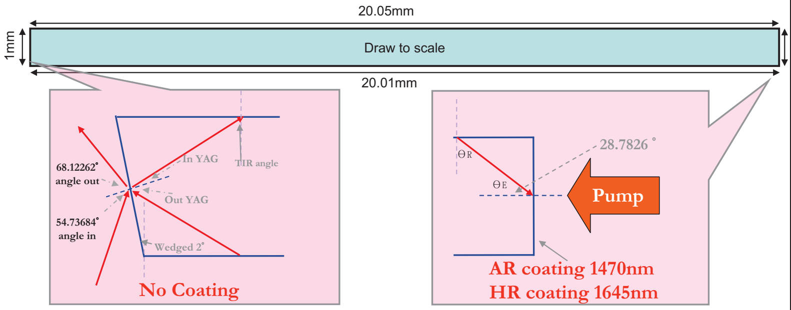

TIR End: (sin-1[n_{air} /n_{YAG}]) Critical angle = 33.329 ➔ θ_E >33.5 for TIR (➔HR coating)

TIR Side: (sin-1[n_{SiO2} /n_{YAG}]) Critical angle = 51.3 ➔ > θ_R > 51.5

Choose the right incident angle vs. exit angle.

If laser incidents at the Brewster angle, the exit angle of the laser will be too big. We have to narrow the incident angle to make the exit angle smaller, hence maximize laser transmission for both angles .

- The End-Angle (*θ* E) is fixed so the ‘Incident Angle’ and ‘Exit Angle’ are evenly separated along the Brewster angle.
- Slab length will be determined upon knowing the width of the width

1mm x 1mm slab (11 TIR bounces)

    - Angle-End = 28.78°
    - Angle in = 55.0877° (transmission 99.41%)
    - Angle out = 68.6496° (transmission 98.33%)
    - Slab length = 20.0255 mm (~20.03mm)
- The width changes the slab length up to 1mm, thus the width should be cut first so that the length can be decided.
- Errors involved in slab length cutting:
    - If length is off by +- 0.05 mm then, Angle_end will be changed by +- 0.06 deg to ensure proper TIR angle in the slab.

Parallelism tolerance of the TIR faces:

The parallelism tolerance (10 seconds) is evaluated in two stages.

- 1st order effect. (Assuming the distances for each TIR bounce are the same, but the angles gradually change after each bounce.)
    - Length “decreases” due to angle change each time:

  - ie. 2nd bounce = 28.78.277°, 4th bounce = 28.7855°….
    1. length shorten = D2[0.5/tan(ang)]x2 = ….. Overall offset is -0.005~0.01mm
- 2nd order effect. (Vertical offset due to different TIR positions.)
  - + 0.01~0.02mm offset (most)
- Assuming total offset is 0.02mm which is 2%(or 4 %) towards the overall width.
  - Loss can be very small because 0.02mm is the wing of the Gaussian waveform.
  - The parallelism of the slab was thus decided to be 20” arcseconds.

Angle tolerance for the corners of the end face (1 arcminute)

- 1 Acrminute = 0.01666°. For length 22.85mm, overall change in vertical height due to 0.01666° = 0.0066mm (which is 0.6% of 1mm)

1.5mm x 1.5mm slab (7 TIR bounces)

  - Angle-End = 28.78°
  - Angle in = 55.0877° (transmission=99.41%)
  - Angle out = 68.6496° (transmission=98.33%)
  - Slab length = 19.1153 mm (~19.12 mm)
- Slab width has smaller effect on slab length than that of the 1x1mm slab. To be safe, the slab length will be determined after the width has been measured.
- Tolerance on the length of the slab
  - If the length is off by +- 0.05 mm, Angle_end will be affected by +- 0.06° to ensure correct TIR in the slab.

Parallelism tolerance of the TIR faces:

The parallelism tolerance (10 seconds) is evaluated in two stages.

- 1st order effect. (Assuming the distances for each TIR bounce are the same, but the angles gradually change after each bounce.)
  - Length “decreases” due to angle change each time:
  - ie. 2nd bounce = 28.78.277, 4th bounce = 28.7855….
    1. length shorten = D2[0.5/tan(ang)]x2 = ….. Overall offset is -0.005~0.01mm
- 2nd order offset. (Vertical offset due to different TIR positions.)
  - + 0.01~0.02mm offset (most)
- A total offset of 0.02mm will be 1.5%(or 3 %) of the overall width.
  - Loss can be very small because 0.02mm is the wing of the Gaussian waveform.
  - A tolerance of 20 arcseconds is selected for the parallelism.

Angle tolerance for the corners of the end face (1 arcminute)

- 1 Acrminute = 0.01666°. For length ~22.85mm, overall change in vertical height due to 0.01666° = 0.0066mm (which is 0.4% of 1.5mm)

Er:YAG Slab requirements

1 mm x 1 mm slab:

- Width = 1mm +- 0.05mm
    - 0.05mm tolerance changes TIR length by about +-1mm
    - Length(gh) is critical as it fixes incident angle at particular length (11bounces)
    - The length will be specified depending on the width.

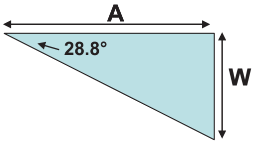

- Length
    - Tan(28.78 °)=W/A ……Angle on the End face.
        - A = 0.5/tan(28.78) =0.91mm
    - TIR_Length_(gh) = 22 x A = 20.03mm. (11bounces)

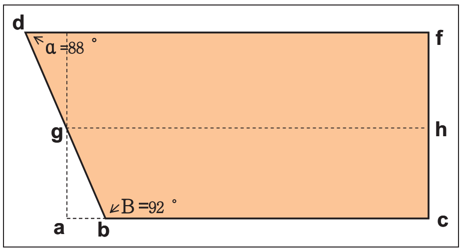

- For 11 bounces each side & Width = 1mm (ideal), Wedge = 2°, (gh) = 20.03mm
- TOP:
    - tan(α) =(hf)/(de)
    - (gh) = TIR_Length
    - Top: (df) = (de) + (gh) = (hf)/ tan(α) + (gh)= 0.01746+20.03=20.05 mm
- Bottom:
    - ab = de = 0.01746 mm
    - Bottom: (bc) = (gh) – (ab) = 20.03 – 0.01746 = 20.01mm

1.5 mm x 1.5 mm slab:

- Width = 1.5mm +- 0.05mm
    - 0.05mm tolerance changes TIR length by about +-1.28mm
    - Length(gh) is critical as it fixes incident angle at particular length (7 bounces)
    - The length will be specified depending on the width.

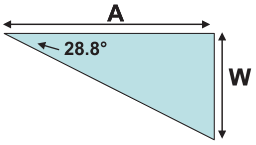

- Length
    - Tan(28.78°)=W/A

    - A = 0.75/tan(28.78) =1.3654 mm
- TIR_Length_(gh) = 14 x A = 19.1152 mm. (7 bounces)

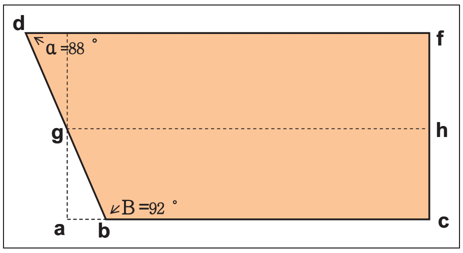

- For 8 bounces each side & Width = 1.5 mm (ideal), Wedge = 2°, (gh) = 19.1152mm
- TOP:
    - tan(α) =(ag)/(ab),➔ (ab)=(ag)/tan(α)
    - (gh) = TIR_Length
    - Top: (df) = (ab) + (gh) = (ag)/ tan(α) + (gh)= 0.02619+19.1152=19.14 mm
- Bottom:
    - ab = de = 0.02619 mm
    - Bottom: (bc) = (gh) – (ab) = 19.1152 – 0.02619 = 19.09mm

Bibliography

[1] C. Grund, "Coherent doppler lidar for boundary layer wind measurement employing a diode-pumped Tm,Lu:YAG laser," *Coherent Laser Radar, 1995 OSA Tech. Dig. Ser*, vol. 19, pp. 14–16, 1995.

[2] Z. Chen and E. Spooner, "Grid power quality with variable speed wind turbines," *Energy Conversion, IEEE Transactions on*, vol. 16, no. 2, pp. 148–154, 2001.

[3] W. Middleton and A. Spilhaus, *Meteorological instruments.* University of Toronto Press Toronto,, Canada, 1953, vol. 286.

[4] T. Maiman, "Stimulated optical radiation in ruby," 1960.

[5] F. McClung and R. Hellwarth, "Giant optical pulsations from ruby," *Applied Optics*, vol. 1, no. 101, pp. 103–105, 1962.

[6] M. Heintze, "Development and testing of an Er:Yb:glass coherent laser radar for wind field mapping." 2010.

[7] X. Sun and J. Abshire, "Signal to noise ratios of pulsed and sinewave modulated direct detection lidar for IPDA measurements," in *Quantum Electronics and Laser Science Conference.* Optical Society of America, 2011.

[8] U. Wandinger, A. Ansmann, and C. Weitkamp, "Atmospheric Raman depolarization-ratio measurements," *Applied optics*, vol. 33, no. 24, pp. 5671–5673, 1994.

[9] S. Mayor, S. Spuler, B. Morley, E. Loew *et al.*, "Polarization lidar at 1.54 μm and observations of plumes from aerosol generators," *Optical Engineering*, vol. 46, p. 096201, 2007.

[10] K. Kunkel, E. Eloranta, and S. Shipley, "Lidar observations of the convective boundary layer," *Journal of Applied Meteorology*, vol. 16, pp. 1306–1311, 1977.

[11] R. Schwiesow, S. Mayor, V. Glover, and D. Lenschow, “Intersection of a sloping aerosol layer observed by airborne lidar with a cloud-capped marine boundary layer,” *Journal of Applied Meteorology*, vol. 29, no. 11, pp. 1111–1119, 1990.

[12] J. Bilbro and W. Vaughan, “Wind Field Measurement in the Nonprecipitous Regions Surrounding Severe Storms by an Airborne Pulsed Doppler Lidar System.” *Bulletin of the American Meteorological Society*, vol. 59, pp. 1095–1101, 1978.

[13] F. Hall Jr, R. Huffaker, R. Hardesty, M. Jackson, T. Lawrence, M. Post, R. Richter, B. Weber *et al.*, “Wind measurement accuracy of the NOAA pulsed infrared Doppler lidar,” *Applied optics*, vol. 23, no. 15, pp. 2503–2506, 1984.

[14] M. Chanin, A. Garnier, A. Hauchecorne, and J. Porteneuve, “A Doppler lidar for measuring winds in the middle atmosphere,” *Geophysical research letters*, vol. 16, no. 11, pp. 1273–1276, 1989.

[15] J. Hawley, R. Targ, S. Henderson, C. Hale, M. Kavaya, and D. Moerder, “Coherent launch-site atmospheric wind sounder: theory and experiment,” *Applied optics*, vol. 32, no. 24, pp. 4557–4568, 1993.

[16] C. Grund, R. Banta, J. George, J. Howell, M. Post, R. Richter, and A. Weickmann, “High-resolution Doppler lidar for boundary layer and cloud research,” *Journal of Atmospheric and Oceanic Technology*, vol. 18, no. 3, pp. 376–393, 2001.

[17] G. Lombardi, J. Butman, D. Terry, and P. Garrett, “Multiple-pulse coherent laser radar waveform,” *12th Coherent Laser Radar Conference*, 2003.

[18] J. Bilbro, G. Fichtl, D. Fitzjarrald, M. Krause, and R. Lee, “Airborne Doppler lidar wind field measurements.” *Bulletin of the American Meteorological Society*, vol. 65, pp. 348–359, 1984.

[19] J. Bilbro, C. DiMarzio, D. Fitzjarrald, S. Johnson, and W. Jones, “Airborne Doppler lidar measurements,” *Applied optics*, vol. 25, no. 21, pp. 3952–3960, 1986.

[20] J. Rothermel, D. Cutten, R. Hardesty, R. Menzies, J. Howell, S. Johnson, D. Tratt, L. Olivier, and R. Banta, “The multi-center airborne coherent atmospheric wind sensor,” *Bulletin of the American Meteorological Society*, vol. 79, no. 4, pp. 581–599, 1998.

[21] J. Rothermel, L. Olivier, R. Banta, R. Hardesty, J. Howell, D. Cutten, S. Johnson, R. Menzies, and D. Tratt, "Remote sensing of multi-level wind fields with high-energy airborne scanning coherent Doppler lidar," *Optics Express*, vol. 2, no. 2, pp. 40–50, 1998.

[22] N. C. S. Division, *Mini- MOPA CO2 Doppler Lidar. NOAA www site, http://www.esrl.noaa.gov/csd/instruments/minimopa/accessed 04Aug2009.* NOAA Chemical Sciences Division, 2009.

[23] S. Mayor, D. Lenschow, R. Schwiesow, J. Mann, C. Frush, and M. Simon, "Validation of NCAR 10.6μm CO2 Doppler lidar radial velocity measurements and comparison with a 915MHz profiler," *Journal of Atmospheric and Oceanic Technology*, vol. 14, no. 5, pp. 1110–1126, 1997.

[24] C. Werner, P. Flamant, O. Reitebuch, F. Koepp, J. Streicher, S. Rahm, E. Nagel, M. Klier, H. Herrmann, C. Loth *et al.*, "Wind infrared Doppler lidar instrument," *Optical Engineering*, vol. 40, p. 115, 2001.

[25] P. Arbuckle *et al.*, "Airborne systems technology application to the windshear threat," 1996.

[26] C. Hale, P. Gatt, and S. Henderson, "Widely tunable 2μm single freqency lasers for Doppler and DIAL applications," *Proceedings of the 11th Coherent Laser Radar Conference*, pp. 168–171, 2001.

[27] S. Henderson, R. Huffaker, M. Kavaya, C. Hale, J. Magee, and L. Myers, "Pulsed coherent solid-state 1.06μm and 2.1μm laser radar systems for remote velocity measurement," in *Proceedings of SPIE*, vol. 1222, 1990, p. 118.

[28] S. Henderson and C. Hale, "Tunable single-longitudinal-mode diode laser pumped Tm:Ho:YAG laser," *Applied optics*, vol. 29, no. 12, pp. 1716–1718, 1990.

[29] S. Henderson, C. Hale, J. Magee, M. Kavaya, and A. Huffaker, "Eye-safe coherent laser radar system at 2.1μm using Tm,Ho:YAG lasers," *Optics letters*, vol. 16, no. 10, pp. 773–775, 1991.

[30] S. Henderson, P. Suni, C. Hale, S. Hannon, J. Magee, D. Bruns, and E. Yuen, "Coherent laser radar at 2 μm using solid-state lasers," *Geoscience and Remote Sensing, IEEE Transactions on*, vol. 31, no. 1, pp. 4–15, 1993.

[31] G. Koch, J. Beyon, B. Barnes, M. Petros, J. Yu, F. Amzajerdian, M. Kavaya, and U. Singh, “High-energy 2 μm Doppler lidar for wind measurements,” *Optical Engineering*, vol. 46, p. 116201, 2007.

[32] S. Hannon, “Wind resource assessment using long range pulsed Doppler lidar,” in *15th Coherent Laser Radar Conference*, vol. 22, 2009.

[33] M. Kavaya, U. Singh, G. Koch, J. Yu, B. Trieu, M. Petros, and P. Petzar, “Development of a Compact, Pulsed, 2-Micron, Coherent-Detection, Doppler Wind Lidar Transceiver; and Plans for Flights on NASA’s DC-8 and WB-57 Aircraft,” 2009.

[34] M. Kavaya, S. Henderson, J. Magee, C. Hale, and R. Huffaker, “Remote wind profiling with a solid-state Nd:YAG coherent lidar system,” *Optics letters*, vol. 14, no. 15, pp. 776–778, 1989.

[35] K. Chan and D. Killinger, “Short-pulse, coherent Doppler Nd:YAG lidar,” *Optical Engineering*, vol. 30, no. 01, pp. 49–54, 1991.

[36] *The Australian Standards AS/NZS IEC 60825.1 and AS/NZS IEC TR 60825.14*, 2011.

[37] *Absorption spectrum measured by Greg Quarles at the Naval Research Laboratory, Washington, D.C.*

[38] V. Gordienko, A. Koryabin, N. Kravtsov, and V. Firsov, “Wind Doppler lidar with 1.5 μm fiber laser,” *Laser Physics Letters*, vol. 5, no. 5, pp. 390–393, 2008.

[39] A. McGrath, J. Munch, G. Smith, and P. Veitch, “Injection-Seeded, Single-Frequency,Q-switched Er:Glass Laser for Remote Sensing,” *Applied optics*, vol. 37, no. 24, pp. 5706–5709, 1998.

[40] M. Heintze, N. Chang, F. Jeanneret, J. Munch, D. Ottaway, and P. Veitch, “Single-pulse measurement of wind velocities using an Er:Yb:glass coherent laser radar,” *Applied Optics*, vol. 50, no. 21, pp. 4017–4023, 2011.

[41] R. Stoneman, R. Hartman, E. Schneider, A. Malm, S. Vetorino, C. Garvin, J. Pelk, S. Hannon, and S. Henderson, “Eyesafe 1.6μm Er:YAG transmitters for coherent laser radar,” 2007.

[42] W. Bosenberg, A. Drobshoff, J. Alexander, L. Myers, and R. Byer, "93% pump depletion, 3.5W continuous-wave, singly resonant optical parametric oscillator," *Optics letters*, vol. 21, no. 17, pp. 1336–1338, 1996.

[43] A. Dolfi-Bouteyre, B. Augère, C. Besson, G. Canat, D. Fleury, T. Gaudo, D. Goular, L. Lombard, C. Planchat, M. Valla *et al.*, "1.5 μm all fiber pulsed lidar for wake vortex monitoring," in *CLEO*. Optical Society of America, 2008.

[44] G. Pearson, P. Roberts, J. Eacock, and M. Harris, "Analysis of the performance of a coherent pulsed fiber lidar for aerosol backscatter applications," *Applied optics*, vol. 41, no. 30, pp. 6442–6450, 2002.

[45] J. Cariou, L. Sauvage, S. Lolli, R. Parmentier, M. Boquet, and S. Loaec, "Planetary Boundary Layer dynamic measurements with new compact long range wind Lidar Windcube WLS70," in *Fourth Symposium on Lidar Atmospheric Applications, 89th American Meteorological Society Annual Meeting (Phoenix, AZ)*, 2009.

[46] K. Bozier, G. Pearson, and C. Collier, "Evaluation of a new autonomous Doppler lidar system during the Helsinki international testbed field campaign," in *Proc., Third Symposium on LIDAR Atmospheric Applications, New Orleans, LA., Amer. Meterolog. Soc*, 2007.

[47] J. Davis, F. Davies, C. Collier, and G. Pearson, "Doppler lidar measurements of boundary layer winds and sensible heat flux," in *IOP Conference Series: Earth and Environmental Science*, vol. 1. IOP Publishing, 2008, p. 012029.

[48] M. Webb, P. Moulton, J. Kasinski, R. Burnham, G. Loiacono, and R. Stolzenberger, "High-average-power KTiAsO4 optical parametric oscillator," *Optics letters*, vol. 23, no. 15, pp. 1161–1163, 1998.

[49] K. Asaka, T. Yanagisawa, and Y. Hirano, "1.5 μm coherent lidar using injection-seeded, LD pumped Er:Yb:glass laser," *Proceedings of the 10th Coherent Laser Radar Conference*, pp. 198–201, 1999.

[50] J. Richards and A. McInnes, "Versatile, efficient, diode-pumped miniature slab laser," *Optics letters*, vol. 20, no. 4, pp. 371–373, 1995.

[51] A. McInnes and J. Richards, "Thermal effects in a coplanar-pumped folded-zigzag slab laser," *Quantum Electronics, IEEE Journal of*, vol. 32, no. 7, pp. 1243–1252, 1996.

[52] J. Cariou, B. Augere, and M. Valla, “Laser source requirements for coherent lidars based on fiber technology,” *Comptes Rendus Physique*, vol. 7, no. 2, pp. 213–223, 2006.

[53] D. Anthon and T. Pier, “Diode-pumped erbium glass lasers,” in *Society of Photo-Optical Instrumentation Engineers (SPIE) Conference Series*, vol. 1627, 1992, pp. 8–12.

[54] A. Levoshkin and J. Montagne, “Efficient diode pumping for Q-switched Yb:Er:glass lasers,” *Applied Optics*, vol. 40, no. 18, pp. 3023–3032, 2001.

[55] S. Setzler, J. Konves, and E. Chicklis, “High-energy, resonantly diode-pumped, eyesafe erbium lasers,” *IEEE*, 2005.

[56] D. K. Killinger, “Phonon-assisted upconversion in 1.64 μm Er:YAG lasers,” *CLEO Tech Dig*, pp. 240–241, 1987.

[57] K. Spariosu and M. Birnbaum, “Room-temperature 1.644 μm Er:YAG lasers,” in *Advanced Solid State Lasers.* Optical Society of America, 1992.

[58] K. Spariosu and M. Birnbaum, “Intracavity 1.549-μm pumped 1.634-μm Er:YAG lasers at 300 K,” *Quantum Electronics, IEEE Journal of*, vol. 30, no. 4, pp. 1044–1049, 1994.

[59] S. Setzler, K. Snell, T. Pollak, P. Budni, Y. Young, and E. Chicklis, “5W repetitively Q-switched Er: LuAG laser resonantly pumped by an erbium fiber laser,” *Optics letters*, vol. 28, no. 19, pp. 1787–1789, 2003.

[60] Y. Young, S. Setzler, K. Snell, P. Budni, T. Pollak, and E. Chicklis, “Efficient 1645-nm Er:YAG laser,” *Optics letters*, vol. 29, no. 10, pp. 1075–1077, 2004.

[61] R. C. Stoneman, *Solid-state lasers and Applications*, A. Sennaroglu, Ed. CRC Press, 2006.

[62] R. Stoneman and A. Malm, “High-power Er:YAG laser for coherent laser radar,” in *CLEO.* Optical Society of America, 2004.

[63] D. Shen, J. Sahu, and W. Clarkson, “Ultra-efficient Er:YAG laser with 60 W output power at 1645 nm end-pumped by an Er-Yb co-doped fibre laser,” in *Lasers and Electro-Optics Europe, 2005. CLEO/Europe. 2005 Conference on.* IEEE, 2005, p. 30.

[64] D. Shen, J. Sahu, and W. Clarkson, “Highly efficient in-band pumped Er:YAG laser with 60 W of output at 1645 nm,” *Optics letters*, vol. 31, no. 6, pp. 754–756, 2006.

[65] P. Jander, J. Sahu, and W. Clarkson, “High-power Er:YAG laser at 1646 nm pumped by an Er, Yb fiber laser,” in *Proceedings of SPIE*, vol. 5620, 2004, p. 297.

[66] J. Kim, D. Shen, J. Sahu, and W. Clarkson, “High-power in-band pumped Er:YAG laser at 1617 nm,” *Opt. Express*, vol. 16, pp. 5807–5812, 2008.

[67] J. Kim, D. Shen, J. Sahu, and W. Clarkson, “Fiber-Laser-Pumped Er:YAG Lasers,” *Selected Topics in Quantum Electronics, IEEE Journal of*, vol. 15, no. 2, pp. 361 –371, march-april 2009.

[68] K. Spariosu, V. Leyva, R. Reeder, and M. Klotz, “Efficient Er:YAG laser operating at 1645 and 1617 nm,” *Quantum Electronics, IEEE Journal of*, vol. 42, no. 2, pp. 182–186, 2006.

[69] D. Chen, T. Rose, S. Beck, and M. Birnbaum, “High Performance 1645-nm Er:YAG Laser,” in *Advanced Solid-State Photonics.* Optical Society of America, 2008.

[70] D. Chen, M. Birnbaum, P. Belden, T. Rose, and S. Beck, “Multiwatt continuous-wave and Q-switched Er:YAG lasers at 1645 nm: performance issues,” *Optics letters*, vol. 34, no. 10, pp. 1501–1503, 2009.

[71] I. Moskalev, V. Fedorov, V. Gapontsev, D. Gapontsev, N. Platonov, and S. Mirov, “Highly efficient, narrow-linewidth, and single-frequency actively and passively Q-switched fiber-bulk hybrid Er:YAG lasers operating at 1645 nm,” *Optics Express*, vol. 16, no. 24, pp. 19 427–19 433, 2008.

[72] S. Setzler, M. Francis, Y. Young, J. Konves, E. Chicklis, B. Syst, and N. Nashua, “Resonantly pumped eyesafe erbium lasers,” *IEEE Journal of Selected Topics in Quantum Electronics*, vol. 11, no. 3, pp. 645–657, 2005.

[73] M. Eichhorn, “High-power resonantly diode-pumped CW Er3+:YAG laser,” *Applied Physics B: Lasers and Optics*, vol. 93, no. 4, pp. 773–778, 2008.

[74] D. Garbuzov, I. Kudryashov, and M. Dubinskii, “Efficiency and Threshold Analysis of Resonantly Diode-Laser-Pumped 1.6μm Er:YAG Laser,” in *Conference on Lasers and Electro-Optics.* Optical Society of America, 2005.

[75] D. Garbuzov, I. Kudryashov, and M. Dubinskii, “Resonantly diode laser pumped 1.6μm-erbium-doped yttrium aluminum garnet solid-state laser,” *Applied Physics Letters*, vol. 86, p. 131115, 2005.

[76] D. Garbuzov, I. Kudryashov, and M. Dubinskii, “110 W, 0.9J, pulsed power from resonantly diode-laser-pumped 1.6μm Er:YAG laser,” *Applied Physics Letters*, vol. 87, p. 121101, 2005.

[77] I. Kudryashov, D. Garbuzov, and M. Dubinskii, “Volume Bragg Grating improves characteristics of resonantly diode pumped Er:YAG 1.65-μm DPSSL,” in *Proc. of SPIE Vol*, vol. 6451, 2007, pp. 64 510P–1.

[78] I. Kudryashov, N. Ter-Gabrielyan, and M. Dubinskii, “Resonantly diode-pumped Er:YAG laser: 1470-nm versus 1530-nm CW pumping case,” in *Proceedings of SPIE*, vol. 7325, 2009, p. 732505.

[79] M. Eichhorn, “First investigations on an Er3+:YAG SSHCL,” *Applied Physics B: Lasers and Optics*, vol. 93, pp. 817–822, 2008.

[80] M. Eichhorn, “Thermal lens effects in an Er3+:YAG laser with crystalline fiber geometry,” *Applied Physics B: Lasers and Optics*, vol. 94, no. 3, pp. 451–457, 2009.

[81] W. Koechner, *Solid-state laser engineering.* Springer series in optical sciences, 1989.

[82] L. Landau and E. Lifshitz, *Quantum Mechanics.* Pergamon Press, 1977.

[83] S. Payne, L. Chase, L. Smith, W. Kway, and W. Krupke, “Infrared cross-section measurements for crystals doped with Er3+, Tm3+, and Ho3+,” *IEEE Journal of Quantum Electronics*, vol. 28, pp. 2619–2630, 1992.

[84] N. Chang, D. Hosken, J. Munch, D. Ottaway, and P. Veitch, “Stable, Single Frequency Er:YAG Lasers at 1.6μm,” *Quantum Electronics, IEEE Journal of*, vol. 46, no. 7, pp. 1039–1042, 2010.

[85] N. Chang, N. Simakov, D. Hosken, J. Munch, D. Ottaway, and P. Veitch, “Resonantly diode-pumped continuous-wave and Q-switched Er:YAG laser at 1645 nm.” *Optics Express*, vol. 18, no. 13, pp. 13 673–13 678, 2010.

[86] J. Kim, J. Mackenzie, and W. Clarkson, “Influence of energy-transfer-upconversion on threshold pump power in quasi-three-level solid-state lasers,” *Opt. Express*, vol. 17, pp. 11 935–11 943, 2009.

[87] J. White, M. Dubinskii, L. Merkle, I. Kudryashov, and D. Garbuzov, “Resonant pumping and upconversion in 1.6 μm Er 3+ lasers,” *JOSA B*, vol. 24, no. 9, pp. 2454–2460, 2007.

[88] N. Barnes, B. Walsh, F. Amzajerdian, D. Reichle, G. Busch, and W. Carrion, “Upconversion measurements in Er:YAG; comparison with 1.6 μm laser performance,” *Optical Materials Express*, vol. 1, no. 4, pp. 678–685, 2011.

[89] J. Kim, J. Sahu, and W. Clarkson, “Impact of energy-transfer-upconversion on the performance of hybrid Er:YAG lasers.” Society of Photo-Optical Instrumentation Engineers, 2008.

[90] P. Peterson, A. Gavrielides, and P. Sharma, “CW theory of a laser diode-pumped two-manifold solid state laser,” *Optics communications*, vol. 109, no. 3-4, pp. 282–287, 1994.

[91] T. Fan and R. Byer, “Modeling and cw operation of a quasi-three-level 946 nm Nd:YAG laser,” *Quantum Electronics, IEEE Journal of*, vol. 23, no. 5, pp. 605–612, 1987.

[92] W. Risk, “Modeling of longitudinally pumped solid-state lasers exhibiting reabsorption losses,” *JOSA B*, vol. 5, no. 7, pp. 1412–1423, 1988.

[93] R. Beach, “CW Theory of quasi-three level end-pumped laser oscillators,” *Optics Communications*, vol. 123, no. 1-3, pp. 385–393, 1996.

[94] A. E. Sigeman, *Lasers*. Sausalito, California: University Science Books, 1986.

[95] P. Lacovara, H. Choi, C. Wang, R. Aggarwal, and T. Fan, “Room-temperature diode-pumped Yb:YAG laser,” *Optics letters*, vol. 16, no. 14, pp. 1089–1091, 1991.

[96] F. Auge, F. Druon, F. Balembois, P. Georges, A. Brun, F. Mougel *et al.*, “Theoretical and experimental investigations of a diode-pumped quasi-three-level laser: The Yb3+-doped Ca4GdO (BO3) 3 (Yb: GdCOB) laser,” *IEEE journal of quantum electronics*, vol. 36, no. 5, pp. 598–606, 2000.

[97] T. Taira, W. Tulloch, R. Byer *et al.*, “Modeling of quasi-three-level lasers and operation of cw Yb:YAG lasers,” *Applied optics*, vol. 36, no. 9, pp. 1867–1874, 1997.

[98] Ozoptics, “Receptacle style fiber collimators and focusers., http://www.ozoptics.com/allnew-pdf/dts0094.pdf,” 2005.

[99] S. J. C. . U. Sciopt Enterprises, P.O. Box 20637, *Paraxia - Resonator and Optics Programs, 2.0 ed., 1992.*

[100] W. Koechner, *Solid-state laser engineering*, 5th ed. Berlin: Springer-Verlag, 1999.

[101] D. J. Hosken, *Deployable Stable Lasers for Gravitational Wave Interferometers.* The University of Adelaide, School of Chemistry and Physics, 2008.

[102] W. Koechner, *Solid-state laser engineering.* Springer series in optical sciences, 1989.

[103] P. W. Milonni and J. H. Eberly, *Lasers.* USA: John Wiley Sons, Inc., 1988.

[104] W. Leeb, “Tunability characteristics of waveguide CO 2 lasers with internal etalons,” *Applied Optics*, vol. 14, no. 7, pp. 1706–1709, 1975.

[105] P. photonics corporation, “Basic physics and design of etalons,” pp. 1–5, 2003.

[106] T. Koonen, *Fabry-Perot Interferometer Filters*, ser. Springer Series in Optical Sciences, H. Venghaus, Ed. Springer Berlin/Heidelberg, 2006, vol. 123.

[107] Thorlabs, *Fabry-Perot Tutorial "Scanning Fabry-Perot Interferometers*, Thorlabs, 2011.

[108] T. Okoshi, K. Kikuchi, and A. Nakayama, “Novel method for high resolution measurement of laser output spectrum,” *Electronics Letters*, vol. 16, p. 630, 1980.

[109] D. Baney and W. V. Sorin, *"High frequency optical frequency analysis," in Fiber Optic Test andMeasurement,*, ser. ch. 5, E. D. Derickson, Ed. Upper Saddle River, NJ: Prentice Hall„ 1997.

[110] J. D. Mansell, J. Hennawi, E. K. gustafson, M. M. Fejer, R. L. Byer, D. Clubley, S. Yoshida, and D. H. Reitze, “Evalating the effect of transmissive optic

thermal lensing on laser beam quality with a shack-hartmann wave-front sensor," *Appl. Opt.*, vol. 40, pp. 366–374, 2001.

[111] P. Webels and C. Fallnich, "Highly sensitive beam quality measurements on large-mode-area fiber amplifiers," *1*, vol. 11, pp. 3346–3351, 2003.

[112] ISO11146, *ISO 11146-1:2005(E), "Lasers and laser-related equipment - Test methods for laser beam widths, divergence angles and beam propagation ratios - Part 1: Stigmatic and simple astigmatic beams."*.

[113] P. B. Chapple, "Beam waist and M2 measurement using a finite slit," *Opt. Eng.*, vol. 33, pp. 2461–2466, 1994.

[114] N. Hodgson and H. Weber, *Laser Resonators and Beam Propagation: Fundamentals, Advanced Concepts and Applications*, 2nd ed. Berline: Springer series in optical sciences, 2005.

[115] E. Siegman, *How to (Maybe) Measure Laser Beam Quality*, Tutorial presentation at the Optical Society of America Annual Meeting, Long Beach, California, October 1997.

[116] D. S. S. Corp., "Solidworks CAD program runs on Microsoft Windows and is being developed by Dassault Systemes SolidWorks Corp., a subsidiary of Dassault Systemes, S. A. (Velizy, Fracne)." 2008.

[117] P. Lightwave, "PLM-170 specs: High Power Multimode Laser Arrays High Power Multimode Laser Arrays."

[118] R. Sundar, K. Ranganathan, and A. Nath, "Performance studies of diode-side-pumped CW Nd:YAG laser in copper coated optical pump cavity," *Optics & Laser Technology*, vol. 39, no. 7, pp. 1426–1431, 2007.

[119] R. W. Hellwarth, "Control of fluorescent pulsations." *In Advances in Quantum Electronics, J. r. Singer, ed. New York: Columbia University Press*, p. 334, 1961.

[120] R. W. Hellwarth, "Q modulation of lasers," *In Lasers, A. K. Levine, ed. New York: Marcel Dekker, Inc.*, vol. 1, p. 253, 1966.

[121] Raicol Crystals Ltd., "http://www.raicol.com," 2010.

[122] M. Skorczakowski, P. Nyga, A. Zajac, and W. Zendzian, "2.94 μm Er:YAG laser Q-switched with RTP Pockels cell," p. 69.

[123] N. Barnes and H. NASA, "Solid-state lasers from an efficiency perspective," *IEEE Journal of Selected Topics in Quantum Electronics*, vol. 13, no. 3, pp. 435–447, 2007.

[124] I. Kudryashov and A. Katsnelson, "1645 nm Q-switched Er:YAG laser with in-band diode pumping," in *Proc. of SPIE Vol*, vol. 7686, 2010, pp. 76 860B–1.

[125] M. Eichhorn, "Quasi-three-level solid-state lasers in the near and mid infrared based on trivalent rare earth ions," *Applied Physics B: Lasers and Optics*, vol. 93, no. 2, pp. 269–316, 2008.

[126] S. Georgescu and V. Lupei, "Q-switch regime of 3-μm Er:YAG lasers," *Quantum Electronics, IEEE Journal of*, vol. 34, no. 6, pp. 1031–1040, 1998.

[127] M. Nemec, W. Zendzian, H. Jelínková, J. Jabczynski, J. Sulc, L. Gorajek, and J. Kwiatkowski, "Q-Switched Er:YAG Lasers Resonantly Pumped by Erbium Fiber Laser," *Laser physics*, vol. 20, no. 3, pp. 661–664, 2010.

[128] W. Krupke and L. Chase, "Ground-state depleted solid-state lasers: principles, characteristics and scaling," *Optical and quantum electronics*, vol. 22, pp. 1–22, 1990.

[129] J. Jabczynski, L. Gorajek, J. Kwiatkowski, M. Kaskow, and W. Zendzian, "Optimization of end-pumped, actively q-switched quasi-three-level lasers," *Optics Express*, vol. 19, no. 17, pp. 15 652–15 668, 2011.

[130] D. Sardar, C. Russell, J. Gruber, and T. Allik, "Absorption intensities and emission cross sections of principal intermanifold and inter-Stark transitions of Er3+ (4f11) in polycrystalline ceramic garnet Y3Al5O12," *Journal of Applied Physics*, vol. 97, no. 12, pp. 123 501–123 501, 2005.

[131] S. Pollack, D. Chang, and N. Moise, "Upconversion-pumped infrared erbium laser," *Journal of applied physics*, vol. 60, no. 12, pp. 4077–4086, 1986.

[132] S. Pollack and D. Chang, "Upconversion-pumped population kinetics for 4I13/2 and 4I11/2 laser states of Er3+ ion in several host crystals," *Optical and quantum electronics*, vol. 22, pp. 75–93, 1990.

[133] H. R. H. Mahr and C. L. Tang., *Quantum Electronics*, vol. 1 (part A), Chap. 4, Academic, 1975.

[134] J. Koetke and G. Huber, “Infrared excited-state absorption and stimulated-emission cross sections of Er 3+-doped crystals,” *Applied Physics B: Lasers and Optics*, vol. 61, no. 2, pp. 151–158, 1995.

[135] P. Le Boulanger, J. Doualan, S. Girard, J. Margerie, and R. Moncorgé, “Excited-state absorption spectroscopy of Er3+-doped Y3Al5O12YVO4, and phosphate glass,” *Physical Review B*, vol. 60, no. 16, p. 11380, 1999.

[136] D. Sardar, W. Bradley, J. Perez, J. Gruber, B. Zandi, J. Hutchinson, C. Trussell, and M. Kokta, “Judd-Ofelt analysis of the Er3+(4f11) absorption intensities in Er3+-doped garnets,” *Journal of Applied Physics*, vol. 93, pp. 2602–2607, 2003.

[137] M. O. Iskandarov, A. A. Nikitichev, and A. I. Stepanov, “Quasi-two-level Er3+:Y3Al5O12 laser for the 1.6μm range,” *J. Opt. Technol.*, vol. 68, no. 12, p. 885, Dec 2001. [Online]. Available: http://jot.osa.org/abstract.cfm?URI=JOT-68-12-885

[138] H. Injeyan, C. Hoefer, and S. Palese, “Optical amplifier comprising an end pumped zig-zag slab gain medium,” Jul. 2 2008, eP Patent 1,646,117.

[139] G. Goodno, Z. Guo, R. Miller, I. Miller, J. Montgomery, S. Adhav, and R. Adhav, “Investigation of β-BaBO as a Q-switch for high power applications,” *Applied physics letters*, vol. 66, p. 1575, 1995.

[140] D. Hosken, D. Mudge, C. Hollitt, K. Takeno, P. Veitch, M. Hamilton, and J. Munch, “Development of power scalable lasers for gravitational wave interferometry,” *Progress of Theoretical Physics Supplement*, vol. 151, pp. 216–220, 2003.

[141] D. Ottaway, P. Veitch, M. Hamilton, C. Hollitt, D. Mudge, and J. Munch, “A compact injection-locked Nd:YAG laser for gravitational wave detection,” *Quantum Electronics, IEEE Journal of*, vol. 34, no. 10, pp. 2006–2009, 1998.